ABSTRACT

Title of dissertation: THE MICRON SCALE PB ISOTOPIC SYSTEMATICS OF THE LOWER CONTINENTAL CRUST

Jeremy Joseph Bellucci
Doctor of Philosophy, 2011

Dissertation directed by: Professor William F. McDonough
Department of Geology

The thermochronology, genetic relationships, and U-Th-Pb history of the deep crust in the North China Craton, the Tanzanian Craton, and the Mozambique Belt have been interrogated using the Pb isotopic system in feldspars from lower crustal xenoliths measured via a novel LA-MC-ICP-MS method developed at the University of Maryland, College Park.

Individual feldspars analyzed from the lower crust beneath the Tanzanian Craton show a large spread in Pb isotopic compositions. The spread in isotopic data reflects radiogenic Pb that accumulated in a closed feldspar system that was below 600°C since 2.4 Ga. The entire suite of feldspar Pb isotopic compositions overlaps the common Pb measurements from the present day surface of the Tanzanian Craton. The combined surface and lower crust Pb isotopic compositions indicate a mantle extraction age of 2.7 Ga. The feldspar thermochronometry of the lower crust, along with other geochemical data, indicate that the crust of the Tanzanian Craton was extracted from the mantle ca. 2.7 Ga, in an arc setting, and cooled to a

temperature below 600°C by 2.4 Ga, and has remained undisturbed since that time.

Common Pb isotopic compositions in feldspars analyzed from the surface and deep crust of the Mozambique belt, which sits adjacent to the Tanzanian Craton show that common Pb isotopic compositions can be used to determine provenance of granulite belts at depth. Common Pb modeling of the lower, middle, and upper crust of the Western Granulites indicate a 2.5x enrichment of U in the upper crust occurred around the time of mantle extraction ca. 2.7 Ga. Additionally, the $^{238}U/^{204}Pb$ in the cratonic lower crust underlying the Mozambique Belt increases with distance away from the surface craton margin. The enrichment of U in the basement away from the surface margin of the craton, could be the reason that the Mozambique belt has been continually re-worked since the Archean, while the craton has been stable.

The Pb isotopic compositions of feldspars analyzed in granulite xenoliths from two different volcanic provinces in the North China Craton (Hannuoba and Nushan) reveal that there was a widespread crustal generation event ca. 2.5 Ga, followed by metamorphism at 1.8 Ga, as well as basaltic underplating ca. 0.15 Ga. The basaltic underplates show a composition that is a mixture between new basalt and ancient material. Felsic granulites, were extracted from the mantle ca. 2.9 Ga, and were emplaced in the crust ca. 1.8 Ga, and re-equilibrated ca. 0.15 Ga. Intermediate granulites, which were the product of the large 2.5 Ga crustal generation event, have internal feldspar isochrons of 1.7 Ga, which indicates while the lower crust was largely overprinted by the Mesozoic underplating, the lower crust was not elevated above 600°C.

The Micron Scale Pb Isotopic Systematics of the Lower Continental Crust

by

Jeremy J. Bellucci

Dissertation submitted to the Faculty of the Graduate School of the
University of Maryland, College Park in partial fulfillment
of the requirements for the degree of
Doctor of Philosophy
2011

Advisory Committee:
Professor William F. McDonough, Chair/Advisor
Professor Roberta L. Rudnick
Professor Richard J. Walker
Dr. Richard Ash
Professor Alice Mignerey, Deans Representative

Dedication

This work is dedicated to my fathers. Thank you for teaching me the value of hard work, responsibility, science, and art, all of which I hope this work is a reflection of.

Acknowledgments

I would like to acknowledge the Geology department at the University of Illinois, specifically Craig Lundstrom and Michael Stewart for introducing me to the fields of geology and geochemistry and the graduate students at the University of Maryland, for many thoughtful discussions and helpful distractions.

I would like to acknowledge my Ph.D. committee, including Drs. William McDonough, Roberta Rudnick, Richard Ash, and Richard Walker. I am very grateful for your continual constructive comments, criticisms, intellect, guidance, and discussions. It takes a lot of effort, patience, and guidance to see a new technique and idea be realized, thank you for being so patient.

Finally, I would like to acknowledge my family and friends, who provided endless moral support and encouragement. I couldn't have completed this journey without you.

Table of Contents

List of Tables

List of Figures

Chapter 1

Introduction

1.1 Contributions

The text and figures in this chapter were created by J. Bellucci.

1.2 The Continental Crust

The Earth is a unique body in our solar system; when compared to the other rocky planets, the Earth displays a bi-modal distribution of topography, with the continental crust "riding high" above the ocean basins. The continental crust comprises only 0.6% of the mass of the Earth, but contains roughly 30% of the most incompatible (during mantle melting) and heat producing elements including Cs, Rb, K, U, Th, and La (Rudnick and Gao, 2003; Taylor and Mclennan, 1995). The bulk composition of the continental crust is andesite (Taylor and Mclennan, 1985; Rudnick and Gao, 2003), but is heterogenous in terms of surface area (laterally), depth (vertically), and age. The continental crust is home to virtually every rock type and the world's oldest rocks, located in the 4.2 Ga Nuvvuagittuq greenstone belt in northern Canada (O'Neil et al., 2008), and minerals, which are represented by the 4.4 Ga detrital zircons found in the Jack Hill's province in Western Australia (Wilde et al., 2001). The continental crust is also home to some of the world's

youngest rocks in rift basins and active volcanoes. The oldest rocks and minerals in the geologic record are preserved in cratons (from the greek word *cratos* for strength). Cratons formed in the Archean from $\sim$ 3.8 - 2.5 Ga and have persisted, mostly unaltered, through geologic time. Many studies have tried to address the question of the formation and persistence of cratons, however the answer remains elusive.

Cratons have many unique properties, including low surface heat flow ($\sim$ 40 mW/m^2) in comparison to tectonically active areas ($>$ 50 mW/m^2), and deep lithospheric keels (mantle roots) that can extend to $\sim$150 km depth or more (Carlson et al., 2005; Nyblade and Pollack, 1993). A potential mechanism to create a low heat flow region is the mobilization of heat producing elements (HPEs, U, Th, K) through the crust. A depletion in HPEs in the lower crust, coupled with erosion of a HPE rich upper crust, and a cold mantle root, would create a low heat flow region which would have a rigid rheology and therefore, be resistant to deformation (e.g., Perry et al., 2006; Sandiford and McLaren, 2002). Accordingly, understanding the differentiation of the crust, specifically in the lower crust, is necessary to understand geological processes, as well as continental crust and craton formation through time.

At $\sim$ 40 wt.% of the continental crust, the lower crust is a significant reservoir for incompatible elements (Rudnick and Fountain, 1995; Rudnick and Gao, 2003). While the upper crust is readily sampled and analyzed, the inaccessibility of the lower crust makes its composition more difficult to ascertain. Based on the predicted temperature and pressure, the lower crust is widely believed to reside in the granulite facies; and for that reason, granulite facies xenoliths, brought to the surface by alkali

basalts or other volcanism (e.g., kimberlites), are thought to be direct samples of the lower crust at the time of volcanic eruption (Rudnick, 1992). Lower crustal xenoliths are predominantly mafic (Rudnick, 1992), and seismic data indicate widespread mafic lower crust (Christensen and Mooney, 1995; Rudnick, 1992; Rudnick and Fountain, 1995; Rudnick and Taylor, 1987). Therefore, granulite facies xenoliths are appropriate for use in determining the composition and thermal history of the current lower continental crust (Rudnick, 1992; Schmitz and Bowring, 2003).

Studies of lower crustal xenoliths allow the origin, differentiation and thermal history of the continental crust to be determined (e.g., Wendlandt et al., 1993; Rudnick, 1992; Rudnick et al., 1998; Schmitz and Bowring, 2003). Traditionally, several isotopic systems have been used to quantify and date crust formation and differentiation, most notably Rb-Sr; Sm-Nd; U-Pb; and Pb-Pb. The U-Th-Pb isotopic system is ideal for studying crustal formation, mixing, and differentiation processes because it provides precise age constraints, as well as time-integrated histories of heat producing and incompatible (during mantle melting) elements (Gancarz and Wasserburg, 1977; Bodet and Scharer, 2001; Kamber et al., 2003).

1.3 The Pb isotopic system

The Pb isotopic system has four isotopes: ^{208}Pb, ^{207}Pb, ^{206}Pb, and ^{204}Pb, with abundances of ∼50, 25, 25, 1%, respectively. Isotopes ^{208}Pb, ^{207}Pb, and ^{206}Pb are daughter products of the spontaneous radioactive decay of ^{232}Th, ^{235}U, and ^{238}U, respectively. Isotope ^{204}Pb is the only non-radiogenic Pb isotope in the Pb isotopic

system. The radioactive decay of ^{232}Th, ^{235}U, and ^{238}U into their respective daughter products follow these generalized decay equations:

$$^{208}Pb = {}^{208}Pb_i + {}^{232}Th * e^{\lambda_3 \text{t-1}} \tag{1.1}$$

$$^{207}Pb = {}^{207}Pb_i + {}^{235}U * e^{\lambda_2 \text{t-1}} \tag{1.2}$$

$$^{206}Pb = {}^{208}Pb_i + {}^{238}U * e^{\lambda_1 \text{t-1}} \tag{1.3}$$

where Pb is the total Pb in the system, Pb_i is the initial Pb concentration (common Pb) and λ is the decay constant for each isotope. The λ values used for ^{232}Th(λ_3), ^{235}U(λ_2), and ^{238}U(λ_1) are 4.9475*10^{11}, 9.8485*10^{10}, 1.55125*10^{10} (Jaffey et al., 1971; Le Roux and Glendenin, 1963) respectively, which translate into half lives of 14 Ga, 4.5 Ga, and 0.7 Ga, respectively. Using the decay constant and abundances of each isotope, an age can be calculated by solving for t. The analytical equipment used in this study is more suited for measuring ratios than gross abundance of an individual isotope. Therefore, we look at the above equations ratioed to the invariant isotope ^{204}Pb and so they take the following form:

$$\frac{^{208}Pb^*}{^{204}Pb} = \frac{^{208}Pb}{^{204}Pb} + \frac{^{232}Th}{^{204}Pb} * e^{\lambda_3 \text{t-1}} \tag{1.4}$$

$$\frac{^{207}Pb^*}{^{204}Pb} = \frac{^{207}Pb}{^{204}Pb} + \frac{^{235}U}{^{204}Pb} * e^{\lambda_2 \text{t-1}} \tag{1.5}$$

$$\frac{^{206}Pb^*}{^{204}Pb} = \frac{^{206}Pb}{^{204}Pb} + \frac{^{238}U}{^{204}Pb} * e^{\lambda_1 \text{t-1}} \tag{1.6}$$

As an example, we will use the parent/daughter relationship of ^{238}U and ^{206}Pb to calculate an age via an "isochron" (Figure 1.1). Similar diagrams and age calculations can be made for each of the 3 (^{232}Th, ^{238}U, and ^{235}U) decay chains. The

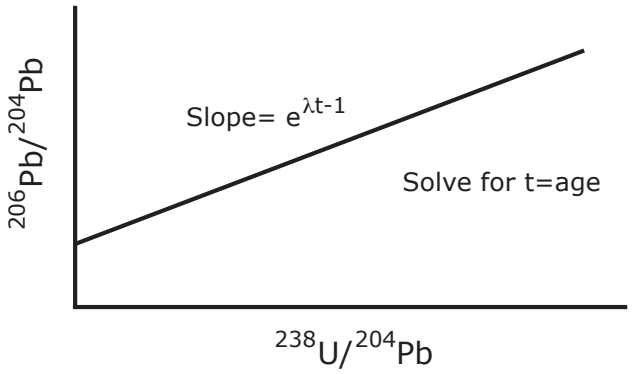

Figure 1.1: An isochron diagram for ^{238}U/^{204}Pb vs. ^{206}Pb/^{204}Pb

system is known as "concordant" if all three ages agree. A concordant system is, unfortunately, rare due to the variable mobility of each chemical species.

If the U, Th, or Pb in a system has been removed recently, resulting in discordance, an age can still be calculated by ^{207}Pb/^{206}Pb dating. The ratio of ^{238}U to ^{235}U is constant at 137.88 (in terrestrial rocks), therefore, the U decay chains can be divided to remove the concentration of U, resulting in the following equation:

$$\frac{\frac{^{207}Pb^*}{^{204}Pb} - \frac{^{207}Pb}{^{204}Pb}}{\frac{^{206}Pb^*}{^{204}Pb} - \frac{^{206}Pb}{^{204}Pb}} = \frac{^{235}U}{^{238}U} * \frac{(e^{\lambda_2 t} - 1)}{(e^{\lambda_1 t} - 1)} \tag{1.7}$$

which can be simplified to:

$$\left(\frac{^{207}Pb}{^{206}Pb}\right)_{corrected} = \frac{1}{137.88} * \frac{(e^{\lambda_2 t} - 1)}{(e^{\lambda_1 t} - 1)} \tag{1.8}$$

Another way of utilizing the U-Pb decay scheme in high U/Pb minerals is by combining the two U series in a "concordia" diagram (Figure 1.2). Measuring the ^{206}Pb/^{238}U and ^{207}Pb/^{235}U ratios in minerals that have abundant U and high closure temperature (the temperature at which the parent and daughter isotopes do not diffuse outside of the given mineral, which is a function of grain size, mineral

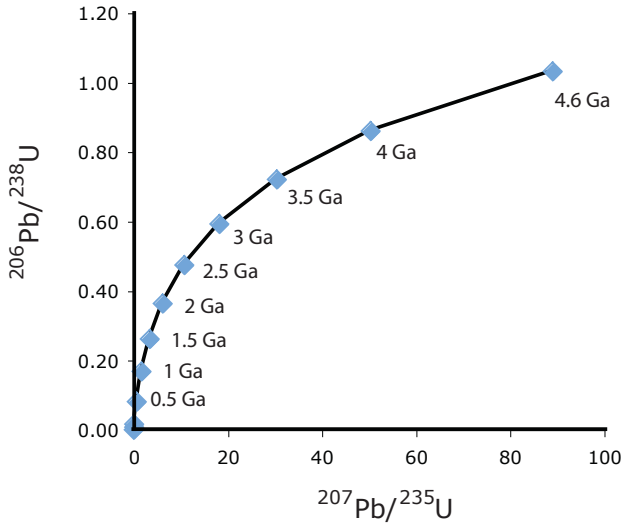

Figure 1.2: Standard Concordia Diagram

lattice shape, and diffusion coefficient of a chemical species, after Dodson, 1973), such as zircon results in a robust age calculation (Figure 1.2).

The main issue with the concordia diagram is if Pb loss has occurred; Pb loss occurs because it has a lower closure temperature than U, which will create a discordant age. A way of utilizing the Pb isotopic system, without the difficulties of recent Pb loss or U mobility, is the Pb-Pb isotopic system. The Pb-Pb system is comprised of two components: common Pb and radiogenic Pb (Pb*). Common Pb is the Pb present at the last equilibrium/crystallization of a rock and is preserved in minerals that have a low U/Pb and Th/Pb (which do not accumulate Pb* over time). Typical common Pb minerals are galena (PbS_2), other sulphides, and alkali or plagioclase feldspar ($KAlSi_3O_8$ - $NaAlSi_3O_8$ - $CaAl_2Si_2O_8$). Radiogenic Pb is located in minerals with a moderate to high U/Pb and Th/Pb which accumulate radiogenic Pb over time. Typical Pb* minerals are monazite

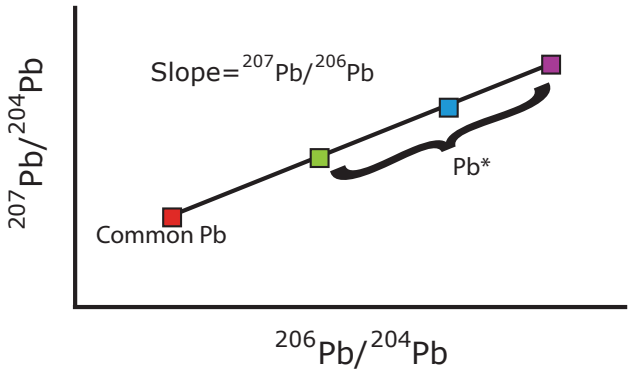

Figure 1.3: Schematic diagram of Pb-Pb isochron

((REE)PO_4), titanite ($CaTiSiO_5$), apatite ($Ca_5(PO_4)_3$(F, Cl, OH)), rutile (TiO_2), garnet ($X_3Y_2(SiO_4)_3$, where X is Ca^{2+}, Mg^{2+}, or Fe^{2+} and Y is Al^{3+}, Fe^{3+}, or Cr^{3+}), allanite ($(Ce,Ca,Y,La)_2(Al,Fe^{+3})_3(SiO_4)_3(OH)$), and zircon ($ZrSiO_4$). Using the two components of the Pb-Pb isotopic system, an age can be calculated (Figure 1.3), solving for the slope and utilizing Equation 1.8. The Pb-Pb method was the first used to calculate the age of the Earth (Patterson, 1956).

The first attempt at creating a common Pb-Pb model for the Earth was undertaken by Holmes (1946) and Houtermans (1946) to date common Pb (non-radiogenic Pb) in geological systems. To accomplish this goal, they predicted the Pb isotopic composition of the Earth as a single reservoir at any point in time, calculating the initial Earth Pb isotopic composition using 3 Ga galenas. Currently the Holmes-Houterman model is used with an initial Pb isotopic composition defined by the Canyon Diablo troilite. The Canyon Diablo troilite is a mineral in an iron meteorite that contains abundant Pb and no U or Th, and is considered to preserve the initial Pb isotopic system of the solar system. Using the initial solar system value and any

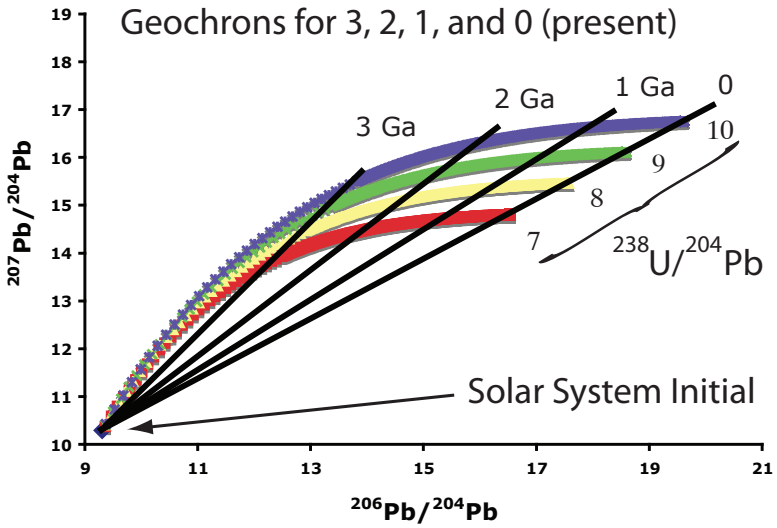

Figure 1.4: $^{207}Pb/^{204}Pb$ vs. $^{206}Pb/^{204}Pb$ growth curves and Geochron projections.

$^{238}U/^{204}Pb$, the Pb isotopic composition at any point in time can be calculated. The array of points of the same time, but different $^{238}U/^{204}Pb$ are called "geochrons" (Figure 1.4). Common Pb measurements can be used to calculate an age if they lie on a Geochron. In addition to an age, any point on the Geochron requires a specific $^{238}U/^{204}Pb$. Therefore, using common Pb dating, a model age and $^{238}U/^{204}Pb$ can be calculated using Figure 1.4. Similarly, assuming a $^{232}Th/^{238}U$, a model age can be calculated following Figure 1.5. In addition to providing age constraints, the Pb isotopic system, in low U/Pb systems, can be used to model the time integrated U-Th-Pb systematics in the reservoir(s) in which that rock resided (e.g., Bodet and Scharer, 2001; Bolhar et al., 2007; Gancarz and Wasserburg, 1977; Kamber et al., 2003; Ludwig and Silver, 1977; Oversby, 1978).

Common Pb ages of igneous rocks are typically inaccurate due to crustal contamination and the presence of radiogenic Pb, which shrouds the true common Pb

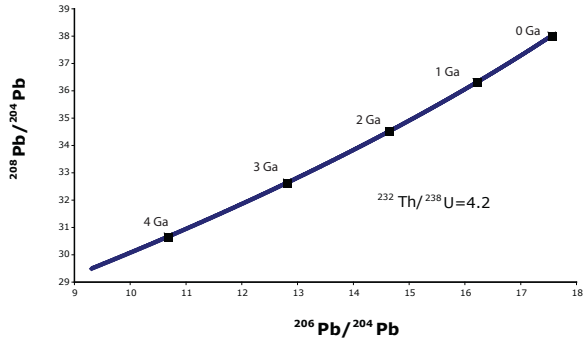

Figure 1.5: $^{208}Pb/^{204}Pb$ vs. $^{206}Pb/^{204}Pb$ growth curve assuming a $^{232}Th/^{238}U$ of 4.2.

isotopic composition (e.g., Holmes, 1946; Houtermans, 1946; Stacey and Kramers, 1975). Common Pb measurements are typically made on leached minerals that have low U/Pb, where the radiogenic Pb from the system is removed. In silicate minerals, common Pb measurements are typically made on both plagioclase and alkali feldspar, which have a low U/Pb value and a relatively low closure temperature (550-600°C; Cherniak, 1995). The radiogenic Pb housed in feldspar has many components which have been attributed to U-bearing phases, grain boundary contamination, and exsolution lamellae Frei and Kamber (1995). Leaching feldspars removes the radiogenic Pb housed in the aforementioned reservoirs and accurate Pb-Pb ages can be gleaned from the measurement of both the leached common Pb component and the multiple leachates, implying a U-Th-Pb system closed to isotopic dffusion (e.g., Frei and Kamber, 1995; Housh and Bowring, 1991). Specifically, alkali feldspar is complicated by exsolution phenomena, which create discreet zones of varying U/Pb and therefore, Pb isotopic compositions. The leaching procedure targets grain boundary contamination and non-feldspar phases, therefore radiogenic

Pb housed in the feldspar will not be fully leached out, masking the true common Pb isotopic composition. Radiogenic in-growth of Pb is of specific concern, especially in old rocks that have time to evolve Pb isotopic compositions, thereby creating a large spread in Pb isotopic compositions within a single or multiple feldspar grains.

1.3.0.1 Spatial resolution

Advances in *in situ* analytical techniques, specifically laser ablation inductively coupled plasma mass spectrometry (ICP-MS), have allowed for microanalyses of discreet zones inside minerals. In particular, discreet zones of Pb isotopic compositions inside feldspar can be sampled. Moreover, multiple feldspars, which could have varying U/Pb, can be analyzed to arrive at a Pb-Pb age and a true common Pb isotopic composition (Bellucci et al., 2011). Common Pb isotopic compositions can be used to model the provenance and genetic relationship of crustal and lithospheric bodies, as well as the time-integrated $^{238}U/^{204}Pb$ and $^{232}Th/^{238}U$ of the crust and mantle from which that crust was derived (e.g., Bellucci et al., 2011; Bodet and Scharer, 2001; Gancarz and Wasserburg, 1977; Zartman and Wasserburg, 1969). Additionally, if a single feldspar crystal has multiple Pb isotopic domains,the rock in which the grain resided must have remained below the closure temperature of Pb in feldspar (to prevent diffusive equilibration).

1.4 Summary

The focus of this thesis is on quantifying the age, thermal history, and U-Th-Pb systematics of Archean lower crust, through the analysis of feldspars in lower crustal xenoliths using LA-MC-ICP-MS. A focus will be placed on understanding the ancient lower crust beneath the Tanzanian Craton, the Mozambique Belt, and the North China Craton. In the appendices to this document, a further exploration of the Pb isotopic system is presented in terms of an archaeological provenance study and Pb-Pb dating of extraterrestrial materials. In addition to the exploration of the Pb isotopic system, a precise and accurate method to measure mono-isotopes (i.e., Rh and Au) via standard addition is presented.

1.5 Thesis Outline

1.5.1 Chapter 2

The analytical method for measuring Pb isotopic compositions *in situ* is presented. Accuracy, precision, as well as sample volume are discussed.

1.5.2 Chapter 3

In Chapter 3, the Pb isotopic data from feldspars in lower crustal xenoliths from the Labait Volcano, which is located on the edge of the Tanzanian Craton, are presented. Implications for age, thermochronometry, and the U-Th-Pb systematics in the Archean mantle are discussed.

1.5.3 Chapter 4

The Pb isotopic data for feldspars from xenoliths from volcanoes in the Mozambique Belt are presented. Implications for provenance, intra-crustal differentiation, Pb isotopic growth in the Archean continental crust, as well as implications for craton stability are discussed.

1.5.4 Chapter 5

The Pb isotopic compositions of feldspars from lower-middle crustal xenoliths in the North China Craton are presented. Implications for age, crustal growth, thermochronometry, and U-Th-Pb systematics of the Archean crust and mantle are discussed.

1.5.5 Chapter 6

This chapter presents general conclusions and a summary of feldpsar thermochronometry, as well as the U-Th-Pb systematics of Archean aged lower.

1.5.6 Appendix A

Appendix A describes the application and results of *in situ* Pb isotopic measurements to determine the provenance of archaeological samples.

1.5.7 Appendix B

Appendix B describes the method for determining accurate $^{207}Pb/^{206}Pb$ ages in a pair of achondrite meteorites.

1.5.8 Appendix C

Appendix C describes the method for determining the absolute concentrations of two mono-isotopic elements (Rh and Au), in iron meteorites via standard addition.

1.5.9 Appendix D

Appendix D contains all of data tables from the individual samples and their multiple feldspar analyses from Chapters 3-6.

Chapter 2

Analytical Method

2.1 Contributions

J. Bellucci, under the direction of W. McDonough and R. Ash, designed the analytical procedure, apparatus, and collected all of the data presented. I. Puchtel assisted in all solution chemistry. J. Bellucci created all of the text, figures, and tables.

This chapter was published as the online supplement to:

Bellucci, J. J., McDonough, W. F., and Rudnick, R. L. (2011). Thermal history and origin of the Tanzanian Craton from Pb isotope thermochronology of feldspars from lower crustal xenoliths. Earth and Planetary Science Letters, 301(3-4):493 501.

2.2 Apparatus

All *in situ* Pb isotopic analyses were conducted using a Nu Plasma HR MC-ICP-MS (Belshaw et al., 1998) coupled with a New Wave UP 213 nm frequency quintupled laser system. All samples were mounted in epoxy or thick (60 μm) sections. A Cetac Aridus system was used in conjunction with the mass spectrometer and laser ablation to inject N_2 gas into the plasma source. Tuning of the mass-

spectrometer was performed using a 20 ng/g Pb solution introduced through the Aridus (see Table 2.1 for typical Aridus settings). During laser ablation ultra-pure 18 MΩ (milli-Q) water was flushed through the Aridus using identical settings as the tune solution. A schematic diagram of the laser ablation apparatus is located in Figure 2.1. Various collector assignments and typical operating conditions for the Nu Plasma, Aridus, and UP-213 are located in Table 2.1.

2.3 Collector Arrangements

2.3.1 Faraday Cups

Isotopes ^{208}Pb, ^{207}Pb, ^{206}Pb, ^{205}Tl, and ^{203}Tl were collected in Faraday cups. Faraday cups can be used for signals $>10^4$ counts per second (cps), below which background noise becomes significant. The ion beam creates a direct current on the detector, thus the current can be measured precisely as a voltage drop across a well-calibrated 10^{11} Ω resistor. An advantage to using Faraday cups is accurately calibrating the gain between detectors by applying a known potential ($\sim$ 10 V) to each cup's amplifier. The instrument then applies a correction, based on the voltage gains or deficiencies through the resistor, to correct for the gain differences between each cup. A disadvantage to using Faraday cups is that a residual charge can build up on the large resistor and affect the ability for the cup to accurately report rapidly changing signals. This affect can be accounted for by modifying the Tau constant on each cups resistor (Hirata et al., 2003; Paul et al., 2005). The modification of the Tau constant results in a faster refresh rate for each cup, and therefore, allows

the accurate recording of rapidly changing signals.

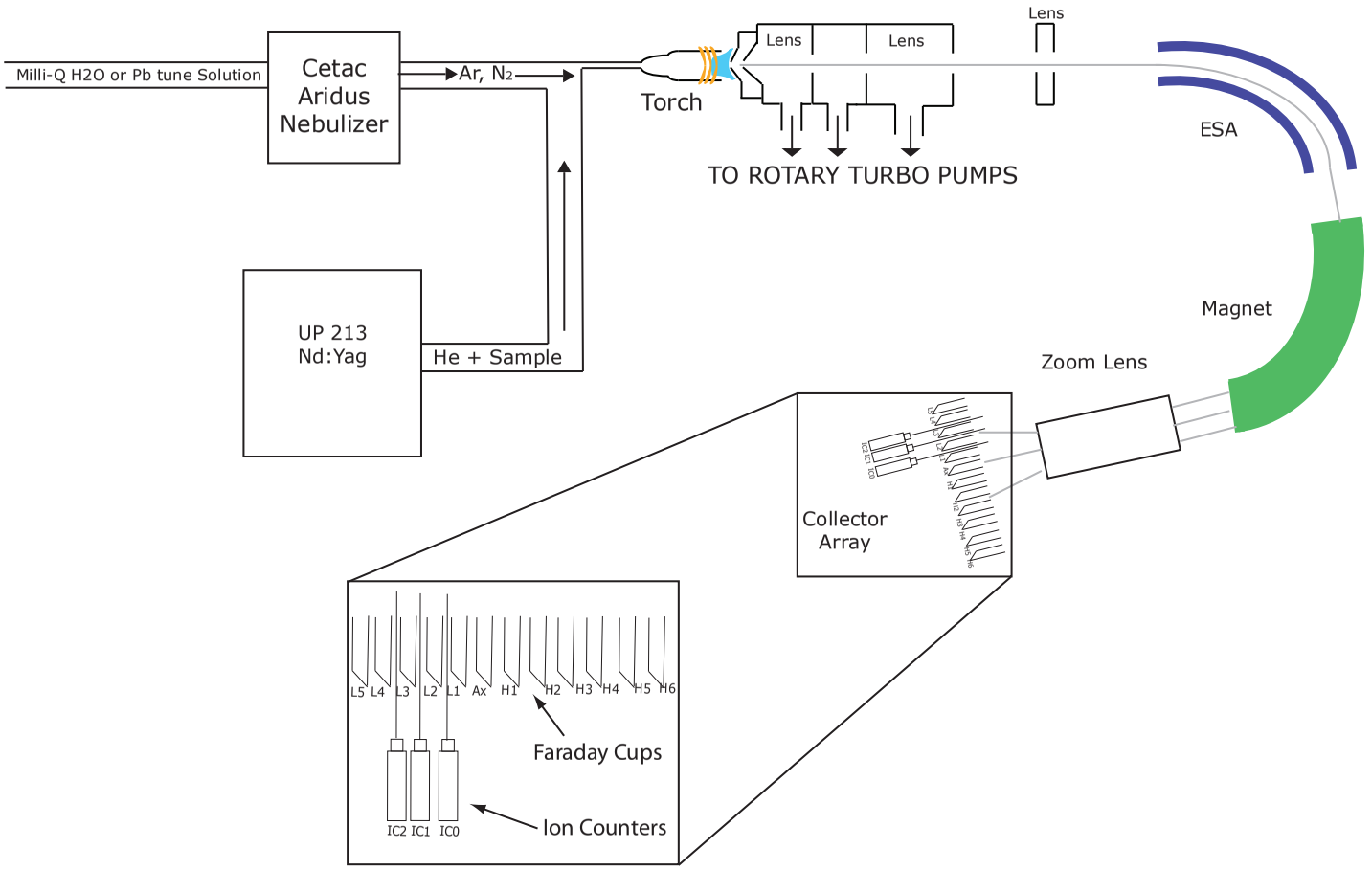

Figure 2.1: Schematic diagram of Nu Plasma with attached laser ablation system.

Table 2.1. Typical operating conditions for *in situ* Pb isotopic analysis and collector assignments for various Pb isotopic analysis

Mass Spectrometer	
	Nu Plasma
Instrumentation:	MC-ICP-MS
Forward Power	1300 W
Reflected Power	<10 W
Cones	Ni
Acceleration Voltage	4000 V
Typical gas Flows	
Coolant	13 L min^{-1}
Auxilary	0.8 L min-1
Nebulizer	0.77 L min-1
Aridus Gas flows	
Sweep Gas	2.20 L min^{-1}
N_2	0.15 L min^{-1}
Laser	
Instrumentation:	New Wave UP 213 213 nm frequency quintupled Nd-Yag
Sweep Gas	
He	0.3 L min^{-1}
Line Diameter	100-150 µm
Line Length	350-550 µm
Analysis Duration	40-80 s
Translation Rate	7 µm s^{-1}
Pulse Frequency	7 hz
Pulse Energy	4.5 J cm^{-2}

Collector[1]	H6	H5	H4	H3	H2	H1	Ax	L1	L2	ICO	L3	IC1	L4	IC2	L5
Solution and High Concentration Pb LA-Analyses Analyte Isotopes			^{208}Pb	^{207}Pb	^{206}Pb	^{205}Tl	^{204}Pb	^{203}Tl	^{204}Hg		^{202}Hg		^{200}Hg		
Laser ablation Interferences						^{208}Pb	^{207}Pb	^{206}Pb	^{205}Tl[2]	^{204}Pb ^{204}Hg	^{203}Tl[2]	^{202}Hg		^{200}Hg	

[1] Collectors H*x* and L*x* are Faraday Cups, and Icx are ion counters.

[2] Although Tl is measured it is not in significant abundance to be used in mass bias corrections.

2.3.2 Ion Counters

Isotopes ^{204}Pb, ^{202}Hg, and ^{200}Hg were collected in parallel ion counters. Ion counters are employed when signal sizes are $<10^4$ cps and not $>10^6$ cps. Ion counters employ a pulse counting method. These detectors are ideal for low abundance isotopes (e.g., ^{204}Pb, which comprises $\sim$1% of the Pb isotopic composition) and gas related interferences (e.g., ^{202}Hg and ^{200}Hg). A significant disadvantage to using the ion counters is that they cannot be cross-calibrated as easily as the Faraday cups, and cannot be automatically calibrated with each Faraday cup. In a later section the gain correction between the ion counters and Faraday cups is discussed (Section 2.7).

2.4 Analytical Concerns

2.4.1 Background

Prior to ablation, an on peak zero was taken for 60s, while the laser was on and masked with the in line laser shutter to correct for any background Hg and Pb. Any measurement outside the 3σ of the mean of the background signal was removed, and the average of the remaining signal was subtracted real-time from each succeeding (0.2s, the integration time) measurement.

2.4.2 Isobaric Interferences

The most significant isobaric interference on the Pb isotopic system is the ^{204}Hg interference on ^{204}Pb. The isotope ^{204}Hg is $\sim 7\%$ of the total Hg in the system, where ^{202}Hg and ^{200}Hg make up $\sim$30% and $\sim$23%, respectively. Hg is ubiquitous in the analytical equipment, plasma gases, and can be in the sample itself. Here we used a correction similar to (Kent, 2008a; Paul et al., 2005).

Background corrected signals for masses 204 and 202 and Equation 2.1 (modified from Paul et al., 2005) were used to strip ^{204}Hg from the ^{204}Pb signal at each integration period (0.2s) during each analysis. The natural abundance ratio of ^{204}Hg/^{202}Hg is 0.2299 and the mass ratio is 1.0099 (de Laeter et al., 2003).

$$^{204}Pb_{corrected} = (204 - 204_{background}) - (202 - 202_{background}) * \frac{\left(\frac{^{204}Hg}{^{202}Hg}\right)_{natural}}{\left(\frac{m_{^{204}Hg}}{m_{^{202}Hg}}\right)^{\alpha_{Hg}}} \quad (2.1)$$

The fractionation factor (α) for Hg was determined using the Exponential fraction law where the fractionation factor is given by Equation 2.2. The natural ^{202}Hg/^{200}Hg is 1.293 and the mass ratio is 1.0100 (de Laeter et al., 2003).

$$\alpha_{Hg} = \frac{ln\left(\frac{\left(\frac{^{202}Hg}{^{200}Hg}\right)_{natural}}{\left(\frac{^{202}Hg}{^{200}Hg}\right)_{measured}}\right)}{ln\left(\frac{m_{^{202}Hg}}{m_{^{200}Hg}}\right)} \quad (2.2)$$

2.5 Analytical Protocols

The Pb isotopic system does not have a non-radiogenic internal isotopic pair to correct for mass fractionation effects. During Pb solution measurements, Tl was

introduced because Tl has been shown to serve as a good proxy for Pb fractionation (e.g., Baker et al., 2004; Weis et al., 2006; White et al., 2000, and references therein). During laser ablation analyses, we have attempted to use Tl as an internal standard, but in most of the samples Tl is not in sufficient abundance to be viable an internal standard. Instead, we have employed the use of standard-sample bracketing, which has been shown as a viable method for *in situ* Pb analysis (e.g., Jochum et al., 2006; Kent, 2008a; Paul et al., 2005; Simon et al., 2007). Our block analyses consisted of two standards before and after 3-8 unknowns. For our standard we used SRM NIST 612, which has been well characterized with respect to the Pb isotopic system (Baker et al., 2004) and has been shown to be homogenous (Kent, 2008b). Furthermore, NIST 612 has a similar concentration (40 μg/g, Pb) to our samples, to where we can use similar laser operating conditions with both standards and samples.

2.6 Mass Bias and Gain Calibration

Ionization of atoms by the plasma, space charge effects (heavier ions push lighter ions further out of the ion stream), and isotopic (and elemental) fractionation at the site of ablation create a mass bias (or mass fractionation) that must be corrected. While the three aforementioned processes affect the ion stream in different stages of introduction to the mass spectrometer, we observed the integrated effects as a single effect. Similar to the Hg fractionation correction, we used the Exponential law to correct for mass fractionation effects, except we normalized to the external standard SRM NIST 612 using the $^{208}Pb/^{206}Pb$ value from Baker et al. (2004),

following Equation 2.3.

$$\alpha_{Pb} = \frac{ln\left(\frac{\left(\frac{^{208}Pb}{^{206}Pb}\right)_{NIST612}}{\left(\frac{^{208}Pb}{^{206}Pb}\right)_{measured}}\right)}{ln\left(\frac{m_{^{208}Pb}}{m_{^{206}Pb}}\right)} \tag{2.3}$$

2.7 Gain Calibration

As a positive consequence of using external normalization, using the α_{Pb} calculated from the measured ^{208}Pb/^{206}Pb value and the known values for the other Pb ratios from Baker et al. (2004), an expected value for the other Pb isotopic ratios was calculated. Taking the ratio of the calculated to measured values for these ratios yielded a gain correction for the following detectors (masses) Ax(207)-L1(206), H1(208)-IC0(204), Ax(207)-IC0(204), and L1(206)-IC0(204), following Equation 2.4 (similar to Kent, 2008a; Paul et al., 2005).

$$GainCorrection = \frac{\left(\frac{^{20x}Pb}{^{20y}Pb}\right)_{calculated}}{\left(\frac{^{20x}Pb}{^{20y}Pb}\right)_{NIST612,measured}} \tag{2.4}$$

Using these Gain Corrections, any unknown ratios were calculated from the measured ratios using Equation 2.5 (similar to Kent, 2008a; Paul et al., 2005).

$$\left(\frac{^{20x}Pb}{^{20y}Pb}\right)_{corrected} = \left[\left(\frac{^{20x}Pb}{^{20y}Pb}\right)_{measured} * \left(\frac{m_{20x}}{m_{20y}}\right)^{\alpha_{Pb}}\right] * GainCorrection \tag{2.5}$$

Table 2.2 reports the robustness of the gain correction per block and long-term drift between each Faraday cup and ICO. Although there is drift, it is solely in the ion-counter and not the Faraday cups or the average Faraday gain correction for the

blocks would not be identical. Additionally, it is shown that the Faraday Cup gain is static through time, after cross-calibrating the Faraday cups before each analytical section.

2.8 Internal Precision

Internal precision is a measure of the reproducibility of measuring an isotopic ratio. This precision is largely based on Poissons counting statistics ($1/\sqrt{n}$, n being the number of ions counted). Because this precision is based on the number of ions, which is finite, one must attempt to optimize ion counting and transport efficiency. Ion efficiency (as percent) is defined as ((ions counted/total atoms ablated) x 100). The typical ionization efficiency for the laser-ablation system detailed above was $\sim$0.15%. The measure of internal precision is displayed below in Figure 2.2.

Table 2.2. Results of gain calibration between Faraday cups H1, Ax, L1 and ICO; and gain calibration between Faraday cups Ax and L1.

	Block 1	Block 2	Block 3	Block 4	Block 5	Block 6	Block Average	2σ	2σ (%)
Gain H1-IC0 ($^{208}Pb/^{204}Pb$)	0.67602	0.67666	0.68192	0.68290	0.68316	0.68110	0.6803	0.006	0.9%
Gain Ax-IC0 ($^{207}Pb/^{204}Pb$)	0.67591	0.67694	0.68188	0.68296	0.68285	0.68123	0.6803	0.006	0.9%
Gain L1-IC0 ($^{206}Pb/^{204}Pb$)	0.67602	0.67666	0.68192	0.68290	0.68316	0.68111	0.6803	0.006	0.9%
Gain Ax-L1 ($^{207}Pb/^{206}Pb$)	0.99983	1.00040	0.99993	1.00008	0.99953	1.00018	1.0000	0.0006	0.06%
Average FC-IC Gain	0.67598	0.67675	0.68191	0.68292	0.68305	0.68115	0.680294		
2σ	0.00013	0.00032	0.00005	0.00007	0.00036	0.00015	0.000002		
2σ (%)	0.02%	0.05%	0.01%	0.01%	0.05%	0.02%	0.0004%		

2.9 External Precision

External precision is the long-term reproducibility of a measured isotopic ratio. This precision takes into account varying machine-operating conditions, variable backgrounds, user based errors, sample heterogeneities, etc. The external precision is usually larger than the internal precision, due to the factors listed above. Along with the internal precision, external precision is normally improved with a larger number of ions counted, because isotopic ratios measured with a larger ion current will be less affected by small variations in signal intensity. Figure 2.3 represents 6 months of analyses of a well characterized standard, BCR2-g ($\sim$10 μg/g Pb), in comparison with the accepted literature value of Paul et al. (2005). Table 2.3 displays the LA-MC-ICPMS values determined for 2 well characterized SRMs (BCR 2-g and NIST 614), the external precision, and the accepted solution values.

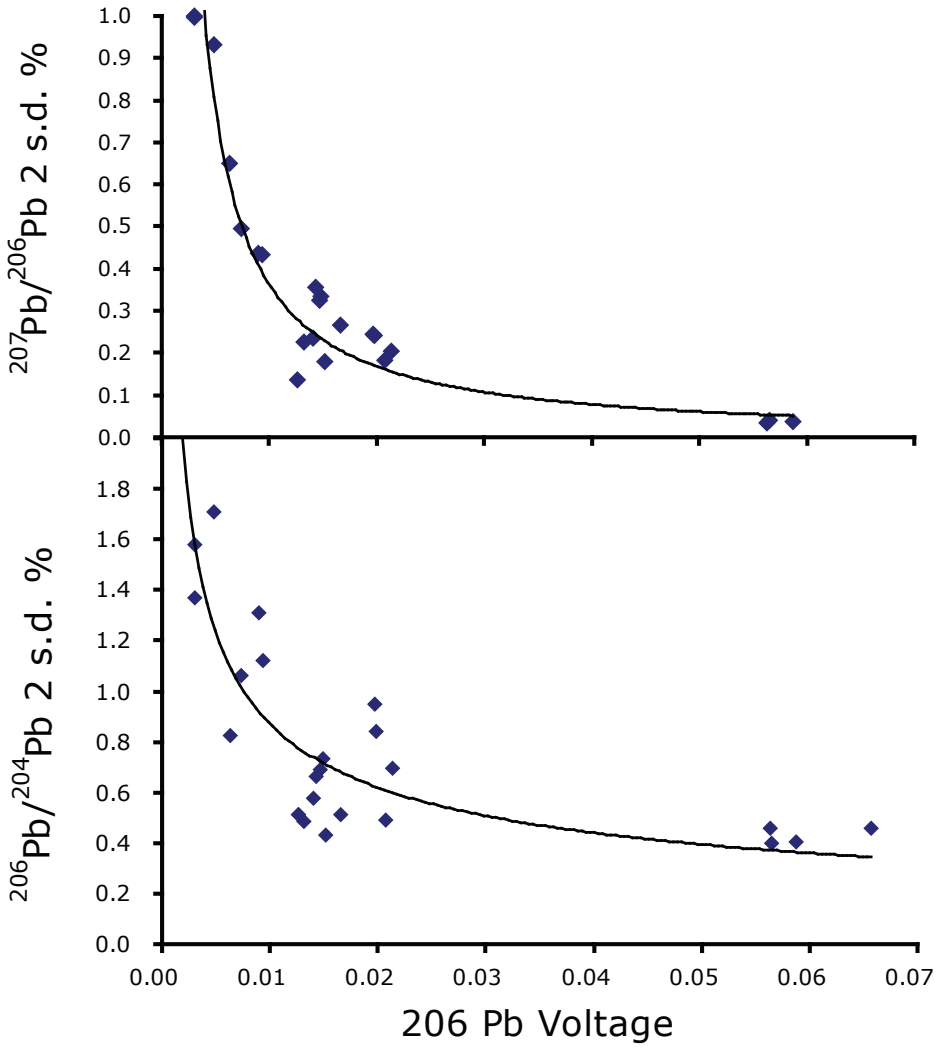

Figure 2.2: 2 s.d.% vs.^{206}Pb voltage for ratios $^{206}Pb/^{204}Pb$ and $^{207}Pb/^{206}Pb$ as a function of Poissons counting statistics.

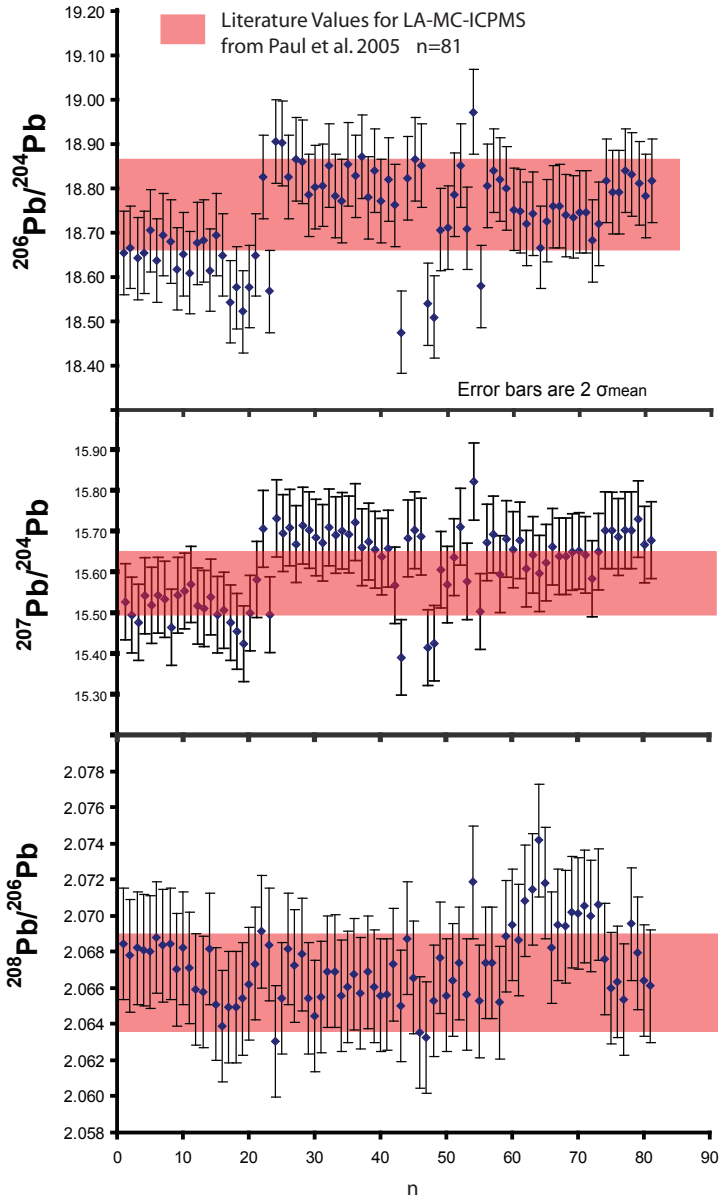

Figure 2.3: 6 months analyses of BCR 2-g, in comparison with the range seen in previous LA-MC-ICP-MS studies.

Table 2.3. Results and external precision of *in situ* Pb isotopic analyses of BCR 2-g and NIST 614 Glasses and solution values

Sample	Concentration Pb	Ablation method	$^{208}Pb/^{204}Pb$	2σ	$^{207}Pb/^{204}Pb$	2σ	$^{206}Pb/^{204}Pb$	2σ	$^{207}Pb/^{206}Pb$	2σ	$^{208}Pb/^{206}Pb$	2σ	Average ^{208}Pb V per analysis	n
BCR 2-g	~10 µg/g	100 µm Spot	38.70	0.12	15.62	0.11	18.74	0.09	0.833	0.005	2.065	0.009	0.008	12
BCR 2-g	~10 µg/g	100 µm line	38.77	0.24	15.62	0.09	18.75	0.09	0.833	0.001	2.068	0.003	0.02	81
NIST 614	~1.6 µg/g	150 µm line	37.33	0.49	15.49	0.19	17.76	0.20	0.872	0.003	2.102	0.006	0.010	6
Solution Values														
BCR 2-g	Paul et al. 2005		37.75		15.622		18.770		0.8325		2.063			
NIST 614	Baker et al. 2004		37.496		15.54		17.837		0.8713		2.102			

2.10 Reporting of error

The main analytical challenge in measuring Pb isotopic ratios is directly related to measuring the ^{204}Pb signal, because it contributes only 1% of the total Pb signal and internal precision is determined (generally) by Poisson's counting statistics. When reporting an individual time-resolved Pb isotopic measurement, in the ^{207}Pb/^{204}Pb vs. ^{206}Pb/^{204}Pb and ^{208}Pb/^{204}Pb vs. ^{206}Pb/^{204}Pb diagrams, the errors should appear as ellipses with an error correlation coefficient, ρ. When reporting an average of multiple feldspar analyses standard error bars of $2\sigma_{mean}$ are used, because it is then a measure of external precision, which is not solely dependent on the counting statistics of ^{204}Pb.

Where ρ in ^{207}Pb/^{204}Pb vs. ^{206}Pb/^{204}Pb is given by:

$$\rho_{7/4-6/4} = \frac{\%\sigma^2{}_{7/4} + \%\sigma^2{}_{6/4} - \%\sigma^2{}_{7/6}}{2 * \%\sigma_{7/4} * \%\sigma_{6/4}} \tag{2.6}$$

And ρ in ^{208}Pb/^{204}Pb vs. ^{206}Pb/^{204}Pb is given by:

$$\rho_{8/4-6/4} = \frac{\%\sigma^2{}_{8/4} + \%\sigma^2{}_{6/4} - \%\sigma^2{}_{8/6}}{2 * \%\sigma_{8/4} * \%\sigma_{6/4}} \tag{2.7}$$

Where $\%\sigma$ is given by:

$$\%\sigma_{8/4} = \frac{\sigma_{\frac{^{208}Pb}{^{204}Pb}}}{\frac{^{208}Pb}{^{204}Pb}} \tag{2.8}$$

$$\%\sigma_{7/4} = \frac{\sigma_{\frac{^{207}Pb}{^{204}Pb}}}{\frac{^{207}Pb}{^{204}Pb}} \tag{2.9}$$

$$\%\sigma_{6/4} = \frac{\sigma_{\frac{^{206}Pb}{^{204}Pb}}}{\frac{^{206}Pb}{^{204}Pb}} \tag{2.10}$$

$$\%\sigma_{7/6} = \frac{\sigma_{\frac{^{207}Pb}{^{206}Pb}}}{\frac{^{207}Pb}{^{206}Pb}} \tag{2.11}$$

$$\%\sigma_{8/6} = \frac{\sigma_{\frac{^{208}Pb}{^{206}Pb}}}{\frac{^{208}Pb}{^{206}Pb}} \tag{2.12}$$

2.11 Comparison with Literature

Several workers have also attempted to measure *in situ* Pb isotopic compositions via LA-MC-ICPMS using parallel Faraday cups and ion counters; primarily Kent (2008b) and Paul et al. (2005). Table 2.4 below displays the accuracy (as shown in Equation 2.6), precision, spot size, and total current for each groups LA-MC-ICP-MS measurements.

$$Accuracy = 100 * \frac{\left[\left(\frac{^{20x}Pb}{^{20y}Pb}\right)_{standard} - \left(\frac{^{20x}Pb}{^{20y}Pb}\right)_{measured}\right]}{\left(\frac{^{20x}Pb}{^{20y}Pb}\right)_{standard}} \tag{2.13}$$

Table 2.4. Comparison of accuracy and precision for other farday cup-ion counter *in situ* measurements

	System	Laser	Ablation Shape and size	Sample	Pb conc in µg g-1	~Σ Pb mV	Ratio	Precision 2σ %	Accuracy %
Paul et al. 2005	Nu-Plasma	Hel-Ex Eximer 193	100 µm Spot	BCR2-g	10	60	$^{208}Pb/^{204}Pb$	0.38	0.2
							$^{207}Pb/^{204}Pb$	0.42	0.21
							$^{206}Pb/^{204}Pb$	0.40	0.21
							$^{207}Pb/^{206}Pb$	0.22	0.12
							$^{208}Pb/^{206}Pb$	0.11	0.16
			100 µm Spot	MPI-KL2-G	2	12	$^{208}Pb/^{204}Pb$	1.47	0.74
							$^{207}Pb/^{204}Pb$	1.76	0.88
							$^{206}Pb/^{204}Pb$	1.43	0.72
							$^{207}Pb/^{206}Pb$	1.06	0.61
							$^{208}Pb/^{206}Pb$	0.70	0.35
Kent et al. 2008	Nu Plasma	New Wave 213 Nd-Yag or DUV 193 ArF Eximer	15-100 µm line	BCR2-g	10	40	$^{208}Pb/^{204}Pb$	0.41	0.03
							$^{207}Pb/^{204}Pb$	0.30	-0.13
							$^{206}Pb/^{204}Pb$	0.61	-0.02
							$^{207}Pb/^{206}Pb$	0.37	0.00
							$^{208}Pb/^{206}Pb$	0.14	0.05
			15-100 µm line	NIST 614	2	30	$^{208}Pb/^{204}Pb$	0.54	0.26
							$^{207}Pb/^{204}Pb$	0.52	-0.47
							$^{206}Pb/^{204}Pb$	0.56	0.10
							$^{207}Pb/^{206}Pb$	0.37	-0.01
							$^{208}Pb/^{206}Pb$	0.36	0.02
This Study	Nu Plasma	New Wave UP 213 Nd-Yag	100 µm line	BCR2-g	10	40	$^{208}Pb/^{204}Pb$	0.61	-0.04
							$^{207}Pb/^{204}Pb$	0.61	-0.03
							$^{206}Pb/^{204}Pb$	0.50	0.05
							$^{207}Pb/^{206}Pb$	0.15	-0.04
							$^{208}Pb/^{206}Pb$	0.17	-0.08
			100 µm line	NIST 614	2	20	$^{208}Pb/^{204}Pb$	1.31	0.41
							$^{207}Pb/^{204}Pb$	1.25	0.33
							$^{206}Pb/^{204}Pb$	1.13	0.45
							$^{207}Pb/^{206}Pb$	0.36	-0.19
							$^{208}Pb/^{206}Pb$	0.28	-0.13

2.12 Trace element analyses

Trace element analyses were performed *in situ* using a New Wave UP:213 coupled with a ThermoFinnigan Element 2 single collector ICP-MS. The instrument settings are available in Table 2.5. Prior to analysis the Element 2 was tuned for maximum sensitivity on ^{43}Ca and ^{232}Th, while minimizing ^{232}ThO. Background counts were determined for 30 s with the laser on and shuttered. Analyses were conducted in low mass resolution with 10 ms dwell times. Concentrations were determined using external standard NIST 612 and normalizing all concentrations to CaO using the Lamtrace Lotus 123 macro (Achterbergh et al., 2001). Calcium oxide concentrations were externally determined with the JXA-8900 SuperProbe electron probe microanalyzer at the University of Maryland.

2.13 Solution Measurements: Dissolution and Column Chemistry

Powdered samples were weighed in quantities of 70-80 mg in a teflon beaker. Powders were cleaned with ethanol in an ultrasonic bath for 2-3 minutes followed by a similar bath in milli-Q water for 2-3 minutes. Samples were then decanted and dried down. The samples were dissolved in a solution of 1 mL concentrated HF and 1 mL concentrated HNO_3, then heated on a hot plate at 140°C for ∼12 hrs. The sample solutions were dried down and this procedure was repeated 3x. After the third dry down, 0.5 mL concentrated HBr was added to the residue. The HBr loaded samples were allowed to equilibrate for 8 hrs, and then dried down. Following dry down, the samples were re-dissolved in 0.6 N HBr.

Table 2.5. Typical operating conditions for *in situ trace element analyses*

Mass spectrometer	
Instrumentation	Thermo Finnigan Element-2
Forward power	1250 W
HV	10 kV
Cones	Ni-alloy
Cool gas flow	16 L min^{-1}
Auxiliary gas flow	1.5 L min^{-1}
Sampler cone	1.0 mm diameter
Skimmer cone	0.4 mm diameter
Scan Optimization	Speed
Guard Electrode	Disabled
Mass resolution (M/DM)	300
Samples per peak	1
Scan Type	Escan
Laser Instrumentation:	New Wave UP 213 213 nm frequency quintupled Nd-Yag
Sample Gas Gas	0.7 L min^{-1}
He gas flow	1.1 L min^{-1}
Spot Diameter	40 µm
Pulse Frequency	7 hz
Pulse Energy	4.5 J cm^{-2}

Ion exchange columns loaded with Biorad AG50W-X8 resin were cleaned 2x using 6N HCl and 1x using milli-Q water. The ion exchange columns were conditioned with 0.5 ml 0.6N HBr. Following column conditioning, samples were loaded onto the exchange resin. After sample loading, the column was washed twice using 0.5 mL 0.6N HBr. The Pb was then eluted using 0.7 mL 6N HCl. This solution was then dried down for ∼12 hrs. The purified Pb was then re-dissolved in 2% HNO_3 and Tl was added in a 2:5 Tl:Pb ratio for mass bias correction.

2.13.1 Lab blank

The procedural lab blank was determined by re-dissolving the dried blank in 2.5 ml of 2% HNO_3. To determine the concentration of Pb in the lab blank, a

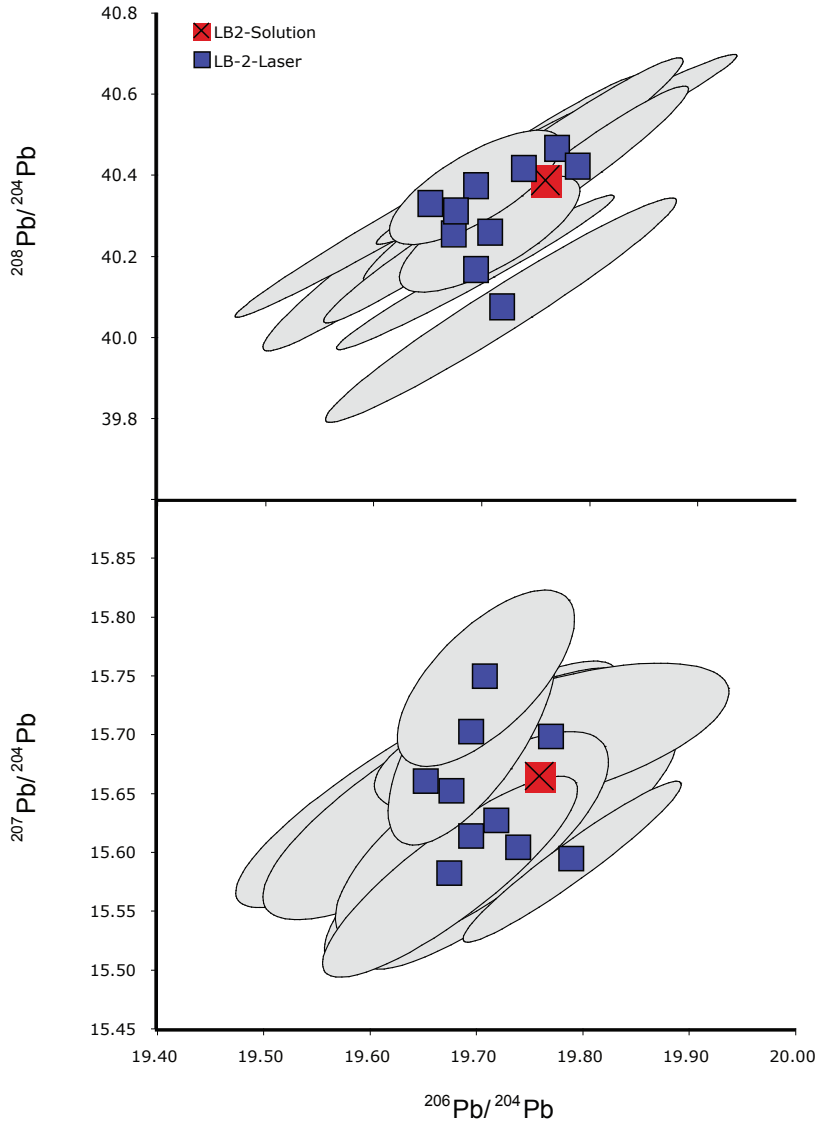

Figure 2.4: A comparison of solution MC-ICPMS analyses with LA-MC-ICPMS analyses of LB2, a melilite from the Labait volcano, Tanzania.

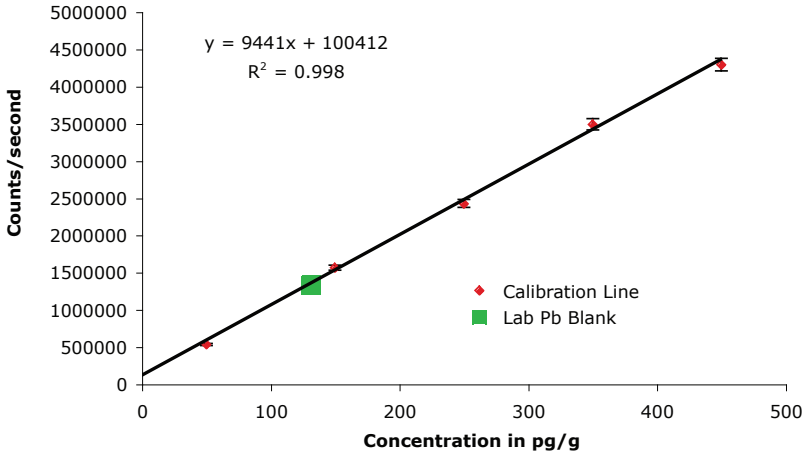

Figure 2.5: Calculation of lab blank

series of 5 solutions with known concentrations of Pb ranging from 50 pg/g-450 pg/g were created in 50 pg/g increments. Each standard solution was measured and a concentration vs. cps line was created from those analyses. Our blank solution was then analyzed. Using the calibration line, the concentration in the blank solution was determined to be 130 pg/g which results in a lab blank of $\sim$ 330 pg (Figure 2.5).

2.14 Time Resolved Spectra

Figure 2.6 is a time resolved spectra from a line analysis across an anti-perthite with an apatite inclusion from sample LB04-87. The isotopic composition of both the plagioclase and apatite from sample LB04-87. Each isotope signal/ratio is on a different scale, which are meant to highlight the variation in $^{206}Pb/^{204}Pb$, which for this sample ranges from 15.5-30 from feldspar to apatite.

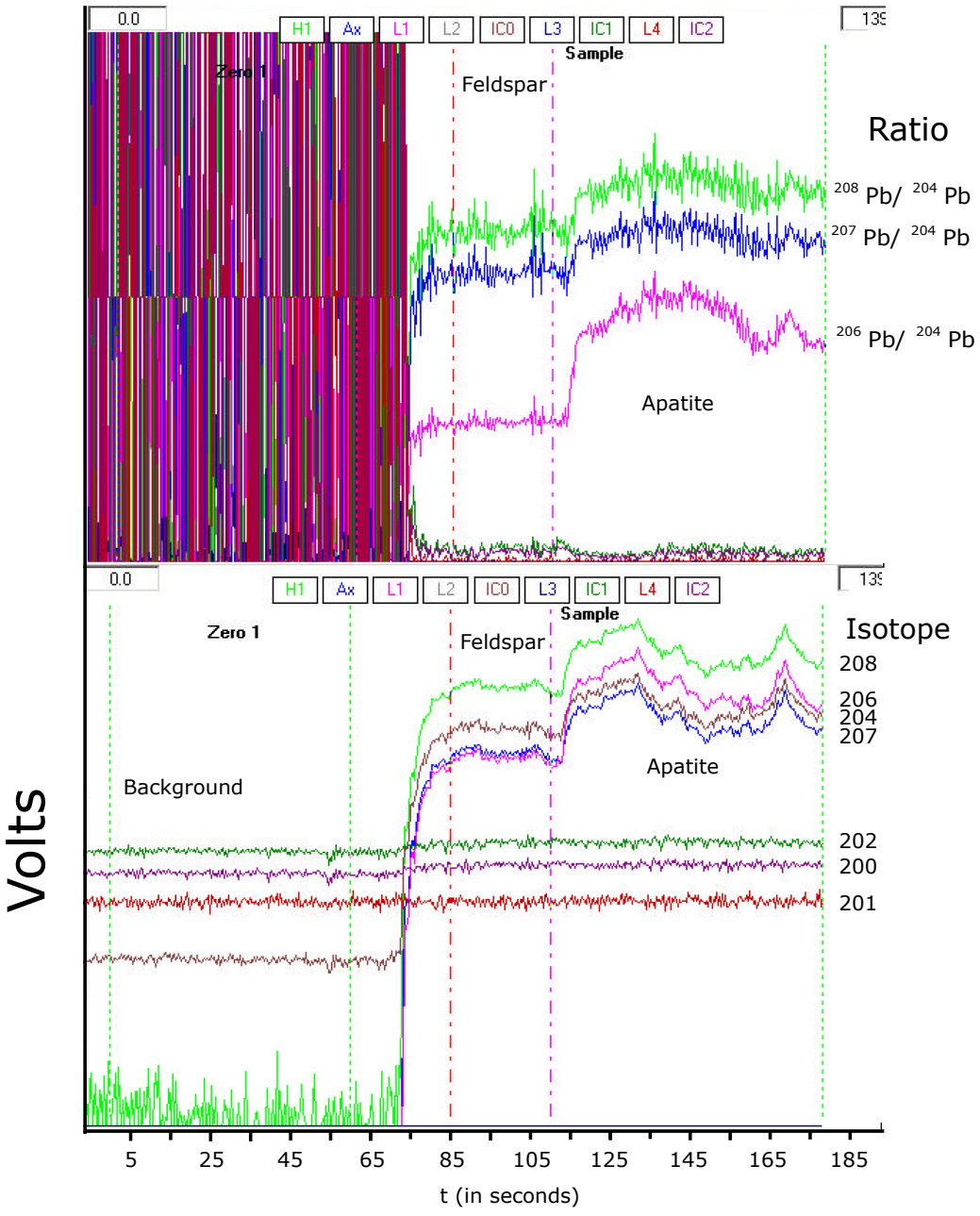

Figure 2.6: A time resolved analysis of a feldspar and an apatite inclusion. Each isotope is reported in volts. Note: the scales for each isotope and ratio are different to illustrate variability in each signal/ratio.

Chapter 3

Thermal history and origin of the Tanzanian Craton from Pb isotope thermochronology of feldspars from lower crustal xenoliths

3.1 Contributions

J. Bellucci collected all of the data presented here. P. Piccoli aided in any microprobe work. All three authors contributed to the interpretation of the data. J. Bellucci created all of the figures (except the geological map), tables, and text. M. Blondes created the geological map.

This chapter has been published in Earth and Planetary Science Letters with the citation:

Bellucci, J. J., McDonough, W. F., and Rudnick, R. L. (2011). Thermal history and origin of the Tanzanian Craton from Pb isotope thermochronology of feldspars from lower crustal xenoliths. Earth and Planetary Science Letters, 301(3-4):493 501.

3.2 Abstract

Common and radiogenic Pb isotopic compositions of plagioclase and anti-perthitic feldspars from granulite-facies lower crustal xenoliths from the Labait Volcano on the eastern margin of the Tanzanian Craton have been measured via laser

ablation MC-ICP-MS. Common Pb in plagioclase and a single stage Pb evolution model indicate that the lower crust of the Tanzanian Craton was extracted from mantle having a $^{238}U/^{204}Pb$ of 8.1 $\pm$ 0.3 and a $^{232}Th/^{238}U$ of 4.3 $\pm$ 0.1 at 2.71$\pm$ 0.09 Ga (all uncertainties are 2σ). Since 2.4 Ga, some orthoclase domains within anti-perthites have evolved with a maximum $^{238}U/^{204}Pb$ of 6 and $^{232}Th/^{238}U$ of 4.3. The spread in Pb isotopic composition in the anti-perthitic feldspars yields single crystal Pb-Pb isochrons of $\sim$ 2.4 Ga, within uncertainty of U-Pb zircon ages from the same sample suite. The Pb isotopic heterogeneities imply that these granulites resided at temperatures <600°C in the lower crust of the Tanzanian Craton from ca. 2.4 Ga to the present. In concert with the chemistry of surface samples, mantle xenoliths, and lower crustal xenoliths, our data imply that the cratonic lithosphere in Tanzania formed ca. $\sim$2.7 Ga, in a convergent margin setting, and has remained undisturbed since 2.7 Ga.

3.3 Introduction

Insights into the origin of the lithosphere and its thermal history can be gained through the study of deep-seated xenoliths carried in basalts and kimberlites (e.g., Carlson et al., 2005; Rudnick, 1992; Rudnick et al., 1998; Schmitz and Bowring, 2003; and references therein). In particular, Pb isotope studies of lower crustal xenoliths can provide insights into the age, composition, cooling history and origin of the lower crust (e.g., Bolhar et al., 2007; Rudnick and Goldstein, 1990; Schmitz and Bowring, 2003).

The oldest pieces of the Earths crust, and therefore, any evidence for early Earth processes, are located in stable lithospheric blocks defined as cratons. Cratons formed in the Archean and have persisted through geologic time. Despite numerous geochemical and geophysical studies, however, debate continues regarding the origin of cratonic lithosphere and the reasons for its longevity. A defining characteristic of cratons is low surface heat flow ($\sim$40 mW/m^2) compared to crust that has been tectonically active since the Archean (>50 mW/m^2) (Nyblade and Pollack, 1993). Cratonic geotherms can be modeled as functions of surface heat flow, conductive heating from the mantle and the distribution of heat producing elements (K, Th, and U) through the lithosphere (e.g., Chapman and Pollack, 1977; Rudnick et al., 1998). A more direct approach to defining cratonic geotherms is through the application of experimentally calibrated geothermometers and geobarometers to the minerals of mantle xenoliths (e.g., Boyd, 1973; Rudnick and Nyblade, 1999). However, this approach fails to capture the time-dependent cooling of cratons and relies upon the assumption that the conditions recorded in the xenoliths reflect equilibration to present-day conditions (e.g., Michuat et al., 2007; Rudnick et al., 1998).

Temporal constraints on the formation of cratonic geotherms, which correspond to lower crustal temperatures of 400-500°C (Chapman and Pollack, 1977; Rudnick et al., 1998), can be determined through the use of radiogenic isotopic systems with different closure temperatures applied to minerals from lower crustal xenoliths (Schmitz and Bowring, 2003). For example, U-Pb thermochronology of accessory phases (e.g., apatite, monazite, zircon, rutile) from lower crustal xenoliths of the Kaapvaal Craton indicate a slow cooling rate of 1°C/Ma for the lower crust

of that craton followed by thermal perturbations in the Proterozoic and Mesozoic (Schmitz and Bowring, 2003).

In addition to insights into thermal history, the Pb isotopic composition of xenoliths can be used to determine the time-integrated U/Pb and Th/Pb composition of the lower crust. If the common Pb isotopic composition of a rock lies on a geochron with identical age as the sample suite, then the Pb isotopic composition and, therefore, the $^{238}U/^{204}Pb$, $^{232}Th/^{204}Pb$, and $^{232}Th/^{238}U$ of the mantle source from which the crust derives may also be inferred (e.g., Bolhar et al., 2007; Möller et al., 1998; Rudnick and Goldstein, 1990).

3.4 Pb isotope systematics of feldspars

The Pb isotopic composition of a rock or mineral is composed of two components: common Pb (initial Pb inherited from the source rock) and radiogenic Pb (Pb*: Pb that is produced in the rock or mineral due to *in situ* radioactive decay of U and Th). Common Pb dominates in minerals having low $^{238}U/^{204}Pb$ and $^{232}Th/^{204}Pb$ and, thus, these minerals may record the Pb isotopic composition at the time of a rocks last equilibration, assuming the mineral has subsequently remained closed to Pb diffusion (e.g., Oversby, 1975; Zartman and Wasserburg, 1969). Common Pb can, therefore, be used to determine provenance (e.g., comparison of thorogenic Pb and uranogenic Pb in common Pb minerals can be used to distinguish different crustal domains, (e.g., Möller et al., 1998), estimate the age of the rocks last isotopic equilibration, and model the $^{238}U/^{204}Pb$, $^{232}Th/^{204}Pb$, and $^{232}Th/^{238}U$

of the previous reservoir in which the Pb resided (e.g., Holmes, 1946; Houtermans, 1946; Stacey and Kramers, 1975).

If the rock in which the common Pb minerals are present is a mantle derivative, then common Pb should reflect the $^{238}U/^{204}Pb$, $^{232}Th/^{204}Pb$, and $^{232}Th/^{238}U$ of the mantle from which the rocks were derived, so long as there is no evidence for crustal contamination, mixing, or re-equlibration between minerals after initial cooling (e.g., Bolhar et al., 2007; Kamber et al., 2003; Möller et al., 1998). Oceanic basalts derive from the mantle but, due to recycling of oceanic crust at subduction zones, do not record mantle composition before ∼180 Ma. In contrast, many continental basalts are contaminated by continental lithosphere (e.g., Farmer, 2003, and references therein) and may not be faithful recorders of the composition of the sublithospheric mantle, particularly for Pb, which is typically in low abundance in basalts (Farmer, 2003). Determining the $^{238}U/^{204}Pb$, $^{232}Th/^{204}Pb$, and $^{232}Th/^{238}U$ ratios in older mantle derivatives is important for tracking the changes in the mantle that have occurred through time, such as the apparent decrease in the Th/U from ∼4 to ∼2 from the Archean mantle to the modern mantle (e.g., Zartman and Haines, 1988; Zartman and Richardson, 2005, and references therein). For this reason, studies of underplated basalts (which are common in granulite-facies xenolith suites, (e.g., Rudnick, 1992) may provide important information about the mantle composition through time.

Radiogenic Pb, which occurs in minerals with moderate to large $^{238}U/^{204}Pb$ and $^{232}Th/^{204}Pb$, can be used to constrain ages, either through U-Pb concordia (for minerals having little common Pb such as monazite, titanite, zircon, apatite,

rutile), or, if there is a spread in the Pb isotopic composition, a Pb-Pb isochron. Traditionally, feldspars (both plagioclase and alkali feldspar) have been used to define the initial Pb isotopic composition of a rock (e.g., Frei et al., 1997; Ludwig and Silver, 1977; Oversby, 1978; Zartman and Wasserburg, 1969). However, some alkali feldspars contain appreciable U and, in these feldspars, Pb produced by radiogenic in-growth can be a significant component of the Pb isotopic composition, complicating its use as a strictly common Pb mineral (e.g., Housh and Bowring, 1991).

The Pb isotopic composition of a feldspar can be a mixture of several reservoirs with varying $^{238}U/^{204}Pb$. These reservoirs include common Pb, U-bearing micro-inclusions, and U-bearing exsolution lamellae (Frei and Kamber, 1995; Frei et al., 1997; Housh and Bowring, 1991). The U concentration of feldspars is correlated with the presence of an alkali component (Smith and Brown, 1988). Therefore, alkali or exsolved feldspars generally contain at least two of the aforementioned domains: a low $^{238}U/^{204}Pb$ region retaining common Pb and a higher $^{238}U/^{204}Pb$ region with more radiogenic Pb. Traditionally, step-wise leaching is used to gain access to the various Pb reservoirs in feldspars, as well as other silicate minerals, in order to construct accurate Pb-Pb isochrons (Frei and Kamber, 1995; Frei et al., 1997; Housh and Bowring, 1991).

The closure temperature (Tc) for Pb diffusion in both orthoclase and andesine (the main feldspar compositions in this study) is calculated to be 600°C using the methods of Dodson (1973), Pb diffusion coefficients from Cherniak (1995), assuming a spherical geometry, a grain radius of 1 mm and a cooling rate of 1°C/Ma (similar to

the lower crust of the Kaapvaal Craton of Schmitz and Bowring (2003)). If distinct Pb isotopic domains reside in a single feldspar crystal, the temperature must have been below 600°C. Furthermore, these different domains should produce a Pb-Pb or U-Pb isochron that yields the time at which the feldspars cooled below the closure temperature.

Here we show that *in situ* Pb isotopic measurements of feldspars by laser ablation multi-collector inductively coupled plasma mass spectrometry (LA-MC-ICP-MS) provides the spatial resolution in individual heterogeneous feldspars that is needed to construct Pb-Pb isochrons. We apply this method to lower crustal xenoliths carried in recent alkali basalts erupted on the margin of the Tanzanian Craton in order to elucidate the thermal history of cratonic lower crust and characterize the Pb isotopic composition of its mantle source.

3.5 Geologic Setting

The Tanzanian Craton comprises Archean terrains that amalgamated ca. 2.6 Ga (Maboko, 2000; Manya et al., 2006) (Figure 3.1). The exposed surface of the Tanzanian Craton is comprised of tonalites, trondhjemite, and granodiorites (TTGs), gneisses, and greenstone belts (Schulter, 1997), all of which have Archean Nd model ages and U-Pb zircon ages of ∼3.0 Ga and 2.6 Ga, respectively (Maboko, 2000; Manya et al., 2006; Möller et al., 1998). Both geophysical and xenolith evidence indicate that the Tanzanian Craton has a stable, deep lithospheric keel (Chesley et al., 1999; Lee and Rudnick, 1999; Ritsema et al., 1998). The lithosphere of the

Tanzanian Craton is characterized by low surface heat flow (34 ± 4 mW/m^2) (Nyblade et al., 1990) and high seismic velocities in the mantle to a depth of 150 ± 20 km (Weerarante et al., 2003).

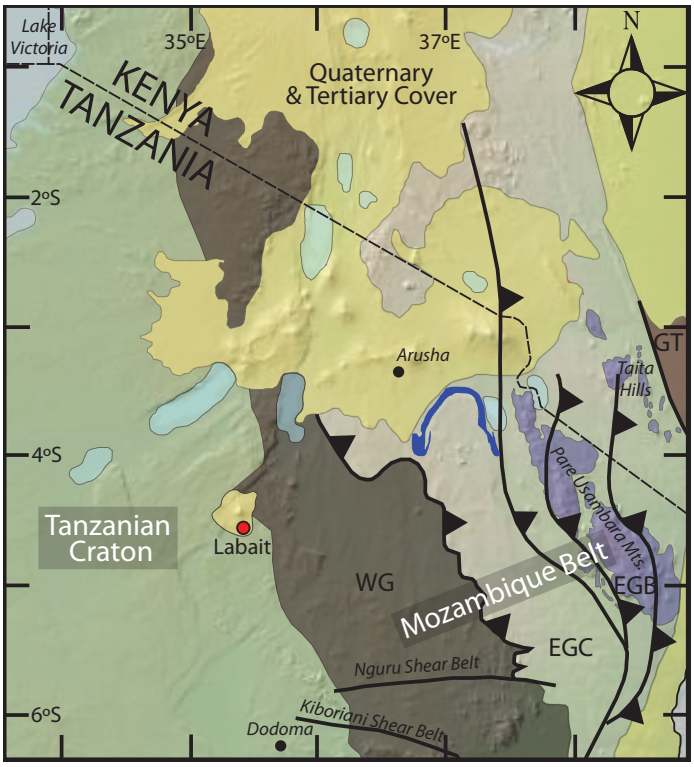

Figure 3.1: Simplified geologic map of northern Tanzania (modified after Cutten et al., 2006 and Fritz et al., 2009). W.G.: Western granulites; E.G.C.: Eastern granulite cover, E.G.B.: Eastern granulite basement; G.T.: Galena Terrane. Map created by M. Blondes.

To the east of the Tanzanian Craton lies the Western Granulite section of the Mozambique belt (Figure 3.1) and to the southeast lies the Usagaran Belt. The Mozambique Belt formed in a Himalayan-scale orogeny (Fritz et al., 2009) and marks the suture between east and west Gondwana (Cutten et al., 2006; Fritz et al., 2009). The western granulites have Archean Nd model ages (Möller et al., 1998) and

U-Pb zircon ages of 2.6-2.8 Ga (Johnson et al., 2003) and were metamorphosed to granulite facies in the Archean, 50-100 Ma after their emplacement into a continental arc (Johnson et al., 2003). Subsequently, the Western Granulites were then reworked during the Pan-African Orogeny ca. 560 Ma (Cutten et al., 2006; Blondes et al., 2011). The southeastern Tanzanian Craton was the overriding plate of a subduction zone ca. 2.0 Ga resulting in the Usagaran mountain belt and suture (e.g., Collins et al., 2004; Möller et al., 1995). There is no evidence for a 2.0 Ga event in northern Tanzania (Blondes et al., 2011; Cutten et al., 2006; Fritz et al., 2009; Johnson et al., 2003; Mansur et al., 2011).

The East-African Rift (EAR) surrounds the Tanzanian Craton, forming the eastern (Gregory) and western (Lake Albert) branches, which first developed at ca. 30-50 Ma, with volcanism continuing today (Dawson, 1992; Nyblade and Brazier, 2002). The Labait Volcano lies on the eastern edge of the Tanzanian Craton (4°34'13.76S, 35°26'1.60E), where the rift splays into a wide region of extension and volcanism. Labait erupted tuff and olivine melilitite carrying a wide array of mantle and crustal xenoliths at $\sim$ 400 Ka (Dawson et al., 1997; Rudnick et al., 1999). Mantle peridotite xenoliths from Labait yield pressure-temperature (P-T) estimates that scatter about a 50 mW/m^2 geotherm and indicate derivation depths of 50-150 km (Lee and Rudnick, 1999). Rhenium depletion Os isotope model ages for the mantle xenoliths range up to 2.8 Ga (Burton et al., 2000; Chesley et al., 1999). Some mantle peridotites from the Labait volcano have experienced overprinting and heating by rift magmas (Aulbach et al., 2008; Chesley et al., 1999; Lee and Rudnick, 1999; Rudnick et al., 1999), but the extent to which the rift has affected the lower

crust of the Tanzanian Craton is unknown.

3.6 Samples

Petrographic, mineral chemistry, whole rock major and trace element geochemistry, Rb-Sr and Sm-Nd isotopic data, as well as some U-Pb zircon ages for the Labait granulite xenoliths are presented in Mansur et al. (2011). U-Pb analyses of zircon and accessory phases from these samples are presented in Blondes et al. (2011). The xenoliths for this study fall into five different groups, based on major mineralogy and trace element chemistry: two pyroxene granulites (n=7), garnet orthopyroxene granulites (n=2), two pyroxene hornblende granulites (n=2), and anorthosite (n=1), all of which derive from the lower crust (Mansur et al., 2011). In addition, we studied a xenolithic two-mica granite (n=1). Plagioclase and/or anti-perthite (orthoclase exsolved from albite) from eleven granulite-facies xenoliths, spanning all varieties, were analyzed here, as well as anti-perthite from the granite xenolith. Table 3.1 lists the major mineralogy of these samples.

The Labait xenoliths, like most other granulite-facies lower crustal xenoliths, have mafic compositions with <54 wt.% SiO_2 (Mansur et al., 2011). They are enriched in light rare-earth elements (REE), have negative Ti and Nb anomalies, and have high La/Nb ratios (between 1.3-7.1), all of which suggest formation as a crystallized basaltic melt in an arc setting (Mansur et al., 2011). Additionally, these samples show striking depletions in Rb, Cs, Th and U, which has been interpreted to have occurred during granulite facies metamorphism (Mansur et al., 2011). Based

Table 3.1. Samples and Major Mineralogy

Sample #	Rock Type	Major Mineralogy
LB04-09	2 Px Gran	Plagioclase Orthopyroxene, Clinopyroxene
LB04-19	2 Px Gran	Anti-perthite, Orthopyroxene, Clinopyroxene
LB04-38	2 Px Gran	Plagioclase, Orthopyroxene, Clinopyroxene
LB04-43	2 Px Gran	Plagioclase, Orthopyroxene, Clinopyroxene
LB04-50	2 Px Gran	Anti-perthite, Orthopyroxene, Garnet
LB04-65	2 Px Gran	Anti-perthite, Orthopyroxene, Clinopyroxene
LB04-87	Granite	Anti-perthite, Orthoclase, Quartz, Biotite, Muscovite
LB04-48	2 Px Hbl Gran	Plagioclase, Clinopyroxene, Orthopyroxene, Hornblende
LB04-27	Anorthosite	Plagioclase, Garnet, Orthopyroxene
LB04-39	Gt Opx Gran	Plagioclase, Orthopyroxene, Garnet
LB04-91	Gt Opx Gran	Anti-perthite, Orthopyroxene, Garnet

Gran: Granulite, Px: Pyroxene, Gt: Garnet, Hbl: Hornblende, Bt: Biotite, Opx: Orthopyroxene

on two-pyroxene Fe-Mg exchange thermobarometry, the Labait xenoliths record a broad range of equilibration temperatures from 480°to 850°C, with most <670°C (assuming a pressure of equilibration of 1 GPa or 33 km depth) (Mansur et al., 2011). The equilibration conditions for these xenoliths are similar to those of the felsic granulites found in the Western Granulite belt (Johnson et al., 2003). One sample, LB04-87, is a granite, which is distinct in both mineralogy and texture (Table 1), and likely derived from the shallow crust. Importantly, no radiogenic Pb is observed in mineral separates of apatite (closure temperature ∼450°C for 100 μm crystals cooled at 2°C/Ma, Cherniak et al., 1991) from the granulite-facies xenoliths, demonstrating their derivation from the present-day lower crust, where the temperature must have exceeded 450°C (Blondes et al., 2011). U-Pb zircon ages and Nd model ages for these samples, 2.643 ± 0.002 Ga and 2.9-3.8 Ga, respectively (Mansur et al., 2011; Blondes et al., 2011); mark their formation during the Archean. These ages coincide with the timing of greenstone belt volcanism in the northern part of the Tanzanian Craton (Manya et al., 2006) and overlap the 3.0-3.1 Ga Nd

model ages from surface samples from the Tanzanian Craton (Möller et al., 1998).

Feldspars from the Labait xenoliths consist of both plagioclase and anti-perthite. The plagioclase composition is $An_{32-55}Ab_{47-64}Or_{0-6}$, while the orthoclase, in anti-perthite, has a composition of $An_{1-3}Ab_{7-23}Or_{73-91}$ (Mansur et al., 2011). One sample, LB04-27, is an anorthosite having plagioclase with a bytownite composition ($An_{87-89}Ab_{11-12}$) (Mansur et al., 2011). All orthoclase observed in these samples are part of the anti-perthite, and therefore, any analyses performed on orthoclase were performed in the same time-resolved analyses as the plagioclase.

3.7 Analytical Methods

3.7.1 Pb isotopic measurements

Samples were prepared either as polished rock slabs mounted in epoxy or 50-60 μm polished thick sections. The Pb isotopic compositions were determined in situ via LA-MC- ICP-MS using a frequency-quintupled solid-state Nd:YAG laser system (213 nm wavelength) and a Nu Plasma MC-ICP-MS (following Kent, 2008a,b; Paul et al., 2005). Full analytical details are provided in the Chapter 2 and a brief overview is given below.

Ion beams of ^{200}Hg, ^{202}Hg, and ^{204}Pb/Hg were monitored using parallel ion counters, whereas isotopes ^{201}Hg, ^{206}Pb, ^{207}Pb, and ^{208}Pb were detected simultaneously as ion currents in parallel Faraday cups equipped with 10^{11} Ω resistors. In order to correct for the isobaric interference of ^{204}Hg on ^{204}Pb, ^{200}Hg/^{202}Hg was monitored to allow subtraction of a fractionation-corrected abundance of ^{204}Hg. The Hg

fractionation factor was calculated using the exponential law and assuming natural isotopic abundances (de Laeter et al., 2003). The Hg fractionation factor was then applied to the $^{204}Hg/^{202}Hg$ ratio and subsequently the ^{204}Hg signal was stripped from the ^{204}Pb signal. The contribution of ^{204}Hg on the ^{204}Pb signal was typically < 0.7 %. Backgrounds were measured on-peak for 60s prior to ablation with the laser on and shuttered. The average of each signals background was subtracted in real time from each individual measurement collected at intervals of 0.2s using the Nu Plasma time resolved software. For accurate isotopic measurements, two corrections must be applied to the background-corrected data: 1) mass fractionation corrections and 2) ion counter-Faraday cup gain corrections. Mass fractionation effects are corrected using standard sample bracketing using SRM NIST 612 as the reference standard and calculating the fractionation factor of $^{208}Pb/^{206}Pb$ using the exponential fractionation law. Using the fractionation factor from $^{208}Pb/^{206}Pb$, an expected $^{20x}Pb/^{204}Pb$ (x=8, 7, or 6) can be calculated. Discrepancies between the Faraday cup and ion counter gains can be corrected by using the ratio between the measured and calculated $^{20x}Pb/^{204}Pb$ values of SRM 612 (Baker et al., 2004).

While the analytical precision using this method is largely dependent on the Pb concentration in the sample, which can range between 10-20 μg/g, repeat measurements (n=85) over a several month period of the basaltic glass standard BCR 2-g, which contains $\sim$10 μg/g Pb, yielded accuracies of $\leq\pm0.1\%$ for $^{20x}Pb/^{204}Pb$ and an external reproducibility of $\leq\pm0.5\%$ for $^{20x}Pb/^{204}Pb$. A detailed discussion regarding the accuracy and precision of this developed method, are located in Chapter 2.

3.7.2 U-Pb

The U-Pb ratio in a feldspar from one sample (LB04-91) was measured by LA-ICP-MS utilizing the same laser ablation system described above coupled to a ThermoFinnigan Element 2 ICP-MS. Ten spots, 40 μm in diameter, were analyzed along a Pb-isotope laser ablation track (Figure 3.5). Further details of the analytical conditions and results are given in the supplementary materials.

3.7.3 Backscatter electron imaging

Backscatter electron images were taken using a JEOL JXA-8900 SuperProbe. Photos were taken in beam scan mode with an accelerating voltage of 15 kV.

3.7.4 Solution Analyses

The Pb isotopic composition of the host basalt was analyzed by both solution MC-ICPMS and LA-MC-ICPMS. The solution measurements were performed using parallel Faraday cups. Pb was purified from dissolved rock using standard HBr anion chromatography. Mass fractionation was accounted for using the exponential fractionation law through the addition of Tl (e.g., Baker et al., 2004). The lab blank was measured to be $\sim$ 330 pg, which corresponds to a sample/blank ratio of $\sim 10^3$. The results are within uncertainty ($\leq$ 0.2%) of the LA-MC-ICPMS. This uncertainty is similar to that obtained for measurements of standard materials. Data are provided in Chapter 2.

3.8 Results

The Labait host melilitite has a Pb isotopic composition similar to that of other rift basalts from Northern Tanzania (e.g., Paslick et al., 1995); Figure 3.2.

The Pb isotopic composition of plagioclase and anti-perthite from the Labait lower crustal xenoliths (n=137) are presented in Figure 3.3 (data tables are located in Appendix 1). Anti-perthites in six samples (four two-pyroxene granulites LB04-19, LB04-50, LB04-82, one gt-opx granulite, LB04- 91 and the granite, LB04-87) display a significant spread in Pb isotopic values. Plagioclase in a further six samples (which include specimens from all four groups of granulites) show no significant spread in their Pb isotopic compositions (all analyses are within analytical uncertainty of each other) and all, except that from the anorthosite, have non-radiogenic compositions that plot near the 2.7 Ga Geochron (Figure 3.3). By contrast, the anorthosite plagioclase has relatively radiogenic Pb that plots near the present-day geochron. During the analysis of plagioclase from the granite, LB04-87, inclusions of very radiogenic Pb ($^{206}Pb/^{204}Pb \sim 28$) were intersected, as reflected in the time resolved spectra. We assume these inclusions are apatite, which is present in the backscatter electron images of LB04-87 (Figure 3.4). A figure of the time resolved spectra from this analysis is located in Chapter 2.

Isochrons were calculated using the program Isoplot (Ludwig, 2003) for each anti-perthite grain, multiple feldspar grains (multiple feldspar) within a given sample, and for each group of samples: 2 px granulites, gt-opx granulites, hbl granulites and the granite (Table 3.2, Figures 3.3 and 3.6). Figure 3.3 illustrates single

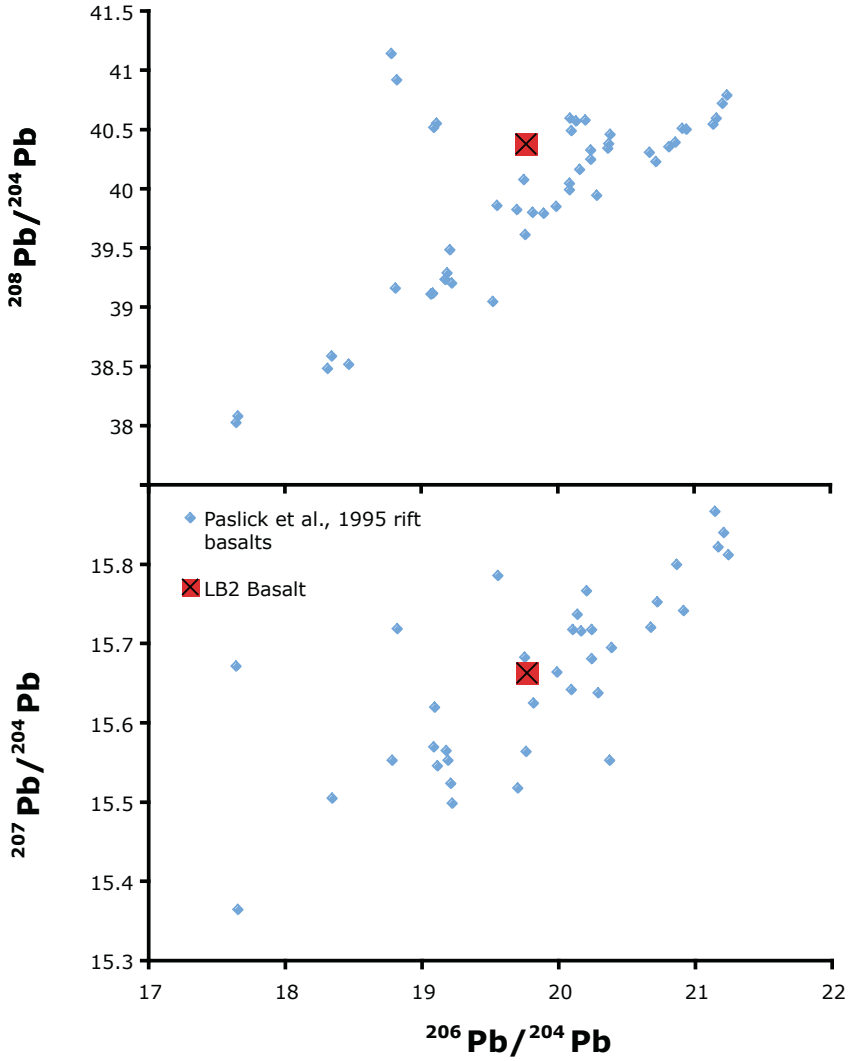

Figure 3.2: Pb isotopic data for LB2 melilite and other Tanzanian rift basalts of Paslick et al. (1995).

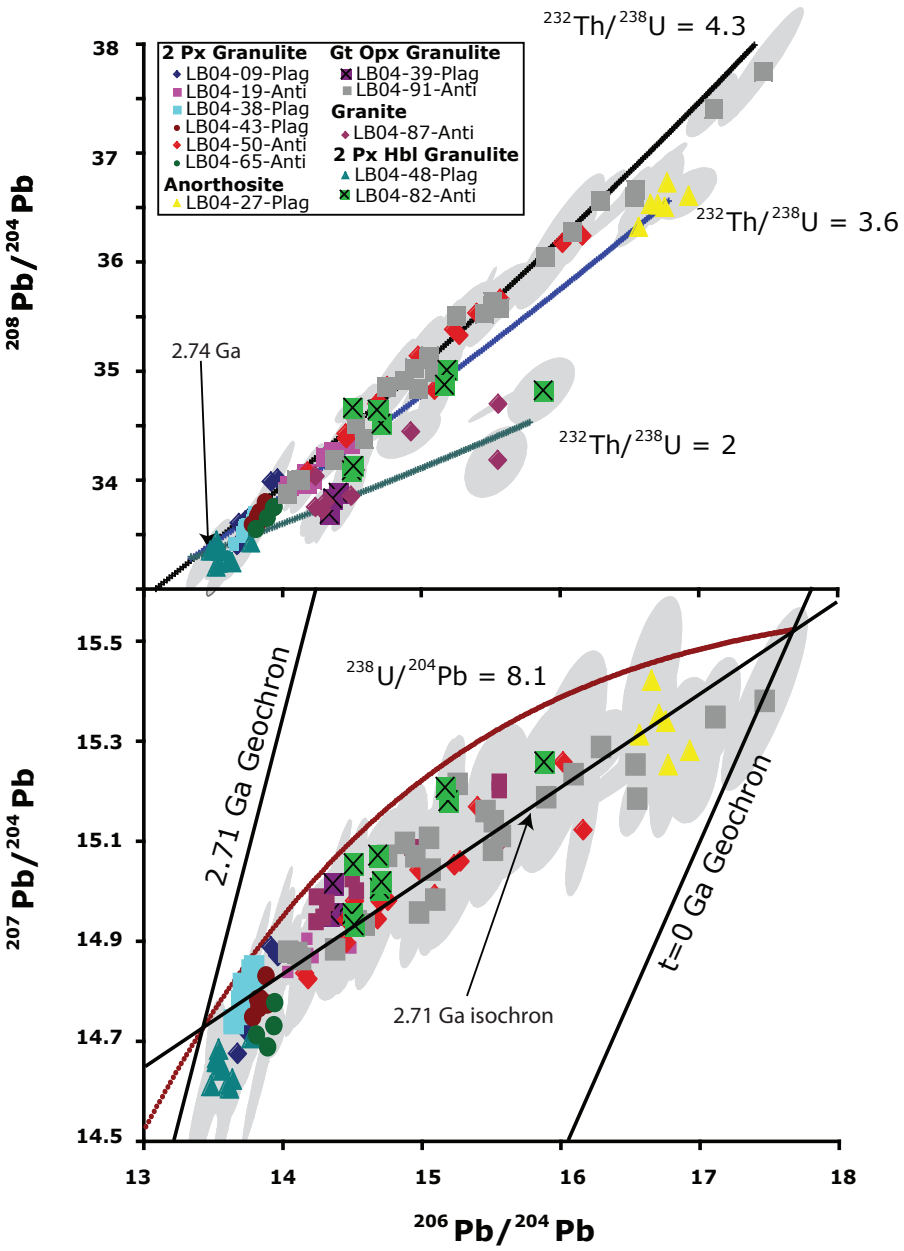

Figure 3.3: Pb isotopic data for feldspars in lower crustal xenoliths from the Tanzanian Craton. The data lie along a 2.71 Ga isochron, shown for reference (calculated with Isoplot, Ludwig (2003)), which is an age that is identical to the average of all other isochrons from individual samples suites (Table 2). A single-stage Pb evolution model from primordial Pb (Chen and Wasserburg, 1983) is illustrated for a $^{238}U/^{204}Pb$ of 8.1 and $^{232}Th/^{238}U$ of 4.3. Evolution of $^{208}Pb/^{204}Pb$ and $^{206}Pb/^{204}Pb$ at $^{232}Th/^{238}U$ of 2 and 3.6 are shown as fractionation of Th from U after extraction from a crustal source having $^{232}Th/^{238}U$ of 4.3 formed at 2.71 Ga. Error ellipses represent $2\sigma_{mean}$ of each analysis.

crystal (± inclusions) isochrons for gt-opx granulite LB04-91 and granite LB04-87. The isochron for sample LB04-91 is defined by a combination of plagioclase and orthoclase zones in a single crystal of anti-perthite. The isochron for sample LB04-87 is defined by both anti-perthite and an apatite inclusion. All isochrons are Archean. The average age of the individual anti-perthites is $\sim$ 2.4 Ga, while multiple phase/sample suite isochron ages average $\sim$ 2.7 Ga (Table 3.2), which is coincident with the U-Pb zircon ages from the Labait xenoliths from Mansur et al. (2011), and Blondes et al. (2011).

The Pb isotopic composition of the Labait feldspars, even with radiogenic in-growth, plot to the left of the present-day geochron. The data form a linear array stretching between the present-day geochron and the 2.71 Ga geochron. The trend seen in the 2 px granulite LB04-38 is a mass fractionation trend and the data points are indistinguishable within analytical uncertainty.

3.9 Discussion

3.9.1 Origin of the linear trends

Linear trends in isotopic data can either reflect mixing between two isotopically distinct components or result from the in-growth of the radiogenic daughter product. Only the latter has any age significance.

One possible source of radiogenic Pb that may have been mixed into the xenoliths is the host lava. Figure 3.5 shows a mixing trajectory between the least radiogenic plagioclases ($\sim$20 μg/g Pb, from samples LB04-48 and LB04-38) and the

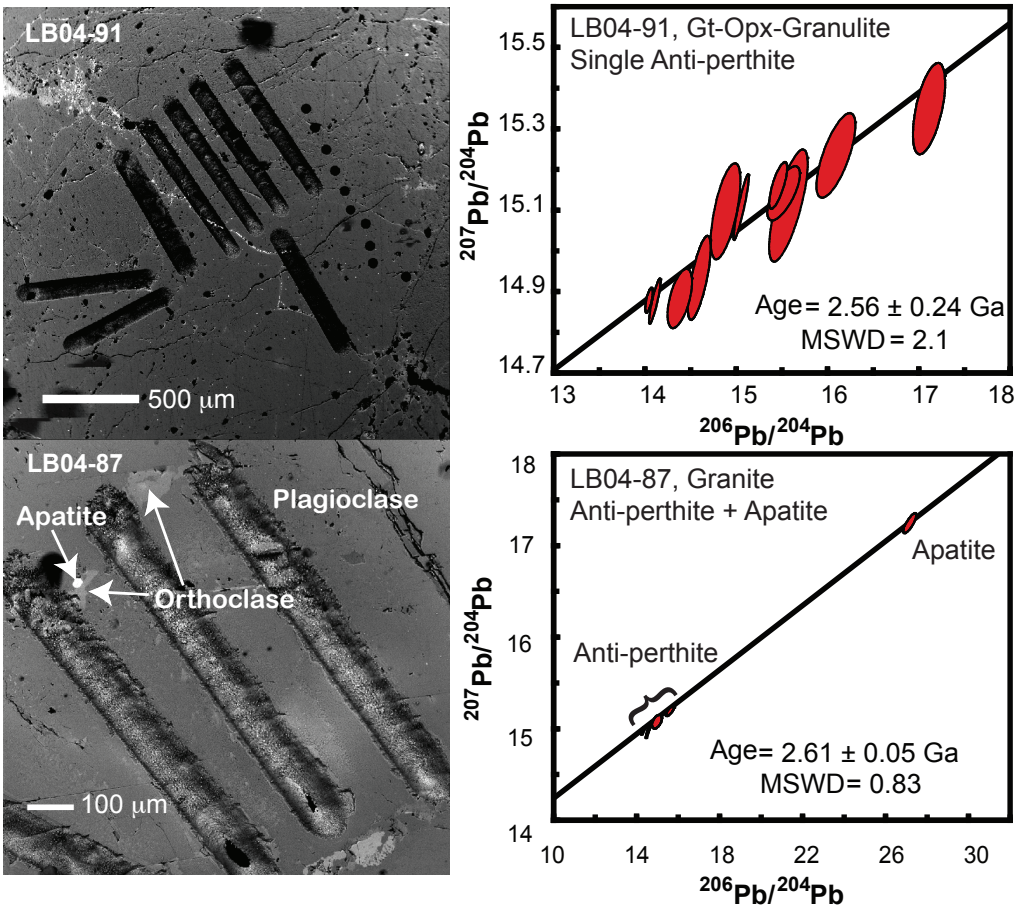

Figure 3.4: Top Left: Backscatter electron image of plagioclase/anti-perthite from sample LB04-91 with corresponding single crystal anti-perthite isochron, shown with laser tracks and laser ablation pits. The multiple data points (top right) are from discrete regions in the feldspar revealed in the time-resolved spectra of the ablation lines. Bottom Left: Backscatter electron image of plagioclase, anti-perthite, and apatite inclusions from granite LB04-87 and corresponding isochron (bottom right). The backscatter electron images were taken using a JEOL JXA-8900 SuperProbe. Photos were taken in beam scan mode with an accelerating voltage of 15 kV.

Labait melilitite (∼8 μg/g). Many of the feldspar analyses plot beyond analytical uncertainty of this mixing line, although some overlap it. To achieve this range in Pb isotopic compositions via host basalt mixing, up to ∼ 80% of the Pb in the most radiogenic samples must have originated from the basalt. This level of mixing is untenable on two accounts. First, the whole-rock Nd isotopic compositions and trace element compositions of the samples do not record any such mixing (Mansur et al., 2011). Second, in order for Pb from the basalt to enter the feldspars, the samples would need to be heated above 600°C (Tc for Pb in feldspar) during the xenoliths entrainment within the basalt. Such heating is precluded on the basis of U-Pb thermochronology of titanite (Tc >550°C) and apatite (Tc>450°C) from lower crustal xenoliths hosted in a similar alkali basalt from a near-by locality (Lashaine, Blondes et al., 2011). Apatite in these samples was open to Pb diffusion at the time of eruption, like those in the Labait xenoliths, but titanite records concordant Paleozoic $^{206}Pb/^{238}U$ ages, reflecting slow cooling following the Pan-African Orogeny. Collectively, these results indicate that the samples remained above apatite closure temperature but below titanite (and feldspar) closure temperature for hundreds of millions of years more than two orders of magnitude longer than the duration of rift volcanism in northern Tanzania. Similar results were obtained for kimberlite-hosted lower crustal xenoliths from the Kaapvaal Craton (Schmitz and Bowring, 2003). We conclude that mixing with the host basalt did not generate the linear correlation seen in the plot of $^{206}Pb/^{204}Pb$ vs. $^{207}Pb/^{204}Pb$.

Because the U/Pb ratio of anti-perthite from gt-opx granulite LB04-91 shows over an order of magnitude change over a distance of ∼800 μm, and correlates with

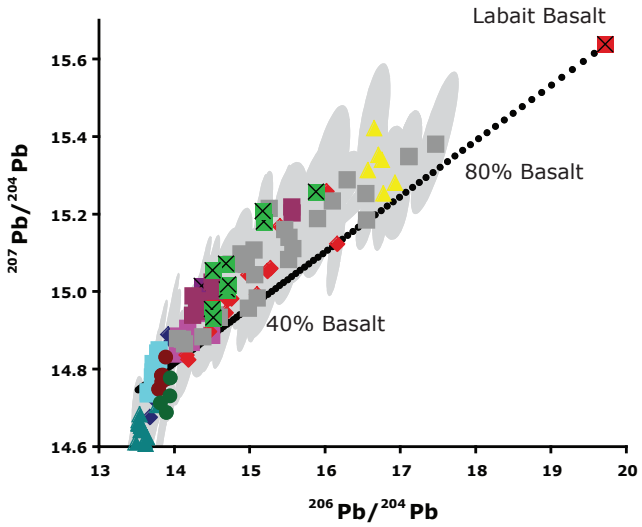

Figure 3.5: Mixing diagram from least radiogenic Pb composition in the Labait lower crustal xenolith feldspars (20 μg/g) and the Labait Basalt (8 μg/g). Error ellipses are $2\sigma_{mean}$ of each feldspar analysis and the error on the Labait host lava is smaller than the symbol.

the ^{206}Pb/^{204}Pb ratio (Figure 3.6), we suggest that the linear correlation reflects an isochron, rather than mixing between two endmember Pb isotopic compositions. Below we explore the thermochronological implications of the feldspar isochrons.

3.9.2 Thermochronometry

Individual feldspars in five samples (2 px granulites LB04-19, LB04-50, LB04-82, gt-opx granulite LB04-91 and the granite, LB04-87) are heterogeneous with respect to their Pb isotopic compositions, indicating that they have resided at temperatures below ~600°C, given the closure temperature of Pb in feldspar calculated above. The Pb isotopic heterogeneities reflect several reservoirs of radiogenic Pb, similar to other U-bearing silicate minerals (Frei and Kamber, 1995) and

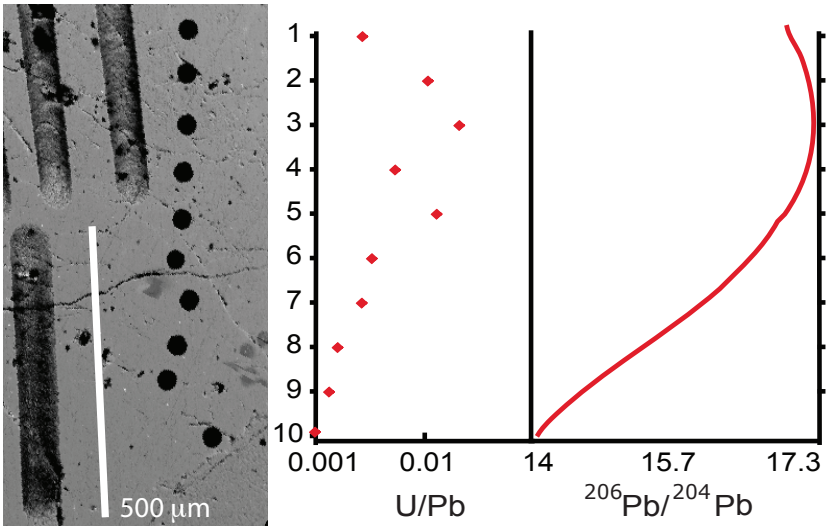

Figure 3.6: Laser ablation pits from anti-perthite in LB04-91 (See Figure 3.2) and corresponding U/Pb measurements performed as spot analyses with LA-ICP-MS, indicating variable U-Pb ratios on a micron scale within the anti-perthite. Right panel shows an estimate of the corresponding $^{206}Pb/^{204}Pb$, based on the time-resolved spectra, matched with the spot U analyses.

yield isochron ages of $\sim$ 2.4 Ga. This result demonstrates that the Pb-Pb system in feldspars is a viable thermochronometer in rocks having coarse-grained (mm) feldspars, significant age, and U and Th concentrations. Because feldspars from the Labait xenoliths record a range of Pb isotopic compositions, the temperature of the lower crust of the Tanzanian Craton must not have been elevated above 600°C at any time following 2.4 Ga, including during the Pan-African Orogeny (ca. 560 Ma) and the development of the East African Rift.

Given the spread in Pb isotopic values and the isochron age, a maximum $^{238}U/^{204}Pb$ can be calculated for the feldspar grains. The largest range in Pb isotopic values for a single feldspar is seen in gt-opx granulite LB04-91, which has $^{206}Pb/^{204}Pb$ varying from 14.87 to 15.38, corresponding to a maximum $^{238}U/^{204}Pb$ of 6. Most of the samples fall on a linear trend on the $^{208}Pb/^{204}Pb$ vs. $^{206}Pb/^{204}Pb$ diagram, corresponding to a $^{232}Th/^{238}U$ of 4.3. Three samples, one from each of three different lithological groups, fall off this trend: gt-opx granulite LB04-39, the single anorthosite, LB04-27 and the granite LB04-87. Assuming these samples were extracted at the same time and from the same mantle source as the other Labait xenoliths (because they follow the same trend as the other samples in the $^{207}Pb/^{204}Pb$ vs. $^{206}Pb/^{204}Pb$ plot), their Pb isotopic composition can be modeled with a $^{232}Th/^{238}U$ of 2, 3.6 and 2, respectively (Figure 3.2). All of the calculated $^{232}Th/^{238}U$ ratios are within the range of the whole rock Th/U (0.7-5.6, Mansur et al., 2011). The variable $^{232}Th/^{238}U$ ratios in the feldspars of these three samples illustrates the potential of the $^{208}Pb/^{204}Pb$ vs. $^{206}Pb/^{204}Pb$ composition in feldspars to be a more sensitive discriminator of provenance than the $^{207}Pb/^{204}Pb$ vs. $^{206}Pb/^{204}Pb$

composition.

3.9.3 Pb isotopic composition of the lower crust and mantle source

In addition to providing constraints on the thermal history of the lower crust of the Tanzanian Craton, the common Pb isotopic composition of Labait feldspars can also be used to place constraints on its age and origin. Based on trace element analyses, most of the Labait lower crustal xenoliths (in particular, the two pyroxene granulites) likely crystallized as basalts from an arc setting and subsequently underwent granulite facies metamorphism (Mansur et al., 2011). Considering that all of these xenoliths have relatively low equilibration temperatures (Mansur et al., 2011), and lie on a linear array in $^{207}Pb/^{204}Pb$ vs. $^{206}Pb/^{204}Pb$ space (except hornblende granulite LB04-48), we interpret them to have formed from the same mantle reservoir at the same time. Therefore, we group all of the Pb isotopic compositions from this suite of xenoliths to get an age of lower crust extraction from the mantle of 2.71± 0.09 Ga (Table 2). This mantle extraction age is similar to that of the Western Granulites (Johnson et al., 2003). In addition, the age recorded by the anti-perthitic feldspars (∼2.4 Ga) could date the age of metamorphism of the lower crust to granulite facies, which is similar to the metamorphic event seen by the western granulites, occurring 50-100 Ma after extraction from the mantle.

The Pb isotopic compositions of the all of the feldspars from the Labait lower crustal xenoliths, except those in hornblende granulite LB04-48, lie within error of a 2.71 Ga isochron (Figure 3.2). The 2.71 Ga isochron intersects the 2.71 Geochron

Table 3.2. Summary of Pb-Pb ages from Labait xenoliths

Sample Suite	Sample (s)	Minerals	Age (in Ga)	2σ
2 Px Granulite	LB04-19	Multiple Plagioclase	2.96	1.50
2 Px Granulite	LB04-43	Multiple Plagioclase	3.54	0.50
2 Px Granulite	LB04-50	Single Anti-perthite	2.74	0.43
2 Px Granulite	LB04-50	Single Anti-perthite	2.30	0.60
2 Px Granulite	LB04-50	Anti-perthite, Ilmenite	2.51	0.35
2 Px Granulite	LB04-65	Anti-perthite, Apatite	2.42	0.69
2 Px Granulite	LB04-65	Anti-perthite, Apatite	2.75	1.60
2 Px Granulite	LB04-65	Multiple Ant-perthite, Multiple Apatite	2.32	0.68
2 Px Granulite	LB04-09, LB04-19, LB04-38, LB04-43, LB04-50, LB04-65		2.71	0.24
Gt-Opx-Granulite	LB04-91	Single Anti-perthite	2.56	0.24
	LB04-91	Single Anti-perthite	2.15	0.68
	LB04-91	Multiple Anti-perthite	2.42	0.26
Gt-Opx Granulite	LB04-39, LB04-91		2.38	0.23
2 Px Hbl Gran	LB04-82	Single Anti-perthite	2.48	0.59
		Multiple Anti-perthite, pyroxene	2.61	0.76
2 Px Hbl Gran	LB04-48, LB04-82		3.40	0.25
Granite	LB04-87	Anti-perthite-Apatite inclusion	2.68	0.15
	LB04-87	Anti-perthite-Apatite inclusion	2.61	0.05
	LB04-87	Multiple Anti-perthie, Apatite	2.62	0.04
		Average Age of Anti-perthite	2.44	0.41
		Average of non Anti-perthite ages	2.71	0.73
		Isochron of the entire sample suite	2.71	0.09

(Holmes, 1946) at $^{206}Pb/^{204}Pb$=13.4 ± 0.4 and $^{207}Pb/^{204}Pb$=14.7 ± 0.4 (2σ), near the common Pb isotopic composition of feldspars in the two least-radiogenic samples, LB04-38 and LB04-48. Using a single-stage Pb evolution model, the primordial Pb isotopic composition of Canyon Diablo troilite (Chen and Wasserburg, 1983), and assuming the intersection between the Labait isochron and geochron represents the isotopic composition of the Tanzanian Craton crust at the time of its extraction from the mantle, this crust derived from a mantle source with a $^{238}U/^{204}Pb$ of 8.1 ± 0.3 (Figure 3.2). Similarly, the $^{232}Th/^{204}Pb$ value for the mantle source was 35 ± 1, with a $^{232}Th/^{238}U$ of 4.3 ± 0.1 (Figure 3.2). This $^{238}U/^{204}Pb$ is similar to that found for Archean komatiites from Canada, Australia, and Africa that indicate mantle $^{238}U/^{204}Pb$ values at ∼2.7 Ga of 7.8-8.5 (Chauvel et al., 1993; Dupre' and

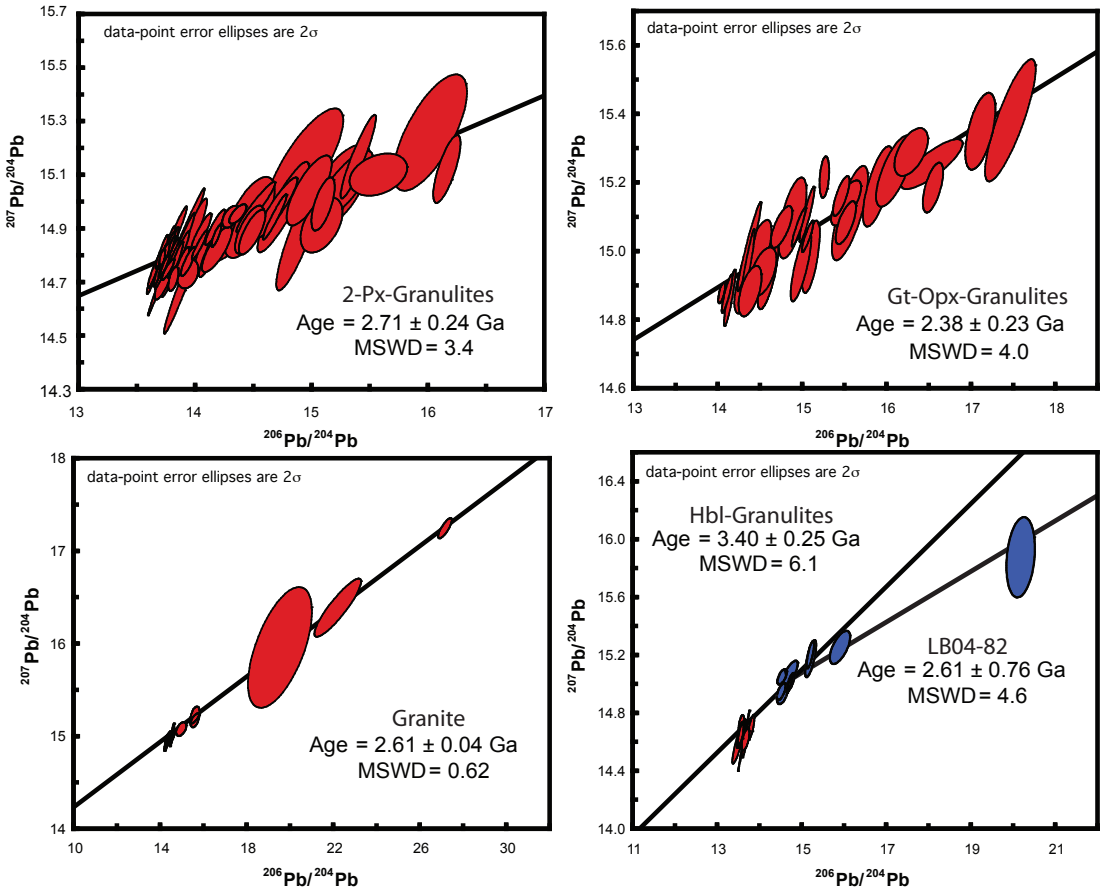

Figure 3.7: Isochrons calculated for each sample suite, two pyroxene granulites, Gt-Opx granulites, granite, and Hbl granulites.

Arndt, 1990). The inferred $^{232}Th/^{238}U$ is consistent with previous observations that the Archean mantle had a $^{232}Th/^{238}U$ of ~ 4 (e.g., Zartman and Haines, 1988; Zartman and Richardson, 2005, and references therein).

Two samples do not follow the general trends defined by the rest of the suite. The anorthosite (LB04-27) has unusually radiogenic plagioclase, which lies close to the present-day geochron. The anorthosite does not fall on the mixing trend with the Labait basalt, suggesting that it may have derived from a deeper (hotter) level than the other samples and may have equilibrated with U-bearing phases more recently. In contrast, plagioclase in hornblende granulite LB04-48 has the least radiogenic Pb isotopic composition of the entire suite and lies below the linear trend defined by the other samples in both $^{208}Pb/^{204}Pb$ vs. $^{206}Pb/^{204}Pb$ and $^{207}Pb/^{204}Pb$ vs. $^{206}Pb/^{204}Pb$ plots (Figure 3.2). The non-radiogenic composition of the common Pb in this sample could reflect its derivation from somewhat older material present in the cratonic lower crust.

The common Pb isotopic composition of the Tanzanian lower crust overlaps with the Pb isotopic composition of feldspars and galenas from outcrops within the Tanzanian Craton, in a similar, slightly curved array (Figure 3.8) (Coomer and Robertson, 1974; Möller et al., 1998). The similarity between Pb isotopic compositions of surface samples and lower crustal xenoliths indicates a similar provenance, and therefore, similar model ages for the upper and lower crust. The linear relationship of the Pb isotopic composition of lower crustal feldspars and surface samples in both $^{208}Pb/^{204}Pb$ vs. $^{206}Pb/^{204}Pb$ and $^{207}Pb/^{204}Pb$ vs. $^{206}Pb/^{204}Pb$ indicates that there have been no additions or major fractionation of U/Pb or Th/Pb in the crust

since the amalgamation of the Tanzanian Craton in a convergent margin setting ca. 2.7 Ga.

3.10 Conclusions

The Pb isotopic composition of feldspars from lower crustal xenoliths from the Tanzanian Craton, in combination with previous studies on surface samples and mantle xenoliths indicate that the crust and lithospheric mantle comprising the Tanzanian Craton formed in the Archean in a convergent margin setting at approximately the same time, ca. $\sim$ 2.7 Ga. Using a single-stage Pb evolution model, the crust of the Tanzanian Craton was extracted from a mantle with a $^{238}U/^{204}Pb$ of 8.1 $\pm$ 0.3 and $^{232}Th/^{238}U$ of 4.3 $\pm$ 0.1. Single anti-perthitic feldspars have isochrons that have an average age of 2.4 Ga, which indicates the time at which the lower crust cooled to a temperature <600°C. After 2.4 Ga, the temperature of the Tanzanian Craton lower crust, as represented by the xenoliths examined here, did not rise above 600°C during either the Pan-African Orogeny or the present-day rifting. The identical common Pb isotopic compositions of the surface samples and lower crust indicate that there was no addition, subtraction, or fractionation of U, Pb, or Th in the crust of the Tanzanian Craton since its formation ca. 2.7 Ga.

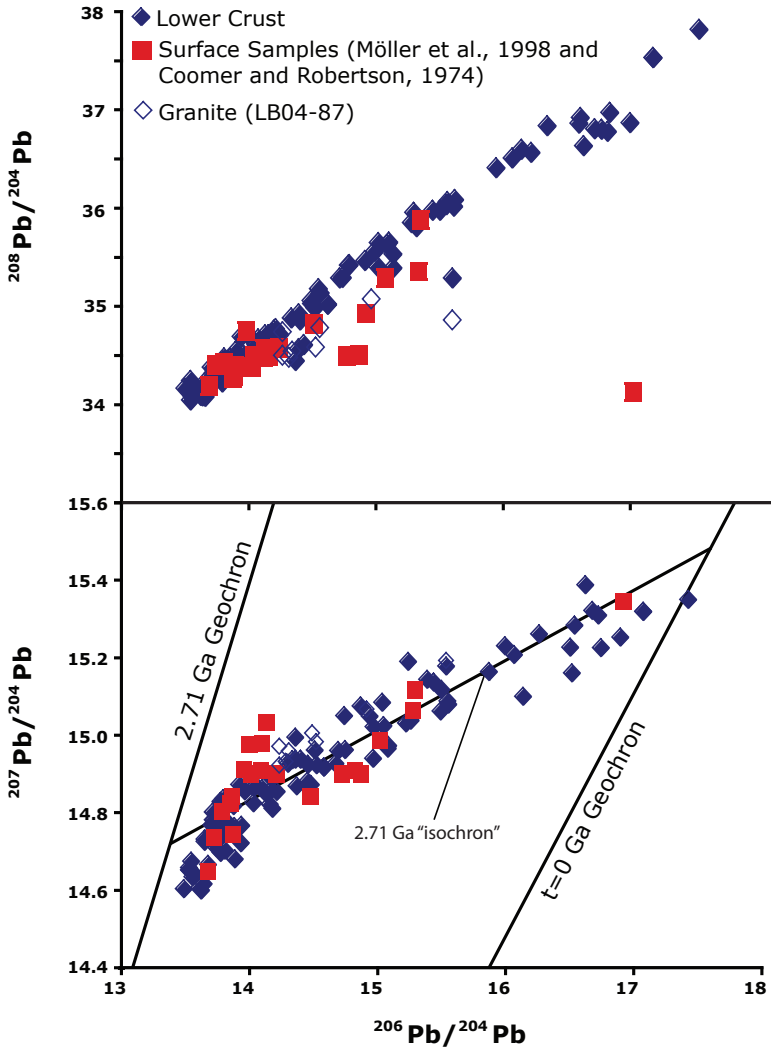

Figure 3.8: Pb isotopic data for feldspars in lower crustal xenoliths compared to surface feldspars (Möller et al., 1998) and galenas/pyrites (Coomer and Robertson, 1974) from the Tanzanian Craton. The granitic sample (LB04-87) is shown in open symbols.

Chapter 4

Lead isotopic evolution of Archean continental crust in the Neoproterozoic Mozambique Belt, Northern Tanzania: Insights into crustal evolution

4.1 Contributions

J. Bellucci made all of the measurements for this study. P. Piccoli aided in the composition of feldspar measurements.W. McDonough and R. Rudnick contributed to the interpretation of the data. The text, tables, and figures, except for the geological map were written/created by J. Bellucci. The geological map of the area was created by M. Blondes.

4.2 Abstract

Common Pb isotopic compositions of feldspars from the present-day lower, middle, and upper crust of the Mozambique Belt in northern Tanzania are used to determine the provenance of the deep crust within a continental orogen, the timing of last equilibration during the East African Orogeny using feldspar thermochronometry, and to constrain the timing and magnitude of intra-crustal differentiation. The Pb isotopic compositions of most feldspars from lower crustal xenoliths in the Mozambique Belt are strikingly similar to those in granulite-facies xenoliths from

the adjacent Tanzanian Craton, due to re-equilibration at 0.56 Ga with U bearing phases during the East African Orogeny. Middle crustal xenoliths from the mobile belt have more variable Pb isotopic compositions, with two suites (Lashaine and Olmani) having compositions that plot outside of the range of the Tanzanian Craton or the Western Granulites that out crop at the surface; these middle-crustal samples are interpreted as an exotic terrain, not yet sampled in the Mozambique Belt, that was accreted during the East African Orogeny.

The homogenous Pb isotopic compositions of alkali feldspars in the deep crust of the Mozambique Belt reflects their resetting at temperatures $> 600°C$ during the East African Orogeny and contrasts with the deep crust of the Tanzania Craton, which remained below 600°C since its formation in the Archean. The Western Granulites, exposed at the surface, show a $\sim$2.5-fold enrichment in U relative to that of the present-day lower crust that was established $\sim$2.7 Ga, close to the time of crust formation. The Th/U ratio of the lower crust of the Mozambique Belt is $\sim$4, whereas the upper crust is $\sim$3. Finally, a west to east increase in lower crustal $^{238}U/^{204}Pb$, which correlates with heat flow measurements in the area, indicates an enrichment in U with distance from the craton margin, which may have contributed to reworking of Archean crust in the Western Granulites in comparison to the stable Tanzanian Craton.

4.3 Introduction

The continental crust is stratified in composition, with the lower crust being more mafic and depleted in heat producing elements (HPEs: U, Th, K) compared to the upper crust (Rudnick and Fountain, 1995; Rudnick and Gao, 2003, and references therein). Intracrustal differentiation leads to this stratification of the HPEs towards the surface, leaving behind a HPE-depleted lower crust, which, in combination with a thick mantle root, would potentially produce a low surface heat flow (e.g., Perry et al., 2006; Sandiford and McLaren, 2002). The process of intra-crustal differentiation would be especially important in cratons, where depletions of HPEs in the lower crust results in a rigid body, resistant to deformation (Sandiford and McLaren, 2002). Therefore, constraining the timing and level of intra-crustal differentiation is paramount to understanding craton/continental crust formation. Thorium and U are two of the largest contributors to heat flow and are the parent isotopes for the Pb isotopic system. The loss of U during granulite metamorphism and the variable geochemical behavior of U, Th and Pb make the Pb isotopic system a sensitive tool for understanding the timing of crust formation and intra-crustal differentiation (e.g., Bolhar et al., 2007; Möller et al., 1998; Oversby, 1978; Rudnick and Goldstein, 1990).

The Pb isotopic system is comprised of two components: common Pb and radiogenic Pb (Pb*). Common Pb reflects the Pb isotopic composition of a rock at the time of the at the most recent equilibrium. It can be preserved in minerals with low $^{238}U/^{204}Pb$ and $^{232}Th/^{204}Pb$. Coupled with independent chronometric

constraints, the Pb isotopic composition of a rock can be used to model its time-integrated $^{238}U/^{204}Pb$, $^{232}Th/^{204}Pb$, and $^{232}Th/^{238}U$ or its source in simple systems (e.g., Bodet and Scharer, 2001; Gancarz and Wasserburg, 1977). The common Pb isotopic composition of a rock can also be used to discriminate between different crustal domains in granulite belts (e.g., Möller et al., 1998).

The Pb isotopic compositions of feldspars have been used as to understand crustal evolution (e.g., Bodet and Scharer, 2001; Bolhar et al., 2007; Gancarz and Wasserburg, 1977; Kamber et al., 2003; Ludwig and Silver, 1977; Oversby, 1978). Alkali feldspars contain common Pb, as well as exsolution lamellae (or U-bearing micro- inclusions) that may contain U and, thus, may evolve Pb* (Bellucci et al., 2011; Housh and Bowring, 1991; Ludwig and Silver, 1977). Laser ablation (LA-) multi-collector (MC-) ICP-MS (LA-MC-ICP-MS) offers a novel way in which to sample individual domains of Pb on the hundreds of micron scale and, for U-bearing feldspars, provides the potential to date the age of last equilibration defined here to be the time at which the feldspars cooled below their closure temperature, ~600°C (determined by the method of Dodson, 1973) (Bellucci et al., 2011; Cherniak, 1995).

Here we report Pb isotopic compositions in feldspars obtained via LA-MC-ICP-MS from the lower, middle and upper crust of the Mozambique Belt of Tanzania. Based on feldspar compositions, the $^{238}U/^{204}Pb$, $^{232}Th/^{204}Pb$, and $^{232}Th/^{238}U$ of each section of crust were determined, along with the timing and degree of intra-crustal differentiation. Comparisons of the common Pb isotopic compositions of the lower and middle crusts of adjacent crustal sections reveal genetic relationships and provide insights into the tectonic architecture, at depth, of the region. Finally,

domains of Pb* in individual feldspars provide clues about the thermal history of the crust of the Mozambique Belt.

4.4 Geologic Setting

Northern Tanzania is comprised of the Tanzanian Craton and the Mozambique Belt (Figure 4.1), the former of which consists of low- to medium-grade metamorphic rocks, with ages that range between 2.6-3.1 Ga (Bellucci et al., 2011; Coomer and Robertson, 1974; Maboko, 2000; Manya et al., 2006; Möller et al., 1998 and references therein). The Tanzanian Craton has low surface heat flow (34 ± 4 mW/m^2, Nyblade and Pollack, 1993) and is underlain by a refractory, Archean (up to 2.8 Ga) lithospheric keel to a depth of 150 ± 20 km (Burton et al., 2000; Chesley et al., 1999; Lee and Rudnick, 1999; Ritsema et al., 1998; Weerarante et al., 2003). Bordering the Tanzanian Craton to the east lies the high-grade Mozambique Belt, which marks a major suture of Gondwana during the East African Orogeny. The East African Rift (EAR) began propagating around the margins of the Tanzanian Craton, through the Mozambique Belt at ca. 0.03-0.05 Ga, and is manifested by the eruption of basalts, some of which carry xenoliths from the upper mantle and deep crust (Dawson, 1992; Nyblade and Brazier, 2002).

In northern Tanzania, the Mozambique Belt consists of two parallel granulite belts that run roughly north-south: the Western Granulites and the Eastern Granulites with their associated cover sequences (Fig. 4.1, modified from Cutten et al., 2006; Fritz et al., 2009; Hepworth, 1972, and references therein). The Western Gran-

ulites have Archean protoliths, as seen in zircon U-Pb dates of 2.6-2.8 Ga (Johnson et al., 2003) and Nd model ages of $\sim$ 3 Ga (Möller et al., 1998), overlapping the ages seen in the Tanzanian Craton. The Western Granulites were initially metamorphosed to granulite facies in the Archean, 0.05-0.1 Ga after formation (Johnson et al., 2003). Subsequently, the East African Orogeny re-worked these materials, resulting in Pb-loss in zircons (Johnson et al., 2003; Mansur et al., 2011), low-U metamorphic rims on zircons with $^{206}Pb/^{238}U$ dates of ca. 0.550 Ga (Cutten et al., 2006) and metamorphic monazites with dates of ca. 0.560 Ga (Blondes et al., 2011).

By contrast, the Eastern Granulites have more diverse ages. Neodymium model ages are generally bimodal, with Mesoproterozoic (1.1-1.5 Ga) and Archean (2.8 to 3.0 Ga) ages found in most of the Eastern Granulites (Möller et al., 1998). The western Uluguru Mountains are an exception. These rocks have Nd model ages falling between 2.1 to 2.6 Ga, which was attributed by Möller et al. (1998) to mixing between Archean and Proterozoic crustal components. U-Pb zircon crystallization dates for Eastern Granulites are similarly diverse, as summarized in Tenczer et al. (2006), ranging from Archean (2.6 to 2.9 Ga) to a wide range of Proterozoic dates (0.75 to 2.02 Ga). Peak metamorphism in the Eastern Granulites is estimated to be 0.640-0.650 Ga based on U-Pb dating of metamorphic zircons and zircon rims, pre-dating that of the Western Granulites, and has been interpreted to be the age of granulite-facies metamorphism at the base of a continental arc (e.g., Cutten et al., 2006; Kröner et al., 2003; Möller et al., 2000) which was subsequently accreted onto the African continent during the Pan-African orogeny at 0.560 Ga (Cutten et al., 2006).

The southeastern border of the Tanzanian Craton was a convergent margin at ca. 2.0 Ga, resulting in the Usagaran Orogeny (Collins et al., 2004; Möller et al., 1995), which may have marked the closure of a marginal sea formed by rifting within the southern Tanzania Craton (Reddy et al., 2003). There is no evidence for a 2.0 Ga event in the region investigated here (Figure 4.1, Cutten et al., 2006; Fritz et al., 2009; Mansur et al., 2011).

The Mozambique Belt has variable heat flow that increases from west to east (40-64 mW/m^2) and high seismic velocities in the mantle (Nyblade, 1997; Nyblade et al., 1990; Weerarante et al., 2003), which indicates a thin <100 km mantle keel. Peridotite xenoliths from this region have refractory compositions (Rudnick et al., 1994) and Archean Os model ages of up to 3.4 Ga (Burton et al., 2000). These observations suggest that Archean lithosphere of the Tanzanian Craton extends to the east within the Mozambique Belt. The Pb isotopic results reported here provide a means of tracing the lower crust of cratonic lithosphere within the deep crust of the Mozambique Belt.

4.5 Samples

All samples derive from the Mozambique Belt in Northern Tanzania (Figure 4.1) and span a wide range in composition, metamorphic grade, vertical and lateral distribution. Samples consist of granulite facies lower crustal xenoliths, amphibolite or granulite facies middle crustal xenoliths, and granulite facies surface outcrops (Table 4.1). Thermochronology of U-bearing accessory phases for the same sample

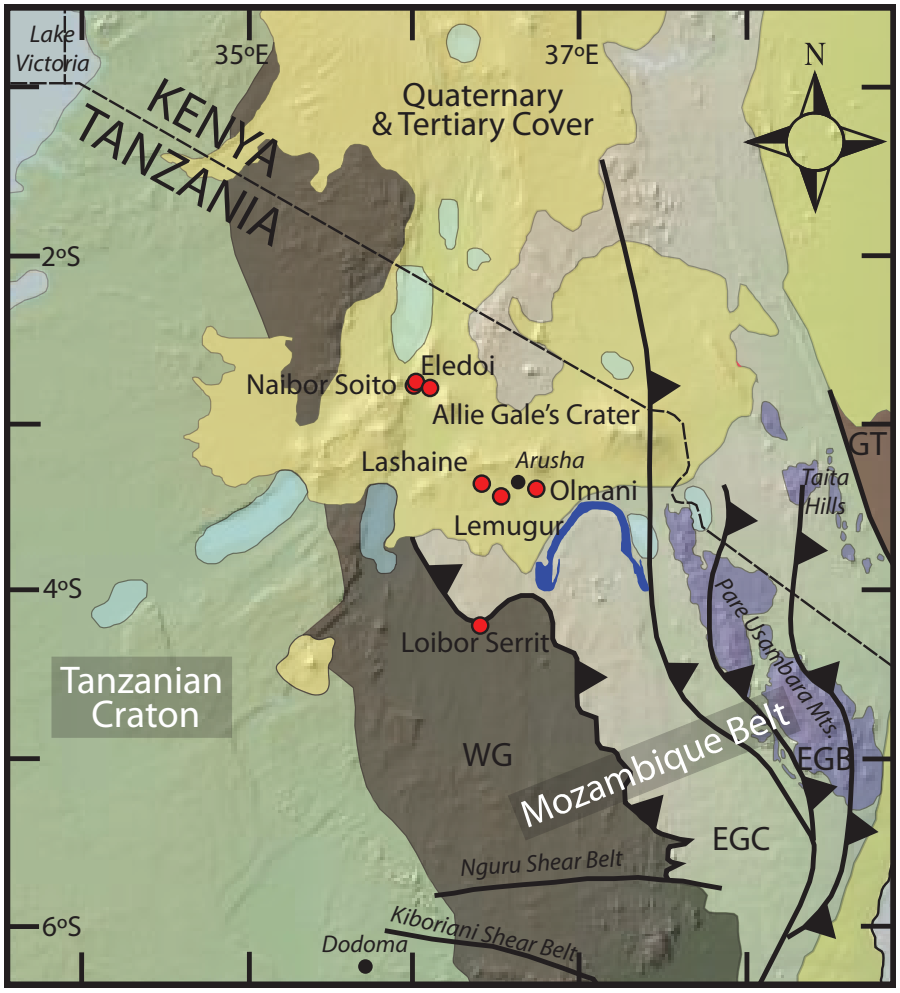

Figure 4.1: Simplified Geologic map of northern Tanzania (after Cutten et al., 2006 and Fritz et al., 2009). Included are surface rock types and locations of the sample locations in this study. EGC: Eatsern Granulite Cover, EGB: Eastern Granulite Basement, GT: Galena Terrain

Table 4.1. Sample Localities, Rock Type, and Depth of Sample

Sample	Rock Type	Major Mineralogy	Accessory Phases	Crustal Level
Allie Gale's Crater (AG)	*2°47'15.00"S, 36° 3'49.32"E*			
AG04-01	Gt Cpx Gran	pl-qtz-cpx-gt	rt, zr, ap	Lower Crust
Naboir Soito (NS)	*2°46'53.04"S, 36° 0'49.86"E*			
NS04-83	Qtz Gran	pl-qtz-cpx-opx	ap, ti	Lower Crust
NS04-94	Qtz Gran	qtz-plag-cpx-opx	ap, zr	Lower Crust
NS04-96	Qtz Gran	pl-qtz-opx-cpx	ap, ti	Lower Crust
NS04-98	Qtz Gran	pl-qtz-opx-cpx	bt, ti	Lower Crust
NS04-13 a	Qtz Gran	pl-qtz-opx-cpx	ap, ti	Lower Crust
NS04-13 b	Qtz Free Gran	pl-opx-cpx	ap, ti	Lower Crust
NS04-43	Qtz Gran	pl-qtz-opx-cpx	ap, ti	Lower Crust
NS04-91 a	Qtz Gran	pl-qtz-opx-cpx	ap, ti	Lower Crust
NS04-91 b	Qtz Free Gran	pl-opx-cpx	ap, ti	Lower Crust
Lashaine (LS)	*3°22'0.00"S, 36°25'60.00"E*			
LS04-08	Gt Cpx Gran	pl-cpx-gt	ap	Lower Crust
LS04-10	Gt Cpx Gran	pl-cpx-gt	ky, ap	Lower Crust
89-727	Gt Cpx Gran	pl-cpx-gt	ap, ky	Lower Crust
89-732	Gt Cpx Gran	pl-cpx-gt	ky, rt	Lower Crust
89-762	Gt Cpx Gran	pl-cpx-gt	ap	Lower Crust
89-726	Gt Cpx Gran	pl-cpx-gt	ky, rt	Lower Crust
LS-17	Gt Cpx Gran	pl-cpx-gt	ky, rt, ap	Lower Crust
LS04-01	Gt Cpx Gran	pl-gt-cpx	ap	Lower Crust
LS04-02	Gt Cpx Gran	pl-cpx-gt	hbl, ky, ap	Lower Crust
89-733	Bio-gt Granulite	pl-bt-cpx-opx-gt	ap, ti, zr	Middle Crust
89-745	Bio-gt Granulite	pl-bt-cpx-opx-gt	ti, zr	Middle Crust
Lemugur (LG)	*3°26'32.32"S, 36°32'27.13"E*			
LG04-37	Amphibolite	qtz-kfs-plag-hbl-bt	ap, rt, zr, ti	Middle Crust
Eledoi (EL)	*2°45'33.45"S, 36° 1'52.52"E*			
EL04-01	Orthogneiss	kfs-qtz-bt-pl	zr, ap	Middle Crust
Olmani (OM)	*3º 23' 50" S, 36º 45' 20" E*			
OM04-13	Felsic Granulite	qtz-pl-gt-bt-cpx-opx	zr, ap, mon	Middle Crust
Loibor Serrit (LS)	*4°10'58.74"S, 36°24'45.30"E*			
LS06-2	Gt Gran	pl-qtz-cpx-gt	am, bi, zr, ap, rt, ti	Surface
LS06-12	Gt Gran gneiss	pl-gt-cpx	zr, ap, rt, ti	Surface

Gran: Granulite; Gt: Garnet, Px: Pyroxene, Qtz: Quart, Opx: Orthopyroxene, Cpx: Clinopyroxene, Kfs: Potassium Feldsdpar, Pl: Plagioclase, Ap: Apatite, Rt: Rutile, Ti: titanite, Ky: Kyanite, Hbl: Hornblende, Am: Amphibole

suites is reported in Blondes et al. (2011). Mineral chemistry, major, trace element and Sr-Nd isotopic data for Lashaine and Naibor Soito xenoliths are reported in Mansur et al. (2011).

4.5.1 Lower Crustal Xenoliths

4.5.1.1 Lashaine

Granulite xenoliths from the Neogene Lashaine volcano in the Mozambique Belt (Figure 4.1) have been the focus of several previous investigations (e.g., Blondes et al., 2011; Cohen et al., 1984; Mansur et al., 2011; Jones et al., 1983). Xenoliths from this locality are dominated by garnet-clinopyroxene granulites, many of which contain kyanite. Pyroxenes in a number of xenoliths are rimmed by garnet, suggesting an isobaric cooling history. Application of two-pyroxene thermometers and garnet-orthopyroxene barometers yield equilibration temperatures of 720-820°C, and pressures of 1.7 to 2.7 GPa, suggesting these samples experienced peak metamorphism at the base of doubly-thickened continental crust during the East African Orogeny (Mansur et al., 2011). Major and trace element compositions from these xenoliths suggest they formed as cumulates from basaltic magmas (Jones et al., 1983; Mansur et al., 2011). Feldspars from the Lashaine xenoliths are unzoned with compositions of $An_{22-45}Ab_{58-76}Or_{2-5}$. Alkali feldspar has not been observed in any of the Lashaine xenoliths.

4.5.1.2 Naboir Soito

Granulite xenoliths from the Neogene Naibor Soito volcano (Figure 4.1) are largely made up of quartz granulites having a major mineralogy of plagioclase, quartz, orthopyroxene, clinopyroxene and garnet. Other samples contain no quartz, but otherwise have similar mineralogy. The whole rock major element compositions

are remarkably similar to lavas from the greenstone belts in the Tanzanian Craton and, like those lavas, may have formed in a convergent margin setting in the Archean (Mansur et al., 2011). Equilibration conditions for these xenoliths are similar to those from Lashaine (820- 880°C, 1.3 to 2.6 GPa), suggesting their equilibration at the base of a doubly-thickened crust (Mansur et al., 2011). The U-Pb ages of zircons from these samples reveal two age clusters: 1) 2.65 Ga, which coincides with the final stages of formation of the Tanzanian Craton (e.g., Bellucci et al., 2011; Maboko, 2000; Manya et al., 2006) and 2) 2.80 Ga, an earlier crust generation event (Mansur et al., 2011). Whole rock Nd model ages range from 2.5-3.1 Ga, consistent with their formation in the Archean (Mansur et al., 2011).

The feldspars in these xenoliths exhibit a wide range in composition and are enriched in K_2O relative to the Lashaine xenoliths. Plagioclase in these samples is $An_{25-48}Ab_{50-68}Or_{2-11}$. Orthoclase is observed in several samples from this locality and has the composition $An_6Ab_{31-34}Or_{60-64}$ (Mansur et al., 2011). Two lower crustal xenoliths from this volcano are compositionally banded (NS04-13 and NS04-91) with interweaving mafic and felsic bands.

4.5.1.3 Allie Gale's Crater

The sample from Allie Gale's Crater is a garnet-clinopyroxene granulite. It is composed of plagioclase, quartz, clinopyroxene, and garnet. Because it is a granulite, we assume that this rock is from the lower crust. No major or trace element analyses have been obtained for this sample. The feldspars from this sample are unzoned

plagioclase and have the composition of $An_{15}Ab_{80}Or_4$.

4.5.2 Middle Crustal Xenoliths

4.5.2.1 Eledoi

Eledoi is an explosion crater containing peridotite xenoliths (Cohen et al., 1984; Dawson and Smith, 1988) located near Naibor Soito and Allie Gale's Crater (Figure 4.1). Sample EL04-01 is a felsic orthogneiss composed of orthoclase, plagioclase, quartz and biotite. The presence of hydrous phases in this sample is consistent with its derivation from the middle crust. The sample contains monazites that have Archean (ca. 2.6 Ga) cores and Pan-African overgrowths (ca. 0.560 Ga) (Blondes et al., 2011). Here we assume, following Blondes et al. (2011) that the younger monazite grew during peak metamorphism during the East African Orogeny. The older age is interpreted to document its original formation in the Archean, which is similar to zircon ages from lower crustal xenoliths from the Tanzanian Craton (Mansur et al., 2011; Blondes et al., 2011) and Western Granulites (Johnson et al., 2003). The plagioclase from this sample has a composition of $An_{15}Ab_{84}Or_2$ and the orthoclase has a composition of $An_0Ab_{56}Or_{44}$.

4.5.2.2 Lashaine

Two biotite-garnet granulite xenoliths from the Lashaine volcano have distinct mineralogies and compositions compared to garnet-clinopyroxene granulites from Lashaine. In addition to containing biotite, these samples are enriched in incompat-

ible trace elements and have compositions similar to potassic basalts (Mansur et al., 2011). They equilibrated at markedly lower temperatures and pressures (600°C, 0.8 GPa) than the Lashaine garnet-clinopyroxene granulites, indicating their derivation from the middle of the doubly-thickened crust of the East African Orogen (Mansur et al., 2011). Both samples yield Nd model ages of 2.8 Ga (Mansur et al., 2011). While the U-Pb ages in zircon from these two Lashaine xenoliths are imprecise due to the very small size of the zircons, they yield highly discordant ages pointing towards the Archean, with a subset having concordant ^{238}U-^{206}Pb ages that cluster around 0.550 Ga (Blondes et al., 2011). Feldspars from these xenoliths are unzoned and have a composition of $An_{30}Ab_{67}Or_3$ (Mansur et al., 2011).

4.5.2.3 Olmani

The Olmani scoria cone is located on the outskirts of Arusha (Figure 4.1) and contains mantle xenoliths that have a distinctive signature of carbonatite overprint (Cohen et al., 1984; Rudnick et al., 1993, 1994; Burton et al., 2000). Sample OM04-13 is a foliated felsic granulite composed of quartz, plagioclase, garnet, biotite orthopyroxene and clinopyroxene. This sample is inferred to derive from the present-day middle crust and contains apatites with concordant U-Pb dates of 0.465±7 to 0.4797±5 Ga (Blondes et al., 2011). Plagioclase from this xenolith is $An_{19}Ab_{79}Or_2$.

4.5.2.4 Lemugur

The Lemugur tuff cone is located to the south of Lashiane and Olmani localities (Figure 4.1). While a large variety of crustal xenoliths are found there, they have not been previously studied. Sample LG04-37 is a foliated amphibolite consisting of plagioclase, alkali-feldspar, quartz, brown amphibole and biotite. Titanites from this xenolith yield concordant dates between 0.5023 ± 4 and 0.5361 ± 5 Ga, while a single apatite yields a younger concordant date of 0.368 ± 12 Ga (Blondes et al., 2011). Both plagioclase and alkali feldspar occur in these xenoliths and have compositions of $An_{15}Ab_{84}Or_1$ and $An_0Ab_{55}Or_{45}$, respectively.

4.5.3 Surface Samples

4.5.3.1 Loibor Serrit

The samples from Loibor Serrit are part of the Western Granulites of the Mozambique Belt (Figure 4.1). Sample LS06-12 is a mafic garnet granulite gneiss cobble composed of poikioblastic garnet, plagioclase and clinopyroxene. Sample LS06-2 is a garnet granulite composed of quartz and plagioclase, garnet, minor clinopyroxene, amphibole and biotite. Rutile, apatite and titanite yield overlapping U-Pb dates ranging between 0.509 and 0.553 Ga, with the exception of one titanite that yields a date of 0.615 Ga and one rutile that yields a date of 0.467 Ga (Blondes et al., 2011). Plagioclases from these two samples have similar compositions of $An_{37-38}Ab_{59-61}Or_{2-3}$.

Table 4.2 Feldspar Compositions

	AG04-01	EL04-01-Pl	EL04-01-Or	LS06-12	LS06-02	LG04-37-Pl	LG04-37-Or	OM04-13
SiO2	63	64	65	58	58	64	64	61
Al_2O_3	23	23	19	25	26	23	19	23
CaO	4	4	0	8	7	4	0	5
Na_2O	8	9	2	7	7	8	1	8
K_2O	1	0	14	0	0	0	14	0
Total	100	100	100	98	99	99	98	97
Si	2.7	2.7	2.6	2.7	2.6	2.7	2.5	2.6
Al	1.2	1.1	0.9	1.4	1.4	1.1	0.9	1.2
Ca	0.2	0.2	0.0	0.4	0.4	0.2	0.0	0.2
Na	0.9	0.9	0.9	0.6	0.6	1.0	0.9	1.0
K	0.0	0.0	0.7	0.0	0.0	0.0	0.7	0.0
An	16	15	0	38	37	15	0	19
Ab	80	84	56	59	61	84	55	79
Or	4	2	44	3	2	1	45	2

4.6 Analytical Methods

4.6.1 Feldspar compositions

Feldspars major element compositions for the samples from Allie Gale's Crater, Eledoi, Loibor Serrit, Lemugur, and Olmani were determined using the JXA-8900 SuperProbe with WD/ED Combined Electron Probe Microanalyzer (EPMA) at the University of Maryland, College Park (UMCP). The compositions reported here are averages of 3 separate analyses from the same crystal domain. The rest of the feldspar compositions are reported in Mansur et al. (2011).

4.6.2 Pb isotopic compositions

All isotopic analyses were conducted using a UP-213 nm wavelength laser coupled to a Nu Plasma multi-collector ICP-MS, following the methods of Kent (2008a,b). All analyses were conducted as lines that are 100-150 μm x 350-550 μm (Table 4.2). Our analytical protocol is fully described in Bellucci et al. (2011); similar procedures were used in this study. Analytical conditions are given in Table 4.2.

A mass fractionation corrected ^{204}Hg abundance was used to subtract the isobaric interference of ^{204}Hg on ^{204}Pb. The Hg mass fractionation factor was calculated using the measured ^{202}Hg/^{200}Hg, a comparison to the natural isotopic abundances of Hg (de Laeter et al, 2003), and the exponential law. Correction for mass fractionation of Pb isotope ratios was performed via standard-sample bracketing, using NIST 612 as the reference material, the Pb isotopic ratios reported in Baker et al. (2004) and using the exponential law. The mass fractionation factor was determined using ^{208}Pb/^{206}Pb. Prior to analyses; all Faraday cups were calibrated to the axial cup. Faraday-ion counter gain calibrations were calculated by taking the ratio of the measured ^{20x}Pb/^{204}Pb (x=208, 207, or 206) vs. the expected ^{20x}Pb/^{204}Pb. The expected ^{20x}Pb/^{204}Pb were calculated using the fractionation factor calculated from the measured ^{208}Pb/^{206}Pb in NIST 612. Typical $2\sigma_{mean}$ precision on multiple analyses of feldspars (n =10) is $\pm$0.3% for ^{20x}Pb/^{204}Pb.

Table 4.3. Typical operating conditions for *in situ* Pb isotopic analysis and collector assignments for various Pb isotopic analysis

Mass Spectrometer	
	Nu Plasma
Instrumentation:	MC-ICP-MS
Forward Power	1300 W
Reflected Power	<10 W
Cones	Ni
Acceleration Voltage	4000 V
Typical gas Flows	
Coolant	13 L min^{-1}
Auxilary	0.8 L min-1
Nebulizer	0.77 L min-1
Aridus Gas flows	
Sweep Gas	2.20 L min^{-1}
N_2	0.15 L min^{-1}
Laser	
Instrumentation:	NewWave UP 213 213 nm frequency quintupled Nd-Yag
Sweep Gas	
He	0.3 L min^{-1}
Line Diameter	100-150 µm
Line Length	350-550 µm
Analysis Duration	40-80 s
Translation Rate	7 µm s^{-1}
Pulse Frequency	7 hz
Pulse Energy	4.5 J cm^{-2}

Collector[1]	H6	H5	H4	H3	H2	H1	Ax	L1	L2	ICO	L3	IC1	L4	IC2	L5
Analyte Isotopes						^{208}Pb	^{207}Pb	^{206}Pb	$^{205}Tl^2$	^{204}Pb	$^{203}Tl^2$				
Interferences										^{204}Hg		^{202}Hg		^{200}Hg	

[1] Collectors H*x* and L*x* are Faraday Cups, and Icx are ion counters.
[2] Although Tl is measured it is not in significant abundance to be used in mass bias corrections.

4.7 Results

The average Pb isotopic compositions of feldspars from the sample suite are summarized in Table 4.3 and plotted in Figure 4.2. Data tables for each individual laser analysis are located in Appendix D.

The spread of Pb isotopic compositions in the $^{206}Pb/^{204}Pb$ vs. $^{207}Pb/\ ^{204}Pb$ plot is large, with $^{206}Pb/^{204}Pb$ ranging from 14-19.4 (Figure 4.2). There is a significant spread in the $^{207}Pb/\ ^{204}Pb$, which is noticeable in the lower crustal xenoliths from Naboir Soito and Lashaine. The most radiogenic samples are middle crustal xenoliths from Lashaine and Olmani (Figure 4.2). The least radiogenic sample is the lower crustal xenolith from Allie Gale's Crater, which plots near the 2.71 Ga Geochron.

The Pb isotopic composition of middle-crustal feldspars from Eledoi and Lemugur also lie within the field defined by the Tanzanian Craton (Bellucci et al., 2011), while those from Lashaine and Olmani lie significantly outside the field of the Tanzanian Craton. The Western Granulite samples (Loibor Serrit) also lie outside the cratonic lower crustal field.

Two of the samples from Naibor Soito are compositionally banded (Table 4.1). Plagioclase from each band has a distinct Pb isotopic composition (Table 4.2), with those from the more felsic band having a more radiogenic Pb composition than those from the mafic band.

The thorogenic Pb system is highly variable, with $^{208}Pb/^{204}Pb$ ranging from 33.7-40.4. Feldspars from two Naibor Soito granulites plot above the field defined

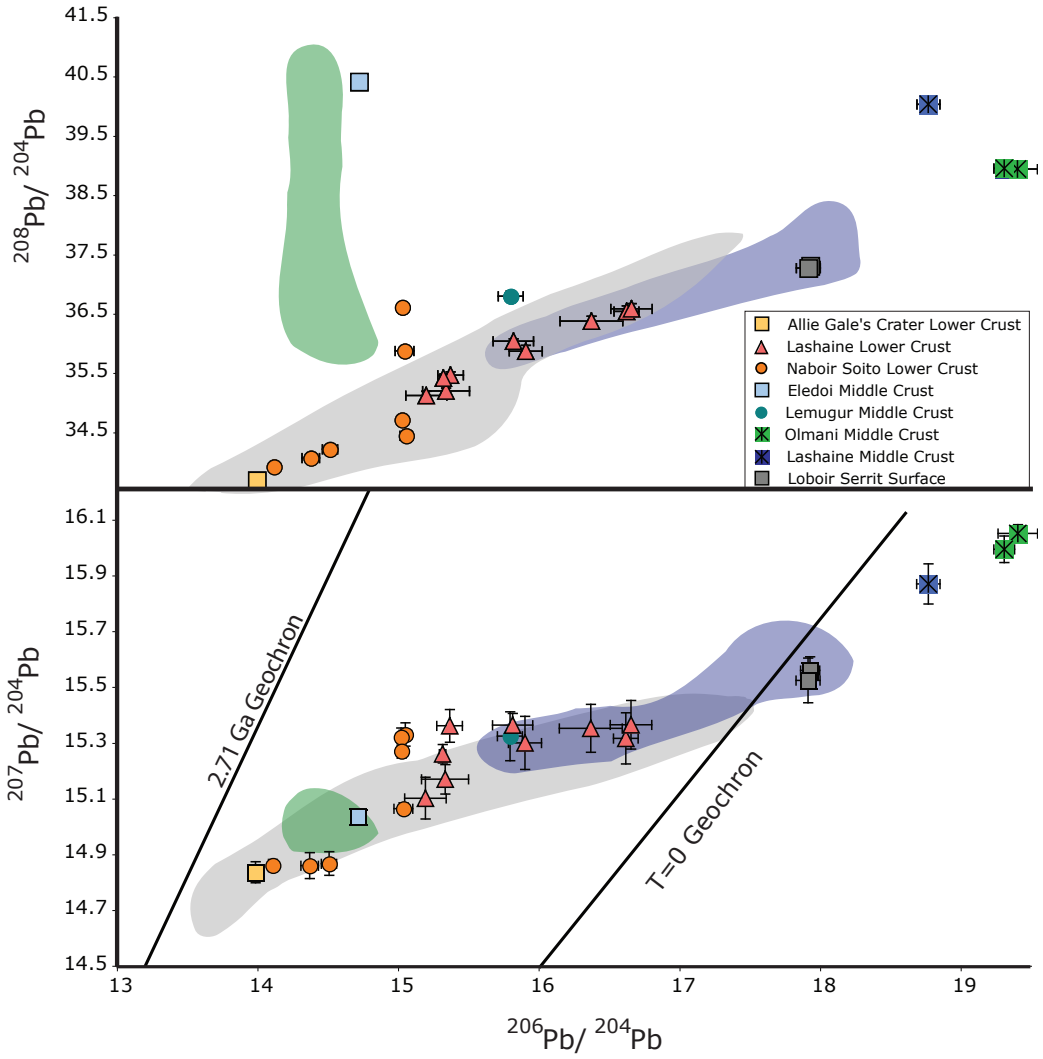

Figure 4.2: For reference, the T=0 (Present Day) and 2.71 Ga Geochrons are shown. The gray field represents the field defined by feldspar Pb isotopic data from the Labait locality on the Tanzanian Craton from Bellucci et al. (2011). They green and purple fields represent the field defined by Pb isotopic data from feldspars from samples recovered from the surface of the Western Granulites outcropped in the southern Mozambique belt and the Pare, Usambara, Uluguru Mountains, the Umba Steppe, and Wami river which represent the Eastern Granulites, respectively from Möller et al. (1998). Error bars represent $2\sigma_{mean}$ of multiple feldspar analyses.

by the lower crust of the Tanzanian Craton on the $^{206}Pb/^{204}Pb$ vs. $^{208}Pb/^{204}Pb$ plot (Fig. 4.2), while all other lower crustal feldspars lie within the field. Feldspars from the middle crustal xenoliths show the largest variability and all plot outside the field of the Tanzanian Craton.

4.8 Discussion

4.8.1 Provenance

The majority of lower crustal xenoliths from the Mozambique Belt have Pb isotopic compositions that plot within the field defined by the Tanzanian Craton's lower crust (Figure 4.2). The tectonic model of the area indicates that the lower crust beneath the western Mozambique Belt is comprised of the Western Granulites (Cutten et al., 2006; Fritz et al., 2009). Therefore, the lower crustal xenoliths from the Mozambique Belt likely represent the Western Granulites, and their Pb isotopic compositions support the interpretation that the Western Granulites are re-worked crust from the Tanzanian Craton. The middle crustal xenoliths from Eledoi and Lemugur also share similar $^{206}Pb/^{204}Pb$ and $^{207}Pb/^{204}Pb$ compositions to the Tanzanian Craton lower crust; we therefore interpret these as being Western Granulites, which formed from re-worked crust of the Tanzanian Craton. The high $^{208}Pb/^{204}Pb$ of the mid-crustal Eledoi orthogneiss (EL04-01) has a similar Pb isotopic composition to the lowland migmatites and granuiltes that occur within the Western Granulites to the south of our study area (Möller et al., 1998) (Figure 4.2), suggesting that these thorogenic compositions may have originated in the craton.

Table 4.4. Pb isotopic compositions of feldspars from Mozambique Belt xenoliths

Sample	Location	Mineral	$^{208}Pb/^{204}Pb$	$2\sigma_{(mean)}$	$^{207}Pb/^{204}Pb$	$2\sigma_{(mean)}$	$^{206}Pb/^{204}Pb$	$2\sigma_{(mean)}$	n
Lower Crust									
NS04-13 mafic	Naboir Soito	pl	34.44	0.10	15.33	0.04	15.05	0.04	7
NS04-13 felsic	Naboir Soito	pl	34.61	0.01	15.41	0.09	15.50	0.11	2
NS04-43	Naboir Soito	pl	34.71	0.07	15.32	0.03	15.02	0.03	8
NS04-83	Naboir Soito	pl	34.21	0.10	14.87	0.04	14.51	0.05	8
NS04-91 mafic	Naboir Soito	pl	36.61	0.08	15.27	0.03	15.02	0.03	6
NS04-91 felsic	Naboir Soito	pl	37.60	0.10	15.29	0.04	15.32	0.04	4
NS04-94	Naboir Soito	pl	33.92	0.06	14.86	0.02	14.11	0.02	8
NS04-96	Naboir Soito	pl	34.07	0.10	14.86	0.05	14.37	0.06	9
NS04-98	Naboir Soito	pl	35.87	0.07	15.06	0.02	15.04	0.07	6
AG04-01	Allie Gale's Crater	pl	33.69	0.09	14.83	0.04	13.99	0.05	8
89-726	Lashaine	pl	35.87	0.26	15.30	0.10	15.90	0.12	9
89-727	Lashaine	pl	36.54	0.12	15.31	0.09	16.62	0.09	10
89-732	Lashaine	pl	36.58	0.22	15.36	0.09	16.65	0.15	10
89-762	Lashaine	pl	36.37	0.24	15.35	0.09	16.37	0.22	8
LS04-01	Lashaine	pl	35.41	0.09	15.26	0.03	15.32	0.02	8
LS04-02	Lashaine	pl	36.03	0.20	15.36	0.04	15.81	0.14	7
LS04-08	Lashaine	pl	35.19	0.18	15.17	0.05	15.34	0.17	8
LS04-10	Lashaine	pl	35.12	0.25	15.10	0.08	15.20	0.15	8
LS-17	Lashaine	pl	35.46	0.16	15.36	0.06	15.37	0.09	8
Middle Crust									
EL04-01	Eledoi	kfs-pl	40.41	0.03	15.03	0.02	14.72	0.02	11
LG04-37	Lemugur	kfs-pl	36.80	0.09	15.32	0.09	15.80	0.09	10
89-733	Lashaine	pl	38.94	0.12	16.05	0.03	19.40	0.14	8
89-745	Lashaine	pl	38.95	0.16	15.99	0.05	19.31	0.07	8
OM04-13	Olmani	pl	40.03	0.15	15.87	0.07	18.77	0.08	8
Surface									
LS06-02	Loibor Serrit	pl	37.31	0.08	15.56	0.05	17.93	0.07	10
LS06-12	Loibor Serrit	pl	37.27	0.15	15.52	0.08	17.91	0.08	8

n=number of feldspars analyzed, pl: plagioclase, kfs: alkali feldspar

By contrast, middle crustal xenoliths from Lashaine and Olmani have distinct Pb isotopic compositions, zircon age populations (Blondes et al., 2011), trace element compositions (Mansur et al., 2011), and a mineralogy that is largely different from both the Eastern and Western Granulites. Therefore, we interpret these xenoliths as being derived from a previously un-sampled, exotic terrain that was accreted onto the African continent during the East African Orogeny.

4.8.2 Pb isotopic modeling

In this section, we will use the common Pb isotopic compositions to calculate the change in $^{238}U/^{204}Pb$ and $^{232}Th/^{238}U$ through time. Since the mantle extraction age of the Eastern Granulites appears to be variable, and the metamorphic history is significantly more complicated than the Western Granulites, the focus of this section will be on the latter. The Pb isotopic model used here is a single-stage Holmes-Houterman model (Holmes, 1946; Houtermans, 1946), using an initial Pb isotopic composition of the Canyon Diablo troiolite (Chen and Wasserburg, 1983) at 4.57 Ga. We assume the crust was extracted from the mantle at 2.71 Ga, like the Tanzanian Craton (Bellucci et al., 2011), and the feldspars experienced equilibration with the surrounding whole rock and U bearing phases during the East African Orogeny, with the peak metamorphism occurring at 0.560 Ga (Blondes et al., 2011; Cutten et al., 2006).

The U-Pb system has two decay equations, two $^{238}U/^{204}Pb$ variables and two age variables. Here we use the mantle extraction age and metamorphic age as

the two age variables, and solve for the two $^{238}U/^{204}Pb$ variables: $(^{238}U/^{204}Pb)_1$ and $(^{238}U/^{204}Pb)_2$. Where $(^{238}U/^{204}Pb)_1$ represents the ratio from 4.57-2.71 Ga and $(^{238}U/^{204}Pb)_2$ is the ratio in the crust from 2.71-0.56 Ga. Unfortunately, the $^{232}Th/^{238}U$ system ($^{238}U/^{204}Pb$ /$^{232}Th/^{204}Pb$) has only one decay equation and two time variables and two $^{232}Th/^{238}U$ terms. Here we assume a $(^{232}Th/^{238}U)_1$ (system initial) of 4.3, similar to that of the Tanzanian Craton (Bellucci et al., 2011) in order to arrive at a solution for $(^{232}Th/^{238}U)_2$, which was the ratio in the crust from 2.71-0.56 Ga.

The Pb isotopic modeling results are displayed in Table 4.3 and in Figure 4.3. Two populations of lower crustal xenoliths are identified based on their initial $^{238}U/^{204}Pb$ values ($(^{238}U/^{204}Pb)_1$): a $(^{238}U/^{204}Pb)_1$ of 8.0 $\pm$ 0.2 (2σ) and a $(^{238}U/^{204}Pb)_1$ of 8.5 $\pm$ 0.4 (2σ). The bulk rock $^{238}U/^{204}Pb$ ($(^{238}U/^{204}Pb)_2$) between 2.71 Ga and 0.560 Ga for all of the lower crustal xenoliths range widely (1.4-7.7), with an average around 4 $\pm$ 5 (2σ). Mid-crustal samples from Eledoi and Lemugur have similar $(^{238}U/^{204}Pb)_1$ (8.2 $\pm$ 0.2, 2σ) and $(^{238}U/^{204}Pb)_2$ (4 $\pm$ 3, 2σ) to the granulite xenoliths. Surface granulites have a $(^{238}U/^{204}Pb)_1$ of 7.8 $\pm$ 0.1 (2σ) and a $(^{238}U/^{204}Pb)_2$ of 10.8 $\pm$ 0.1 (2σ). Similarly, the whole rock concentration of U in the surface samples from the Western Granulites ($\sim$ 8 μg/g, Johnson et al., 2003) is an order of magnitude relative to the lower crustal xenoliths from Lashaine and Naboir Soito ($\sim$ 0.2 μg/g, Mansur et al., 2011). Whole rock $(^{232}Th/^{238}U)$ values between 2.71 Ga and 0.560 Ga ($(^{232}Th/^{238}U)_2$) are highly variable (Figure 4.5). The lower crustal xenoliths have an average $(^{232}Th/^{238}U)_2$ of 4.0 $\pm$ 2.7 (2σ). The $(^{232}Th/^{238}U)_2$ value of the mid-crustal xenoliths is unconstrained (i.e., $(^{232}Th/^{238}U)_2$ ranges from

3.5-20) and surface samples have a $(^{232}Th/^{238}U)_2$ of 3.33 ± 0.03 (2σ).

The Pb isotopic composition of the present-day lower crust beneath the Western Granulites is less radiogenic than the upper crust, reflecting the difference in $(^{238}U/^{204}Pb)_2$ for these samples. Given a mantle extraction time of ca. 2.71 Ga (Bellucci et al., 2011; Johnson et al., 2003), the lower crust in this region has evolved with an average $^{238}U/^{204}Pb$ of 4, while the upper crust (Western Granulites) has evolved with a $^{238}U/^{204}Pb$ of 11 (Figure 4.3). This represents an enrichment of U in the upper crust relative to the lower crust of ∼2.5, which happened near the time of mantle extraction. By contrast, the $^{232}Th/^{238}U$ of the lower and upper crust are similar at 4 and 3, respectively. The present-day middle crust is heterogeneous and has $^{232}Th/^{238}U$ ranging from 7 to 20. The latter value is most likely not typical of the middle crust. The slight enrichments in ^{207}Pb seen in some Naibor Soito and Lashaine lower crustal xenoliths relative to the lower crust of the Tanzanian Craton, requires their derivation from a mantle source region with higher (8.5 vs. 8.1) time-integrated $(^{238}U/^{204}Pb)_1$.

The lower crust beneath the Mozambique Belt, as sampled by granulite xenoliths from Allie Gale's Crater, Naboir Soito, and Lashaine shows an increase in $(^{238}U/^{204}Pb)_2$ from 1-5.5 with distance from the craton margin, while the $^{232}Th/^{238}U$ stays relatively constant at ∼ 3 (Table 4.5, Figure 4.3). A similar trend is seen in the middle crustal xenoliths from Eledoi and Lemugur. The enrichment in U towards the east would result in a higher heat flow and a weaker rheology. The weaker rheology could be the reason the Western Granulites experienced multiple tectonic events since the Archean, while the Tanzanian Craton has been stable since its formation

(e.g., Sandiford and McLaren, 2002).

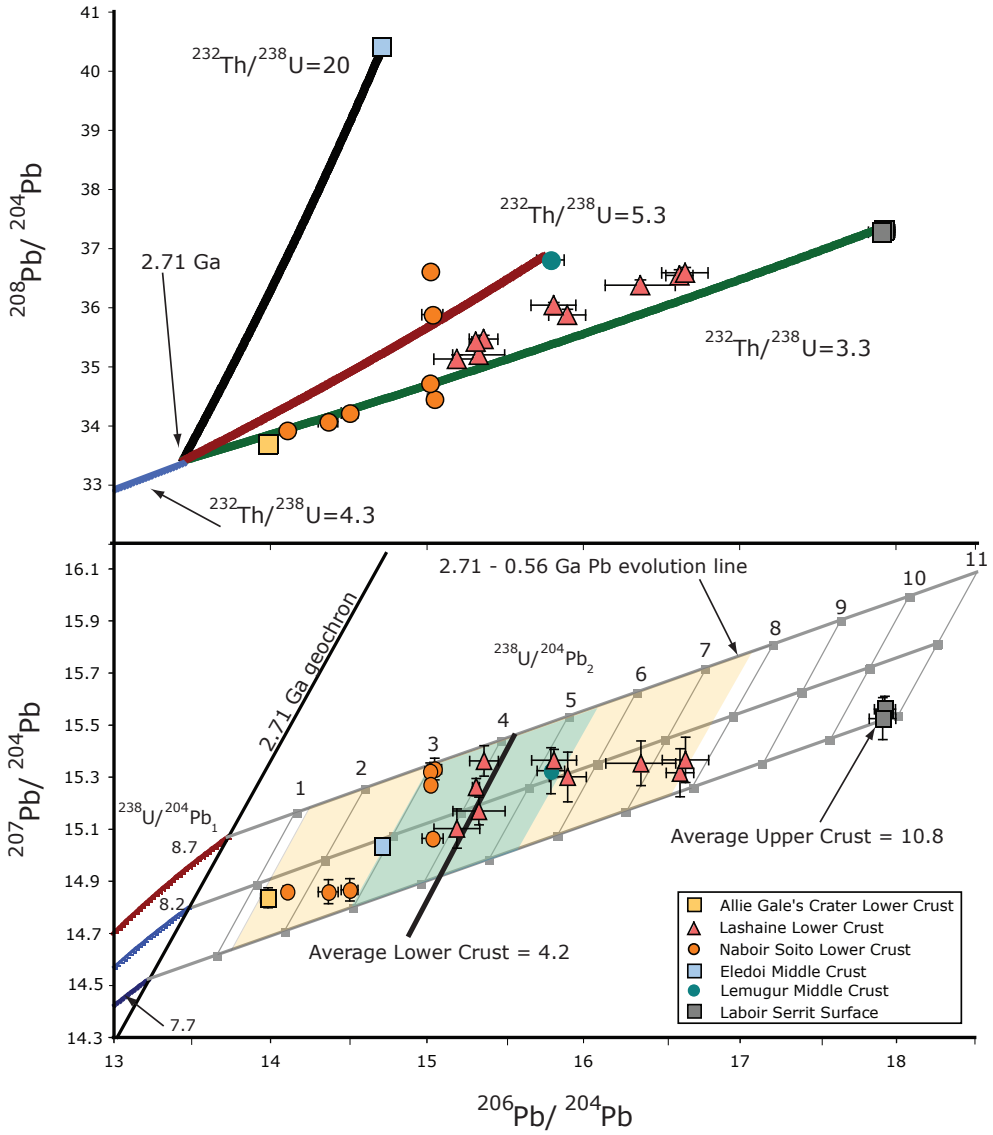

Figure 4.3: Results from the Pb isotopic modeling of the Western Granulites. Growth curves in the $^{207}Pb/^{204}Pb$ vs. $^{206}Pb/^{204}Pb$ diagram are for the low, average, and high $(^{238}U/^{204}Pb)_1$, which are 7.7, 8.2, and 8.7, respectively. The linear features are Pb growth projections from 2.71 to 0.560 Ga, the tie lines represent the values of $(^{238}U/^{204}Pb)_2$. The orange field shows the spread in calculated $(^{238}U/^{204}Pb)_2$ values for the lower crust, and the green field shows the spread in calculated $(^{238}U/^{204}Pb)_2$ values for the middle crust. Growth curves in the $^{207}Pb/^{204}Pb$ vs. $^{206}Pb/^{204}Pb$ are shown with variable $^{232}Th/^{238}U$.

Table 4.5. Modeled U/Pb, Th/Pb, and Th/U of the mantle and the Western Granulites lower, middle, and upper crust

Sample	Location	T_1 (MA)	T_2 (MA)	$(^{238}U/^{204}Pb)_1$	$(^{238}U/^{204}Pb)_2$	$(^{232}Th/^{238}U)$*
Lower Crust						
NS04-13 a	Naboir Soito	2710	560	8.7	3.1	2.5
NS04-43	Naboir Soito	2710	560	8.7	3.0	3.3
NS04-83	Naboir Soito	2710	560	7.9	2.8	3.2
NS04-91 a	Naboir Soito	2710	560	8.5	3.2	8.3
NS04-94	Naboir Soito	2710	560	8.0	1.6	3.4
NS04-96	Naboir Soito	2710	560	7.9	2.4	3.1
NS04-98	Naboir Soito	2710	560	8.1	3.8	5.9
AG04-01	Allie Gale's Crater	2710	560	8.1	1.3	2.7
89-726	Lashaine	2710	560	8.2	5.6	3.9
89-727	Lashaine	2710	560	7.9	7.7	3.8
89-732	Lashaine	2710	560	8.0	7.6	3.8
89-762	Lashaine	2710	560	8.1	6.8	3.9
LS04-01	Lashaine	2710	560	8.4	4.0	4.2
LS04-02	Lashaine	2710	560	8.4	5.2	4.3
LS04-08	Lashaine	2710	560	8.2	4.3	3.7
LS04-10	Lashaine	2710	560	8.1	4.1	3.8
LS-17	Lashaine	2710	560	8.6	3.9	4.2
Middle Crust						
EL04-01	Eledoi	2710	560	8.2	3	20
LG04-37	Lemugur	2710	560	8.3	5	6
Surface						
LS06-02	Loibor Serrit	2710	560	7.8	10.8	3.3
LS06-13	Loibor Serrit	2710	560	7.7	10.8	3.3

T1: The time of extraction of the Tanzanian Craton (Bellucci et al., 2010),T2: Age of Pan-African Metamorphism (Blondes et al., 2010, Cutten et al., 2006), $(^{238}U/^{204}Pb)1$: mantle $(^{238}U/^{204}Pb)$, $(^{238}U/^{204}Pb)2$: bulk rock $(^{238}U/^{204}Pb)$; $(^{232}Th/^{238}U)$* Modeled $(^{232}Th/^{238}U)$ from a mantle $(^{232}Th/^{238}U)$ evolution from 4.57 Ga-2.74 Ga of 4.3, similar to the Tanzanian Craton (Bellucci et al., 2010)

Table 4.6. Lower Crust Averages of $(^{238}U/^{204}Pb)_2$ and $(^{232}Th/^{238}U)_2$ from West to East

Locality, West to East	km away from craton border	$(^{238}U/^{204}Pb)_2$	2σ	$(^{232}Th/^{238}U)_2$	2σ
Lower Crust					
Naboir Soito	57	2.8	1.3	4.2	4.2
Allie Gale's Crater	62	1.3	N/A	3	N/A
Lashaine	106	5.5	3.1	4.0	0.5
Middle Crust					
Eledoi	60	2.9	N/A	20	N/A
Lemugur	118	5.3	N/A	6	N/A

4.8.3 Timing of Last Equilibration

Linear trends in Pb isotopic data can reflect mixing between two isotopically distinct components or radiogenic in-growth, which can date the most recent equilibration event. Two compositionally banded lower crustal granulite xenoliths from Naibor Soito have plagioclases with distinct Pb isotopic compositions between bands (Figure 4.5), with the felsic bands having more radiogenic plagioclases than those in the mafic bands. While the uncertainty on each analysis is too large to yield a true isochron, the slope on the $^{206}Pb/^{204}Pb$ vs. $^{207}Pb/^{204}Pb$ plot suggests a date of 0.560 Ga. The Pb isotopic compositions of the feldspars are unlikely to be influenced by host basalt infiltration, given the similar Pb concentration in the feldspar and basalt at $\sim$ 5-10 μg/g (Paslick et al., 1995). Moreover, linear regressions through $^{208}Pb/^{204}Pb$ vs. $^{206}Pb/^{204}Pb$ of the banded samples do not intersect the Pb isotopic composition of the rift basalts (Figure 4.5), which rules out mixing as a cause of the linear trends and instead suggests isotopic disequilibria, resulting from the in growth of U in the plagioclases in these samples. We suggest that the differences in the Pb isotopic composition between the different bands reflects the last whole rock equilibration, which occured during the East African Orogeny.

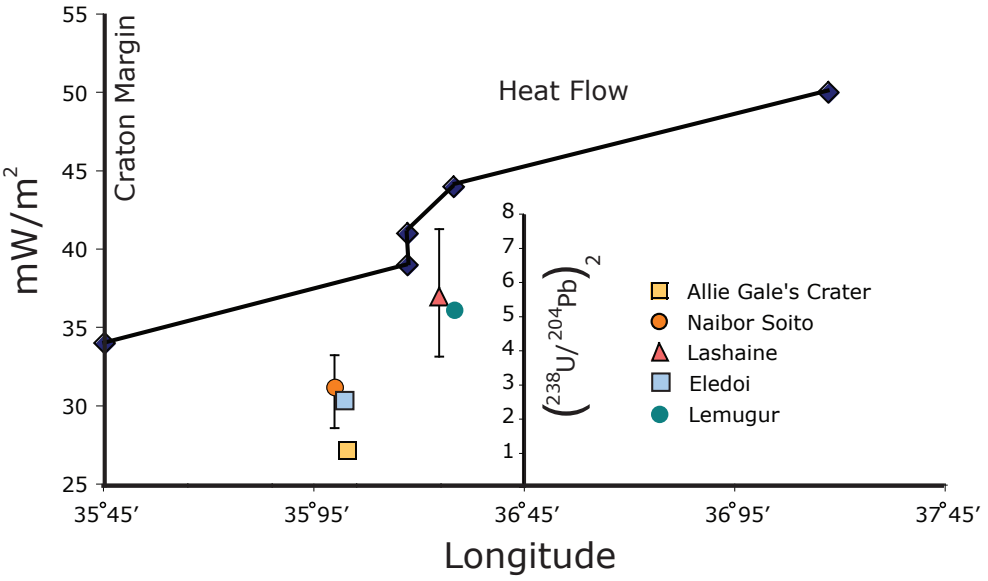

Figure 4.4: Results from the Pb isotopic modeling of the Western Granulite lower crust and corresponding heat flow measurements from Nyblade and Pollack (1993) and Nyblade (1990), with latitude locations moving away from the craton margin. The error bars on the $(^{238}U/^{204}Pb)_2$ data points represent the range in values for each xenolith locality.

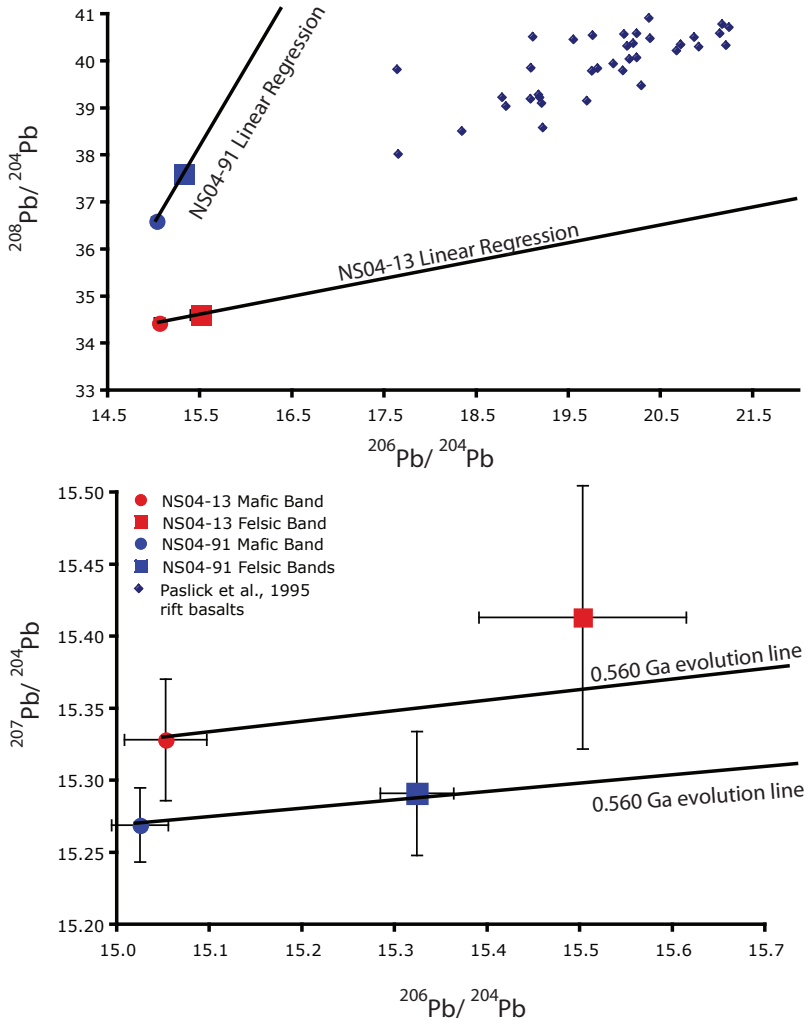

Figure 4.5: Lower Panel: $^{207}Pb/^{204}Pb$ vs. $^{206}Pb/^{204}Pb$ with banded samples and projected 0.560 Ga isochron. Upper Panel: $^{208}Pb/^{204}Pb$ vs. $^{206}Pb/^{204}Pb$ with banded samples plotted with linear regressions and the Tanzanian Rift basalts (Paslick et al., 1995). Error bars represent $2\sigma_{mean}$ of multiple feldspar analyses

4.9 Conclusions

The individual feldspars measured in this study are homogenous with respect to their Pb isotopic compositions, which indicates that the lower and middle crusts were heated to >600°C during the East African Orogeny, while the lower crust of the Tanzanian Craton remained below that temperature (Bellucci et al., 2011). By contrast, compositional bands within two Naibor Soito lower crustal xenoliths have distinct Pb isotopic compositions that reflect their evolution under different U/Pb ratio since their last equilibration in the East African Orogeny. The middle crust beneath the Lashaine and Olmani volcanoes has highly radiogenic Pb, distinct from either the Tanznaian Craton lower crust or any samples measured thus far from the Mozambique Belt. These rocks may have derived from an exotic terrane that accreted to the Tanzanian Craton during the East African Orogeny. Their presence in the present-day middle crust is consistent with a thrust boundary separating accreted middle crustal material from reworked Tanzanian Craton in the lower crust. Based on the time-integrated Pb isotopic modeling of feldspars in the lower crustal xenoliths, mid-crustal xenoliths, and surface samples from the Western Granulites of the Mozambique Belt, the following observations can be made:

1. The $^{238}U/^{204}Pb$ of the Archean crust beneath the Mozambique Belt is ∼4 and the $^{232}Th/^{238}U$ is ∼4.

2. The $^{238}U/^{204}Pb$ of the Archean middle crust is also ∼ 4 and the $^{232}Th/^{238}U$ is highly variable ranging from 3-20; the latter most likely not being representative of the middle crust.

3. The Archean upper crust, as sampled by the Western Granulites, evolved with a $^{238}U/^{204}Pb$ of $\sim$10, indicating a $\sim$2.5-fold enrichment in U in the upper crust relative to the lower crust since its formation in the Archean. By contrast, the $^{232}Th/^{238}U$ in both the upper and lower crusts are similar.

4. A few lower crustal xenoliths have feldspars with an elevated $^{207}Pb/^{204}Pb$, indicating their devivation from a mantle source with a slightly higher $^{238}U/^{204}Pb$ (8.5) than that of the Tanzanian Craton proper (8.2).

5. The $^{238}U/^{204}Pb$ in the lower crust of the Western Granulites increases with distance away from the craton margin, which corresponds to progressively higher heat flow measurements as one goes away from the craton. The increased heat production and flow, could explain why the Western Granulites have been re-worked twice since the Archean, while the craton has remained stable.

Chapter 5

Thermal history and Pb growth in the lower crust of the North China Craton

5.1 Contributions

J. Bellucci made all of the measurements for this study. W. McDonough and R. Rudnick contributed to the interpretation of the data. The text, tables, and figures, except for the geological map were written/created by J. Bellucci. The geological map of the area was created by J. Liu.

5.2 Abstract

The Pb isotopic compositions of plagioclase and alkali feldspars from granulite facies lower crustal xenoliths from the Hannuoba volcanic province and Nushan Volcano on the North China Craton have been measured by laser ablation MC-ICP-MS. The common Pb isotopic compositions of these xenoliths corroborate previous studies that have documented multiple generations of lower crust growth and modification at ca. 2.5, 1.8-1.9, and 0.097-0.150 Ga, that generated intermediate, felsic, and mafic granulites, respectively. Plagioclase in the mafic xenoliths from Hannuoba have unradiogenic Pb consistent with the mixing of ancient and Mesozoic aged material during the last crustal formation event. Hannuoba felsic xenolith's

preserve a fossil isochron that is consistent with their formation in the Archean and resetting in the Mesozoic. The intermediate granulites from Hannuoba and Nushan contain both plagioclase and alkali feldspar that have internal isochrons with ages of ∼1.7, which is the age of last metamorphism in the crust and the age of the lithospheric mantle in the northernTrans-North China Orogen. The preservation of internal feldspar isochrons in the intermediate granulites suggest residence in the lower-middle crust with a temperature <600°C since 1.7 Ga.

5.3 Introduction

Cratons, pieces of continental crust and lithospheric mantle that formed in the Archean and persisted for billions of years, contain the majority of the geologic record of the Earth. Two defining characteristics of cratons are a low heat flow, in comparison to more recently tectonic active provinces and a deep mantle lithospheric keel (Nyblade and Pollack, 1993; Carlson et al., 2005). Mantle and deep crustal xenoliths can be used to provide insights into the origin and thermal history of cratons, and therefore the processes that led to cratonization (e.g., Carlson et al., 2005; Rudnick, 1992; Rudnick et al., 1998; Schmitz and Bowring, 2003; and references therein). The North China Craton (NCC) is of specific interest because it has undergone both craton formation and destruction processes. Studies of mantle xenoliths indicate that the NCC once had a deep lithospheric keel, and by inference, a low surface heat flow but that sometime in the Mesozoic (ca. 220 Ma) the keel was evidently lost and replaced with young, fertile mantle (Gao et al., 2002; Griffin

et al., 1998; Menzies et al., 1993). As a likely consequence of mantle keel loss, the NCC presently has a high heat flow (Hu et al., 2000; Tao and Shen, 2008).

Removal of the lithospheric mantle resulted in a lower crust beneath the NCC that is heterogeneous in terms of both composition and formation history. The lower crust of the NCC has witnessed cratonization, tectonic reactivation, and is therefore, an important locality to understand the differentiation during lithosphere formation. The U-Th-Pb isotopic system is ideal for studying crustal formation, mixing, and differentiation processes because it provides precise age constraints, as well as time-integrated histories of heat producing and incompatible (during mantle melting) elements (Gancarz and Wasserburg, 1977; Bodet and Scharer, 2001; Kamber et al., 2003).

The Pb isotopic system is comprised of two components: common Pb, the Pb present in the rock at the last equilibrium, and radiogenic Pb (Pb*), Pb that accumulates from the *in situ* spontaneous decay of U and Th. Radiogenic Pb is used to constrain ages of rocks and minerals, while common Pb is used to model the U-Th-Pb history of a system, determine genetic relationships and provenance of multiple terraines (e.g., Bellucci et al., 2011; Bodet and Scharer, 2001; Gancarz and Wasserburg, 1977; Möller et al., 1998). The Pb isotopic system in old feldspars can be complicated as they may contain domains of variable U/Pb ratios (Bellucci et al., 2011; Frei and Kamber, 1995; Gancarz and Wasserburg, 1977; Housh and Bowring, 1991). Variable U/Pb in some old feldspars results in a spread in Pb isotopic ratios, which reflect the time at which the feldspar cooled below its closure temperature (600°C; Cherniak, 1995; Bellucci et al., 2011). Utilizing laser abla-

tion multi-collector ICP-MS (LA-MC-ICP-MS), each domain of unique Pb isotopic composition in a given feldspar, or between multiple feldspars, can be measured potentially providing a Pb-Pb isochron, a temperature constraint, and the common Pb isotopic composition of a rock.

Crustal xenoliths from the Hannuoba basalt flows and the Nushan Volcano span three crustal formation/modification events ca. 2.5, 1.8-1.9, and 0.097-0.150 Ga (Huang et al., 2004; Liu et al., 2004). The objective here is to utilize the Pb isotopic system in feldspars, to model the formation of each crustal event, assess potential genetic relationships, and determine the thermochronology of the ancient crust in the NCC.

5.4 Geologic History

The North China Craton has had a complex geologic history and can be divided into three areas based on age, lithology, and tectonic evolution: the Eastern Block, Western Block, and the Trans-North China Orogen (TNCO) (Figure 5.1). The TNCO is comprised of Archean rocks ($\sim$ 2.5 Ga) that were re-worked ca. 1.85 Ga as result of the amalgamation of the Eastern and Western Blocks of the NCC (Kern et al., 1996; Kröner et al., 1988; Li et al., 2001, 2000; Zhao et al., 2000, 2001; Kusky et al., 2001). The lithospheric mantle beneath the TNCO is dated to ca. 1.9 Ga in the north and 2.5 Ga in the south (Gao et al., 2002; Liu et al., 2010).

The Western Block has a surface heat flow higher than most cratons (50-60 mW/m^2, Hu et al., 2000; Tao and Shen, 2008) and is comprised of $\sim$45 km of

Archean aged crust and >150 km of mantle lithosphere (Li et al., 2006; Tian et al., 2009; Chen, 2010). The most recent thermo-tectonic event in the Western Block was a N-S continent-continent collision resulting in the formation of the Khondalite Belt at 1.9 Ga (Lu et al., 1996; Kusky and Li, 2003; Zhao et al., 2005, 2010, and references therein).

The Eastern Block has a significantly higher heat flow than the Western Block (>64 mW/m^2, Hu et al., 2000; Tao and Shen, 2008) and a thinner crust (30-40 km; Li et al., 2006 and lithospheric mantle (<100 km; Tian et al., 2009; Chen, 2010). Diamond bearing kimberlites erupted in the Eastern Block of the NCC during the Ordovician also carried refractory garnet peridotites that have Archean Os model ages (Gao et al., 2002; Griffin et al., 1998; Menzies et al., 1993; Wu et al., 2006; Zhang et al., 2008). Magmatism has been prevalent in the NCC since the Early Mesozoic, and some of these volcanoes carry both lower crustal and mantle xenoliths. Mantle xenoliths carried in Cenozoic basalts erupted in the Eastern Block were equilibrated at high temperatures, have fertile bulk compositions, and modern mantle-like Os isotopic compositions (Gao et al., 2002; Griffin et al., 1998; Menzies et al., 1993; Rudnick et al., 2004; Wu et al., 2003, 2006; Xu, 2001; Zheng et al., 2006). The difference between the mantle xenoliths entrained during the Ordovician and the Cenozoic indicates that the old, cold Archean lithospheric root was removed sometime in the Mesozoic. Studies of the intra-plate magmatism in the NCC indicate that the lithospheric mantle removal occurred sometime around 220 Ma (Gao et al., 2004). Lower crustal xenoliths exhumed in the Cenozoic provide a record of the cratonization at ca. 2.5 Ga, final amalgamation at ca. 1.9 Ga, and the effect of

basaltic underplating, which followed the removal of the lithospheric keel.

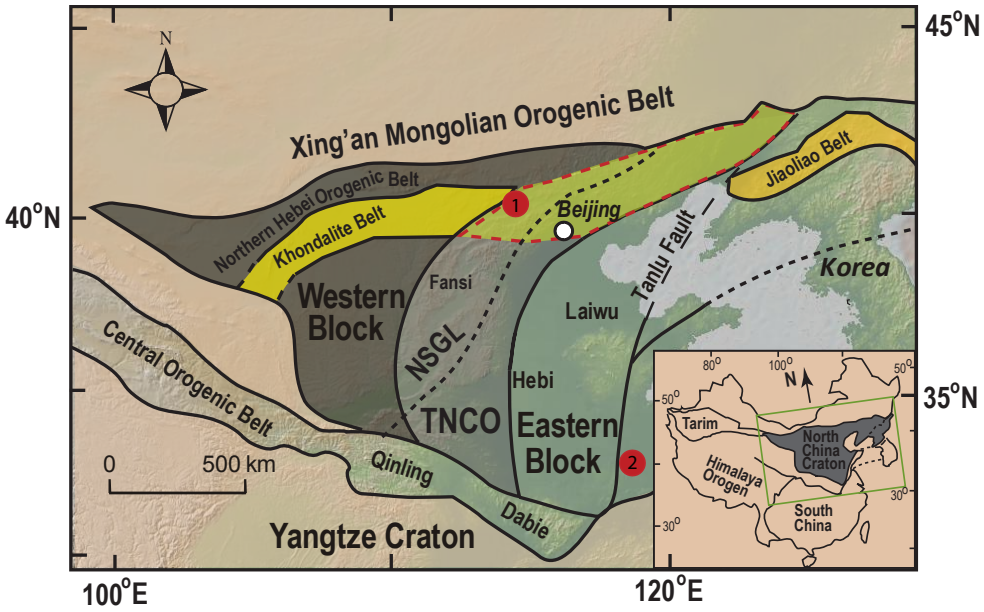

Figure 5.1: Simplified geologic map of China modified from from Zhao et al. (2005, 1999). Xenolith localities shown with red markers. 1: Hannuoba. 2: Nushan. NSGL: North-South Gravity Lineament; TNCO: Trans-North China Orogen. Map made by J. Liu.

5.5 Samples

Table 5.1. Samples and Major Mineralogy, and Depth of Origin

Locality	Sample	Rock Type	Major Mineralogy	Depth of Origin in km
Hannuoba	ZB-20	Felsic Granulite	Plag, Kspar, Qtz, Cpx	~30[1]
Hannuoba	ZB-21	Felsic Granulite	Kspar, Qtz, Cpx	~30[1]
Hannuoba	ZB-18	Metasediment	Qtz, Plag, Kspar, Grt	~30[1]
Hannuoba	DMP-73	Intermediate Granulite	Pl, Cpx, Opx, Kspar	~35[1]
Hannuoba	DMP-01	Intermediate Granulite	Plag, Kspar, Qtz, Cpx, Opx	~35[1]
Hannuoba	DMP-27	Intermediate Granulite	Plag, Cpx, Opx, Kspar	~35[1]
Hannuoba	DMP-28	2 Px Granulite	Cpx, Plag, Opx	~40[1]
Hannuoba	DMP-09	2 Px Granulite	Cpx, Opx, Plag	~40[1]
Hannuoba	DMP-03	2 Px Granulite	Plag, Opx, Cpx	~40[1]
Hannuoba	DMP-71	2 Px Granulite	Cpx, Pl, Opx	~40[1]
Hannuoba	DMP-72	2 Px Granulite	Cpx, Plag, Opx	~40[1]
Hannuoba	DMP-75	Mafic Granulite	Plag, Cpx, Opx, Kspar	~40[1]
Hannuoba	DMP-07	Mafic Granulite	Plag, Opx, Cpx, Kspar	~40[1]
Hannuoba	DMP-62	Mafic Granulite	Plag, Cpx	~40[1]
Nushan	NS214	Intermediate Granulite	Plag, Cpx, Opx, Qtz	~20[2]
Nushan	NS204	Mafic Granulite	Plag, Cpx, Opx	~29[2]

Plag: Plagioclase, Kspar: Potassium Feldspar, Cpx: Clinopyroxene, , Opx: Orthopyroxene, Qtz: Quartz, Px: Pyroxene. 1: Liu et al. (2001) 2: Huang et al. (2004)

5.5.1 Hannuoba

The Hannuoba basalts erupted through the northern part of the TNCO (Figure 5.1) ca. 0.014-0.027 Ga (Zhu, 1998). They carried to the surface a plethora of crustal and mantle xenoliths. Crustal xenoliths have been recovered from two localities: Zhouba (ZB) and Damaping (DMP), and have been described extensively by Chen et al. (2001); Fan and Liu (1996); Liu et al. (2001, 2004). The major mineralogy and depth of origin for the samples in this study are presented in Table 5.1.

The crustal xenoliths from Hannuoba have equilibration temperatures of 725-900°C (Chen et al., 2001; Fan and Liu, 1996; Liu et al., 2001, 2003). The compositional model of the lower crust beneath Hannuoba, based on seismic velocities, indicate lower crustal xenolith derivation from ∼25-40 km depth. The Zhouba xenoliths were derived from 25-35 km and consist of meta-sediments (metapelites) and felsic granulites, which have Archean Nd model ages (2.7 Ga). Based on U-Pb in zircon analyses they were emplaced into the lower crust ca. 1.8-1.9 Ga and re-metamorphosed during basaltic underplating ca. 0.120 Ga (Liu et al., 2004, 2001). They have low Mg #s, and flat to depleted HREE distributions, positive Eu K, and Ba anomalies, depletions in Th, U, Nb, and Ta.

The crustal xenoliths from Damaping are distinct from the Zhouba xenoliths in terms of trace element chemistry, mineralogy, and depth of origin. Intermediate xenoliths derive from ∼ 35 km, are large ion lithophile (LILE) and LREE enriched, have Nd model ages that range between 3.0-1.8 Ga, U-Pb zircon upper intercept ages of 2.5 Ga and lower intercept ages of 0.08 Ga, and are interpreted as the products

of fractional crystallization of basalts (Liu et al., 2001, 2004). The mafic Damaping xenoliths derive from somewhat greater depths of 35-41 km, are depleted in LILE, LREE enriched, some with positive Eu anomalies, have spurious Nd model ages (T_{DM}=1.5-5 Ga) and U-Pb in zircon ages of 0.097-0.150 Ga and are interpreted to be cumulates from basaltic magmas that assimilated 55-85% pre-existing crustal material (Liu et al., 2001, 2004). In summary, the samples suite has good depth constraints, with the felsic granulites being shallowest, followed by the intermediate granulites, and, at the base of the crust, the Mesozoic-aged mafic granulites, which formed by basaltic underplating and mixing between new and ancient crust.

5.5.2 Nushan

The Nushan Volcano is located in the Eastern Block of the NCC on the eastern side of the Tanlu Fault zone (Figure 5.1). The lower crust beneath the Nushan Volcano has been proposed to be related to the 2.5 Ga crust-forming event that generated the intermediate granulites from the Hannuoba locality (Huang et al., 2004). Based on U-Pb zircon ages, the protoliths of the Nushan xenoliths formed ca. 2.5 Ga and were metamorphosed to granulite facies ca. 1.8 Ga (Huang et al., 2004). The two xenoliths from Nushan have a mafic-intermediate composition (51-55 wt.% SiO_2), are HREE and LILE depleted, with enrichments in Ba, K, Zr, and Hf, with no Eu anomalies, Nd model ages (T_{DM}) that range from 3.4-2.4 Ga (Huang et al., 2004). As such, the Nushan xenoliths are thought to represent crystallized 2.5 Ga basalts that have assimilated more ancient material (Huang et al., 2004). Like

the Hannuoba location, there was an event of Mesozoic underplating ca. 140 Ma, which added material to the lower crust (Huang et al., 2004). No Mesozoic aged xenoliths were available for study here.

Utilizing the *in situ* feldspar Pb isotopic compositions from these samples we will shed light on the timing of the last thermal perturbation, the U-Th-Pb history of the lower crust beneath each volcano, and any Pb isotopic heterogeneities prevalent in the lower crust of the NCC.

5.6 Analytical Methods

All Pb isotopic compositions in this study were measured following the protocols outlined in Chapters 2-5. Analyses were conducted as lines, with the dimensions of 150 μm x 350-400 μm.

5.7 Results

Data are reported in Table 5.2 and plotted in Figure 5.2 individual analyses for each sample are provided in Appendix D. The Pb isotopic trends are mostly linear in both $^{207}Pb/^{204}Pb$ vs. $^{206}Pb/^{204}Pb$ and $^{208}Pb/^{204}Pb$ vs. $^{206}Pb/^{204}Pb$ plots. The least radiogenic samples are the Nushan granulites, followed by the Hannuoba intermediate granulites, Hannuoba mafic granulites, with the Hannuoba felsic granulites being the most radiogenic. This sequence is mirrored in the whole rock Pb isotopic compositions of Liu et al. (2004). All of the common Pb measurements plot to the left of the t=0.15 Ga (the last episdoe of crustal formation) Geochron, except

for one felsic granulite. None of the Pb isotopic compositions plot close to the 2.5 Ga Geochron, which is the hypothesized age of the protolith of both the intermediate Hannuoba and Nushan granulites. Individual feldspars in several xenoliths show a discernible spread in Pb isotopic compositions (DMP-75, DMP-73, DMP-27, and NS214), but our spatial resolution and analytical precision are too low to achieve precise ages. However, grouping the Hannuoba intermediate granulites and felsic granulites yield ages of 1.7 $\pm$ 0.4 and 2.9 $\pm$ 0.2 Ga, respectively (Figure 5.3 and 5.5). During the analysis of ZB-18 a zircon was intersected during the linear ablation track, which provides a feldspar-zircon Pb-Pb isochron of 1.7 $\pm$ 0.4 Ga (2σ), identical to the U-Pb zircon ages reported by Liu et al. (2004) for other felsic granulite xenoliths. Using the common Pb isotopic compositions of these xenoliths, we will model the formation, history, and thermochrology of the lower-middle crust beneath the NCC to test the formation hypotheses put forth by Liu et al. (2004) and Huang et al. (2004).

Table 5.2 Pb isotopic compositions for NCC xenoliths

Sample		Rock Type	Feldspar analyzed	$^{208}Pb/^{204}Pb$	$2\sigma_{(mean)}$	$^{207}Pb/^{204}Pb$	$2\sigma_{(mean)}$	$^{208}Pb/^{204}Pb$	$2\sigma_{(mean)}$	$^{207}Pb/^{206}Pb$	$2\sigma_{(mean)}$	$^{208}Pb/^{206}Pb$	$2\sigma_{(mean)}$	n
Hannuoba	ZB-20	Felsic Granulite	Plag & Kspar	38.57	0.08	15.70	0.03	18.30	0.05	0.858	0.002	2.107	0.002	10
Hannuoba	ZB-21	Felsic Granulite	Plag	37.84	0.03	15.54	0.01	17.40	0.02	0.893	0.000	2.175	0.001	10
Hannuoba	ZB-18	Metasediment	Plag	37.91	0.23	15.39	0.08	17.04	0.07	0.900	0.003	2.217	0.009	20
Hannuoba	DMP-73	Intermediate Granulite*	Plag & Kspar	37.13	0.11	15.39	0.03	16.95	0.13	0.909	0.005	2.189	0.010	16
Hannuoba	DMP-01	Intermediate Granulite	Plag & Kspar	36.41	0.08	15.23	0.03	16.23	0.03	0.939	0.001	2.244	0.002	15
Hannuoba	DMP-27	Intermediate Granulite*	Plag & Kspar	35.88	0.08	15.28	0.02	15.91	0.08	0.960	0.004	2.257	0.007	23
Hannuoba	DMP-28	2 Px Granulite	Plag	37.18	0.11	15.29	0.09	16.61	0.12	0.921	0.009	2.238	0.015	6
Hannuoba	DMP-09	2 Px Granulite	Plag	36.70	0.29	15.33	0.08	16.72	0.28	0.917	0.014	2.197	0.039	16
Hannuoba	DMP-03	2 Px Granulite	Plag	37.10	0.11	15.45	0.05	16.69	0.13	0.926	0.008	2.218	0.006	6
Hannuoba	DMP-71	2 Px Granulite	Plag	36.61	0.35	15.28	0.05	16.31	0.19	0.937	0.012	2.251	0.022	9
Hannuoba	DMP-72	2 Px Granulite	Plag	36.84	0.21	15.38	0.11	17.29	0.14	0.890	0.009	2.131	0.014	27
Hannuoba	DMP-75	Mafic Granulite*	Pl&Kfs	37.48	0.14	15.49	0.04	17.28	0.09	0.897	0.003	2.170	0.006	16
Hannuoba	DMP-07	Mafic Granulite	Kfs	37.21	0.15	15.40	0.05	17.15	0.06	0.897	0.005	2.173	0.013	10
Hannuoba	DMP-62	Mafic Granulite	Plag & Kspar	37.19	0.19	15.37	0.03	16.77	0.10	0.916	0.005	2.224	0.003	12
Nushan	NS214	Intermediate Granulite*	Plag	35.77	0.13	15.13	0.04	15.10	0.15	0.997	0.014	2.370	0.016	10
Nushan	NS204	Mafic Granulite	Plag	35.51	0.11	15.30	0.03	15.46	0.13	0.989	0.009	2.296	0.012	24

*Displays a spread in feldspar Pb isotopic compositions; n: number of feldspars

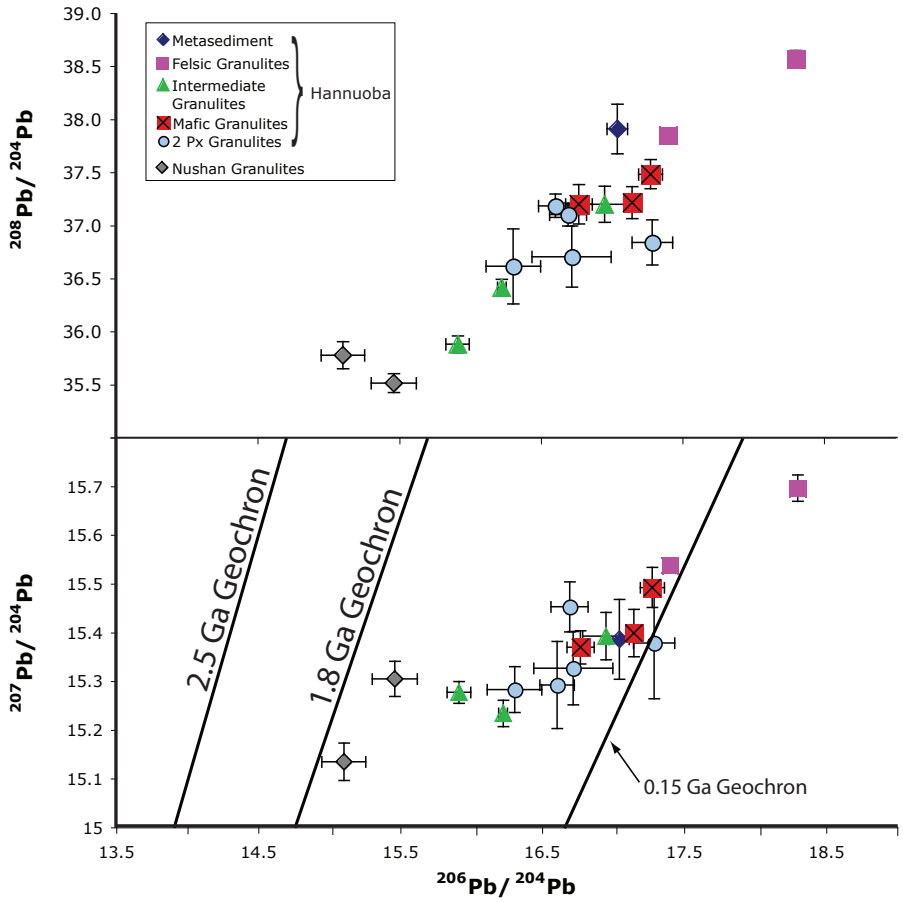

Figure 5.2: Results for feldspar Pb-Pb isotopic compositions from both Hannuoba and Nushan Xenoliths. Error bars are $2\sigma_{mean}$ of multiple plagioclase and alkali feldspar analyses, see Table 5.2. Geochrons shown for t=2.5 Ga, t=1.8 Ga, and t=0.15 Ga.

5.8 Discussion

5.8.1 Origin of the Mafic Granulites

Based on trace element compositions, zircon ages, and Nd-Sr isotopic compositions the mafic granulites (mafic granulites, 2 px-granulites) were interpreted to

be a 0.09-0.15 Ga mixture of older material and a Mesozoic basalts of 55-85% (Liu et al., 2004). The mafic granulites plot to the left of the 0.15 Ga Geochron (Figure 5.2), which requires a preexisting older material mixing with Mesozoic basalts.

5.8.2 Origin of the Felsic Granulites

The felsic granulites are more radiogenic than either the mafic granulites or intermediate granulites. The feldspar age between the two felsic granulites is 2.9 ± 0.2 Ga (Figure 5.5), which is older than the Nd model ages for these samples (T_{DM} =2.2-2.4 Ga, Liu et al., 2004). A two point isochron is often not reliable, but we can rule out mixing in this circumstance because sample ZB-20 is more radiogenic ($^{206}Pb/^{204}Pb$=18.5) than the recent Hannuoba basalts ($^{206}Pb/^{204}Pb$=18, Choi et al., 2008). Therefore, the Pb isotopic composition of ZB-20 is most likely a result of Pb growth and not mixing. Combining the U-Pb zircon ages of (Liu et al., 2004) and our mantle extraction age the felsic granulites were formed in the Archean ca. 2.9 Ga, emplaced in the lower crust ca. 1.8 Ga, and re-metamorphosed ca. 0.15 Ga.

5.8.3 Origin of the Nushan granulites

The granulites from Nushan are the least radiogenic measured here. The more intermediate sample, NS214 shows a range in feldspar isotopic compositions. The composition of NS201 and the least radiogenic composition of NS214 lie on a secondary growth Pb growth line of 2.5 Ga-1.7 Ga (Figure 5.4).

5.8.4 Thermochronology

The intermediate granulites from Hannuoba and one xenolith from Nushan (NS214) show a range in individual feldspar Pb isotopic compositions (Figures 5.3 and 5.4). The intermediate granuiltes from Hannuoba have similar trace element chemistry, mineralogy, Nd isotopic compositions, and U-Pb zircon ages, and grouping the three yields a feldspar isochron of 1.7 $\pm$ 0.6 Ga (2σ, Figure 5.3), which is comparible to the age of the TNCO and the lithosphere beneath Hannuoba (Gao et al., 2002; Liu et al., 2010). The intermediate granulites have an almost identical history to the Nushan Granulites: formation at 2.5 Ga, metamorphism at 1.9 Ga, and both localities experienced basaltic underplating ca. 0.15 Ga (Huang et al., 2004; Liu et al., 2001, 2004). Due to the presence of individual domains of Pb isotopic compositions in single feldspar grains in the Hannuoba intermediate granulites and NS214, the temperature at which these rocks resided since $\sim$ 1.7 has evidently been $<$ 600°C, the closure temperature of Pb in feldspar (after Dodson, 1973 and using the diffusion coefficients from Cherniak, 1995). This result is in contrast with the major Pb loss in the zircons from the intermediate granulites. Lead loss in zircons occurs at $\sim$ 900°C (Cherniak and Watson, 2001), whereas the closure temperature of Pb in feldspar is $\sim$600°C (Cherniak, 1995). Therefore, the presence of preserved Pb isotopic heterogeneities in the feldspars on the intermediate granulites is an unexpected and enigmatic result.

5.8.5 Pb isotopic modeling

The intermediate granulites from Hannuoba and Nushan represent the most ancient lower crust in the region, and have a well constrained thermal history. Using a multiple stage Pb growth model, the mantle $^{238}U/^{204}Pb$ and and $^{232}Th/^{238}U$ from which the intermediate granulite crust was derived and the $^{238}U/^{204}Pb$ and and $^{232}Th/^{238}U$ of the protolith from 2.5 Ga-1.9 Ga can be constrained. Here we use a single stage Pb growth model (Holmes, 1946; Houtermans, 1946) using primordial Pb from the Canyon Diablo troilite (Chen and Wasserburg, 1983). The Pb isotopic model for the Hannuoba intermediate granulites results in a mantle $^{238}U/^{204}Pb$ at 2.5 Ga of 8 and a $^{232}Th/^{238}U$ of 4.3 (Figure 5.3). The isotopic model for the Nushan intermediate granulites results in a mantle $^{238}U/^{204}Pb$ at 2.5 Ga of 8.0 and a $^{232}Th/^{238}U$ of 4.3 (Figure 5.4). Both of the estimates for the Archean mantle from Nushan and Hannuoba are similar to other estimates of the Archean mantle (Bellucci et al., 2011; Dupre' and Arndt, 1990; Chauvel et al., 1993; Zartman and Richardson, 2005; Zartman and Haines, 1988). The $^{238}U/^{204}Pb$ of the protolith of the intermediate granulites from Hannuoba between 2.5-1.9 Ga is 7. The $^{238}U/^{204}Pb$ values record a small change in $^{238}U/^{204}Pb$ after extraction from the mantle and indicates a depletion in U at 2.5 Ga (Figure 5.3). The $^{232}Th/^{238}U$ of the Hannuoba xenoliths is constant from 4.57-present with a value of 4.3 (Figure 5.3). The $^{238}U/^{204}Pb$ of the protoliths of the intermediate granulites from Nushan between 2.5-1.9 Ga has two values: 4.2 and 10 (Figure 5.4). The intermediate granulite shows a strong depletion of U at 2.5 which corresponds to an increase

$^{232}Th/^{238}U$ to 9.2 (Figure 5.4).

The felsic granulites from Hannuoba preserve a fossil feldspar Pb-Pb isochron of 2.9 Ga. Using a simple 2 stage Pb model with extraction from the mantle ca. 2.9 and equilibration with radiogenic phases ca. 0.15 Ga, yields a mantle $^{238}U/^{204}Pb$ of 8.2 and a whole rock $^{238}U/^{204}Pb$ of 7.6 and 9.2 (Figure 5.5). Similarly, the Pb growth in the felsic granulites can be modeled with a mantle $^{232}Th/^{238}U$ of 4.3 and whole rock $^{232}Th/^{238}U$ of 4.0 and 4.2. The simplicity of this model implies that there was no additions or subtractions in U, Th, or Pb during the 1.9 Ga metamorphic event to this section of crust. Both estimates of $^{232}Th/^{238}U$ and $^{238}Th/^{204}Pb$ of the mantle at 2.9 Ga are consistent with other estimates of the Archean mantle (Bellucci et al., 2011; Chauvel et al., 1993; Dupre' and Arndt, 1990; Zartman and Richardson, 2005).

5.8.6 Conclusions

The common Pb isotopic compositions of feldspars from lower crustal xenoliths from Hannuoba and Nushan have been measured via LA-MC-ICP-MS. The common Pb isotopic composition of the mafic xenoliths from Hannuoba reflect mixing of 30-70 % of ancient material and newer basalt. The common Pb isotopic compositions of the felsic xenoliths from Hannuoba record a fossil isochron of 2.9 $\pm$ 0.2 Ga, which indicates formation in the Archean. The common Pb isotopic composition of the xenoliths from Nushan reveal a two stage history with protolith formation at ca. 2.5 Ga from a mantle with a $^{238}U/^{204}Pb$ of 8, and evolving from 2.5-1.9 Ga with

variable $^{238}U/^{204}Pb$ between 4-10, from 1.7 Ga individual Pb isotopic domains in sample NS214 evolved with a $^{238}U/^{204}Pb$ of 0-2.3. The Pb isotopic compositions of feldspars from the intermediate granulites from Hannuoba can be modeled with a similar history, indicating an origin ca. 2.5 Ga. Individual Pb isotopic domains in the intermediate granulites evolved from 1.7 Ga-present with a $^{238}U/^{204}Pb$ of 0-8. The presence of distinct isotopic domains in the feldspars of the Hannuoba intermediate granulites and the Nushan intermediate granulites indicate they resided at a temperature of $< 600°C$ since 1.7 Ga in the lower crust, which is in contrast with the major Pb loss in zircons from these xenoliths that occurred in the Mesozoic.

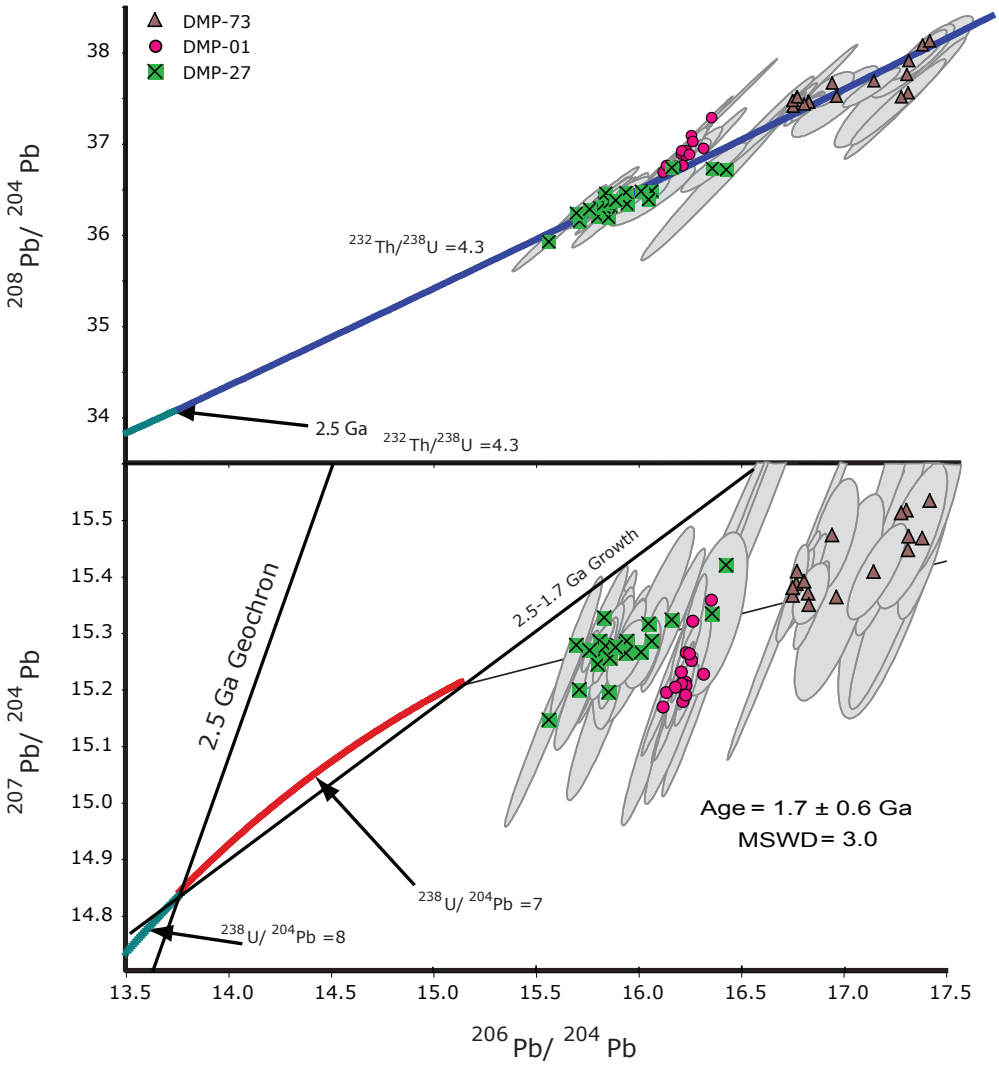

Figure 5.3: Lead growth model and thermochronometry for 2.5 Ga xenoliths from Hannuoba. Error elipses are $2\sigma_{mean}$ of an individual Pb feldspar isotopic domain. Feldspar Pb-Pb isochron records an age of 1.7 ± 0.6 Ga.

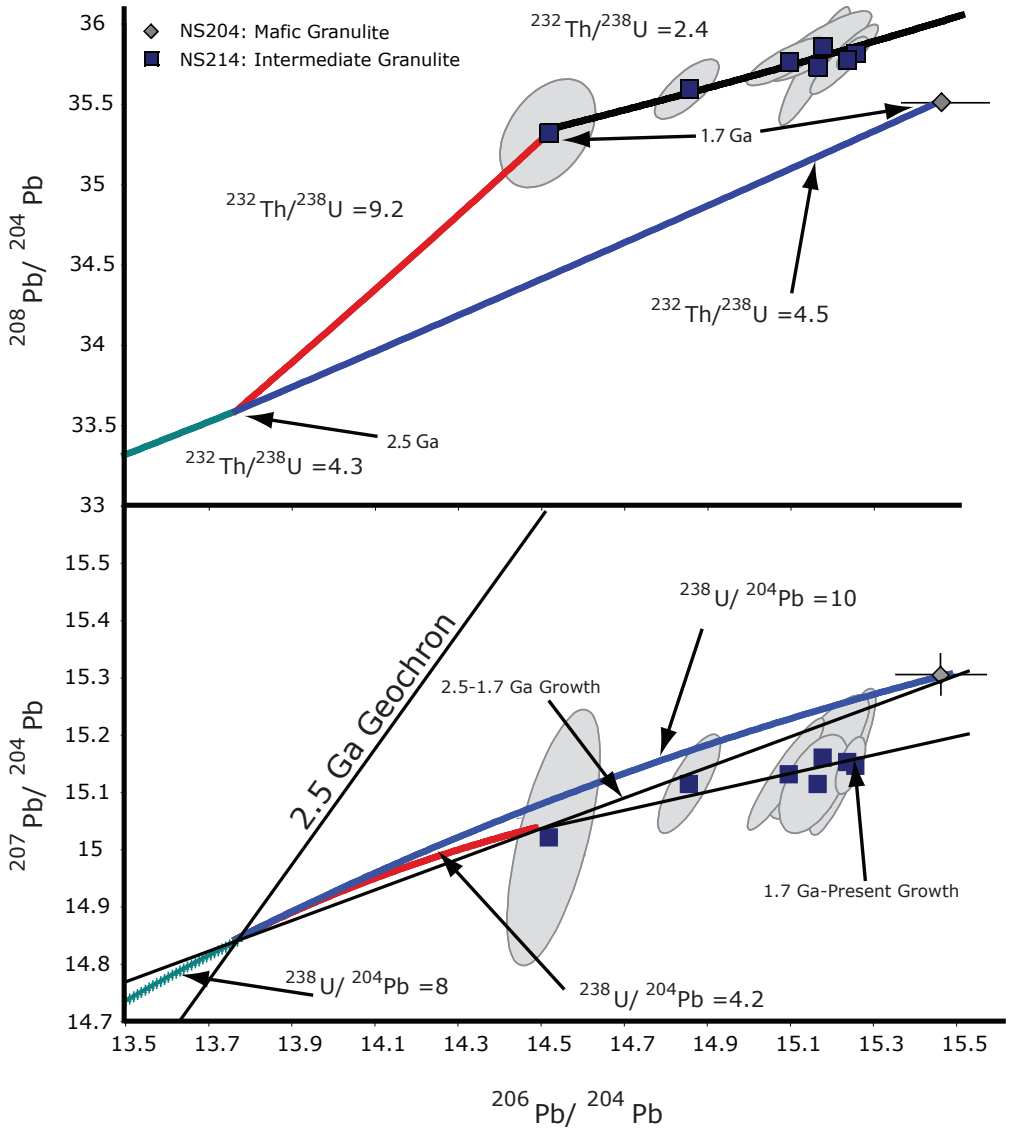

Figure 5.4: Lead growth model and thermochronometry for 2.5 Ga xenoliths from Nushan. Error elipses are $2\sigma_{mean}$ of an individual Pb feldspar isotopic domain. The feldspar Pb isotopic compositions lie along a growth line from 1.7 Ga-present.

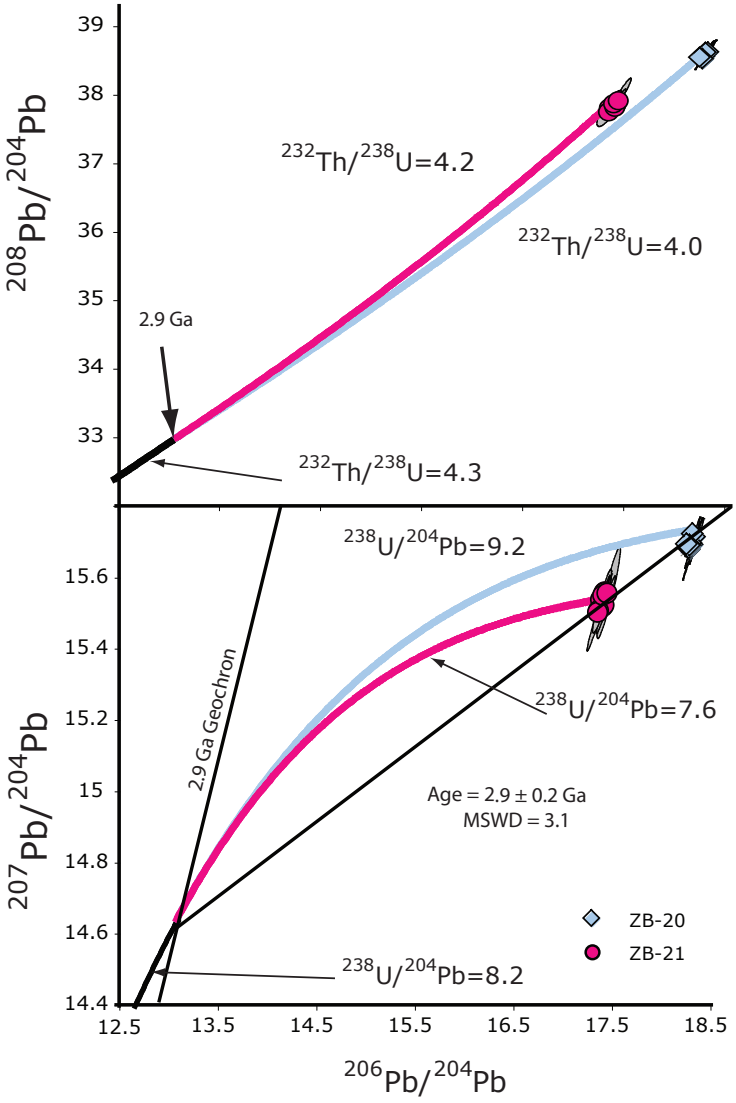

Figure 5.5: Lead growth model for the Hannuoba felsic granulites. Pb growth curves have a mantle $^{238}U/^{204}Pb$ of 8.2 and whole rock $^{238}U/^{204}Pb$s of 7.6 and 9.2. Similarly $^{232}Th/^{238}U$ growth curves of 4.0 and 4.2 are shown with a mantle $^{238}U/^{204}Pb$ of 4.3.

Chapter 6

Conclusions

6.1 Pb isotopic analyses

Here I presented a novel approach for measuring *in situ* Pb isotopic compositions utilizing LA-MC-ICP-MS. Using this method we have shown that the spatial resolution and precision is enough to discern individual Pb isotopic domains in feldspars that contain both common and radiogenic Pb compositions, which return Pb-Pb ages that agree with previous age age estimates of each locality. Using external chronology and the common Pb isotopic composition of a rock the U-Th-Pb of a system or rock can be modeled. Additionally, if discreet Pb isotopic domains exist in a single feldspar grain, the feldspar must have resided below its closure temperature (600°C). Therefore, LA-MC-ICP-MS of feldspar grains yields an accurate Pb-Pb age, a common Pb measurement, and a temperature constraint.

6.2 U-Th-Pb in Archean aged crust

Feldspars from lower crustal xenoliths from three Archean terraines (The Tanzaian Craton, the Mozambique Belt, and the North China Craton) with differing geologic histories have been used to constrain the timing, formation, thermochronometry, and the U-Th-Pb history in each region. The feldspars from the lower crust

of the Tanzanian craton indicated that the crust lithosphere comprising the craton was extracted from the mantle at ca. 2.7 Ga, and the lower crust cooled to a temperature <600°C by 2.4 Ga. Feldspars from the Mozambique Belt indicate that granulite terrains can be distinguished at depth, an intra-crustal differentiation event happened ca. 2.7 Ga that enriched the upper crust in U by a factor of 2, the temperature of the lower crust of the Mozambique belt was elevated above 600°C, and the edge of the cratonic lower crust has a higher $^{238}U/^{204}Pb$ than the craton, which could be the reason why the edges of cratons are more willing to deform than the craton centers. The feldspars from the lower crust of the North China craton reveal that a 2.5 Ga crust forming event generated a spatially significant amount of intermediate crust, that was metamorphosed ca. 1.7 Ga, coincident with the final amalgamation of the craton and has the lower-middle crust has resided at <600°C, since that time. Additionally, the hypotheses set forth by Liu et al. (2004), whereby the felsic granulites were Archean and emplaced in the lower crust ca. 1.8 Ga and the mafic granulites were a product of mixing between ancient and Mesozoic basalt, were confirmed.

Appendix A

Forensic and Anthropological Applications

The following appendix and work is in large part collaboration with Dr. Javier Iñañez, who is a post-doctoral fellow at the Smithsonian institute for science. I pioneered the method to analyze the Pb isotopic compositions of the materials, collected the data, made the Pb-Pb figures, and interpreted the provenance of the Pb isotopic data, while Dr. Iñañez interpreted the archaeological/anthropological significance of the samples. These data have been published with the following citations:

Iñañez, J.G., Bellucci, J.J., Rodriguez-Alegria, E., Ash, R.D., McDonough, W.F. and Speakman, R.J. (2010) Romita pottery revisited: a reassessment of the provenance of ceramics from Colonial Mexico by LA-MC-ICP-MS. Journal of Archaeological Science, 37, 2698-2704.

A.1 Introduction

In addition to providing age constraints and insights into a wide variety of geological applications, the Pb isotopic system can be a powerful tool in archaeometry (archaeological science) and forensics. The Pb isotopic composition of materials is dependent on the initial Pb isotopic composition, time, geologic history, and the relative abundances of U, Th, and Pb. The geochemical behavior of U, Th, and Pb

are largely different, and therefore fractionations during magmatic and metamorphic processes are large and therefore, resolvable differences in Pb isotopic compositions are created. The largely different chemical behaviors of U, Th, and Pb result in a wide variety of current Pb isotopic compositions in geographically diverse regions. Large, natural variations in Pb isotopic compositions make the the Pb isotopic system ideal for understanding the provenance of materials (e.g., Brill and Wampler, 1967; Pollard et al., 2007; Pollard, 2009; Stos-Gale and Gale, 2009, and references therein). Additionally, utilizing LA-MC-ICP-MS, a large data set can be acquired rapidly, and combined with other physical, chemical, and isotopic data, Pb isotopic compositions can fingerprint a wide variety of forensic materials, including, but not limited to: metals, oxides, ballistic samples, ceramics, and organic materials (e.g., human tissue).

Specifically for our study, we are interested in the production of ceramics in Meso-America during the Spanish colonial period, and where the Pb used to manufacture the glazes originated. Spain and Mexico have largely different geologic histories with Spain being mostly re-worked pre-Cambrian materials, and Meso-America's geology is largely controlled by current ongoing continental arc. Therefore, the Pb isotopic compositions from each region will be distinct and any mixing, exchange, and provenance between the two countries will be revealed.

A.2 Romita Ware

Romita pottery is a Colonial period ceramic found in abundance in and around Mexico city (Lister and Lister, 1982). Romita wear is covered with a transparent Pb glaze (wt. % concentrations) and has many typological forms that look European with traditional European motifs and not traditional Aztec motifs (e.g., corn, eagle, cactus) (Lister and Lister, 1982). The type of Pb glazing used on the Romita ware was not present before the colonization of Mexico, so if the Romita ware, were indeed made indigenously, it would represent a technological jump for the native peoples. The main question to be addressed is: Were indigenous people making typologically European ceramics with native Pb? To address this question we analyzed 8 Romita ceramics, 5 sherds from Puebla, a major production center of indigenous Mexicanos, and 10 sherds from Spain (Talavera and Seville). Analytical procedures were outlined in Chapter 2, but instead of a mixed array of Faraday-Ion Counter, we used all Faraday cups, and sample-standard bracketing with NIST610. Utilizing this analytical method combined with the large abundance of Pb in the samples a high degree of both internal and external precision (based on triplicate analyses of samples) on $^{20x}Pb/^{204}Pb$ of 0.05% and <0.1%, respectively. Analytical conditions are shown in Table A.1.

A.3 Romita Ware Results

Results are shown in Figures A1 and A2 and Table A2. The ceramics analyzed here are shown along with fields from previously analyzed ceramics from Joel et al.

Table A.1. Typical operating conditions for *in situ* Pb isotopic analyses

Mass Spectrometer		
Instrumentation:	Nu Plasma MC-ICP-MS	
Forward Power	1300 W	
Reflected Power	<10 W	
Cones	Ni	
Acceleration Voltage	4000 V	
Gas Flows		
Coolant	13 L min^{-1}	
Auxilary	0.8 L min^{-1}	
Nebulizer	0.77 L min^{-1}	
Aridus Gas Flows		
Sweep Gas	2.20 L min^{-1}	
N_2	0.15 L min^{-1}	
Helium Flow	0.4 L min^{-1}	
Laser		
Instrumentation:	New Wave UP 213	
	Standard NIST 610	**Sample**
Line Width	150 µm	6-8 µm
Line Length	350-400 µm	350-400 µm
Translation Rate	7 µm s^{-1}	7 µm s^{-1}
Pulse Frequency	7 hz	5-10 hz
Energy Density	4-5 J cm^{-2}	4-5 J cm^{-2}
Typical ^{208}Pb V	0.57	1-6

(1988) and ores from Mexcio (Cumming et al., 1979) and Spain (Santos-Zalduegui et al., 2004).

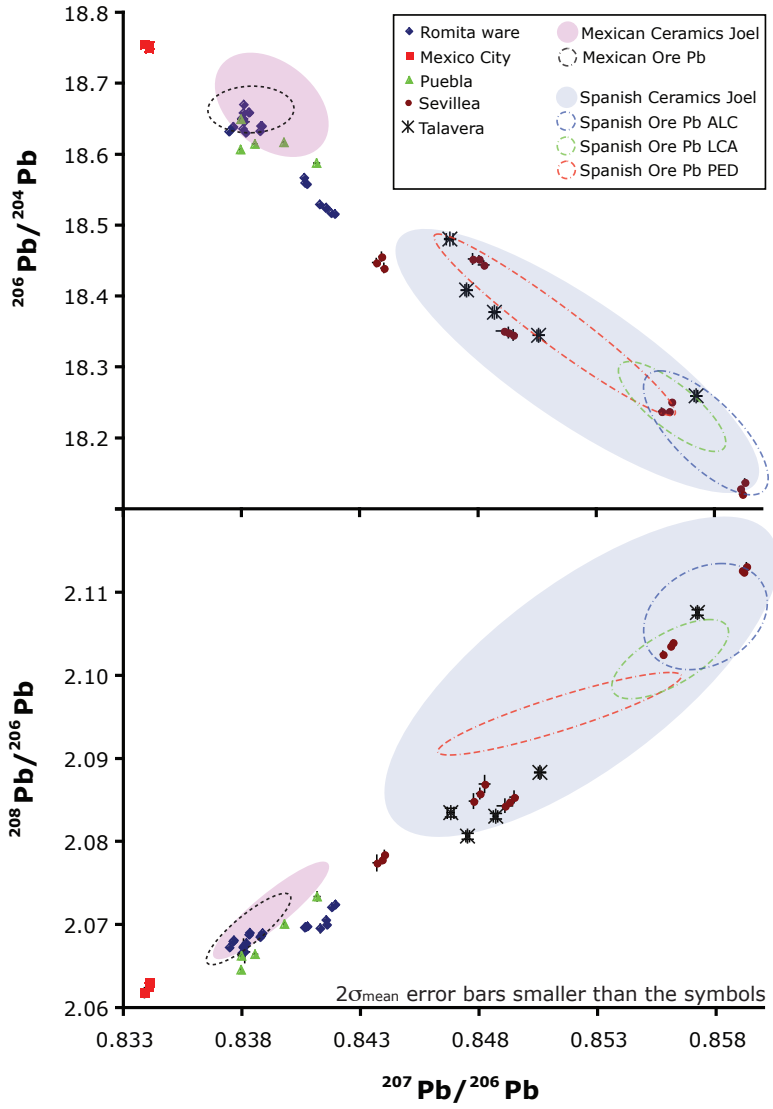

Figure A.1: Pb-Pb diagram with samples recovered from both Spain and Mexico and with fields from literature ceramics and ores.

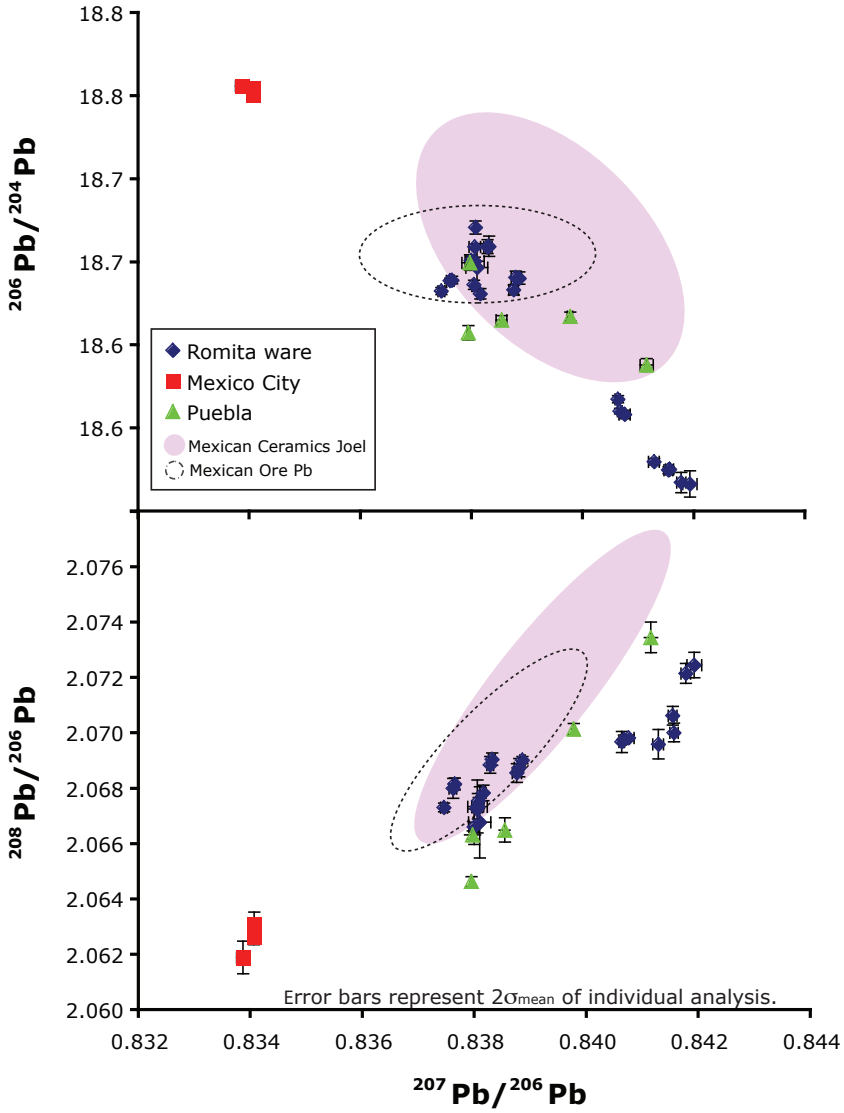

Figure A.2: Pb-Pb diagram with Romita Ware and other samples recovered from Mexico.

Table A.2 Pb isotopic compositions of ceramics measured in this study.

Sample	Group	Location	$^{208}Pb/^{204}Pb$	$2\sigma_{(mean)}$	$^{207}Pb/^{204}Pb$	$2\sigma_{(mean)}$	$^{206}Pb/^{204}Pb$	$2\sigma_{(mean)}$	$^{207}Pb/^{206}Pb$	$2\sigma_{(mean)}$	$^{208}Pb/^{206}Pb$	$2\sigma_{(mean)}$
MTM103	Romita	Mexico	38.377	0.015	15.591	0.006	18.517	0.008	0.84191	0.00013	2.0725	0.0005
Duplicate	Romita	Mexico	38.377	0.013	15.587	0.004	18.518	0.006	0.84176	0.00008	2.0722	0.0004
MTM122	Romita	Mexico	38.521	0.002	15.614	0.001	18.631	0.003	0.83815	0.00005	2.0679	0.0003
Duplicate	Romita	Mexico	38.526	0.007	15.618	0.003	18.637	0.003	0.83803	0.00003	2.0673	0.0001
Duplicate	Romita	Mexico	38.523	0.008	15.617	0.003	18.671	0.004	0.83806	0.00003	2.0676	0.0001
MTM128	Romita	Mexico	38.612	0.006	15.643	0.005	18.660	0.006	0.83830	0.00006	2.0691	0.0002
Duplicate	Romita	Mexico	38.536	0.047	15.624	0.015	18.647	0.014	0.83808	0.00020	2.0668	0.0013
Duplicate	Romita	Mexico	38.600	0.010	15.643	0.004	18.660	0.004	0.83827	0.00006	2.0689	0.0003
MTM130	Romita	Mexico	38.563	0.009	15.637	0.003	18.641	0.004	0.83884	0.00005	2.0690	0.0001
Duplicate	Romita	Mexico	38.563	0.014	15.637	0.004	18.641	0.004	0.83878	0.00008	2.0688	0.0003
Duplicate	Romita	Mexico	38.537	0.009	15.631	0.003	18.634	0.003	0.83875	0.00008	2.0686	0.0003
MTM153	Romita	Mexico	38.423	0.006	15.607	0.002	18.568	0.002	0.84062	0.00005	2.0697	0.0004
Duplicate	Romita	Mexico	38.409	0.007	15.601	0.003	18.559	0.003	0.84074	0.00010	2.0698	0.0001
Duplicate	Romita	Mexico	38.414	0.006	15.602	0.002	18.561	0.002	0.84066	0.00005	2.0698	0.0002
MTM155	Romita	Mexico	38.344	0.007	15.588	0.002	18.526	0.000	0.84155	0.00007	2.0700	0.0003
Duplicate	Romita	Mexico	38.348	0.009	15.587	0.002	18.530	0.002	0.84127	0.00010	2.0696	0.0005
Duplicate	Romita	Mexico	38.355	0.005	15.589	0.001	18.525	0.002	0.84153	0.00008	2.0707	0.0003
MTM159	Romita	Mexico	38.549	0.013	15.630	0.003	18.651	0.002	0.83798	0.00009	2.0666	0.0006
Duplicate	Romita	Mexico	38.561	0.015	15.632	0.003	18.651	0.002	0.83804	0.00017	2.0674	0.0010
Duplicate	Romita	Mexico	38.578	0.010	15.639	0.003	18.659	0.001	0.83805	0.00010	2.0674	0.0005
MTM167	Romita	Mexico	38.545	0.007	15.613	0.002	18.639	0.002	0.83760	0.00007	2.0680	0.0004
Duplicate	Romita	Mexico	38.524	0.006	15.606	0.002	18.633	0.002	0.83745	0.00006	2.0673	0.0002
Duplicate	Romita	Mexico	38.551	0.006	15.615	0.002	18.639	0.002	0.83763	0.00004	2.0682	0.0002
MXY003	Mexico City	Mexico	38.677	0.010	15.646	0.002	18.755	0.002	0.83405	0.00008	2.0631	0.0004
MXY005	Mexico City	Mexico	38.661	0.010	15.644	0.002	18.756	0.001	0.83386	0.00012	2.0619	0.0006
MXY007	Mexico City	Mexico	38.663	0.006	15.643	0.002	18.751	0.002	0.83405	0.00005	2.0626	0.0003
MXF202	Puebla	Mexico	38.418	0.011	15.595	0.004	18.608	0.004	0.83793	0.00003	2.0647	0.0002
MXF206	Puebla	Mexico	38.471	0.010	15.613	0.003	18.615	0.003	0.83853	0.00010	2.0665	0.0004
MXF008	Puebla	Mexico	38.542	0.022	15.627	0.006	18.650	0.005	0.83795	0.00014	2.0663	0.0002
MXF187	Puebla	Mexico	38.532	0.006	15.632	0.003	18.618	0.003	0.83976	0.00005	2.0702	0.0002
MXF198	Puebla	Mexico	38.535	0.011	15.635	0.003	18.588	0.004	0.84114	0.00012	2.0735	0.0006
MJ0177	Seville	Spain	38.281	0.009	15.570	0.003	18.122	0.004	0.85913	0.00010	2.1125	0.00036
Duplicate	Seville	Spain	38.301	0.008	15.576	0.002	18.130	0.002	0.85906	0.00005	2.1127	0.00022
Duplicate	Seville	Spain	38.330	0.010	15.586	0.004	18.139	0.005	0.85924	0.00010	2.1132	0.00046
MJ0178	Seville	Spain	38.345	0.014	15.610	0.005	18.238	0.005	0.85572	0.00011	2.1026	0.00038
Duplicate	Seville	Spain	38.361	0.006	15.613	0.001	18.239	0.003	0.85604	0.00007	2.1036	0.00038
Duplicate	Seville	Spain	38.402	0.009	15.628	0.003	18.252	0.003	0.85615	0.00005	2.1041	0.00022
TRI004	Seville	Spain	38.347	0.018	15.574	0.006	18.457	0.006	0.84388	0.00009	2.0779	0.00052
Duplicate	Seville	Spain	38.322	0.020	15.563	0.007	18.441	0.006	0.84398	0.00011	2.0785	0.00046
Duplicate	Seville	Spain	38.315	0.019	15.564	0.005	18.448	0.006	0.84366	0.00015	2.0775	0.00093
TRI007	Seville	Spain	38.251	0.019	15.582	0.007	18.350	0.008	0.84925	0.00008	2.0848	0.00028
Duplicate	Seville	Spain	38.240	0.017	15.580	0.007	18.352	0.003	0.84906	0.00032	2.0844	0.00079
Duplicate	Seville	Spain	38.254	0.012	15.584	0.006	18.346	0.007	0.84945	0.00018	2.0854	0.00069
TRI008	Seville	Spain	38.465	0.022	15.642	0.008	18.453	0.007	0.84773	0.00017	2.0850	0.00085
Duplicate	Seville	Spain	38.473	0.017	15.644	0.006	18.445	0.005	0.84820	0.00022	2.0870	0.00101
Duplicate	Seville	Spain	38.499	0.024	15.651	0.007	18.453	0.005	0.84800	0.00013	2.0859	0.00062
TAL006	Talavera	Spain	38.274	0.019	15.595	0.008	18.378	0.009	0.84867	0.00010	2.0831	0.00032
TAL011	Talavera	Spain	38.314	0.013	15.601	0.005	18.409	0.005	0.84749	0.00008	2.0807	0.00036
TAL013	Talavera	Spain	38.308	0.012	15.603	0.005	18.346	0.005	0.85053	0.00006	2.0884	0.00006
MJ0118	Talavera	Spain	38.520	0.014	15.652	0.004	18.481	0.006	0.84677	0.00014	2.0836	0.00052
MJ0119	Talavera	Spain	38.472	0.012	15.651	0.005	18.260	0.007	0.85718	0.00007	2.1077	0.00034

A.4 Romita Ware Conclusions

The Pb glaze on the Romita ware's isotopic composition is clearly of Mexican origin, and manufactured by indigenous people. The Pb isotopic composition of the Puebla samples is similar to some of the Romita ware , but largely distinct from the ceramics recovered at Mexico City. In conclusion, the Pb isotopic composition of the glaze on the Romita ware indicates production outside Mexico City from indigenous Pb.

Appendix B

Achondrite Phosphate Pb-Pb Chronology

The following appendix is the result of a large collaboration to determine the age and petrogenesis of a pair of unique meteorites. I made the analyses and the Pb-Pb age assignments of the two phosphate minerals in these meteorites. The final average and age assignment for the published paper was made by Dr. Richard Ash. The data was published with the following citation:

Day, J. M. D., Ash, R., Yang, Y., Bellucci, J. J., Rumble III, D., McDonough, W. F., Walker, R., and Taylor, L. (2009). Early formation of evolved asteroidal crust. Nature, 457:179182.

B.1 Introduction

Andesite, the average composition of the continental crust, was thought to only be formed through plate tectonic activity on the planet Earth, but with the discovery of a pair of differentiated meteorites Graves Nunatak (GRA) 06128 and 06129, subduction was shown not to be the only mechanism by which to generate andesite (Day et al., 2009). The andesite on the GRA06128/9 parent body occured through the early partial melting of an undifferentiated, volatile rich parent body (Day et al., 2009). GRA06128/9 have abundant sodium-rich plagioclase, olivine, two pyroxenes, phosphates, and sulphides, with a bulk composition of andesite-trachy

andesite (Day et al., 2009). The apatites and merillites in GRA06128/9 have a large concentration of U (0.1-3 μg/g) and below detection Pb concentrations in the sulphide and plagioclase. The absence of common Pb and abundance of U in the phosphate phases makes them ideal for ^{207}Pb/^{206}Pb dating.

B.2 Method

^{207}Pb-^{206}Pb ages were determined using the same trace element method described in Chapter 2. The phosphates analyzed were identified using the SX-50 electron microprobe analyzer at the University of Tennessee and the JEOL-8900 Super-probe at the University of Maryland by Dr. James Day. All data reduction was made offline using Microsoft Excel. Background Pb signals were taken on mass, and subtracted from each isotopic measurement during ablation. Each ratio was determined using the background corrected Pb isotopic measurements. The average and $2\sigma_{mean}$ of the background corrected ratios, after ratios outside 3σ were discarded, were used to determine the age and error for each phosphate. An exponential fractionation law was used to correct for mass fractionation by means of bracketing the phosphate analyses with standard reference materials (NIST 610, NIST 612, BCR-2g). Ratios of ^{207}Pb/^{206}Pb for each SRM (Baker et al., 2004) were used to calculate the fractionation factor (α) (following Jochum et al., 2006). Differences in α between the three SRMS had a negligible effect on calculated ages. The ^{207}Pb/^{206}Pb ages were calculated using Isoplot/Ex (Ludwig, 2003).

B.3 Results

The results of the Pb isotopic analyses of the phosphates are available in Table B.1. The weighted mean of ages from the Cl-apatites and Merrilites from GRA06128 are indistinguishable at 4511±18 Ma and 4543±73 Ma (95% confidence level), respectively (Figure B.1). The weighted mean of ages from the Cl-apatites and Merrilites from GRA06129 are indistinguishable at 4564±60 Ma and 4602±61 Ma (95% confidence level), respectively (Figure B.1). Combining the Apatites and Merrilites from the pair yield indistinguishable ages of 4529±30 Ma and 4578±47 Ma (Figure B.1).

Table B.1 ^{207}Pb-^{206}Pb ages of phosphates in GRA 06128 and GRA 06129

Mineral	Spot size (μm)	^{207}Pb Total Counts	^{207}Pb / ^{206}Pb	2σ (mean)	Age	2σ
	GRA 06128, 51					
Cl-Apatite	35	37168	0.595	0.027	4496	66
Cl-Apatite	55	34716	0.605	0.028	4520	67
Cl-Apatite	55	64020	0.585	0.020	4471	50
Cl-Apatite	55	51046	0.607	0.014	4525	35
Cl-Apatite	55	61247	0.605	0.013	4521	31
Cl-Apatite	55	31628	0.592	0.032	4490	79
Cl-Apatite	30	16505	0.600	0.026	4509	63
Merrilite	55	3370	0.647	0.082	4618	183
Merrilite	55	15236	0.622	0.040	4559	93
Merrilite	30	822	0.463	0.608	4128	1949
Merrilite	55	3197	0.568	0.065	4428	168
	GRA 06129, 25					
Cl-Apatite	30	9270	0.600	0.049	4508	118
Cl-Apatite	30	7683	0.825	0.212	4965	366
Cl-Apatite	40	34133	0.678	0.041	4684	86
Cl-Apatite	40	18892	0.629	0.045	4577	103
Cl-Apatite	40	43563	0.687	0.039	4705	81
Cl-Apatite	40	50341	0.595	0.035	4495	85
Cl-Apatite	40	27366	0.620	0.032	4555	74
Cl-Apatite	40	28789	0.679	0.047	4686	99
Cl-Apatite	55	96875	0.615	0.025	4543	60
Cl-Apatite	80	27446	0.597	0.018	4500	44
Merrilite	40	22719	0.653	0.040	4631	89
Merrilite	55	25947	0.628	0.038	4574	87

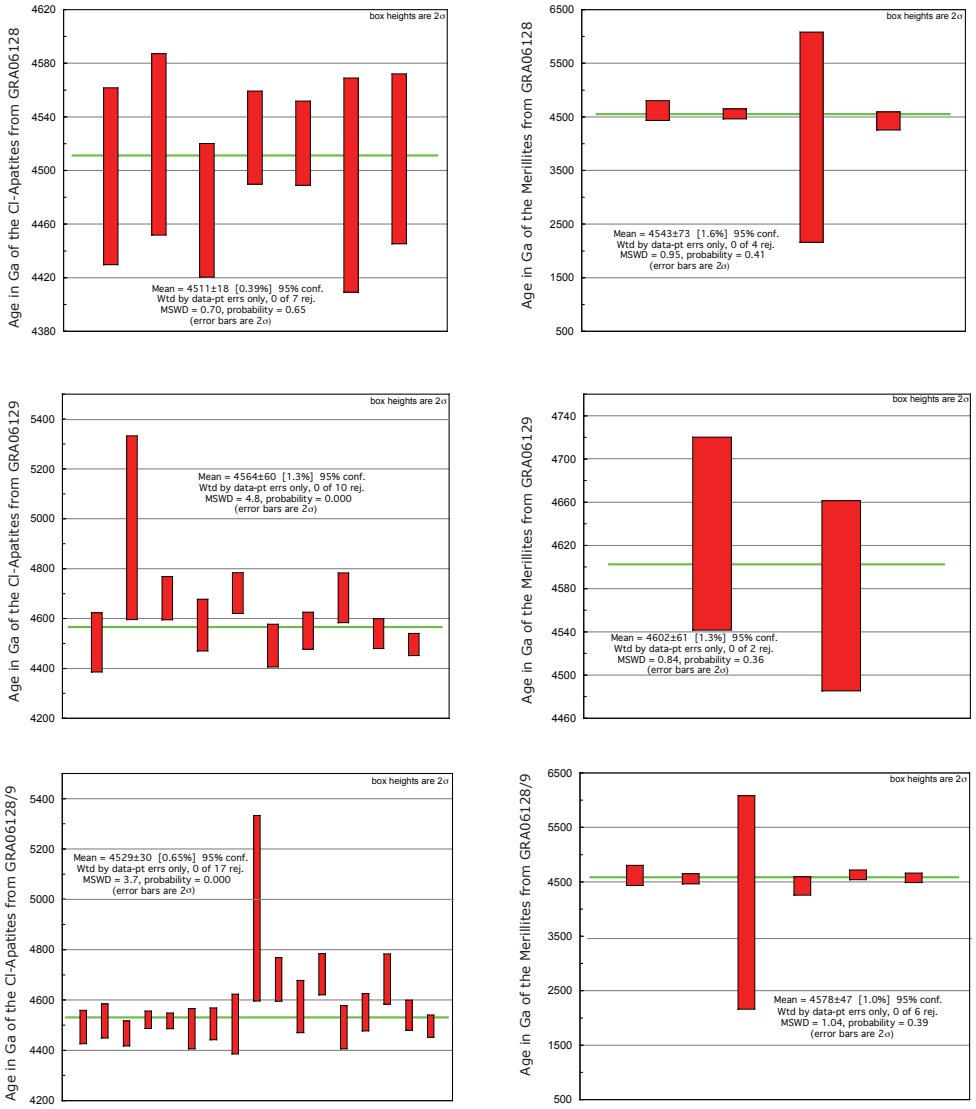

Figure B.1: Weighted means for all age calculations for GRA6128/9

B.4 Discussion

The age of the andesitic meteorite indicates that evolved crustal production happened in the solar system in the first ∼100 Ma.

Appendix C

Standard Addition

The following work was to undertaken to finish a data set originally compiled by Jenise Honesto, a University of Maryland Master's Student and was published in conjunction with her data in:

Walker, R., McDonough, W., Honesto, J., Chabot, N., McCoy, T., Ash, R., and Bellucci, J. J. (2008). Modeling fractional crystallization of group IVB iron meteorites. Geochimica et Cosmochimica Acta, 72: 2198-2216.

Additionally the method presented here was re-published in a review written by Dr. Ricardo Arevalo Jr, William F. McDonough, and myself with the following citation:

Arevalo, R. J., Bellucci, J. J., and McDonough, W. (2010). GGR Biennial Review: Advances in Laser Ablation and Solution ICP-MS from 2008-2009 with particular emphasis on sensitivity enhancements, mitigation of fractionation effects and exploration of new applications. Geostandards and Geoanalytical Research, 34(4): 327-341.

C.1 Introduction

The abundances of the Highly Siderophile Elements (HSE) Ru, Rh, Pd, Os, Ir, Pt, Re and Au can be used to constrain the conditions of formation of the iron me-

teorites including pre-accretionary nebular processes, accretion of the parent body, oxygen fugacity, and crystallization history of the parent melt. The combination of isotopic analyses (Pt-Re-Os) and high precision abundance analyses (e.g., isotope dilution analyses) of the HSE provide sensitive indicators that allow for critical testing of these processes as well as establishing co-genetic relationships of samples. In terms of condensation characteristics, most of the HSE are refractory, with Rh having a volatility comparable to Mg and Si, Pd being slightly less refractory and Au being the most volatile. Both Rh and Au are mono-isotopic elements and thus, high-precision isotope dilution techniques cannot be used for their analyses. Here we use a standard addition analysis technique with ICP-MS for 10 IVB iron meteorites. This method yields ±6-8.5% (2σ) precision results for Rh and Au determinations.

C.2 Method

Samples were cut with a diamond-wafering blade using de-ionized water as a coolant. To avoid cross-contamination the blade was cleaned after each cut by cutting a piece of carborundum and by changing the cooling water. Each sample was then manually polished by a separate piece of carbo-rundum. Primary solutions were created by dissolving $\sim$ 50 mg of iron meteorite in 10 mL of ultra pure aqua regia and a drop of HF (to prevent precipitation). Complete dissolution was achieved by heating ($\sim$120°C) these mixtures in sealed Teflon vials for 24 hours. These solutions were subsequently diluted with 90-100mL of 18.2 MΩ water and weighed to ensure the proper dilution factor. Analyses were conducted using a Thermo

Finnigan Element2 IC-PMS at the University of Maryland.

The meteorites Hoba and Ternera were used to construct calibration curves for the ^{197}Au measurements, while Hoba and Cape of Good Hope were used for the ^{103}Rh measurements. The initial Au and Rh calibration solutions contained 2.5 mL of the primary dissolved meteorite solution, 2.5 mL ultra pure 2% HNO_3, and 0.25 mL 10 ppb Yb solution drift monitor in 2% HNO_3. Six standard addition Au solutions were created from a 100 ppt Au, Pd, Pt, Ir, Rh, Ru solution added at .05 mL, maintaining a constant volume, which resulted in standard addition curve of 0 ppt - 50 ppt in 10 ppt increments. Six standard addition Rh solutions were created with a 10 ppb solution of Au, Pd, Pt, Ir, Rh, which resulted in a standard addition curve of 0 ppb-5 ppb in increments of $\sim$1 ppb (Figure C.1). For the remaining samples solutions were created using 2.5 mL of each primary meteorite solution, 2.5 mL HNO_3, and 0.25 mL 10 ppb Yb. External precision for Rh and Au concentrations in the standards were determined from a drift-corrected calibration curve. The concentrations of the samples were determined relative to the drift-corrected calibration curve. Gold and Rh abundances are shown below in Table B.1.

C.3 Results and Discussion

External precision, based on multiple analyses of Au in Hoba data is <6% (2σ, Figure C.2) and is <8.5% (2σ or better for the Rh data and compare favorably with that for neutron activation analysis (Rasmussen et al., 1984; Ryan et al., 1990)

Table C.1 Concentrations of Rh and Au in IVB Irons

IVB Irons	Au	2s	Rh	2s
Cape of Good Hope	0.044	0.002	3.5	0.18
Hoba	0.064	0.004	3.54	0.29
Iquique	0.049	0.003	3.41	0.08
Santa Clara	0.091	0.004	3.86	0.15
Skookum	0.105	0.005	3.76	0.23
Tawallah Valley	0.152	0.008	3.53	0.04
Ternera	0.13	0.005	3.96	0.25
Tlacotopec	0.051	0.003	3.43	0.25
Warburton Range	0.111	0.005	3.75	0.08
Weaver Mountain	0.095	0.004	3.61	0.15

and Laser Ablation- ICP-MS (Campbell and Humayun, 2005). Our Au data are on average 13% lower than Rasmussen et al. (1984) and Campbell and Humayun (2005) and irreconcilable with that reported by INAA Ryan et al. (1990). Our standard addition Rh data do not correlate with that reported in Ryan et al. (1990) or Campbell and Humayun (2005). The precision obtained from this data set is comparable to that achieved by both LA-ICPMS and INAA (Table B.2)

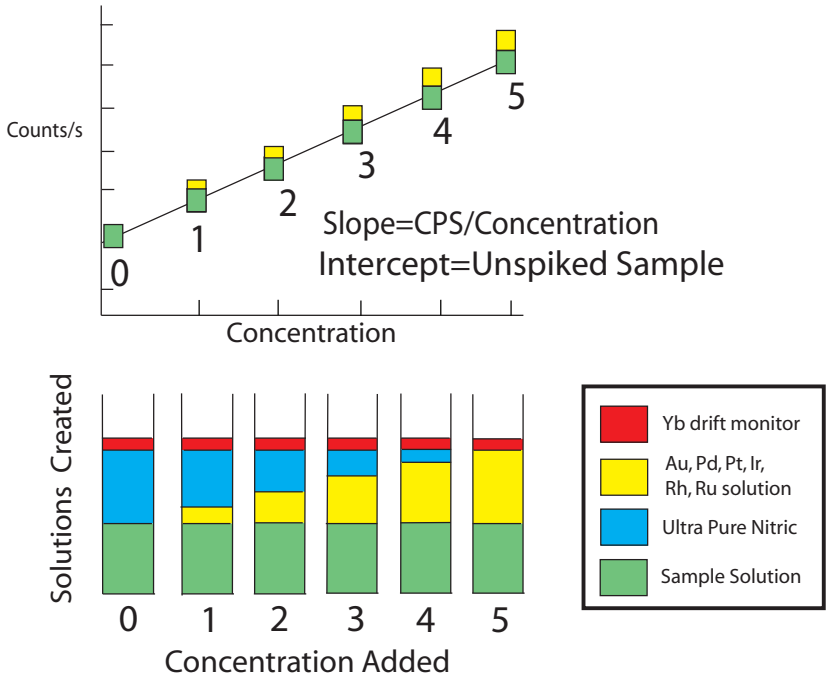

Figure C.1: A schematic diagram of the standard addition method used here, with increased amounts of dopant with the corresponding decreased amount of sample solution, which maintains a constant volume and matrix.

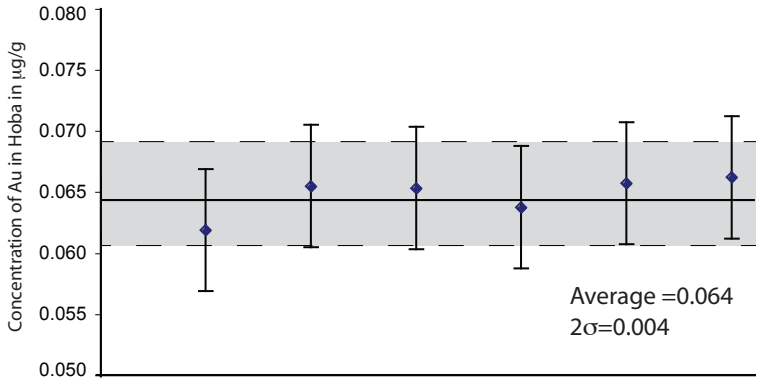

Figure C.2: Repeat analysis of the Hoba IVB iron meteorite by the Standard Addition measured here. The grey box illustrates the 2σ, external precision.

Table C.2. External Precision for Rh and Au

Method	Au	Rh
Standard Addition	6%	8%
INAA	4-6%	NA
LA-ICP-MS (C&H)	6%	5%
LA-ICP-MS (UMD)	12%	8%

Appendix D

Data Tables

Data tables in this appendix provide are from analyses of Pb isotopes in feldspars that are summarized presented in Chapters 2-6. The data tables are arranged alphabetically by xenolith location and subsequently by sample number.

Sample: Allie Gale's Crater

Mineral	$^{208}Pb/^{204}Pb$	$2\sigma_{(mean)}$	$^{207}Pb/^{204}Pb$	$2\sigma_{(mean)}$	$^{206}Pb/^{204}Pb$	$2\sigma_{(mean)}$	$^{207}Pb/^{206}Pb$	$2\sigma_{(mean)}$	$^{208}Pb/^{206}Pb$	$2\sigma_{(mean)}$
Feldspar	33.8	0.2	14.87	0.09	13.98	0.09	1.064	0.005	2.412	0.010
Feldspar	33.8	0.2	14.95	0.11	14.01	0.10	1.066	0.005	2.410	0.009
Feldspar	33.5	0.2	14.82	0.09	13.92	0.09	1.065	0.004	2.408	0.009
Feldspar	33.7	0.3	14.82	0.13	14.03	0.12	1.058	0.005	2.410	0.006
Feldspar	33.5	0.3	14.77	0.12	13.89	0.13	1.060	0.004	2.405	0.006
Feldspar	33.6	0.3	14.83	0.11	13.95	0.10	1.063	0.003	2.411	0.006
Feldspar	33.8	0.1	14.81	0.06	14.07	0.08	1.048	0.004	2.393	0.008
Feldspar	33.8	0.3	14.80	0.10	14.05	0.08	1.053	0.004	2.406	0.009
Average	33.69		14.83		13.99		1.060		2.407	
$2\sigma_{mean}$	0.09		0.04		0.05		0.004		0.004	
%	0.3%		0.3%		0.3%		0.4%		0.2%	

Sample: Chudleigh BC

Mineral	$^{208}Pb/^{204}Pb$	$2\sigma_{(mean)}$	$^{207}Pb/^{204}Pb$	$2\sigma_{(mean)}$	$^{206}Pb/^{204}Pb$	$2\sigma_{(mean)}$	$^{207}Pb/^{206}Pb$	$2\sigma_{(mean)}$
Feldspar	36.91	0.31	15.70	0.26	17.64	0.23	0.89	0.01
Feldspar	37.07	0.24	15.68	0.16	17.13	0.16	0.91	0.01
Feldspar	37.50	0.24	15.70	0.09	17.61	0.14	0.89	0.00
Feldspar	36.98	0.13	15.52	0.13	17.31	0.12	0.90	0.01
Feldspar	37.27	0.26	15.78	0.11	17.36	0.14	0.91	0.01
Feldspar	37.28	0.21	15.64	0.14	17.21	0.10	0.91	0.01
Feldspar	37.43	0.37	15.23	0.26	17.33	0.23	0.88	0.01
Feldspar	37.06	0.20	15.69	0.14	17.55	0.20	0.89	0.01
Average Feldspar	37.19		15.62		17.39		0.899	
$2\sigma_{mean}$	0.15		0.12		0.13		0.009	
%	0.4%		0.8%		0.8%		1.0%	

Sample: Chudleigh 83-107

Mineral	$^{208}Pb/^{204}Pb$	$2\sigma_{(mean)}$	$^{207}Pb/^{204}Pb$	$2\sigma_{(mean)}$	$^{206}Pb/^{204}Pb$	$2\sigma_{(mean)}$	$^{207}Pb/^{206}Pb$	$2\sigma_{(mean)}$	$^{208}Pb/^{206}Pb$	$2\sigma_{(mean)}$
Feldspar	37.57	0.43	15.29	0.22	18.45	0.19	0.83	0.01	2.02	0.02
Feldspar	37.91	0.43	15.56	0.29	18.32	0.29	0.84	0.01	2.07	0.02
Feldspar	37.47	0.62	15.59	0.32	17.87	0.48	0.87	0.02	2.11	0.03
Feldspar	38.19	0.43	15.56	0.20	18.40	0.23	0.85	0.01	2.08	0.02
Feldspar	38.61	0.43	15.68	0.43	18.35	0.44	0.84	0.01	2.09	0.04
Average Feldspar	37.95		15.54		18.28		0.846		2.072	
$2\sigma_{mean}$	0.42		0.13		0.21		0.01		0.03	
%	1.1%		0.9%		1.1%		1.7%		1.3%	

Sample: Chudleigh 83-112

Mineral	$^{208}Pb/^{204}Pb$	$2\sigma_{(mean)}$	$^{207}Pb/^{204}Pb$	$2\sigma_{(mean)}$	$^{206}Pb/^{204}Pb$	$2\sigma_{(mean)}$	$^{207}Pb/^{206}Pb$	$2\sigma_{(mean)}$	$^{208}Pb/^{206}Pb$	$2\sigma_{(mean)}$
Feldspar	38.89	0.29	15.57	0.10	18.56	0.18	0.84	0.00	2.08	0.01
Feldspar	39.18	0.30	15.73	0.14	18.72	0.20	0.84	0.01	2.09	0.02
Feldspar	38.80	0.20	15.58	0.13	18.65	0.16	0.83	0.01	2.09	0.01
Feldspar	39.28	0.23	15.93	0.12	18.62	0.12	0.86	0.01	2.10	0.01
Feldspar	39.20	0.23	15.81	0.12	18.78	0.12	0.84	0.00	2.09	0.01
Feldspar	38.81	0.22	15.65	0.13	18.63	0.12	0.84	0.01	2.09	0.00
Average Feldspar	39.03		15.71		18.66		0.84		2.09	
$2\sigma_{mean}$	0.18		0.11		0.06		0.01		0.01	
%	0.5%		0.7%		0.3%		0.7%		0.3%	

Sample: Damaping DMP-01

Mineral	$^{208}Pb/^{204}Pb$	$2\sigma_{(mean)}$	$^{207}Pb/^{204}Pb$	$2\sigma_{(mean)}$	$^{206}Pb/^{204}Pb$	$2\sigma_{(mean)}$	$^{207}Pb/^{206}Pb$	$2\sigma_{(mean)}$	$^{208}Pb/^{206}Pb$	$2\sigma_{(mean)}$
Feldspar	36.39	0.09	15.21	0.04	16.23	0.03	0.937	0.001	2.243	0.003
Feldspar	36.41	0.11	15.21	0.05	16.23	0.04	0.938	0.001	2.243	0.002
Feldspar	36.39	0.10	15.23	0.04	16.21	0.04	0.940	0.001	2.246	0.001
Feldspar	36.43	0.10	15.27	0.05	16.23	0.05	0.941	0.001	2.248	0.003
Feldspar	36.19	0.38	15.17	0.17	16.12	0.17	0.942	0.003	2.245	0.005
Feldspar	36.27	0.36	15.18	0.15	16.21	0.15	0.936	0.003	2.235	0.007
Feldspar	36.45	0.40	15.23	0.17	16.31	0.17	0.934	0.002	2.238	0.004
Feldspar	36.38	0.10	15.19	0.04	16.23	0.05	0.936	0.001	2.242	0.003
Feldspar	36.27	0.23	15.20	0.09	16.13	0.10	0.940	0.001	2.247	0.002
Feldspar	36.59	0.40	15.25	0.15	16.26	0.16	0.938	0.002	2.245	0.003
Feldspar	36.79	0.61	15.36	0.24	16.35	0.26	0.939	0.001	2.249	0.002
Feldspar	36.43	0.26	15.21	0.11	16.21	0.11	0.939	0.001	2.248	0.002
Feldspar	36.26	0.11	15.20	0.06	16.18	0.04	0.939	0.002	2.244	0.004
Feldspar	36.39	0.15	15.26	0.07	16.25	0.08	0.941	0.004	2.238	0.008
Feldspar	36.53	0.15	15.32	0.07	16.26	0.05	0.942	0.002	2.248	0.004
Feldspar Average	36.41		15.23		16.23		0.939		2.244	
$2\sigma_{mean}$	0.08		0.03		0.03		0.001		0.002	
%	0.2%		0.2%		0.2%		0.1%		0.1%	

Sample: Damaping DMP-03

Mineral	$^{208}Pb/^{204}Pb$	$2\sigma_{(mean)}$	$^{207}Pb/^{204}Pb$	$2\sigma_{(mean)}$	$^{206}Pb/^{204}Pb$	$2\sigma_{(mean)}$	$^{207}Pb/^{206}Pb$	$2\sigma_{(mean)}$	$^{208}Pb/^{206}Pb$	$2\sigma_{(mean)}$
Feldspar	37.00	0.17	15.50	0.09	16.73	0.10	0.926	0.003	2.216	0.005
Feldspar	37.22	0.21	15.41	0.10	16.76	0.10	0.919	0.003	2.218	0.006
Feldspar	37.22	0.17	15.53	0.11	16.70	0.08	0.930	0.003	2.224	0.007
Feldspar	37.22	0.17	15.39	0.15	16.91	0.12	0.910	0.006	2.204	0.013
Feldspar	36.92	0.56	15.39	0.28	16.42	0.30	0.937	0.010	2.222	0.024
Feldspar	37.03	0.17	15.50	0.10	16.64	0.12	0.931	0.006	2.222	0.010
Feldsapr Average	37.10		15.45		16.69		0.926		2.218	
$2\sigma_{(mean)}$	0.11		0.05		0.13		0.008		0.006	
%	0.3%		0.3%		0.8%		0.8%		0.3%	

Sample: Damaping DMP-07

Mineral	$^{208}Pb/^{204}Pb$	$2\sigma_{(mean)}$	$^{207}Pb/^{204}Pb$	$2\sigma_{(mean)}$	$^{206}Pb/^{204}Pb$	$2\sigma_{(mean)}$	$^{207}Pb/^{206}Pb$	$2\sigma_{(mean)}$	$^{208}Pb/^{206}Pb$	$2\sigma_{(mean)}$
Feldspar	37.35	0.30	15.35	0.19	17.13	0.17	0.888	0.009	2.181	0.011
Feldspar	37.44	0.16	15.42	0.11	17.06	0.13	0.904	0.006	2.195	0.012
Feldspar	36.90	0.28	15.28	0.18	17.18	0.16	0.892	0.010	2.168	0.016
Feldspar	37.20	0.23	15.51	0.13	17.17	0.13	0.896	0.009	2.160	0.016
Feldspar	36.88	0.24	15.35	0.15	17.18	0.16	0.892	0.010	2.148	0.017
Feldspar	37.52	0.31	15.48	0.15	17.11	0.25	0.903	0.009	2.194	0.020
Feldspar	37.13	0.17	15.50	0.15	17.02	0.13	0.914	0.008	2.189	0.018
Feldspar	37.26	0.19	15.34	0.15	17.07	0.11	0.900	0.007	2.182	0.014
Feldspar	37.45	0.26	15.40	0.16	17.20	0.17	0.893	0.001	2.177	0.018
Feldspar	36.95	0.28	15.37	0.14	17.33	0.17	0.890	0.010	2.135	0.016
Feldspar Average	37.21		15.40		17.15		0.897		2.173	
$2\sigma_{(mean)}$	0.15		0.05		0.06		0.005		0.013	
%	0.4%		0.3%		0.3%		0.6%		0.6%	

Sample: Damaping: DMP-09

Mineral	$^{208}Pb/^{204}Pb$	$2\sigma_{(mean)}$	$^{207}Pb/^{204}Pb$	$2\sigma_{(mean)}$	$^{206}Pb/^{204}Pb$	$2\sigma_{(mean)}$	$^{207}Pb/^{206}Pb$	$2\sigma_{(mean)}$	$^{208}Pb/^{206}Pb$	$2\sigma_{(mean)}$
Feldspar	37.53	0.39	15.42	0.26	17.83	0.25	0.865	0.011	2.119	0.014
Feldspar	36.74	1.45	15.49	1.00	16.94	0.95	0.914	0.042	2.177	0.083
Feldspar	36.69	0.53	15.19	0.41	16.02	0.39	0.948	0.030	2.307	0.057
Feldspar	37.17	0.42	15.60	0.46	16.27	0.53	0.959	0.036	2.295	0.067
Feldspar	36.32	0.67	15.37	0.44	16.25	0.42	0.946	0.032	2.222	0.054
Feldspar	36.16	0.46	15.22	0.30	16.18	0.32	0.941	0.022	2.230	0.038
Feldspar	35.38	0.89	15.14	0.86	17.10	0.65	0.885	0.048	2.047	0.077
Feldspar	36.65	0.54	15.37	0.37	17.06	0.42	0.901	0.024	2.158	0.038
Feldspar	35.75	1.00	15.10	0.83	16.63	0.67	0.908	0.042	2.119	0.069
Feldspar	36.76	0.68	15.32	0.49	17.00	0.51	0.901	0.030	2.167	0.056
Feldspar	36.70	0.33	15.14	0.32	16.26	0.25	0.931	0.020	2.272	0.030
Feldspar	37.49	0.33	15.37	0.25	16.47	0.30	0.933	0.022	2.272	0.036
Feldspar	36.90	0.51	15.45	0.30	16.19	0.37	0.954	0.022	2.264	0.046
Feldspar	37.14	0.39	15.52	0.26	17.84	0.32	0.870	0.014	2.074	0.028
Feldspar	36.89	0.40	15.19	0.23	16.64	0.25	0.913	0.010	2.220	0.018
Feldspar	36.96	0.68	15.33	0.40	16.84	0.30	0.910	0.014	2.213	0.028
Feldspar Average	36.70		15.33		16.72		0.92		2.20	
$2\sigma_{(mean)}$	0.29		0.08		0.28		0.01		0.04	
%	1%		0%		2%		2%		2%	

Sample: Damaping DMP-27

Mineral	$^{208}Pb/^{204}Pb$	$2\sigma_{(mean)}$	$^{207}Pb/^{204}Pb$	$2\sigma_{(mean)}$	$^{206}Pb/^{204}Pb$	$2\sigma_{(mean)}$	$^{207}Pb/^{206}Pb$	$2\sigma_{(mean)}$	$^{208}Pb/^{206}Pb$	$2\sigma_{(mean)}$
Feldspar	35.81	0.17	15.27	0.08	15.86	0.09	0.962	0.003	2.260	0.004
Feldspar	36.21	0.90	15.42	0.30	16.43	0.35	0.940	0.004	2.218	0.005
Feldspar	35.70	0.23	15.24	0.09	15.80	0.11	0.963	0.002	2.260	0.003
Feldspar	35.69	0.35	15.19	0.15	15.85	0.17	0.958	0.003	2.252	0.005
Feldspar	35.80	0.14	15.28	0.06	15.83	0.08	0.964	0.002	2.262	0.004
Feldspar	35.98	0.13	15.29	0.06	16.06	0.06	0.950	0.002	2.237	0.006
Feldspar	35.65	0.14	15.20	0.09	15.71	0.10	0.969	0.003	2.272	0.008
Feldspar	35.98	0.11	15.27	0.05	16.01	0.07	0.953	0.004	2.246	0.005
Feldspar	36.23	0.24	15.33	0.12	16.36	0.13	0.941	0.007	2.226	0.007
Feldspar	35.80	0.09	15.29	0.03	15.81	0.05	0.966	0.002	2.264	0.003
Feldspar	35.96	0.16	15.28	0.07	15.94	0.08	0.959	0.002	2.253	0.004
Feldspar	35.84	0.14	15.29	0.06	15.94	0.08	0.957	0.002	2.248	0.005
Feldspar	35.97	0.12	15.26	0.05	15.94	0.08	0.958	0.004	2.254	0.006
Feldspar	35.89	0.30	15.32	0.14	16.05	0.18	0.950	0.004	2.244	0.011
Feldspar	36.24	0.30	15.32	0.10	16.16	0.13	0.949	0.002	2.244	0.005
Feldspar	35.90	0.17	15.33	0.08	15.83	0.09	0.969	0.002	2.267	0.004
Feldspar	35.74	0.23	15.28	0.10	15.70	0.10	0.974	0.002	2.276	0.003
Feldspar	35.42	0.36	15.15	0.15	15.56	0.17	0.973	0.002	2.297	0.004
Feldspar	35.85	0.12	15.27	0.05	15.83	0.05	0.965	0.002	2.265	0.002
Feldspar	35.96	0.23	15.28	0.11	15.84	0.12	0.965	0.002	2.265	0.004
Feldspar	35.86	0.21	15.26	0.10	15.86	0.07	0.960	0.005	2.257	0.006
Feldspar	35.78	0.06	15.27	0.03	15.76	0.03	0.969	0.001	2.271	0.002
Feldspar	35.88	0.19	15.27	0.09	15.89	0.07	0.960	0.003	2.261	0.005
Feldspar Average	35.88		15.28		15.91		0.960		2.257	
$2\sigma_{mean}$	0.08		0.02		0.08		0.004		0.007	
%	0.2%		0.1%		0.5%		0.4%		0.3%	

Sample: Damaping DMP-28

Mineral	$^{208}Pb/^{204}Pb$	$2\sigma_{(mean)}$	$^{207}Pb/^{204}Pb$	$2\sigma_{(mean)}$	$^{206}Pb/^{204}Pb$	$2\sigma_{(mean)}$	$^{207}Pb/^{206}Pb$	$2\sigma_{(mean)}$	$^{208}Pb/^{206}Pb$	$2\sigma_{(mean)}$
Feldspar	37.07	0.26	15.23	0.13	16.42	0.18	0.928	0.008	2.257	0.017
Feldspar	37.24	0.02	15.35	0.12	16.55	0.13	0.928	0.006	2.251	0.015
Feldspar	37.09	0.28	15.18	0.13	16.70	0.17	0.909	0.004	2.213	0.011
Feldspar	37.43	0.33	15.26	0.19	16.84	0.19	0.906	0.005	2.221	0.013
Feldspar	37.14	0.26	15.24	0.18	16.52	0.16	0.923	0.008	2.249	0.013
Feldspar	37.11	0.00	15.48	0.10	16.61	0.19	0.932	0.010	2.235	0.019
Feldspar Average	37.18		15.29		16.61		0.921		2.238	
$2\sigma_{mean}$	0.1		0.09		0.12		0.009		0.015	
%	0.3%		0.6%		0.7%		1.0%		0.7%	

Sample: Damaping DMP-62

Mineral	$^{208}Pb/^{204}Pb$	$2\sigma_{(mean)}$	$^{207}Pb/^{204}Pb$	$2\sigma_{(mean)}$	$^{206}Pb/^{204}Pb$	$2\sigma_{(mean)}$	$^{207}Pb/^{206}Pb$	$2\sigma_{(mean)}$	$^{208}Pb/^{206}Pb$	$2\sigma_{(mean)}$
Feldspar	37.20	0.26	15.31	0.12	16.66	0.12	0.918	0.004	2.227	0.007
Feldspar	37.00	0.21	15.34	0.12	16.65	0.08	0.921	0.003	2.220	0.007
Feldspar	37.20	0.21	15.38	0.11	16.80	0.10	0.920	0.003	2.218	0.004
Feldspar	37.29	0.21	15.43	0.11	16.80	0.11	0.918	0.004	2.216	0.007
Feldspar	37.09	0.13	15.31	0.08	16.66	0.08	0.922	0.003	2.230	0.005
Feldspar	38.08	1.10	15.43	0.28	17.21	0.46	0.891	0.014	2.227	0.032
Feldspar	37.24	0.21	15.32	0.11	16.72	0.12	0.917	0.007	2.230	0.012
Feldspar	37.24	0.15	15.33	0.07	16.75	0.08	0.914	0.005	2.218	0.006
Feldspar	37.11	0.16	15.32	0.08	16.75	0.10	0.914	0.005	2.219	0.006
Feldspar	37.22	0.12	15.50	0.09	16.71	0.07	0.926	0.002	2.226	0.005
Feldspar	36.91	0.19	15.36	0.10	16.61	0.12	0.922	0.005	2.229	0.011
Feldspar	36.74	1.45	15.39	1.00	16.94	0.95	0.909	0.042	2.228	0.083
Feldspar Average	37.19		15.37		16.77		0.916		2.224	
$2\sigma_{mean}$	0.19		0.03		0.10		0.005		0.003	
%	0.5%		0.2%		0.6%		0.6%		0.1%	

Sample: Damaping DMP-71

Mineral	$^{208}Pb/^{204}Pb$	$2\sigma_{(mean)}$	$^{207}Pb/^{204}Pb$	$2\sigma_{(mean)}$	$^{206}Pb/^{204}Pb$	$2\sigma_{(mean)}$	$^{207}Pb/^{206}Pb$	$2\sigma_{(mean)}$	$^{208}Pb/^{206}Pb$	$2\sigma_{(mean)}$
Feldspar	35.92	0.30	15.23	0.25	16.11	0.34	0.946	0.014	2.290	0.042
Feldspar	36.49	0.58	15.33	0.40	16.02	0.39	0.957	0.024	2.281	0.046
Feldspar	36.87	0.46	15.30	0.32	16.36	0.39	0.935	0.022	2.226	0.052
Feldspar	36.57	0.42	15.28	0.26	16.62	0.28	0.919	0.012	2.200	0.024
Feldspar	37.27	0.35	15.29	0.30	16.82	0.37	0.909	0.016	2.214	0.020
Feldspar	37.10	0.37	15.17	0.30	16.46	0.28	0.922	0.015	2.244	0.030
Feldspar	36.98	0.30	15.22	0.26	16.26	0.19	0.936	0.012	2.275	0.036
Feldspar	36.62	0.54	15.29	0.28	16.18	0.37	0.945	0.019	2.280	0.042
Feldspar	35.67	0.65	15.42	0.35	15.93	0.41	0.968	0.022	2.248	0.046
Feldspar Average	36.61		15.28		16.31		0.937		2.251	
$2\sigma_{mean}$	0.35		0.05		0.19		0.012		0.022	
%	1.0%		0.3%		1.2%		1.3%		1.0%	

Sample: Damaping DMP-27

Mineral	$^{208}Pb/^{204}Pb$	$2\sigma_{(mean)}$	$^{207}Pb/^{204}Pb$	$2\sigma_{(mean)}$	$^{206}Pb/^{204}Pb$	$2\sigma_{(mean)}$	$^{207}Pb/^{206}Pb$	$2\sigma_{(mean)}$	$^{208}Pb/^{206}Pb$	$2\sigma_{(mean)}$
Feldspar	36.35	0.52	14.85	0.30	17.39	0.37	0.854	0.019	2.112	0.030
Feldspar	37.24	0.49	15.47	0.17	17.83	0.25	0.868	0.010	2.097	0.024
Feldspar	37.41	0.36	15.37	0.28	18.00	0.32	0.854	0.010	2.085	0.022
Feldspar	36.58	0.80	15.49	0.56	17.46	0.49	0.887	0.026	2.105	0.047
Feldspar	36.36	0.87	15.51	0.54	17.18	0.54	0.903	0.015	2.099	0.032
Feldspar	36.47	0.54	15.64	0.35	17.34	0.35	0.902	0.014	2.098	0.070
Feldspar	36.43	0.89	14.98	0.56	16.84	0.53	0.890	0.026	2.154	0.049
Feldspar	36.52	1.34	15.38	0.65	17.64	0.74	0.872	0.017	2.075	0.030
Feldspar	35.72	0.57	15.35	0.33	16.37	0.35	0.938	0.024	2.164	0.036
Feldspar	36.14	0.42	15.31	0.24	17.43	0.17	0.879	0.013	2.083	0.026
Feldspar	36.36	0.64	14.84	0.45	17.35	0.54	0.856	0.016	2.083	0.045
Feldspar	36.59	0.35	15.10	0.24	17.22	0.19	0.877	0.009	2.112	0.020
Feldspar	37.24	0.96	15.54	0.73	17.39	0.40	0.894	0.024	2.144	0.049
Feldspar	36.42	0.45	15.03	0.26	17.27	0.21	0.870	0.018	2.112	0.028
Feldspar	36.87	0.42	15.60	0.19	17.68	0.23	0.882	0.011	2.096	0.018
Feldspar	38.13	1.39	15.96	0.59	17.69	0.70	0.902	0.006	2.140	0.012
Feldspar	37.45	0.76	15.95	0.40	17.47	0.40	0.913	0.026	2.136	0.055
Feldspar	37.58	0.56	15.56	0.35	17.29	0.40	0.900	0.019	2.165	0.034
Feldspar	36.37	0.35	14.83	0.24	17.24	0.26	0.860	0.017	2.116	0.042
Feldspar	37.07	0.92	15.30	0.52	17.60	0.56	0.870	0.015	2.126	0.024
Feldspar	36.78	0.33	15.35	0.15	16.78	0.15	0.915	0.004	2.188	0.009
Feldspar	37.38	0.49	15.48	0.19	17.13	0.23	0.904	0.005	2.180	0.006
Feldspar	36.62	0.40	15.23	0.19	16.63	0.18	0.915	0.005	2.198	0.008
Feldspar	36.54	0.70	15.31	0.38	16.77	0.39	0.913	0.007	2.173	0.018
Feldspar	37.40	0.59	15.58	0.26	17.14	0.25	0.909	0.004	2.187	0.009
Feldspar	37.56	0.49	15.58	0.23	17.59	0.40	0.886	0.017	2.140	0.028
Feldspar	37.00	0.10	15.60	0.04	17.09	0.05	0.913	0.002	2.165	0.001
Feldspar Average	36.84		15.38		17.29		0.890		2.131	
$2\sigma_{mean}$	0.21		0.11		0.14		0.009		0.014	
%	1%		1%		1%		1%		1%	

Sample: Damaping DMP-73

Mineral	$^{208}Pb/^{204}Pb$	$2\sigma_{(mean)}$	$^{207}Pb/^{204}Pb$	$2\sigma_{(mean)}$	$^{206}Pb/^{204}Pb$	$2\sigma_{(mean)}$	$^{207}Pb/^{206}Pb$	$2\sigma_{(mean)}$	$^{208}Pb/^{206}Pb$	$2\sigma_{(mean)}$
Feldspar-1	37.01	0.19	15.39	0.08	16.77	0.08	0.918	0.001	2.207	0.003
Feldspar-1	37.19	0.19	15.41	0.07	17.15	0.12	0.900	0.004	2.172	0.006
Feldspar-1	37.58	0.25	15.47	0.12	17.38	0.11	0.892	0.004	2.160	0.006
Feldspar-1	36.96	0.10	15.37	0.04	16.83	0.07	0.912	0.003	2.195	0.005
Feldspar-1	36.96	0.14	15.35	0.06	16.83	0.07	0.913	0.002	2.194	0.003
Feldspar-1	36.91	0.16	15.37	0.07	16.75	0.08	0.917	0.002	2.208	0.003
Feldspar-1	36.97	0.60	15.38	0.25	16.75	0.26	0.917	0.001	2.206	0.003
Feldspar-1	36.93	0.17	15.39	0.07	16.81	0.08	0.914	0.002	2.198	0.003
Feldspar-1	37.41	0.28	15.47	0.10	17.32	0.14	0.895	0.005	2.165	0.008
Feldspar	37.01	0.09	15.41	0.04	16.77	0.04	0.919	0.002	2.208	0.001
Feldspar	37.26	0.65	15.52	0.30	17.31	0.28	0.899	0.009	2.157	0.014
Feldspar	37.06	0.60	15.45	0.23	17.31	0.25	0.889	0.004	2.151	0.006
Feldspar	37.01	0.42	15.51	0.18	17.28	0.19	0.897	0.004	2.167	0.006
Feldspar	37.02	0.35	15.36	0.15	16.96	0.18	0.905	0.006	2.182	0.011
Feldspar	37.63	0.26	15.53	0.11	17.42	0.12	0.892	0.004	2.162	0.008
Feldspar	37.16	0.18	15.47	0.08	16.94	0.09	0.907	0.004	2.186	0.008
Feldspar Average	37.13		15.39		16.95		0.909		2.189	
$2\sigma_{mean}$	0.11		0.03		0.13		0.01		0.01	
%	0.3%		0.2%		0.8%		0.6%		0.5%	

Sample: Damaping DMP-07

Mineral	$^{208}Pb/^{204}Pb$	$2\sigma_{(mean)}$	$^{207}Pb/^{204}Pb$	$2\sigma_{(mean)}$	$^{206}Pb/^{204}Pb$	$2\sigma_{(mean)}$	$^{207}Pb/^{206}Pb$	$2\sigma_{(mean)}$	$^{208}Pb/^{206}Pb$	$2\sigma_{(mean)}$
Feldspar	37.39	0.10	15.45	0.04	17.22	0.05	0.898	0.001	2.172	0.001
Feldspar	37.39	0.17	15.45	0.07	17.17	0.08	0.899	0.001	2.178	0.001
Feldspar	37.59	0.12	15.55	0.05	17.28	0.06	0.900	0.001	2.176	0.003
Feldspar	37.50	0.37	15.53	0.15	17.22	0.15	0.902	0.002	2.175	0.005
Feldspar	37.42	0.08	15.48	0.04	17.19	0.04	0.900	0.001	2.176	0.001
Feldspar	37.11	0.66	15.36	0.32	17.14	0.30	0.896	0.011	2.166	0.034
Feldspar	37.44	0.19	15.48	0.08	17.22	0.10	0.898	0.002	2.176	0.006
Feldspar	37.44	0.31	15.47	0.12	17.19	0.13	0.900	0.001	2.178	0.002
Feldspar	37.50	0.28	15.51	0.12	17.26	0.14	0.901	0.002	2.173	0.004
Feldspar	37.51	0.47	15.51	0.18	17.30	0.23	0.899	0.004	2.169	0.009
Feldspar	37.40	0.30	15.47	0.12	17.20	0.14	0.900	0.001	2.176	0.001
Feldspar	37.37	0.21	15.46	0.08	17.20	0.09	0.899	0.001	2.173	0.002
Feldspar	37.15	0.63	15.40	0.37	17.24	0.44	0.898	0.020	2.176	0.042
Feldspar	37.45	0.07	15.47	0.03	17.20	0.04	0.899	0.001	2.178	0.001
Feldspar	37.64	0.45	15.54	0.26	17.69	0.28	0.884	0.008	2.154	0.012
Feldspar	38.37	0.63	15.74	0.33	17.71	0.37	0.882	0.011	2.133	0.022
Feldspar Average	37.48		15.49		17.28		0.897		2.170	
$2\sigma_{mean}$	0.14		0.04		0.09		0.003		0.006	
%	0.4%		0.3%		0.5%		0.3%		0.3%	

Sample: Eifel S30

Mineral	$^{208}Pb/^{204}Pb$	$2\sigma_{(mean)}$	$^{207}Pb/^{204}Pb$	$2\sigma_{(mean)}$	$^{206}Pb/^{204}Pb$	$2\sigma_{(mean)}$	$^{207}Pb/^{206}Pb$	$2\sigma_{(mean)}$	$^{208}Pb/^{206}Pb$	$2\sigma_{(mean)}$
Feldspar	38.58	0.11	15.61	0.06	18.69	0.06	0.835	0.002	2.063	0.004
Feldspar	38.96	0.16	15.77	0.08	18.83	0.09	0.837	0.002	2.069	0.004
Feldspar	38.83	0.12	15.67	0.06	18.75	0.06	0.837	0.003	2.072	0.005
Feldspar	39.01	0.33	15.85	0.13	18.81	0.15	0.842	0.004	2.072	0.008
Feldspar	39.01	0.16	15.76	0.07	18.79	0.09	0.839	0.002	2.073	0.003
Feldspar	38.96	0.16	15.67	0.07	18.98	0.07	0.825	0.002	2.051	0.004
Average Feldspar	38.89		15.72		18.81		0.84		2.07	
$2\sigma_{mean}$	0.13		0.07		0.08		0.00		0.01	
%	0.3%		0.5%		0.4%		0.6%		0.3%	

Sample: Eifel S-35

Mineral	$^{208}Pb/^{204}Pb$	$2\sigma_{(mean)}$	$^{207}Pb/^{204}Pb$	$2\sigma_{(mean)}$	$^{206}Pb/^{204}Pb$	$2\sigma_{(mean)}$	$^{207}Pb/^{206}Pb$	$2\sigma_{(mean)}$	$^{208}Pb/^{206}Pb$	$2\sigma_{(mean)}$
Feldspar	38.34	0.16	15.68	0.06	18.21	0.07	0.861	0.001	2.105	0.001
Feldspar	38.48	0.23	15.72	0.10	18.28	0.11	0.860	0.002	2.104	0.004
Feldspar	38.33	0.13	15.66	0.06	18.21	0.06	0.860	0.001	2.104	0.003
Feldspar	38.38	0.24	15.70	0.11	18.23	0.11	0.859	0.001	2.103	0.004
Feldspar	38.26	0.09	15.65	0.04	18.17	0.05	0.861	0.002	2.105	0.004
Feldspar	38.38	0.16	15.66	0.07	18.23	0.08	0.861	0.001	2.106	0.004
Average Feldspar	38.36		15.68		18.22		0.860		2.105	
$2\sigma_{mean}$	0.06		0.02		0.03		0.001		0.001	
%	0.2%		0.1%		0.2%		0.1%		0.0%	

Sample: Eifel S30

Mineral	$^{208}Pb/^{204}Pb$	$2\sigma_{(mean)}$	$^{207}Pb/^{204}Pb$	$2\sigma_{(mean)}$	$^{206}Pb/^{204}Pb$	$2\sigma_{(mean)}$	$^{207}Pb/^{206}Pb$	$2\sigma_{(mean)}$	$^{208}Pb/^{206}Pb$	$2\sigma_{(mean)}$
Feldspar	38.58	0.11	15.61	0.06	18.69	0.06	0.835	0.002	2.063	0.004
Feldspar	38.96	0.16	15.77	0.08	18.83	0.09	0.837	0.002	2.069	0.004
Feldspar	38.83	0.12	15.67	0.06	18.75	0.06	0.837	0.003	2.072	0.005
Feldspar	39.01	0.33	15.85	0.13	18.81	0.15	0.842	0.004	2.072	0.008
Feldspar	39.01	0.16	15.76	0.07	18.79	0.09	0.839	0.002	2.073	0.003
Feldspar	38.96	0.16	15.67	0.07	18.98	0.07	0.825	0.002	2.051	0.004
Average Feldspar	38.89		15.72		18.81		0.84		2.07	
$2\sigma_{mean}$	0.13		0.07		0.08		0.00		0.01	
%	0.3%		0.5%		0.4%		0.6%		0.3%	

Sample: Eledoi EL04-01

Mineral	$^{208}Pb/^{204}Pb$	$2\sigma_{(mean)}$	$^{207}Pb/^{204}Pb$	$2\sigma_{(mean)}$	$^{206}Pb/^{204}Pb$	$2\sigma_{(mean)}$	$^{207}Pb/^{206}Pb$	$2\sigma_{(mean)}$	$^{208}Pb/^{206}Pb$	$2\sigma_{(mean)}$
Feldspar	40.35	0.21	15.01	0.08	14.71	0.07	1.021	0.001	2.743	0.001
Feldspar	40.47	0.31	15.07	0.11	14.76	0.11	1.021	0.001	2.742	0.001
Feldspar	40.43	0.08	15.05	0.03	14.72	0.03	1.022	0.001	2.744	0.002
Feldspar	40.40	0.08	15.04	0.03	14.74	0.03	1.020	0.001	2.742	0.002
Feldspar	40.45	0.06	15.04	0.02	14.73	0.02	1.022	0.000	2.747	0.001
Feldspar	40.37	0.14	15.02	0.05	14.70	0.05	1.022	0.000	2.747	0.001
Feldspar	40.39	0.13	15.02	0.04	14.71	0.04	1.021	0.000	2.747	0.001
Feldspar	40.49	0.13	15.06	0.05	14.74	0.05	1.022	0.000	2.748	0.001
Feldspar	40.37	0.07	15.01	0.02	14.69	0.02	1.022	0.000	2.748	0.001
Feldspar	40.38	0.08	15.02	0.03	14.69	0.03	1.022	0.000	2.748	0.001
Feldspar	40.40	0.08	15.02	0.02	14.69	0.02	1.023	0.000	2.749	0.001
Feldspar Average	40.41		15.03		14.72		1.0216		2.746	
$2\sigma_{mean}$	0.03		0.01		0.01		0.0005		0.002	
%	0.1%		0.1%		0.1%		0.0%		0.1%	

Sample: Labait LB04-19

Mineral	$^{208}Pb/^{204}Pb$	$2\sigma_{(mean)}$	$^{207}Pb/^{204}Pb$	$2\sigma_{(mean)}$	$^{206}Pb/^{204}Pb$	$2\sigma_{(mean)}$	$^{207}Pb/^{206}Pb$	$2\sigma_{(mean)}$	$^{208}Pb/^{206}Pb$	$2\sigma_{(mean)}$
Feldspar	33.90	0.12	14.84	0.04	14.02	0.05	1.058	0.002	2.413	0.003
Feldspar	33.96	0.14	14.89	0.06	14.04	0.07	1.058	0.003	2.413	0.005
Feldspar	34.22	0.09	14.95	0.03	14.30	0.06	1.045	0.004	2.391	0.006
Feldspar	34.27	0.07	14.96	0.03	14.35	0.06	1.041	0.003	2.385	0.005
Feldspar	34.07	0.13	14.91	0.05	14.16	0.07	1.054	0.002	2.407	0.004
Feldspar	34.02	0.23	14.87	0.09	14.21	0.12	1.046	0.005	2.394	0.008
Feldspar	33.98	0.08	14.88	0.03	14.17	0.04	1.049	0.001	2.395	0.002
Feldspar	34.34	0.17	14.89	0.07	14.48	0.09	1.029	0.004	2.368	0.007
Average	34.10		14.90		14.22		1.047		2.396	
$2\sigma_{mean}$	0.12		0.03		0.11		0.007		0.031	
%	0.3%		0.2%		0.8%		0.7%		1.3%	

Sample: Labait LB04-27

Mineral	$^{208}Pb/^{204}Pb$	$2\sigma_{(mean)}$	$^{207}Pb/^{204}Pb$	$2\sigma_{(mean)}$	$^{206}Pb/^{204}Pb$	$2\sigma_{(mean)}$	$^{207}Pb/^{206}Pb$	$2\sigma_{(mean)}$	$^{208}Pb/^{206}Pb$	$2\sigma_{(mean)}$
Feldspar	36.62	0.19	15.28	0.12	16.92	0.17	0.903	0.011	2.16	0.018
Feldspar	36.51	0.14	15.34	0.04	16.75	0.09	0.914	0.004	2.18	0.007
Feldspar	36.54	0.24	15.42	0.13	16.64	0.17	0.928	0.008	2.20	0.014
Feldspar	36.33	0.16	15.31	0.07	16.56	0.13	0.923	0.004	2.19	0.010
Feldspar	36.54	0.11	15.35	0.07	16.70	0.10	0.919	0.005	2.19	0.008
Feldspar	36.74	0.22	15.25	0.12	16.76	0.11	0.908	0.006	2.19	0.012
Average	36.55		15.33		16.72		0.916		2.185	
$2\sigma_{mean}$	0.11		0.05		0.10		0.008		0.011	
%	0.3%		0.3%		0.6%		0.8%		0.5%	

Sample: Labait LB04-38

Mineral	$^{208}Pb/^{204}Pb$	$2\sigma_{(mean)}$	$^{207}Pb/^{204}Pb$	$2\sigma_{(mean)}$	$^{206}Pb/^{204}Pb$	$2\sigma_{(mean)}$	$^{207}Pb/^{206}Pb$	$2\sigma_{(mean)}$	$^{208}Pb/^{206}Pb$	
Feldspar	33.64	0.22	14.85	0.11	13.78	0.11	1.077	0.002	2.442	0.004
Feldspar	33.65	0.12	14.84	0.05	13.76	0.04	1.079	0.002	2.445	0.004
Feldspar	33.59	0.12	14.82	0.05	13.70	0.04	1.083	0.001	2.453	0.003
Feldspar	33.61	0.09	14.81	0.03	13.73	0.03	1.079	0.002	2.450	0.003
Feldspar	33.49	0.14	14.76	0.06	13.69	0.06	1.078	0.001	2.449	0.002
Feldspar	33.45	0.11	14.75	0.05	13.64	0.04	1.082	0.001	2.453	0.003
Feldspar	33.41	0.13	14.74	0.07	13.64	0.05	1.080	0.002	2.450	0.003
Feldspar	33.52	0.09	14.80	0.04	13.71	0.03	1.079	0.001	2.448	0.003
Feldspar	33.73	0.13	14.83	0.07	13.78	0.06	1.078	0.002	2.448	0.004
Feldspar	33.67	0.08	14.84	0.04	13.77	0.04	1.080	0.001	2.449	0.003
Feldspar	33.65	0.16	14.79	0.06	13.77	0.06	1.074	0.001	2.444	0.002
Feldspar	33.69	0.07	14.83	0.04	13.77	0.04	1.076	0.001	2.445	0.003
Feldspar	33.58	0.06	14.80	0.02	13.70	0.02	1.080	0.002	2.452	0.004
Feldspar	33.54	0.15	14.78	0.07	13.69	0.06	1.080	0.001	2.450	0.002
Feldspar	33.57	0.09	14.78	0.05	13.70	0.03	1.079	0.001	2.451	0.004
Feldspar	33.61	0.09	14.77	0.04	13.71	0.03	1.077	0.001	2.448	0.002
Average	33.59		14.80		13.72		1.079		2.449	
$2\sigma_{mean}$	0.04		0.02		0.02		0.001		0.002	
%	0.1%		0.1%		0.2%		0.1%		0.1%	

Sample: Labait LB04-39

Mineral	$^{208}Pb/^{204}Pb$	$2\sigma_{(mean)}$	$^{207}Pb/^{204}Pb$	$2\sigma_{(mean)}$	$^{206}Pb/^{204}Pb$	$2\sigma_{(mean)}$	$^{207}Pb/^{206}Pb$	$2\sigma_{(mean)}$	$^{208}Pb/^{206}Pb$	$2\sigma_{(mean)}$
Feldspar	33.9	0.4	14.96	0.11	14.39	0.18	1.035	0.009	2.350	0.011
Feldspar	33.7	0.2	14.96	0.09	14.33	0.07	1.045	0.002	2.357	0.003
Feldspar	33.8	0.2	15.02	0.11	14.35	0.11	1.046	0.002	2.358	0.003
Feldspar Average	33.8		14.98		14.36		1.042		2.355	
$2\sigma_{mean}$	0.12		0.04		0.04		0.007		0.005	
%	0.3%		0.3%		0.3%		0.7%		0.2%	

Sample: Labait LB04-43

Mineral	$^{208}Pb/^{204}Pb$	$2\sigma_{(mean)}$	$^{207}Pb/^{204}Pb$	$2\sigma_{(mean)}$	$^{206}Pb/^{204}Pb$	$2\sigma_{(mean)}$	$^{207}Pb/^{206}Pb$	$2\sigma_{(mean)}$	$^{208}Pb/^{206}Pb$	$2\sigma_{(mean)}$
Feldspar	33.63	0.23	14.77	0.10	13.81	0.10	1.070	0.002	2.434	0.003
Feldspar	33.81	0.23	14.83	0.10	13.86	0.10	1.068	0.002	2.435	0.003
Feldspar	33.76	0.09	14.78	0.05	13.87	0.05	1.065	0.002	2.433	0.003
Feldspar	33.69	0.12	14.79	0.05	13.81	0.05	1.069	0.002	2.436	0.004
Feldspar	33.72	0.12	14.79	0.05	13.82	0.05	1.069	0.001	2.439	0.003
Feldspar	33.61	0.20	14.75	0.09	13.77	0.08	1.072	0.002	2.442	0.003
Ilmenite	34.90	0.34	15.14	0.17	14.93	0.27	1.00	0.01	2.34	0.02
Feldspar Average	33.70		14.79		13.83		1.069		2.437	
$2\sigma_{mean}$	0.06		0.02		0.03		0.002		0.003	
%	0.2%		0.2%		0.2%		0.2%		0.1%	

Sample: Labait LB04-48

Sample	$^{208}Pb/^{204}Pb$	$2\sigma_{(mean)}$	$^{207}Pb/^{204}Pb$	$2\sigma_{(mean)}$	$^{206}Pb/^{204}Pb$	$2\sigma_{(mean)}$	$^{207}Pb/^{206}Pb$	$2\sigma_{(mean)}$	$^{208}Pb/^{206}Pb$	$2\sigma_{(mean)}$
Feldspar	33.4	0.3	14.61	0.12	13.47	0.13	1.083	0.005	2.463	0.010
Feldspar	33.3	0.1	14.63	0.06	13.63	0.08	1.075	0.005	2.437	0.008
Feldspar	33.5	0.1	14.66	0.08	13.52	0.08	1.084	0.004	2.477	0.009
Feldspar	33.2	0.1	14.66	0.06	13.52	0.05	1.083	0.004	2.454	0.006
Feldspar	33.3	0.1	14.61	0.09	13.61	0.06	1.088	0.004	2.444	0.010
Feldspar	33.4	0.1	14.67	0.06	13.52	0.06	1.084	0.005	2.469	0.010
Feldspar	33.3	0.1	14.69	0.09	13.53	0.07	1.086	0.007	2.459	0.012
Feldspar	33.4	0.1	14.66	0.07	13.55	0.05	1.084	0.004	2.465	0.005
Feldspar	33.4	0.1	14.64	0.06	13.54	0.07	1.081	0.003	2.460	0.005
Feldspar	33.3	0.2	14.62	0.18	13.60	0.11	1.077	0.004	2.452	0.008
Feldspar	33.4	0.2	14.71	0.07	13.76	0.06	1.072	0.003	2.431	0.005
Average Feldspar	33.3		14.65		13.57		1.081		2.456	
$2\sigma_{mean}$	0.06		0.03		0.08		0.004		0.011	
%	0.2%		0.2%		0.6%		0.4%		0.5%	

Sample: Labait LB04-50

Sample	$^{208}Pb/^{204}Pb$	$2\sigma_{(mean)}$	$^{207}Pb/^{204}Pb$	$2\sigma_{(mean)}$	$^{206}Pb/^{204}Pb$	$2\sigma_{(mean)}$	$^{207}Pb/^{206}Pb$	$2\sigma_{(mean)}$	$^{208}Pb/^{206}Pb$	$2\sigma_{(mean)}$
Feldspar-1	34.4	0.3	14.94	0.12	14.45	0.18	1.027	0.010	2.453	0.013
Feldspar-1	34.1	0.2	14.83	0.07	14.17	0.10	1.044	0.005	2.402	0.007
Feldspar-1	34.7	0.3	14.98	0.09	14.69	0.15	1.017	0.005	2.362	0.007
Feldspar-1	35.7	0.3	15.10	0.06	15.56	0.20	0.965	0.012	2.285	0.020
Feldspar-1	36.2	0.5	15.26	0.18	16.01	0.26	0.948	0.011	2.261	0.016
Feldspar-1	35.4	0.3	15.05	0.13	15.23	0.22	0.985	0.011	2.315	0.016
Feldspar-1	34.6	0.3	14.98	0.08	14.51	0.14	1.034	0.005	2.385	0.008
Feldspar-1	35.5	0.3	15.17	0.13	15.39	0.12	0.984	0.003	2.316	0.004
Feldspar-2	35.3	0.4	15.06	0.11	15.27	0.20	0.982	0.009	2.306	0.013
Feldspar-2	34.0	0.2	14.84	0.09	14.15	0.11	1.049	0.003	2.406	0.005
Feldspar-2	34.7	0.2	14.95	0.07	14.67	0.08	1.020	0.002	2.367	0.004
Feldspar-2	36.3	0.2	15.13	0.10	16.15	0.10	0.937	0.004	2.246	0.006
Feldspar-2	34.4	0.2	14.90	0.07	14.45	0.10	1.030	0.005	2.381	0.008
Feldspar-2	34.9	0.3	14.98	0.14	14.75	0.18	1.019	0.006	2.365	0.009
Feldspar-2	35.1	0.3	15.04	0.11	14.97	0.16	1.006	0.007	2.349	0.011
Feldspar-2	34.8	0.2	14.99	0.08	15.09	0.08	1.018	0.005	2.366	0.007
Feldspar-1 Average	35.1		15.0		15.0		1.00		2.35	
$2\sigma_{mean}$	0.5		0.1		0.5		0.02		0.05	
%	4%		4%		4%		4%		4%	
Feldspar-2 Average	35.0		15.0		14.9		1.01		2.35	
$2\sigma_{mean}$	0.5		0.1		0.4		0.02		0.04	
%	4%		4%		4%		4%		4%	

Sample: Labait LB04-65

Mineral	$^{208}Pb/^{204}Pb$	$2\sigma_{(mean)}$	$^{207}Pb/^{204}Pb$	$2\sigma_{(mean)}$	$^{206}Pb/^{204}Pb$	$2\sigma_{(mean)}$	$^{207}Pb/^{206}Pb$	$2\sigma_{(mean)}$	$^{208}Pb/^{206}Pb$	$2\sigma_{(mean)}$
Feldspar-1	33.6	0.1	14.72	0.04	13.80	0.04	1.067	0.003	2.434	0.005
Apatite-1	34.9	0.2	14.92	0.08	15.08	0.15	0.989	0.009	2.319	0.013
Feldspar-2	33.7	0.3	14.69	0.15	13.88	0.13	1.059	0.003	2.419	0.006
Apatite-2	34.7	0.4	14.89	0.17	14.89	0.17	1.004	0.006	2.340	0.009
Feldspar-3	33.8	0.1	14.78	0.04	13.93	0.05	1.062	0.002	2.424	0.004
Feldspar-3	33.8	0.1	14.73	0.04	13.92	0.07	1.057	0.006	2.422	0.009
Feldspar Average	33.7		14.73		13.88		1.061		2.42	
$2\sigma_{mean}$	0.09		0.04		0.06		0.004		0.006	
%	0.3%		0.3%		0.4%		0.4%		0.3%	
Apatite Average	34.8		14.90		15.0		1.00		2.33	
$2\sigma_{mean}$	0.2		0.03		0.19		0.01		0.02	
%	0.7%		0.2%		1.3%		1.5%		0.9%	

Sample: Labait LB04-82

Mineral	$^{208}Pb/^{204}Pb$	$2\sigma_{(mean)}$	$^{207}Pb/^{204}Pb$	$2\sigma_{(mean)}$	$^{206}Pb/^{204}Pb$	$2\sigma_{(mean)}$	$^{207}Pb/^{206}Pb$	$2\sigma_{(mean)}$	$^{208}Pb/^{206}Pb$	$2\sigma_{(mean)}$
Pyroxene	56.33	1.72	15.88	0.23	20.16	0.28	0.785	0.014	2.799	0.099
Feldspar	34.66	0.12	15.01	0.05	14.69	0.06	1.020	0.002	2.356	0.004
Feldspar	34.53	0.11	15.02	0.05	14.70	0.07	1.021	0.003	2.345	0.008
Feldspar	34.10	0.10	14.96	0.05	14.49	0.09	1.035	0.005	2.358	0.011
Feldspar	34.14	0.12	14.93	0.05	14.51	0.10	1.030	0.006	2.359	0.012
Feldspar	34.65	0.22	15.07	0.08	14.68	0.15	1.026	0.008	2.366	0.014
Felspar 2	34.67	0.10	15.06	0.04	14.50	0.09	1.037	0.005	2.388	0.010
Felspar 2	34.83	0.24	15.26	0.09	15.87	0.19	0.960	0.009	2.205	0.022
Felspar 2	35.02	0.21	15.18	0.10	15.18	0.10	0.995	0.005	2.305	0.008
Felspar 2	34.88	0.24	15.21	0.08	15.16	0.07	0.991	0.003	2.300	0.01
Feldspar Average	34.6		15.08		14.86		1.01		2.33	
$2\sigma_{mean}$	0.2		0.08		0.31		0.02		0.04	
%	1%		1%		2%		2%		2%	

Sample: Labait LB04-82

Mineral	$^{208}Pb/^{204}Pb$	$2\sigma_{(mean)}$	$^{207}Pb/^{204}Pb$	$2\sigma_{(mean)}$	$^{206}Pb/^{204}Pb$	$2\sigma_{(mean)}$	$^{207}Pb/^{206}Pb$	$2\sigma_{(mean)}$	$^{208}Pb/^{206}Pb$	$2\sigma_{(mean)}$
Grain 1-Plag	33.86	0.24	15.03	0.10	14.49	0.10	1.037	0.003	2.344	0.008
Grain 1-Plag	33.76	0.15	14.94	0.07	14.23	0.07	1.049	0.003	2.369	0.006
Grain 1-Plag	33.74	0.17	14.95	0.08	14.28	0.11	1.050	0.004	2.372	0.010
Grain 1-Plag	33.81	0.15	14.98	0.07	14.30	0.12	1.046	0.006	2.361	0.014
Grain 1-Kspar	34.19	0.25	15.22	0.09	15.54	0.18	0.983	0.011	2.216	0.024
Grain 1-Apatite	36.76	0.58	16.40	0.26	22.17	0.88	0.741	0.020	1.662	0.045
Grain 1-Apatite	35.52	0.12	15.97	0.53	19.48	1.22	0.831	0.042	1.851	0.099
Grain 2-Plag	34.05	0.09	14.99	0.03	14.23	0.07	1.053	0.004	2.391	0.006
Grain 2-Plag	34.10	0.18	15.00	0.07	14.52	0.11	1.032	0.003	2.345	0.007
Grain 2-Plag	34.45	0.18	15.09	0.06	14.92	0.18	1.008	0.011	2.307	0.024
Grain 2-Kspar	34.71	0.10	15.21	0.04	15.55	0.16	0.977	0.008	2.236	0.015
Grain 2-Apatite	39.48	0.20	17.25	0.09	27.13	0.26	0.635	0.004	1.454	0.008
Grain 1-Plag Average	33.79		14.98		14.32		1.045		2.362	
$2\sigma_{mean}$	0.06		0.04		0.11		0.006		0.012	
%	0.2%		0.3%		0.8%		0.6%		0.5%	
Grain 2-Plag Average	34.2		15.03		14.55		1.03		2.35	
$2\sigma_{(mean)}$	0.3		0.06		0.40		0.03		0.05	
%	1%		0%		3%		2%		2%	

Sample: Labait LB04-91

Mineral	$^{208}Pb/^{204}Pb$	$2\sigma_{(mean)}$	$^{207}Pb/^{204}Pb$	$2\sigma_{(mean)}$	$^{206}Pb/^{204}Pb$	$2\sigma_{(mean)}$	$^{207}Pb/^{206}Pb$	$2\sigma_{(mean)}$	$^{208}Pb/^{206}Pb$	$2\sigma_{(mean)}$
Grain 1 Feldspar	34.2	0.2	14.89	0.06	14.36	0.11	1.034	0.007	2.383	0.009
Grain 1 Feldspar	35.5	0.1	15.16	0.05	15.45	0.08	0.977	0.003	2.302	0.005
Grain 1 Feldspar	35.1	0.2	15.11	0.07	15.04	0.07	1.002	0.002	2.336	0.004
Grain 1 Feldspar	35.6	0.2	15.14	0.05	15.51	0.15	0.974	0.007	2.299	0.010
Grain 1 Feldspar	35.6	0.3	15.11	0.11	15.56	0.18	0.966	0.007	2.287	0.010
Grain 1 Feldspar	36.3	0.2	15.24	0.08	16.08	0.18	0.944	0.008	2.256	0.011
Grain 1 Feldspar	34.9	0.3	15.10	0.10	14.87	0.14	1.013	0.007	2.353	0.010
Grain 1 Feldspar	33.9	0.1	14.88	0.02	14.03	0.03	1.060	0.002	2.414	0.003
Grain 1 Feldspar	34.0	0.1	14.88	0.04	14.09	0.05	1.056	0.002	2.414	0.003
Grain 1 Feldspar	34.4	0.2	14.94	0.08	14.58	0.10	1.029	0.005	2.369	0.008
Grain 1 Feldspar	37.4	0.2	15.35	0.09	17.10	0.15	0.898	0.006	2.188	0.011
Grain 1 Feldspar	34.4	0.2	14.94	0.08	14.58	0.10	1.029	0.005	2.369	0.008
Grain 1 Feldspar	37.4	0.2	15.35	0.09	17.10	0.15	0.898	0.006	2.188	0.011
Grain 2 Feldspar	37.8	0.4	15.38	0.15	17.45	0.25	0.876	0.007	2.160	0.011
Grain 2 Feldspar	35.5	0.1	15.22	0.05	15.25	0.05	0.994	0.004	2.327	0.006
Grain 2 Feldspar	36.6	0.4	15.26	0.06	16.52	0.03	0.920	0.001	2.223	0.020
Grain 2 Feldspar	35.0	0.1	15.07	0.05	14.94	0.07	1.004	0.002	2.342	0.004
Grain 2 Feldspar	35.0	0.2	14.99	0.09	15.08	0.09	0.990	0.005	2.319	0.009
Grain 2 Feldspar	36.6	0.2	15.29	0.06	16.28	0.16	0.935	0.008	2.244	0.011
Grain 2 Feldspar	34.9	0.2	15.07	0.05	14.74	0.10	1.021	0.005	2.366	0.008
Grain 2 Feldspar	36.1	0.3	15.19	0.10	15.88	0.15	0.956	0.006	2.271	0.009
Grain 2 Feldspar	34.0	0.1	14.87	0.07	14.12	0.06	1.055	0.002	2.410	0.004
Grain 2 Feldspar	34.8	0.2	14.96	0.08	14.97	0.10	1.004	0.004	2.334	0.004
Grain 2 Feldspar	36.7	0.1	15.19	0.06	16.54	0.10	0.917	0.004	2.216	0.006
Grain 2 Feldspar	34.5	0.2	14.94	0.06	14.52	0.13	1.031	0.008	2.379	0.011
Grain 2 Feldspar	35.1	0.1	15.05	0.04	15.05	0.06	1.001	0.002	2.337	0.003
Grain 2 Feldspar	35.6	0.1	15.09	0.05	15.50	0.10	0.975	0.005	2.297	0.006
Grain 1 Average	35.3		15.1		15.3		0.99		2.32	
$2\sigma_{mean}$	0.7		0.09		0.6		0.03		0.04	
%	2%		1%		4%		3%		2%	
Grain 2 Average	35.6		15.1		15.5		0.98		2.30	
$2\sigma_{mean}$	0.5		0.1		0.5		0.03		0.04	
%	2%		1%		3%		3%		2%	

Sample: Laboir Serritt LS06-2

Mineral	$^{208}Pb/^{204}Pb$	$2\sigma_{(mean)}$	$^{207}Pb/^{204}Pb$	$2\sigma_{(mean)}$	$^{206}Pb/^{204}Pb$	$2\sigma_{(mean)}$	$^{207}Pb/^{206}Pb$	$2\sigma_{(mean)}$	$^{208}Pb/^{206}Pb$	$2\sigma_{(mean)}$
Feldspar	37.41	0.11	15.62	0.07	18.10	0.10	0.86	0.00	2.07	0.01
Feldspar	37.31	0.22	15.63	0.10	17.95	0.11	0.87	0.00	2.08	0.01
Feldspar	37.40	0.15	15.52	0.08	17.90	0.09	0.87	0.00	2.09	0.01
Feldspar	37.02	0.13	15.46	0.06	17.84	0.89	0.86	0.00	2.01	0.10
Feldspar	37.16	0.15	15.42	0.08	17.76	0.09	0.87	0.00	2.09	0.01
Feldspar	37.48	0.21	15.57	0.09	18.10	0.12	0.86	0.00	2.07	0.01
Feldspar	37.32	0.16	15.60	0.10	17.91	0.09	0.87	0.00	2.09	0.00
Feldspar	37.26	0.24	15.61	0.14	17.85	0.14	0.88	0.00	2.09	0.00
Feldspar	37.37	0.22	15.50	0.10	17.95	0.11	0.87	0.00	2.09	0.00
Feldspar	37.34	0.40	15.65	0.21	17.91	0.24	0.88	0.01	2.09	0.01
Feldspar Average	37.31		15.56		17.93		0.868		2.08	
$2\sigma_{mean}$	0.08		0.05		0.07		0.003		0.02	
%	0.2%		0.3%		0.4%		0.4%		0.7%	

Sample: Laboir Serrit LS06-12

Sample	$^{208}Pb/^{204}Pb$	$2\sigma_{(mean)}$	$^{207}Pb/^{204}Pb$	$2\sigma_{(mean)}$	$^{206}Pb/^{204}Pb$	$2\sigma_{(mean)}$	$^{207}Pb/^{206}Pb$	$2\sigma_{(mean)}$	$^{208}Pb/^{206}Pb$	$2\sigma_{(mean)}$
Feldspar	37.17	0.24	15.51	0.14	17.84	0.17	0.87	0.01	2.08	0.01
Feldspar	37.21	0.10	15.51	0.06	17.96	0.06	0.87	0.00	2.07	0.01
Feldspar	37.38	0.10	15.55	0.05	18.00	0.07	0.87	0.00	2.08	0.01
Feldspar	37.12	0.08	15.45	0.07	17.86	0.05	0.86	0.00	2.08	0.01
Feldspar	37.45	0.42	15.58	0.24	17.89	0.21	0.87	0.01	2.09	0.01
Feldspar	37.11	0.30	15.40	0.13	17.82	0.14	0.87	0.00	2.08	0.01
Feldspar	37.67	0.20	15.76	0.13	18.15	0.14	0.86	0.01	2.08	0.01
Feldspar	37.04	0.18	15.42	0.10	17.78	0.10	0.86	0.00	2.08	0.01
Feldspar Average	37.27		15.52		17.91		0.865		2.081	
$2\sigma_{mean}$	0.15		0.08		0.08		0.004		0.004	
%	0%		1%		0%		0%		0%	

Sample: Lashaine LS-17

Mineral	$^{208}Pb/^{204}Pb$	$2\sigma_{(mean)}$	$^{207}Pb/^{204}Pb$	$2\sigma_{(mean)}$	$^{206}Pb/^{204}Pb$	$2\sigma_{(mean)}$	$^{207}Pb/^{206}Pb$	$2\sigma_{(mean)}$	$^{208}Pb/^{206}Pb$	$2\sigma_{(mean)}$
Feldspar	35.09	0.30	15.28	0.16	15.22	0.18	1.005	0.010	2.318	0.022
Feldspar	35.47	0.30	15.36	0.20	15.40	0.17	1.000	0.009	2.298	0.019
Feldspar	35.76	0.35	15.28	0.13	15.38	0.12	0.991	0.010	2.320	0.013
Feldspar	35.65	0.46	15.28	0.12	15.65	0.39	0.973	0.017	2.260	0.034
Feldspar	35.49	0.24	15.43	0.14	15.34	0.12	1.009	0.006	2.318	0.010
Feldspar	35.25	0.22	15.36	0.13	15.30	0.12	1.010	0.006	2.212	0.009
Feldspar	35.65	0.22	15.51	0.12	15.37	0.10	1.005	0.006	2.309	0.013
Feldspar	35.34	0.17	15.37	0.12	15.27	0.10	1.004	0.006	2.321	0.012
Feldspar Average	35.5		15.36		15.37		1.000		2.29	
$2\sigma_{mean}$	0.2		0.06		0.09		0.009		0.03	
%	0%		0.4%		0.6%		1%		1%	

Sample: Lashaine LS04-01

Mineral	$^{208}Pb/^{204}Pb$	$2\sigma_{(mean)}$	$^{207}Pb/^{204}Pb$	$2\sigma_{(mean)}$	$^{206}Pb/^{204}Pb$	$2\sigma_{(mean)}$	$^{207}Pb/^{206}Pb$	$2\sigma_{(mean)}$	$^{208}Pb/^{206}Pb$	$2\sigma_{(mean)}$
Feldspar	35.50	0.17	15.30	0.10	15.35	0.08	0.997	0.004	2.309	0.008
Feldspar	35.21	0.22	15.25	0.11	15.30	0.11	0.998	0.005	2.310	0.010
Feldspar	35.51	0.29	15.27	0.13	15.31	0.12	0.999	0.006	2.320	0.010
Feldspar	35.51	0.20	15.24	0.09	15.33	0.09	1.001	0.005	2.324	0.008
Feldspar	35.35	0.22	15.31	0.08	15.30	0.11	1.002	0.005	2.311	0.011
Feldspar	35.40	0.17	15.25	0.11	15.29	0.11	0.996	0.004	2.314	0.010
Feldspar	35.28	0.18	15.16	0.10	15.28	0.10	0.993	0.005	2.315	0.012
Feldspar	35.55	0.22	15.29	0.09	15.38	0.09	1.002	0.044	2.318	0.010
Feldspar Average	35.4		15.26		15.32		0.999		2.315	
$2\sigma_{mean}$	0.1		0.03		0.02		0.002		0.004	
%	0.2%		0.2%		0.2%		0.2%		0.2%	

Sample: Lashaine LS04-02

Mineral	$^{208}Pb/^{204}Pb$	$2\sigma_{(mean)}$	$^{207}Pb/^{204}Pb$	$2\sigma_{(mean)}$	$^{206}Pb/^{204}Pb$	$2\sigma_{(mean)}$	$^{207}Pb/^{206}Pb$	$2\sigma_{(mean)}$	$^{208}Pb/^{206}Pb$	$2\sigma_{(mean)}$
Feldspar	36.2	0.2	15.40	0.08	16.08	0.11	0.951	0.006	2.252	0.008
Feldspar	36.4	0.1	15.43	0.06	16.02	0.07	0.963	0.005	2.271	0.007
Feldspar	36.2	0.2	15.42	0.09	15.85	0.08	0.973	0.003	2.283	0.007
Feldspar	36.1	0.1	15.36	0.08	15.85	0.08	0.967	0.004	2.270	0.006
Feldspar	35.7	0.1	15.29	0.07	15.63	0.10	0.977	0.004	2.294	0.009
Feldspar	35.9	0.1	15.32	0.07	15.60	0.09	0.982	0.007	2.307	0.011
Feldspar	35.7	0.2	15.31	0.13	15.68	0.13	0.975	0.009	2.276	0.015
Feldspar Average	36.0		15.4		15.8		0.97		2.28	
$2\sigma_{mean}$	0.2		0.04		0.14		0.01		0.01	
%	1%		0%		1%		1%		1%	

Sample: Lashaine LS04-08

Mineral	$^{208}Pb/^{204}Pb$	$2\sigma_{(mean)}$	$^{207}Pb/^{204}Pb$	$2\sigma_{(mean)}$	$^{206}Pb/^{204}Pb$	$2\sigma_{(mean)}$	$^{207}Pb/^{206}Pb$	$2\sigma_{(mean)}$	$^{208}Pb/^{206}Pb$	$2\sigma_{(mean)}$
Feldspar	35.13	0.11	15.18	0.07	15.22	0.07	1.001	0.002	2.310	0.006
Feldspar	35.36	0.12	15.21	0.06	15.49	0.09	0.982	0.005	2.284	0.008
Feldspar	35.05	0.18	15.16	0.09	15.10	0.07	1.000	0.003	2.318	0.008
Feldspar	35.10	0.18	15.15	0.09	15.24	0.10	0.993	0.004	2.305	0.008
Feldspar	34.77	0.14	15.02	0.05	15.03	0.09	0.998	0.006	2.311	0.008
Feldspar	35.17	0.16	15.18	0.06	15.30	0.09	0.993	0.005	2.298	0.010
Feldspar	35.40	0.37	15.16	0.16	15.61	0.22	0.974	0.008	2.266	0.012
Feldspar	35.57	0.24	15.28	0.08	15.68	0.18	0.976	0.008	2.265	0.012
Feldspar Average	35.2		15.2		15.3		0.990		2.29	
$2\sigma_{mean}$	0.2		0.1		0.2		0.008		0.01	
%	0%		0%		1%		1%		1%	

Sample: Lashaine LS04-10

Mineral	$^{208}Pb/^{204}Pb$	$2\sigma_{(mean)}$	$^{207}Pb/^{204}Pb$	$2\sigma_{(mean)}$	$^{206}Pb/^{204}Pb$	$2\sigma_{(mean)}$	$^{207}Pb/^{206}Pb$	$2\sigma_{(mean)}$	$^{208}Pb/^{206}Pb$	$2\sigma_{(mean)}$
Feldspar	34.61	0.27	15.21	0.17	14.94	0.18	1.01	0.01	2.32	0.03
Feldspar	35.50	0.20	15.08	0.16	15.52	0.15	0.98	0.01	2.28	0.02
Feldspar	34.83	0.40	15.05	0.31	14.96	0.28	1.00	0.02	2.32	0.04
Feldspar	35.31	0.34	15.25	0.24	15.18	0.18	1.01	0.02	2.31	0.02
Feldspar	35.35	0.17	15.21	0.10	15.21	0.09	1.00	0.01	2.33	0.01
Feldspar	35.40	0.20	15.01	0.13	15.42	0.16	0.97	0.02	2.29	0.02
Feldspar	34.70	0.32	14.97	0.17	15.07	0.22	0.99	0.01	2.30	0.03
Feldspar	35.25	0.22	15.02	0.14	15.27	0.15	0.98	0.01	2.30	0.03
Feldspar Average	35.1		15.10		15.20		0.99		2.31	
$2\sigma_{mean}$	0.2		0.08		0.15		0.01		0.01	
%	1%		0.5%		1%		1%		0%	

Sample: Lashaine 89-726

Mineral	$^{208}Pb/^{204}Pb$	$2\sigma_{(mean)}$	$^{207}Pb/^{204}Pb$	$2\sigma_{(mean)}$	$^{206}Pb/^{204}Pb$	$2\sigma_{(mean)}$	$^{207}Pb/^{206}Pb$	$2\sigma_{(mean)}$	$^{208}Pb/^{206}Pb$	$2\sigma_{(mean)}$
Feldspar	35.26	0.35	15.20	0.20	15.82	0.16	0.97	0.01	2.24	0.02
Feldspar	35.89	0.30	15.36	0.20	15.95	0.21	0.97	0.01	2.26	0.02
Feldspar	35.65	0.25	15.28	0.17	16.14	0.17	0.95	0.01	2.23	0.02
Feldspar	35.46	0.29	15.18	0.14	15.91	0.19	0.96	0.01	2.23	0.01
Feldspar	36.27	0.34	15.19	0.24	15.74	0.21	0.97	0.01	2.30	0.02
Feldspar	35.66	0.25	15.12	0.14	15.61	0.21	0.98	0.01	2.28	0.02
Feldspar	36.34	0.54	15.51	0.45	16.10	0.47	0.96	0.02	2.26	0.05
Feldspar	36.37	0.49	15.52	0.31	15.79	0.21	0.98	0.02	2.32	0.04
Feldspar	35.90	0.41	15.31	0.17	16.06	0.28	0.96	0.01	2.25	0.03
Feldspar Average	35.87		15.30		15.90		0.97		2.26	
$2\sigma_{mean}$	0.26		0.10		0.12		0.01		0.02	
%	0.7%		0.6%		0.7%		0.6%		0.9%	

Sample: Lashaine 89-727

Sample	$^{208}Pb/^{204}Pb$	$2\sigma_{(mean)}$	$^{207}Pb/^{204}Pb$	$2\sigma_{(mean)}$	$^{206}Pb/^{204}Pb$	$2\sigma_{(mean)}$	$^{207}Pb/^{206}Pb$	$2\sigma_{(mean)}$	$^{208}Pb/^{206}Pb$	$2\sigma_{(mean)}$
Feldspar	36.59	0.28	15.26	0.21	16.58	0.17	0.92	0.01	2.21	0.02
Feldspar	36.80	0.22	15.57	0.15	16.62	0.14	0.94	0.01	2.22	0.02
Feldspar	36.22	0.31	15.31	0.31	16.73	0.24	0.91	0.02	2.16	0.03
Feldspar	36.47	0.28	15.11	0.23	16.43	0.21	0.92	0.01	2.22	0.03
Feldspar	36.35	0.28	15.38	0.23	16.72	0.16	0.91	0.01	2.18	0.03
Feldspar	36.52	0.27	15.29	0.24	16.82	0.19	0.91	0.02	2.18	0.03
Feldspar	36.63	0.26	15.44	0.14	16.39	0.19	0.94	0.01	2.24	0.02
Feldspar	36.82	0.22	15.44	0.19	16.64	0.17	0.93	0.01	2.21	0.02
Feldspar	36.54	0.22	15.12	0.19	16.54	0.21	0.91	0.01	2.20	0.03
Feldspar	36.41	0.24	15.23	0.16	16.73	0.17	0.91	0.01	2.19	0.02
Feldspar Average	36.54		15.31		16.62		0.921		2.20	
$2\sigma_{mean}$	0.12		0.09		0.09		0.007		0.02	
%	0.3%		0.6%		0.5%		0.8%		0.7%	

Sample: Lashaine 89-732

Mineral	$^{208}Pb/^{204}Pb$	$2\sigma_{(mean)}$	$^{207}Pb/^{204}Pb$	$2\sigma_{(mean)}$	$^{206}Pb/^{204}Pb$	$2\sigma_{(mean)}$	$^{207}Pb/^{206}Pb$	$2\sigma_{(mean)}$	$^{208}Pb/^{206}Pb$	$2\sigma_{(mean)}$
Feldspar	36.70	0.26	15.45	0.12	16.78	0.19	0.92	0.01	2.19	0.01
Feldspar	36.61	0.17	15.12	0.16	16.67	0.13	0.91	0.01	2.19	0.01
Feldspar	36.48	0.28	15.31	0.16	16.74	0.23	0.91	0.01	2.19	0.02
Feldspar	36.41	0.28	15.41	0.14	16.32	0.23	0.94	0.01	2.24	0.03
Feldspar	35.83	0.31	15.21	0.23	16.20	0.18	0.94	0.01	2.21	0.02
Feldspar	36.72	0.28	15.52	0.15	16.74	0.19	0.92	0.01	2.19	0.02
Feldspar	36.96	0.24	15.57	0.21	16.98	0.15	0.92	0.01	2.18	0.02
Feldspar	36.67	0.23	15.39	0.12	16.61	0.16	0.93	0.01	2.20	0.02
Feldspar	37.09	0.17	15.39	0.12	16.84	0.23	0.91	0.01	2.19	0.02
Feldspar	36.33	0.21	15.27	0.17	16.67	0.19	0.92	0.01	2.18	0.01
Feldspar Average	36.58		15.36		16.65		0.92		2.20	
$2\sigma_{mean}$	0.22		0.09		0.15		0.01		0.01	
%	0.6%		0.6%		0.9%		0.7%		0.5%	

Sample: Lashaine 89-733

Mineral	$^{208}Pb/^{204}Pb$	$2\sigma_{(mean)}$	$^{207}Pb/^{204}Pb$	$2\sigma_{(mean)}$	$^{206}Pb/^{204}Pb$	$2\sigma_{(mean)}$	$^{207}Pb/^{206}Pb$	$2\sigma_{(mean)}$	$^{208}Pb/^{206}Pb$	$2\sigma_{(mean)}$
Feldspar	38.75	0.30	16.04	0.12	19.14	0.15	0.84	0.00	2.03	0.00
Feldspar	39.17	0.12	16.00	0.06	19.54	0.06	0.82	0.00	2.00	0.00
Feldspar	38.84	0.26	16.07	0.05	19.49	0.01	0.82	0.00	2.04	0.00
Feldspar	39.04	0.17	16.02	0.06	19.18	0.07	0.84	0.00	2.03	0.00
Feldspar	38.96	0.02	16.02	0.09	19.40	0.18	0.82	0.01	2.00	0.01
Feldspar	39.13	0.21	16.12	0.07	19.51	0.16	0.83	0.00	2.01	0.01
Feldspar	38.91	0.26	16.10	0.10	19.71	0.21	0.81	0.01	1.96	0.03
Feldspar	38.71	0.11	16.02	0.05	19.25	0.07	0.83	0.00	2.01	0.01
Feldspar Avera	38.94		16.05		19.40		0.83		2.01	
$2\sigma_{mean}$	0.12		0.03		0.14		0.01		0.02	
%	0.3%		0.2%		0.7%		0.7%		0.8%	

Sample: Lashaine 89-745

Mineral	$^{208}Pb/^{204}Pb$	$2\sigma_{(mean)}$	$^{207}Pb/^{204}Pb$	$2\sigma_{(mean)}$	$^{206}Pb/^{204}Pb$	$2\sigma_{(mean)}$	$^{207}Pb/^{206}Pb$	$2\sigma_{(mean)}$	$^{208}Pb/^{206}Pb$	$2\sigma_{(mean)}$
Feldspar	38.84	0.32	15.95	0.14	19.28	0.15	0.829	0.004	2.015	0.004
Feldspar	39.08	0.32	15.93	0.13	19.41	0.15	0.821	0.003	2.015	0.002
Feldspar	38.69	0.14	16.02	0.05	19.20	0.09	0.837	0.002	2.020	0.003
Feldspar	38.91	0.46	16.05	0.19	19.23	0.21	0.834	0.002	2.023	0.002
Feldspar	39.36	0.49	16.07	0.19	19.38	0.23	0.827	0.005	2.021	0.011
Feldspar	38.71	0.19	15.91	0.07	19.22	0.12	0.830	0.002	2.017	0.003
Feldspar	38.88	0.25	16.07	0.10	19.26	0.13	0.837	0.001	2.022	0.001
Feldspar	39.13	0.42	15.95	0.10	19.49	0.25	0.817	0.007	2.008	0.006
Feldspar Average	38.95		15.99		19.31		0.829		2.018	
$2\sigma_{mean}$	0.16		0.05		0.07		0.005		0.004	
%	0.4%		0.3%		0.4%		0.6%		0.2%	

Sample: Lashaine 89-762

Mineral	$^{208}Pb/^{204}Pb$	$2\sigma_{(mean)}$	$^{207}Pb/^{204}Pb$	$2\sigma_{(mean)}$	$^{206}Pb/^{204}Pb$	$2\sigma_{(mean)}$	$^{207}Pb/^{206}Pb$	$2\sigma_{(mean)}$	$^{208}Pb/^{206}Pb$	$2\sigma_{(mean)}$
Feldspar	35.9	0.4	15.1	0.2	16.1	0.3	0.945	0.008	2.231	0.017
Feldspar	36.1	0.2	15.2	0.1	15.8	0.1	0.962	0.006	2.276	0.014
Feldspar	36.7	0.2	15.5	0.1	16.7	0.2	0.931	0.012	2.204	0.018
Feldspar	36.0	0.4	15.4	0.1	16.1	0.2	0.948	0.009	2.224	0.012
Feldspar	36.6	0.4	15.4	0.1	16.6	0.3	0.927	0.010	2.207	0.014
Feldspar	36.5	0.3	15.3	0.1	16.5	0.2	0.938	0.006	2.222	0.012
Feldspar	36.6	0.2	15.5	0.1	16.5	0.1	0.937	0.005	2.219	0.009
Feldspar	36.7	0.2	15.4	0.1	16.7	0.2	0.928	0.009	2.204	0.014
Feldspar Average	36.4		15.4		16.4		0.939		2.223	
$2\sigma_{mean}$	0.2		0.1		0.2		0.008		0.017	
%	1%		1%		1%		1%		1%	

Sample: Lemugur LG04-37

Mineral	$^{208}Pb/^{204}Pb$	$2\sigma_{(mean)}$	$^{207}Pb/^{204}Pb$	$2\sigma_{(mean)}$	$^{206}Pb/^{204}Pb$	$2\sigma_{(mean)}$	$^{207}Pb/^{206}Pb$	$2\sigma_{(mean)}$	$^{208}Pb/^{206}Pb$	$2\sigma_{(mean)}$
Feldspar	36.95	0.39	15.37	0.16	15.83	0.17	0.974	0.001	2.334	0.003
Feldspar	36.82	0.15	15.37	0.06	15.85	0.08	0.972	0.002	2.324	0.005
Feldspar	36.90	0.15	15.38	0.06	15.78	0.07	0.972	0.002	2.332	0.002
Feldspar	36.80	0.19	15.39	0.08	15.79	0.08	0.974	0.001	2.333	0.001
Feldspar	36.78	0.08	15.35	0.03	15.76	0.04	0.974	0.002	2.331	0.003
Feldspar	36.67	0.14	15.33	0.06	15.78	0.06	0.973	0.002	2.326	0.003
Feldspar	36.74	0.14	15.29	0.06	15.79	0.06	0.971	0.002	2.330	0.005
Feldspar	36.98	0.60	15.39	0.26	15.90	0.24	0.970	0.002	2.329	0.011
Feldspar	36.50	0.32	15.23	0.13	15.70	0.15	0.963	0.002	2.330	0.003
Feldspar	36.81	0.91	15.12	0.22	15.76	0.45	0.972	0.009	2.339	0.020
Feldspar Average	36.80		15.32		15.80		0.972		2.331	
$2\sigma_{mean}$	0.09		0.05		0.03		0.002		0.003	
%	0.2%		0.4%		0.2%		0.2%		0.1%	

Sample: McBride 85-100

Mineral	$^{208}Pb/^{204}Pb$	$2\sigma_{(mean)}$	$^{207}Pb/^{204}Pb$	$2\sigma_{(mean)}$	$^{206}Pb/^{204}Pb$	$2\sigma_{(mean)}$	$^{207}Pb/^{206}Pb$	$2\sigma_{(mean)}$	$^{208}Pb/^{206}Pb$	$2\sigma_{(mean)}$
Feldspar	38.73	0.17	15.69	0.07	18.46	0.07	0.85	0.00	2.10	0.00
Feldspar	38.80	0.29	15.69	0.10	18.40	0.11	0.85	0.00	2.11	0.00
Feldspar	38.94	0.10	15.70	0.04	18.45	0.05	0.85	0.00	2.11	0.00
Feldspar	38.94	0.13	15.75	0.06	18.49	0.07	0.85	0.00	2.11	0.00
Feldspar	38.97	0.12	15.75	0.05	18.62	0.05	0.85	0.00	2.09	0.00
Average Feldspar	38.87		15.71		18.48		0.850		2.105	
$2\sigma_{mean}$	0.10		0.03		0.07		0.002		0.007	
%	0.2%		0.2%		0.4%		0.2%		0.3%	

Sample: McBride 85-120

Mineral	$^{208}Pb/^{204}Pb$	$2\sigma_{(mean)}$	$^{207}Pb/^{204}Pb$	$2\sigma_{(mean)}$	$^{206}Pb/^{204}Pb$	$2\sigma_{(mean)}$	$^{207}Pb/^{206}Pb$	$2\sigma_{(mean)}$	$^{208}Pb/^{206}Pb$	$2\sigma_{(mean)}$
Feldspar	38.83	0.13	15.71	0.06	18.20	0.07	0.864	0.001	2.133	0.003
Feldspar	38.77	0.16	15.68	0.05	18.10	0.06	0.866	0.002	2.135	0.003
Feldspar	38.70	0.11	15.66	0.05	18.13	0.06	0.864	0.002	2.134	0.002
Feldspar	38.53	0.23	15.53	0.10	18.07	0.10	0.860	0.001	2.130	0.002
Feldspar	38.75	0.17	15.68	0.07	18.09	0.10	0.866	0.002	2.140	0.004
Feldspar	38.85	0.11	15.74	0.06	18.21	0.06	0.864	0.002	2.132	0.003
Average Feldspar	38.74		15.67		18.13		0.864		2.134	
$2\sigma_{mean}$	0.10		0.06		0.05		0.002		0.003	
%	0.2%		0.4%		0.3%		0.2%		0.1%	

Sample: McBride 83-157

Mineral	$^{208}Pb/^{204}Pb$	$2\sigma_{(mean)}$	$^{207}Pb/^{204}Pb$	$2\sigma_{(mean)}$	$^{206}Pb/^{204}Pb$	$2\sigma_{(mean)}$	$^{207}Pb/^{206}Pb$	$2\sigma_{(mean)}$	$^{208}Pb/^{206}Pb$	$2\sigma_{(mean)}$
Feldspar	39.83	0.11	15.65	0.04	18.18	0.06	0.86	0.00	2.19	0.00
Feldspar	39.75	0.23	15.63	0.09	18.11	0.11	0.86	0.00	2.19	0.00
Feldspar	39.92	0.14	15.68	0.06	18.19	0.06	0.86	0.00	2.19	0.00
Feldspar	39.84	0.24	15.71	0.10	18.19	0.10	0.86	0.00	2.19	0.00
Feldspar	39.85	0.14	15.66	0.06	18.18	0.06	0.86	0.00	2.19	0.00
Feldspar	39.61	0.29	15.64	0.10	18.14	0.12	0.86	0.00	2.19	0.00
Feldspar	39.91	0.09	15.68	0.04	18.19	0.04	0.86	0.00	2.19	0.00
Feldspar	39.95	0.27	15.64	0.11	18.18	0.12	0.86	0.00	2.19	0.00
Average Feldspar	39.83		15.66		18.17		0.861		2.192	
$2\sigma_{mean}$	0.22		0.05		0.06		0.002		0.005	
%	0.6%		0.3%		0.3%		0.3%		0.2%	

Sample: McBride 83-160

Mineral	$^{208}Pb/^{204}Pb$	$2\sigma_{(mean)}$	$^{207}Pb/^{204}Pb$	$2\sigma_{(mean)}$	$^{206}Pb/^{204}Pb$	$2\sigma_{(mean)}$	$^{207}Pb/^{206}Pb$	$2\sigma_{(mean)}$	$^{208}Pb/^{206}Pb$	$2\sigma_{(mean)}$
Feldspar	39.10	0.22	15.72	0.09	18.93	0.10	0.830	0.002	2.064	0.003
Feldspar	39.15	0.37	15.79	0.14	18.90	0.17	0.835	0.002	2.069	0.003
Feldspar	38.67	0.13	15.63	0.05	18.63	0.09	0.839	0.002	2.077	0.002
Feldspar	38.88	0.27	15.66	0.09	18.75	0.14	0.837	0.003	2.074	0.003
Average Feldspar	38.95		15.70		18.80		0.835		2.071	
$2\sigma_{(mean)}$	0.22		0.07		0.14		0.004		0.005	
%	0.6%		0.4%		0.7%		0.4%		0.3%	

Sample: McBride 83-162

Mineral	$^{208}Pb/^{204}Pb$	$2\sigma_{(mean)}$	$^{207}Pb/^{204}Pb$	$2\sigma_{(mean)}$	$^{206}Pb/^{204}Pb$	$2\sigma_{(mean)}$	$^{207}Pb/^{206}Pb$	$2\sigma_{(mean)}$	$^{208}Pb/^{206}Pb$	$2\sigma_{(mean)}$
Feldspar	38.53	0.16	15.64	0.06	18.56	0.07	0.8430	0.0003	2.0768	0.0008
Feldspar	38.60	0.14	15.66	0.06	18.58	0.07	0.8433	0.0004	2.0778	0.0008
Feldspar	38.72	0.10	15.70	0.04	18.61	0.06	0.8434	0.0005	2.0785	0.0008
Feldspar	38.84	0.09	15.72	0.03	18.69	0.03	0.8425	0.0003	2.0782	0.0007
Feldspar	38.48	0.23	15.62	0.09	18.51	0.10	0.8439	0.0006	2.0788	0.0009
Feldspar	38.79	0.06	15.73	0.03	18.66	0.03	0.8431	0.0003	2.0792	0.0008
Average Feldspar	38.66		15.68		18.60		0.8432		2.0782	
$2\sigma_{mean}$	0.12		0.04		0.05		0.0004		0.0007	
%	0.3%		0.2%		0.3%		0.05%		0.03%	

Sample: Naboir Soito NS04-05

Mineral	$^{208}Pb/^{204}Pb$	$2\sigma_{(mean)}$	$^{207}Pb/^{204}Pb$	$2\sigma_{(mean)}$	$^{206}Pb/^{204}Pb$	$2\sigma_{(mean)}$	$^{207}Pb/^{206}Pb$	$2\sigma_{(mean)}$	$^{208}Pb/^{206}Pb$	$2\sigma_{(mean)}$
Feldspar	34.31	0.20	15.02	0.07	14.39	0.09	1.045	0.002	2.386	0.002
Feldspar	34.23	0.13	14.97	0.05	14.34	0.06	1.045	0.002	2.386	0.003
Feldspar	34.26	0.10	14.96	0.04	14.41	0.06	1.040	0.003	2.379	0.005
Feldspar	34.43	0.18	14.99	0.07	14.45	0.07	1.035	0.001	2.381	0.002
Feldspar	34.37	0.07	14.96	0.03	14.42	0.04	1.038	0.001	2.385	0.001
Feldspar	34.45	0.15	14.97	0.06	14.54	0.07	1.029	0.002	2.369	0.004
Feldspar Average	34.3		14.98		14.42		1.038		2.381	
$2\sigma_{mean}$	0.07		0.02		0.1		0.005		0.005	
%	0.2%		0.1%		0.4%		0.5%		0.2%	

Sample: Naboir Soito NS04-13

Mineral	$^{208}Pb/^{204}Pb$	$2\sigma_{(mean)}$	$^{207}Pb/^{204}Pb$	$2\sigma_{(mean)}$	$^{206}Pb/^{204}Pb$	$2\sigma_{(mean)}$	$^{207}Pb/^{206}Pb$	$2\sigma_{(mean)}$	$^{208}Pb/^{206}Pb$	$2\sigma_{(mean)}$
Feldspar-Band1	34.34	0.15	15.25	0.06	14.99	0.06	1.02	0.00	2.29	0.00
Feldspar-Band1	34.51	0.14	15.35	0.05	15.07	0.05	1.02	0.00	2.29	0.00
Feldspar-Band1	34.47	0.08	15.32	0.04	15.05	0.04	1.02	0.00	2.29	0.00
Feldspar-Band1	34.54	0.25	15.36	0.11	15.05	0.11	1.02	0.00	2.29	0.00
Feldspar-Band1	34.19	0.18	15.26	0.09	14.98	0.07	1.02	0.00	2.29	0.00
Feldspar-Band1	34.54	0.42	15.38	0.17	15.15	0.18	1.02	0.00	2.28	0.00
Feldspar-Band1	34.52	0.25	15.38	0.10	15.08	0.11	1.02	0.00	2.29	0.00
Feldspar-Band2	34.61	0.05	15.37	0.02	15.45	0.02	0.99	0.00	2.24	0.02
Feldspar-Band2	34.62	0.14	15.46	0.07	15.56	0.06	0.99	0.00	2.22	0.02
Band1 Average	34.44		15.33		15.05		1.018		2.290	
$2\sigma_{mean}$	0.10		0.04		0.04		0.001		0.003	
%	0.29%		0.27%		0.29%		0.10%		0.14%	
Band2 Average	34.61		15.41		15.50		0.993		2.23	
$2\sigma_{mean}$	0.01		0.09		0.11		0.002		0.02	
%	0.02%		0.59%		0.72%		0.20%		0.82%	

Sample: Naboir Soito NS04-43

Mineral	$^{208}Pb/^{204}Pb$	$2\sigma_{(mean)}$	$^{207}Pb/^{204}Pb$	$2\sigma_{(mean)}$	$^{206}Pb/^{204}Pb$	$2\sigma_{(mean)}$	$^{207}Pb/^{206}Pb$	$2\sigma_{(mean)}$	$^{208}Pb/^{206}Pb$	$2\sigma_{(mean)}$
Feldspar	34.71	0.18	15.33	0.08	15.06	0.08	1.018	0.001	2.307	0.001
Feldspar	34.75	0.27	15.34	0.12	15.08	0.13	1.020	0.001	2.309	0.001
Feldspar	34.78	0.11	15.34	0.05	15.04	0.05	1.020	0.001	2.312	0.001
Feldspar	34.63	0.20	15.28	0.09	14.99	0.09	1.019	0.001	2.310	0.001
Feldspar	34.81	0.34	15.35	0.15	15.04	0.15	1.021	0.001	2.315	0.001
Feldspar	34.78	0.08	15.35	0.04	15.02	0.04	1.022	0.000	2.316	0.001
Feldspar	34.72	0.12	15.33	0.05	15.00	0.05	1.022	0.001	2.314	0.002
Feldspar	34.53	0.15	15.22	0.07	14.94	0.06	1.021	0.001	2.311	0.002
Feldspar Average	34.7		15.32		15.02		1.020		2.312	
$2\sigma_{mean}$	0.1		0.03		0.03		0.001		0.002	
%	0.2%		0.2%		0.2%		0.1%		0.1%	

Sample: Naboir Soito NS04-83

Mineral	$^{208}Pb/^{204}Pb$	$2\sigma_{(mean)}$	$^{207}Pb/^{204}Pb$	$2\sigma_{(mean)}$	$^{206}Pb/^{204}Pb$	$2\sigma_{(mean)}$	$^{207}Pb/^{206}Pb$	$2\sigma_{(mean)}$	$^{208}Pb/^{206}Pb$	$2\sigma_{(mean)}$
Feldspar	34.18	0.13	14.84	0.06	14.58	0.05	1.018	0.003	2.343	0.005
Feldspar	34.14	0.24	14.81	0.12	14.53	0.11	1.018	0.003	2.350	0.006
Feldspar	34.14	0.20	14.84	0.08	14.39	0.08	1.031	0.002	2.368	0.005
Feldspar	33.99	0.26	14.80	0.08	14.40	0.11	1.028	0.002	2.358	0.004
Feldspar	34.20	0.14	14.84	0.07	14.51	0.07	1.023	0.002	2.359	0.006
Feldspar	34.39	0.22	14.92	0.11	14.58	0.12	1.021	0.004	2.355	0.004
Feldspar	34.42	0.15	14.98	0.07	14.51	0.07	1.029	0.002	2.368	0.004
Feldspar	34.25	0.13	14.90	0.06	14.57	0.05	1.023	0.003	2.348	0.006
Feldspar Average	34.21		14.87		14.51		1.024		2.356	
$2\sigma_{mean}$	0.10		0.04		0.05		0.004		0.007	
%	0.3%		0.3%		0.4%		0.4%		0.3%	

Sample: Naboir Soito NS04-91

Mineral	$^{208}Pb/^{204}Pb$	$2\sigma_{(mean)}$	$^{207}Pb/^{204}Pb$	$2\sigma_{(mean)}$	$^{206}Pb/^{204}Pb$	$2\sigma_{(mean)}$	$^{207}Pb/^{206}Pb$	$2\sigma_{(mean)}$	$^{208}Pb/^{206}Pb$	$2\sigma_{(mean)}$
Feldspar-Band 1	36.54	0.12	15.23	0.05	15.05	0.05	1.013	0.002	2.443	0.005
Feldspar-Band 1	36.59	0.19	15.25	0.07	14.99	0.08	1.016	0.003	2.442	0.004
Feldspar-Band 1	36.58	0.14	15.28	0.06	15.01	0.08	1.016	0.002	2.435	0.004
Feldspar-Band 1	36.69	0.17	15.25	0.07	15.05	0.07	1.012	0.002	2.437	0.004
Feldspar-Band 1	36.77	0.11	15.31	0.05	15.07	0.06	1.015	0.002	2.439	0.004
Feldspar-Band 1	36.48	0.11	15.30	0.04	14.98	0.05	1.021	0.002	2.435	0.004
Feldspar-Band 2	37.86	0.27	15.29	0.12	15.34	0.11	0.994	0.002	2.464	0.005
Feldspar-Band 2	37.44	0.10	15.30	0.06	15.34	0.04	0.997	0.002	2.442	0.004
Feldspar-Band 2	37.56	0.13	15.32	0.06	15.32	0.06	0.997	0.002	2.448	0.005
Feldspar-Band 2	37.54	0.09	15.26	0.05	15.30	0.04	0.997	0.002	2.456	0.004
Band1 Average	36.6		15.27		15.02		1.016		2.439	
$2\sigma_{mean}$	0.1		0.03		0.03		0.002		0.003	
%	0.2%		0.2%		0.2%		0.2%		0.1%	
Band2 Average	37.6		15.29		15.32		0.996		2.452	
$2\sigma_{mean}$	0.2		0.05		0.04		0.003		0.019	
%	0.5%		0.3%		0.3%		0.3%		0.8%	

Sample: Naboir Soito NS04-94

Mineral	$^{208}Pb/^{204}Pb$	$2\sigma_{(mean)}$	$^{207}Pb/^{204}Pb$	$2\sigma_{(mean)}$	$^{206}Pb/^{204}Pb$	$2\sigma_{(mean)}$	$^{207}Pb/^{206}Pb$	$2\sigma_{(mean)}$	$^{208}Pb/^{206}Pb$	$2\sigma_{(mean)}$
Feldspar	33.86	0.12	14.79	0.05	14.15	0.05	1.046	0.001	2.394	0.003
Feldspar	33.83	0.06	14.85	0.03	14.07	0.03	1.054	0.001	2.404	0.003
Feldspar	33.66	0.20	14.75	0.09	13.96	0.10	1.057	0.003	2.412	0.004
Feldspar	33.65	0.22	14.78	0.09	13.97	0.09	1.058	0.002	2.410	0.004
Feldspar	33.99	0.17	14.90	0.07	14.09	0.09	1.058	0.001	2.412	0.003
Feldspar	34.06	0.09	14.91	0.04	14.19	0.05	1.052	0.002	2.402	0.004
Feldspar	34.27	0.29	15.01	0.10	14.30	0.12	1.048	0.003	2.395	0.003
Feldspar	34.02	0.12	14.88	0.05	14.16	0.06	1.050	0.002	2.401	0.002
Feldspar Average	33.92		14.86		14.11		1.053		2.404	
$2\sigma_{mean}$	0.15		0.06		0.08		0.003		0.005	
%	0.4%		0.4%		0.6%		0.3%		0.2%	

Sample: Naboir Soito NS04-96

Mineral	$^{208}Pb/^{204}Pb$	$2\sigma_{(mean)}$	$^{207}Pb/^{204}Pb$	$2\sigma_{(mean)}$	$^{206}Pb/^{204}Pb$	$2\sigma_{(mean)}$	$^{207}Pb/^{206}Pb$	$2\sigma_{(mean)}$	$^{208}Pb/^{206}Pb$	$2\sigma_{(mean)}$
Feldspar	34.15	0.13	14.87	0.06	14.40	0.06	1.034	0.003	2.372	0.004
Feldspar	34.25	0.15	14.96	0.07	14.41	0.08	1.034	0.002	2.368	0.005
Feldspar	34.20	0.11	14.87	0.04	14.45	0.05	1.031	0.002	2.369	0.003
Feldspar	34.20	0.12	14.96	0.06	14.42	0.06	1.035	0.001	2.371	0.004
Feldspar	33.95	0.07	14.84	0.04	14.42	0.04	1.031	0.002	2.360	0.003
Feldspar	33.86	0.09	14.78	0.04	14.37	0.03	1.028	0.002	2.359	0.003
Feldspar	34.14	0.25	14.86	0.11	14.47	0.10	1.029	0.002	2.362	0.005
Feldspar	33.92	0.08	14.77	0.04	14.23	0.04	1.038	0.002	2.383	0.004
Feldspar	33.92	0.23	14.81	0.10	14.20	0.09	1.042	0.003	2.383	0.005
Feldspar Average	34.066		14.86		14.37		1.033		2.370	
$2\sigma_{mean}$	0.100		0.05		0.06		0.003		0.006	
%	0.3%		0.3%		0.4%		0.3%		0.3%	

Sample: Naboir Soito NS04-98

Mineral	$^{208}Pb/^{204}Pb$	$2\sigma_{(mean)}$	$^{207}Pb/^{204}Pb$	$2\sigma_{(mean)}$	$^{206}Pb/^{204}Pb$	$2\sigma_{(mean)}$	$^{207}Pb/^{206}Pb$	$2\sigma_{(mean)}$	$^{208}Pb/^{206}Pb$	$2\sigma_{(mean)}$
Feldspar	34.39	0.11	15.06	0.05	14.67	0.05	1.028	0.001	2.346	0.002
Feldspar	34.43	0.18	15.12	0.08	14.65	0.08	1.031	0.001	2.347	0.001
Feldspar	34.48	0.20	15.12	0.09	14.69	0.08	1.029	0.001	2.347	0.002
Feldspar	34.50	0.14	15.13	0.06	14.68	0.07	1.030	0.001	2.348	0.002
Feldspar	34.56	0.14	15.14	0.06	14.70	0.06	1.030	0.001	2.351	0.002
Feldspar	34.43	0.11	15.12	0.04	14.72	0.07	1.026	0.003	2.339	0.004
Feldspar Average	34.47		15.11		14.69		1.029		2.346	
$2\sigma_{mean}$	0.05		0.02		0.02		0.001		0.003	
%	0.1%		0.2%		0.1%		0.1%		0.1%	

Sample: Nushan NS204

Mineral	$^{208}Pb/^{204}Pb$	$2\sigma_{(mean)}$	$^{207}Pb/^{204}Pb$	$2\sigma_{(mean)}$	$^{206}Pb/^{204}Pb$	$2\sigma_{(mean)}$	$^{207}Pb/^{206}Pb$	$2\sigma_{(mean)}$	$^{208}Pb/^{206}Pb$	$2\sigma_{(mean)}$
Feldspar	35.50	0.26	15.21	0.15	15.72	0.194	0.968	0.011	2.266	0.022
Feldspar	35.17	0.11	15.20	0.09	15.31	0.078	0.990	0.004	2.299	0.007
Feldspar	35.33	0.33	15.19	0.15	15.38	0.175	0.987	0.005	2.293	0.008
Feldspar	35.51	0.14	15.33	0.07	15.45	0.065	0.990	0.003	2.297	0.004
Feldspar	35.48	0.21	15.26	0.11	15.43	0.113	0.988	0.003	2.297	0.009
Feldspar	35.61	0.15	15.32	0.10	15.53	0.101	0.985	0.002	2.292	0.006
Feldspar	35.28	0.33	15.36	0.14	15.15	0.143	1.016	0.003	2.334	0.007
Feldspar	35.43	0.25	15.43	0.11	15.32	0.131	1.005	0.005	2.316	0.009
Feldspar	35.43	0.23	15.40	0.09	15.24	0.117	1.009	0.003	2.325	0.006
Feldspar	35.21	0.15	15.28	0.07	15.10	0.081	1.013	0.003	2.333	0.005
Feldspar	35.39	0.23	15.34	0.07	15.16	0.099	1.015	0.003	2.335	0.005
Feldspar	35.54	0.23	15.44	0.10	15.24	0.115	1.011	0.003	2.327	0.005
Feldspar	35.35	0.12	15.38	0.07	15.19	0.071	1.015	0.002	2.335	0.005
Feldspar	35.24	0.17	15.27	0.11	15.19	0.111	1.005	0.004	2.318	0.008
Feldspar	35.36	0.19	15.20	0.07	15.40	0.145	0.987	0.006	2.296	0.010
Feldspar	35.65	0.13	15.24	0.06	15.68	0.065	0.971	0.003	2.270	0.007
Feldspar	35.90	0.38	15.31	0.14	16.14	0.229	0.946	0.007	2.225	0.012
Feldspar	35.46	0.16	15.33	0.08	15.40	0.090	0.994	0.004	2.302	0.006
Feldspar	35.65	0.35	15.30	0.12	15.54	0.155	0.986	0.005	2.289	0.008
Feldspar	35.22	0.28	15.25	0.15	15.19	0.134	0.999	0.006	2.302	0.010
Feldspar	35.80	0.17	15.30	0.03	15.80	0.148	0.967	0.009	2.266	0.012
Feldspar	35.43	0.13	15.26	0.06	15.37	0.097	0.994	0.006	2.304	0.010
Feldspar	36.18	0.21	15.37	0.10	16.14	0.113	0.948	0.005	2.246	0.011
Feldspar	36.12	0.15	15.32	0.07	16.07	0.076	0.953	0.003	2.249	0.004
Feldspar Average	35.51		15.30		15.46		0.989		2.296	
$2\sigma_{mean}$	0.11		0.03		0.13		0.009		0.012	
%	0.3%		0.2%		0.8%		0.9%		0.5%	

Sample: Nushan NS214

Mineral	$^{208}Pb/^{204}Pb$	$2\sigma_{(mean)}$	$^{207}Pb/^{204}Pb$	$2\sigma_{(mean)}$	$^{206}Pb/^{204}Pb$	$2\sigma_{(mean)}$	$^{207}Pb/^{206}Pb$	$2\sigma_{(mean)}$	$^{208}Pb/^{206}Pb$	$2\sigma_{(mean)}$
Feldspar	35.76	0.12	15.13	0.08	15.10	0.08	1.005	0.002	2.370	0.007
Feldspar	35.81	0.08	15.15	0.04	15.26	0.03	0.941	0.002	2.348	0.004
Feldspar	35.78	0.18	15.15	0.10	15.24	0.07	0.993	0.004	2.351	0.005
Feldspar	35.59	0.15	15.11	0.07	14.86	0.06	1.015	0.003	2.397	0.007
Feldspar	35.73	0.30	15.11	0.07	15.17	0.07	0.992	0.004	2.359	0.011
Feldspar	35.32	0.27	15.02	0.18	14.52	0.09	1.027	0.010	2.429	0.019
Feldspar	35.86	0.18	15.16	0.09	15.18	0.10	0.999	0.004	2.360	0.009
Feldspar Average	35.77		15.13		15.10		1.00		2.37	
$2\sigma_{mean}$	0.13		0.04		0.15		0.01		0.02	
%	0.4%		0.3%		1.0%		1.4%		0.7%	

Sample: Olmani OM04-03

Mineral	$^{208}Pb/^{204}Pb$	$2\sigma_{(mean)}$	$^{207}Pb/^{204}Pb$	$2\sigma_{(mean)}$	$^{206}Pb/^{204}Pb$	$2\sigma_{(mean)}$	$^{207}Pb/^{206}Pb$	$2\sigma_{(mean)}$	$^{208}Pb/^{206}Pb$	$2\sigma_{(mean)}$
Feldspar	39.99	0.19	15.89	0.09	18.71	0.08	0.85	0.00	2.14	0.06
Feldspar	39.82	0.33	15.84	0.02	18.67	0.21	0.85	0.01	2.12	0.02
Feldspar	40.01	0.29	15.94	0.11	18.75	0.14	0.85	0.00	2.13	0.00
Feldspar	40.01	0.28	15.87	0.13	18.71	0.11	0.85	0.00	2.14	0.01
Feldspar	39.73	0.43	15.65	0.16	18.70	0.23	0.84	0.01	2.12	0.01
Feldspar	40.23	0.24	15.83	0.13	18.91	0.11	0.84	0.00	2.13	0.01
Feldspar	40.42	0.24	15.94	0.15	18.99	0.16	0.84	0.00	2.13	0.01
Feldspar	40.04	0.21	15.98	0.09	18.69	0.09	0.85	0.00	2.14	0.01
Feldspar Average	40.03		15.87		18.77		0.847		2.132	
$2\sigma_{mean}$	0.15		0.07		0.08		0.005		0.005	
%	0.4%		0.5%		0.4%		0.6%		0.3%	

Sample: Zhouba ZB-18

Mineral	$^{208}Pb/^{204}Pb$	$2\sigma_{(mean)}$	$^{207}Pb/^{204}Pb$	$2\sigma_{(mean)}$	$^{206}Pb/^{204}Pb$	$2\sigma_{(mean)}$	$^{207}Pb/^{206}Pb$	$2\sigma_{(mean)}$	$^{208}Pb/^{206}Pb$	$2\sigma_{(mean)}$
Feldspar	38.51	0.97	15.50	0.44	16.98	0.42	0.913	0.015	2.259	0.020
Feldspar	38.90	1.74	15.79	1.19	16.75	1.33	0.897	0.006	2.217	0.014
Feldspar	38.78	1.65	15.65	0.66	17.24	0.74	0.908	0.005	2.249	0.008
Feldspar	38.48	0.43	15.42	0.19	16.96	0.19	0.912	0.001	2.269	0.002
Feldspar	38.08	1.42	15.47	0.66	16.99	0.81	0.898	0.016	2.209	0.038
Feldspar	38.01	0.64	15.32	0.26	17.12	0.28	0.895	0.004	2.219	0.008
Feldspar	37.90	1.41	15.66	0.63	17.16	0.63	0.908	0.011	2.208	0.026
Feldspar	36.99	0.24	15.01	0.12	16.87	0.12	0.889	0.008	2.201	0.015
Feldspar	37.81	0.43	15.32	0.19	17.13	0.23	0.895	0.004	2.202	0.011
Feldspar	38.15	0.69	15.34	0.33	17.10	0.39	0.894	0.005	2.227	0.014
Feldspar	37.28	0.47	15.09	0.23	17.00	0.26	0.896	0.010	2.195	0.016
Feldspar	37.84	0.71	15.35	0.30	17.15	0.33	0.894	0.003	2.205	0.005
Feldspar	37.33	0.35	15.30	0.19	17.01	0.21	0.898	0.007	2.204	0.020
Feldspar	37.97	0.97	15.36	0.38	17.20	0.42	0.895	0.003	2.205	0.006
Feldspar	38.17	0.45	15.54	0.17	17.37	0.19	0.896	0.003	2.198	0.007
Feldspar	37.92	0.49	15.35	0.21	17.15	0.21	0.895	0.002	2.211	0.004
Feldspar	37.52	1.22	15.28	0.54	16.93	0.53	0.903	0.009	2.216	0.016
Feldspar	37.00	1.16	15.24	0.52	16.68	0.60	0.910	0.010	2.213	0.028
Feldspar	37.77	0.26	15.36	0.11	17.08	0.11	0.900	0.002	2.213	0.005
Feldspar	37.70	0.38	15.35	0.17	17.01	0.19	0.909	0.004	2.226	0.014
Zircon	59.87	5.90	27.99	4.89	135.43	42.12	0.229	0.042	5.482	0.129
Feldspar Average	37.91		15.39		17.04		0.900		2.217	
$2\sigma_{mean}$	0.23		0.08		0.07		0.003		0.009	
%	0.6%		0.5%		0.4%		0.3%		0.4%	

Sample: Zhouba ZB-20

Mineral	$^{208}Pb/^{204}Pb$	$2\sigma_{(mean)}$	$^{207}Pb/^{204}Pb$	$2\sigma_{(mean)}$	$^{206}Pb/^{204}Pb$	$2\sigma_{(mean)}$	$^{207}Pb/^{206}Pb$	$2\sigma_{(mean)}$	$^{208}Pb/^{206}Pb$	$2\sigma_{(mean)}$
Feldspar	38.53	0.17	15.68	0.07	18.29	0.08	0.8576	0.0003	2.1075	0.0006
Feldspar	38.51	0.10	15.68	0.04	18.29	0.05	0.8579	0.0006	2.1068	0.0005
Feldspar	38.60	0.10	15.69	0.04	18.32	0.05	0.8567	0.0004	2.1084	0.0011
Feldspar	38.62	0.10	15.71	0.04	18.34	0.05	0.8570	0.0005	2.1067	0.0008
Feldspar	38.59	0.09	15.69	0.04	18.32	0.04	0.8571	0.0005	2.1068	0.0011
Feldspar	38.56	0.07	15.70	0.03	18.30	0.03	0.8576	0.0002	2.1072	0.0005
Feldspar	38.56	0.07	15.69	0.03	18.30	0.03	0.8578	0.0002	2.1076	0.0006
Feldspar	38.62	0.08	15.72	0.04	18.32	0.04	0.8586	0.0003	2.1072	0.0007
Feldspar	38.53	0.13	15.69	0.05	18.29	0.06	0.8582	0.0003	2.1068	0.0007
Feldspar	38.55	0.07	15.69	0.03	18.26	0.03	0.8595	0.0005	2.1096	0.0014
Feldspar Average	38.57		15.70		18.30		0.858		2.107	
$2\sigma_{mean}$	0.08		0.03		0.05		0.002		0.002	
%	0.2%		0.2%		0.3%		0.2%		0.1%	

Sample: Zhouba ZB-21

Mineral	$^{208}Pb/^{204}Pb$	$2\sigma_{(mean)}$	$^{207}Pb/^{204}Pb$	$2\sigma_{(mean)}$	$^{206}Pb/^{204}Pb$	$2\sigma_{(mean)}$	$^{207}Pb/^{206}Pb$	$2\sigma_{(mean)}$	$^{208}Pb/^{206}Pb$	$2\sigma_{(mean)}$
Feldspar	37.83	0.15	15.54	0.06	17.38	0.07	0.894	0.001	2.177	0.002
Feldspar	37.86	0.07	15.55	0.03	17.41	0.03	0.894	0.001	2.175	0.001
Feldspar	37.84	0.06	15.52	0.03	17.40	0.02	0.893	0.001	2.175	0.001
Feldspar	37.87	0.07	15.56	0.03	17.42	0.03	0.893	0.001	2.173	0.001
Feldspar	37.85	0.15	15.52	0.06	17.41	0.08	0.891	0.001	2.171	0.002
Feldspar	37.81	0.13	15.51	0.05	17.36	0.06	0.892	0.001	2.176	0.003
Feldspar	37.76	0.21	15.50	0.09	17.35	0.10	0.893	0.001	2.176	0.002
Feldspar	37.82	0.10	15.56	0.05	17.41	0.05	0.893	0.002	2.173	0.003
Feldspar	37.87	0.11	15.55	0.04	17.40	0.05	0.894	0.001	2.176	0.011
Feldspar	37.92	0.23	15.56	0.10	17.44	0.10	0.892	0.002	2.173	0.004
Feldspar Average	37.84		15.54		17.40		0.8929		2.175	
$2\sigma_{mean}$	0.03		0.01		0.02		0.0005		0.001	
%	0.1%		0.1%		0.1%		0.1%		0.1%	

Bibliography

Achterbergh, E., Ryan, C., Jackson, S., and Griffin, W. (2001). Appendix 3: Data reduction software for LA-ICP-MS in: P. Sylvester (Editor), Laser Ablation-ICP-MS in the Earth Sciences. *Mineralogical Association of Canada*, Short Course Series(243).

Aulbach, S., Rudnick, R. L., and McDonough, W. F. (2008). Li-Sr-Nd isotope signatures of the plume and cratonic lithospheric mantle beneath the margin of thhe rifted Tanzanian Craton (Labait). *Contributions to Mineralogy and Petrology*, 155:79–92.

Baker, J., Peate, D., Waight, T., and Meyzen, C. (2004). Pb isotopic analysis of standards and samples using a Pb-207-Pb-204 double spike and thallium to correct for mass bias with a double-focusing MC-ICP-MS. *Chemical Geology*, 211(3-4):275–303.

Bellucci, J. J., McDonough, W. F., and Rudnick, R. L. (2011). Thermal history and origin of the Tanzanian Craton from Pb isotope thermochronology of feldspars from lower crustal xenoliths. *Earth and Planetary Science Letters*, 301(3-4):493–501.

Belshaw, N., Freedman, P., O'Nions, R., Frank, M., and Guo, Y. (1998). A new variable dispersion double-focusing plasma mass spectrometer with performance illustrated for Pb isotopes. *Journal of Mass Spectrometry*, 181:55–88.

Blondes, M. S., Rudnick, R. L., Ramezani, J., Piccoli, P. M., and Bowring, S. A. (2011). Slow cooling in the lowermost crust of a continent-continent collision: Evidence from accessory phase U-Pb thermochronology of deep crustal xenoliths from the Mozambique Belt, Tanzania. *Earth and Planetary Science Letters*, In Review.

Bodet, F. and Scharer, U. (2001). Pb isotope systematics and time-integrated Th/U of SE-Asian continental crust recorded by single K-feldspar grains in large rivers. *Chemical Geology*, 177(3-4):265–285.

Bolhar, R., Kamber, B. S., and Collerson, K. D. (2007). U-Th-Pb fractionation in Archean lower continental crust: Implications for terrestrial Pb isotope systematics . *Earth and Planetary Science Letters*, 254(1-2):127–145.

Boyd, F. R. (1973). A pyroxene geotherm. *Geochimica et Cosmochimica Acta*, 37:2533–2546.

Brill, R. and Wampler, J. (1967). Isotope studies of ancient lead. *American Journal of Archaeology*, 71:63–77.

Burton, K., Schiano, P., Birck, J., Allegre, C., Rehkamper, M., Halliday, A., and Dawson, J. (2000). The distribution and behaviour of rhenium and osmium

amongst mantle minerals and the age of the lithospheric mantle beneath Tanzania. *Earth and Planetary Science Letters*, 183(1-2):93–106.

Campbell, A. and Humayun, M. (2005). Compositions of group IVB iron meteorites and their parent melt. *Geochimica et Cosmochimica Acta*, 69:4733–4744.

Carlson, R. W., Pearson, D. G., and James, D. E. (2005). Physical, chemical, and chronological characteristics of the continental mantle. *Reviews of Geophysics*, 43:2–24.

Chapman, D. S. and Pollack, H. N. (1977). Regional geotherms and lithospheric thickness. *Geology*, 5:265–268.

Chauvel, C., Dupre', B., and Arndt, N. (1993). Pb and Nd isotopic correlation in Belingwe komatiites and basalts In: Bickle, M.J., Nisbet, E.G. (Eds). *The Geology of the Belingwe Greenstone Belt, Zimbabwe: A Study of the Evolution of Archean Continental Crust*, Balkema, Rotterdam: Geological Society of Zimbabwe Special Publication(2):167–174.

Chen, J. and Wasserburg, G. (1983). The isotopic composition of silver and lead in 2 iron-meteorites-Cape-York and Grant. *Geochimica et Cosmochimica Acta*, 47(10):1725–1737.

Chen, L. (2010). Concordant structural variations from the surface to the base of the upper mantle in the North China Craton and its tectonic implications. *Lithos*, 120(1-2):96–115.

Chen, S., O'Reilly, S., Zhou, X., Griffin, W., Zhang, G., Sun, M., Feng, J., and Zhang, M. (2001). Thermal and petrological structure of the lithosphere beneath Hannuoba, Sino-Korean Craton, China: Evidence from xenoliths. *Lithos*, 56(4):267–301.

Cherniak, D. J. (1995). Diffusion of lead in plagioclase and K-feldspar-an investigation using Rutherford backscattering and resonant nuclear-reaction analysis. *Contributions to Mineralogy and Petrology*, 120(3-4):358–371.

Cherniak, D. J., Lanford, W. A., and Reyerson, F. J. (1991). Lead diffusion in apatite and zircon using ion-implantation and Rutherford backscattering techniques. *Geochimica et Cosmochimica Acta*, 55(6):1663–1673.

Cherniak, D. J. and Watson, E. (2001). Pb diffusion in zircon. *Chemical Geology*, 172(1-2):5–24.

Chesley, J. T., Rudnick, R. L., and Lee, C. T. (1999). Re-Os systematics of mantle xenoliths from the East African Rift: Age, structure, and history of the Tanzanian craton. *Geochimica et Cosmochimica Acta*, 63(7-8):1203–1217.

Choi, S., Mukasa, S., X.H., Z., Xian, X., and Androniko, A. (2008). Mantle dynamics beneath East Asia constrained by Sr, Nd, Pb and Hf isotopic systematics of ultramafic xenoliths and their host basalts from Hannuoba, North China. *Chemical Geology*, 248(1-2):40–61.

Christensen, N. I. and Mooney, W. D. (1995). Seismic Velocity Structure and Composition of the Continental Crust: A Global View. *Journal of Geophysical Research-Solid Earth*, 100:9761–9788.

Cohen, R., O'Nions, R. K., and Dawson, J. B. (1984). Isotope Geochemistry of Xenoliths from East-Africa-Implications for Development of Mantle Reservoirs and their Interaction. *Earth and Planetary Science Letters*, 68(2):209–220.

Collins, A., Reddy, S., Buchan, C., and Mruma, A. (2004). Temporal constraints on Palaeoproterozoic eclogite formation and exhumation (Usagaran Orogen, Tanzania). *Earth and Planetary Science Letters*, 224(1-2):175–192.

Coomer, P. G. and Robertson, D. K. (1974). A lead isotope study of Archean mineralized areas in Tanzania. *Journal of the Geological Society*, 130:449–460.

Cumming, G., Kesler, S., and Krstic, D. (1979). Isotopic composition of lead in Mexican Mineral Deposits. *Economic Geology*, 74:1395–1407.

Cutten, H., Johnson, S. P., and De Waele, B. (2006). Protolith ages and timing of metasomatism related to the formation of whiteschists at Mautia Hill, Tanzania: Implications for the assembly of Gondwana. *Journal of Geology*, 114(683-698).

Dawson, J., James, D., Paslick, C., and Halliday, A. (1997). Ultrabasic potassic low-volume magmatism and continental rifting in north-central Tanzania: Association with enhanced heat flow. *Geologiya i Geofizika*, 38(1):67–77.

Dawson, J. and Smith, J. (1988). Metasomatised and veined upper-mantle xenoliths from Pello Hill, Tanzania: evidence for anomalously-light mantle beneath the Tanzanian sector of the East African Rift Valley. *Contributions to Mineralogy and Petrology*, 100(510-527).

Dawson, J. B. (1992). Neogene tectonics and volcanicity in the North tanzania sector of the Gregory rift-valley-Contrasts with the Kenya sector. *Tectonophysics*, 204(1-2):81–92.

Day, J. M. D., Ash, R., Yang, Y., Bellucci, J. J., Rumble III, D., McDonough, W. F., Walker, R., and Taylor, L. (2009). Early formation of evolved asteroidal crust. *Nature*, 457:179–182.

de Laeter, J. R., Bohlke, J. K., Bievre, P. D., Hidaka, H., Peiser, H. S., Rosman, K. J. R., and Taylor, P. D. P. (2003). Atomic weights of the elements: Review 2000. *Pure and Applied Chemistry*, 75(6):683–800.

Dodson, M. H. (1973). Closure temperature in cooling geochronological and petrological systems. *Contributions to Mineralogy and Petrology*, 40:259–274.

Dupre', B. and Arndt, N. (1990). Pb isotopic compositions of Archean komatiites and sulfides. *Chemical Geology*, 85:35–56.

Fan, Q. and Liu, R. (1996). The high-temperature granulite xenoliths in Hannuoba basalt. *China Science Bulletin*, 41:235–238.

Farmer, G. L. (2003). Continental Basaltic Rocks. *In the Crust (ed. R.L. Rudnick) Vol. 3, Treatise on Geochemistry (eds. H.D. Holand and K.K. Turekian)*, Oxford:Elsevier-Pergamon:85–121.

Frei, R. and Kamber, B. S. (1995). Single mineral Pb-Pb dating. *Earth and Planetary Science Letters*, 129(1-4):261–268.

Frei, R., Villa, I. M., Nagler, T. F., Kramers, J. D., Przybylowicz, W. J., Prozesky, V. M., Hoffman, B. A., and Kamber, B. S. (1997). Single mineral dating by the Pb-Pb step-leaching method: Assessing the mechanisms. *Geochimica et Cosmochimica Acta*, 61(2):393–414.

Fritz, H., Tenczer, V., Hauzenberger, C., Wallbrecher, E., and Muhongo, S. (2009). Hot granulite nappes - Tectonic styles and thermal evolution of the Proterozoic granulite belts in East Africa. *Tectonophysics*, 477(3-4, Sp. Iss. SI):160–173.

Gancarz, A. and Wasserburg, G. (1977). Initial Pb of the Amîtsoq gneiss, West Greenland, and implications for the age of the Earth. *Geochimica et Cosmochimica Acta*, 41(9):1283–1301.

Gao, S., Rudnick, R., Yuan, H., Liu, X., Liu, Y., Xu, W., Ling, W., Ayers, J., Wang, X., and Wang, Q. (2004). Recycling lower continental crust in the North China craton. *Nature*, 432(7019):892–897.

Gao, S., Rudnick, R. L., Carlson, R. W., McDonough, W. F., and Liu, Y. (2002). Re-Os evidence for replacement of ancient mantle lithosphere beneath the North China Craton. *Earth and Planetary Science Letters*, 198:307–322.

Griffin, W., Zhang, A., O'Reilly, S., and Ryan, C. (1998). Phanerozoic evolution of the lithosphere beneath the Sino-Korean Craton. *Mantle Dynamics and Plate Interactions in East Asia, American Geophysical Union*, pages 107–126.

Hepworth, J. (1972). The Mozambique orogenic belt and its foreland in northeast Tanzania: a photogeologically-based study. *Journal of the Geological Society London*, 128:491–494.

Hirata, T., Hayana, Y., and Ohno, T. (2003). Improvements in precision of isotopic ratio measurements using laser ablation-multiple collector-ICP-mass spectrometry: reduction in changes in measured isotopic ratios. *Journal of Analytical Atomic Spectrometry*, 18(1283-1288).

Holmes, A. (1946). An estimate of the age of the Earth. *Nature*, 157:680–684.

Housh, T. and Bowring, S. A. (1991). Lead isotopic heterogeneities within alkali feldspars-Implications for the determination of initial lead isotopic compositions. *Geochimica et Cosmochimica Acta*, 55(8):2309–2316.

Houtermans, F. (1946). Die Isotopenhaufigkeiten im naturlichen Blei und das Alter de Urans. *Naturwissenschaften*, 33:185–286.

Hu, S., He, L., and Wang, J. (2000). Heat flow in the continental area of china: A new data set. *Earth and Planetary Science Letters*, 179:407–419.

Huang, X., Xu, Y., and Liu, D. (2004). Geochronology, petrology and geochemistry of the granulite xenoliths from Nushan, east China: Implication for a heterogeneous lower crust beneath the Sino-Korean Craton. *Geochimica et Cosmochimica Acta*, 68(1):127–149.

Jaffey, A., Flynn, K., Glendenin, L., Bentley, W., and Essling, A. (1971). Precision measurement of half-lives and specific activities of ^{235}U and ^{238}U. *Physics Review*, 4:1889–1906.

Jochum, K., Stoll, B., and Herwig, K. (2006). Improved in situ Pb isotope analysis of low Pb samples by LA-ICP-MS using a solid-state 193 nm Nd: YAG laser. *Geochimica et Cosmochimica Acta*, 70(A294).

Joel, E., Olin, J., Blackman, M., and Barnes, I. (1988). Lead isotope studies of Spanish, Spanish-colonial and Mexican majolica. *In: Farqubar, R.M., Hancock, R.G.V., Pavlish, L.A. (Eds). Proceedings of the 26th International Archaeometry Symposium. University of Toronto Archaeometry Laboratory, Toronto*, pages 188–185.

Johnson, S. P., Cutten, H. N. C., Muhongo, S., and Waele, B. (2003). Neoarchean magmatism and metamorphism of the western granulites in the central domain of the Mozambique belt, Tanzania: U-Pb shrimp geochronology and PT estimates. *Tectonophysics*, 375(1-4):125–145.

Jones, A., Smith, J., Dawson, J., and Hansen, E. (1983). Metamorphism, Partial Melting, and K-Metasomatism of Garnet-Scapolite-Kyanite Granulite Xenoliths from Lashaine, Tanzania. *Journal of Geology*, 91(2):143–165.

Kamber, B., Collerson, K., Moorbath, S., and Whitehouse, M. (2003). Inheritance of early Archaean Pb-isotope variability from long-lived Hadean protocrust. *Contributions to Mineralogy and Petrology*, 145(1):25–46.

Kent, A. J. R. (2008a). In situ analysis of Pb isotope ratios using laser ablation MC-ICP-MS: Controls on precision and accuracy and comparison between Faraday cup and ion counting systems. *Journal of Analytical Atomic Spectrometry*, 23(7):968–975.

Kent, A. J. R. (2008b). Lead isotope homogeneity of NIST SRM 610 and 612 glass reference materials: Constraints from laser ablation multicollector ICP-MS(LA-MC-ICP-MS) analysis. *Geostandards and Geoanalytical Research*, 32(2):129–147.

Kern, H., Gao, S., and Liu, Q. (1996). Seismic properties and densities of the middle and lower crustal rocks exposed along the North China Geoscience Transect. *Earth and Planetary Science Letters*, 139(3-4):439–455.

Kröner, A., Compston, W., Zhang, G., Guo, A., and Todt, W. (1988). Age and Tectonic Setting of Late Archean Greenstone-Gneiss Terrain in Henan Province, China, as Revealed by Single-Grain Zircon Dating. *Geology*, 16(3):211–215.

Kröner, A., Muhongo, S., Hegner, E., and Wingate, M. (2003). Single-zircon geochronology and Nd isotopic systematics of Proterozoic high-grade rocks from the Mozambique belt of southern Tanzania (Masasi area): implications for Gondwana assembly. *Journal of the Geological Society London*, 160(745-757).

Kusky, T. and Li, J. (2003). Paleoproerozoic tectonic evolution of the North China Craton. *Journal of Asian Earth Sciences*, 22(4):383–397.

Kusky, T., Li, J., and Tucker, R. (2001). The Archean Dongwanzi ophiolite complex, North China craton: 2.505-billion-year-old oceanic crust and mantle. *Science*, 292(5519):1142–1145.

Le Roux, L. and Glendenin, L. (1963). Half-life of ^{232}Th. *Proceedings of the National Meeting on Nuclear Energy, Pretoria South Africa*, pages 83–94.

Lee, C. T. and Rudnick, R. L. (1999). Compositionally stratified cratonic lithosphere: petrology and geochemistry of peridotite xenoliths from the Labait tuff cone, Tanzania. *Proceedings of the Seventh International Kimberlite Conference*, pages 503–521.

Li, C., van der Hilst, R., and Toksoz, A. (2006). Constraining P-wave velocity variaitons in the upper mantle beath Southeast Asia. *Physics of the Earth and Planetary Interiors*, 154:180–195.

Li, J., Hou, G., Huang, X., Zhang, Z., and Qian, X. (2001). Constraints on the sueprcontinental cycles: Evidence from Precambrian geology of North China Craton. *Acta Petrologica Sinica*, 17(177-186).

Li, J., Qian, X., Huang, X., and Liu, S. (2000). Tectonic framework of the North China Craton and its cratonization in the early Precambrian. *Acta Petrologica Sinica*, 16:1–10.

Lister, F. and Lister, R. (1982). Sixteenth Century Majolica Pottery in the Valley of Mexico. *In: Anthropological Papers Series of the University of Arizona, The University of Arizona Press, Tuscon*, 39.

Liu, J., Rudnick, R., Walker, R., Gao, S., Wu, F., and Piccoli, P. M. (2010). Processes controlling highly siderophile element fractionations in xenolithic peridotites and their influence on Os isotopes. *Earth and Planetary Science Letters*, 297(1-2):287–297.

Liu, Y., Gao, S., Jin, S., Hu, S., Sun, M., Zhao, Z., and Feng, J. (2001). Geochemistry and petrogenesis of lower crustal xenoliths from Hannuoba, North China: Implications for the contintinental lower crustal composition and evolution at convergent margin. *Geochimica et Cosmochimica Acta*, 65(15):2589–2604.

Liu, Y., Gao, S., Liu, X., Chen, X., Zhang, W., and Wang, X. (2003). Thermodynamic evolution of lithosphere of the North China Craton: records from lower crust and upper mantle xenoliths from Hannuoba. *China Science Bulletin*, 48:1575–1581.

Liu, Y., Gao, S., Yuan, H., Zhou, L., Liu, X., Wang, X., Hu, Z., and Wang, L. (2004). U-Pb zircon ages and Nd, Sr, and Pb isotopes of lower crustal xenoliths from North China Craton: insights on evolution of lower continental crust. *Chemical Geology*, 211(1-2):87–109.

Lu, L., Xu, X., and Liu, F. (1996). Early Precambrian Khondalite Series of North China. *Changchun Publishing House, Changchun*, pages 1–272.

Ludwig, K. R. (2003). Isoplot. Program and documentation, version 2.95. *Revised edition of US Open-File report*, pages 91–445.

Ludwig, K. R. and Silver, L. T. (1977). Lead-isotope inhomogeneity in Precambrian igneous K-feldspars. *Geochimica et Cosmochimica Acta*, 41(10):1457–1471.

Maboko, M. A. H. (2000). Nd and Sr isotopic investigation of the Archean-Proterozoic boundary in north eastern Tanzania: constraints on the nature of Neoproterozoic tectonism in the Mozambique Belt. *Precambrian Research*, 102(1-2):87–98.

Mansur, A., Manya, S., Timpa, S., and Rudnick, R. L. (2011). Origin of Archean lower continental crust, northern Tanzania: A xenolith study. *Journal of Petrology*, In Review.

Manya, S., Kobayashi, K., Maboko, M. A. H., and Nakamura, E. (2006). Ion microprobe zircon U-Pb dating of the late Archean metavolcanics and associated granites of the Musoma-Mara Greenstone Belt, Northeast Tanzania: Implications for the geological evolution of the Tanzania Craton. *Journal of African Earth Sciences*, 45(3):355–366.

Menzies, M., Fan, W., and Zhang, M. (1993). Paleozoic and Cenozoic lithoprobes and the loss of >120 km of Archean lithosphere, Sino-Korean craton. *Geological Society of London, Special Publication Magmatic Processes and Plate Tectonics*, 76(71-81).

Michuat, C., Jaupart, C., and Bell, D. (2007). Transient geotherms in Archean continental lithosphere: New constraints on thickness and heat production of the subcontinental lithospheric mantle. *Journal of Geophysical Research-Solid Earth*, 112(B4):B04408.

Möller, A., Appel, P., Mezger, K., and Schenk, V. (1995). Evidence for a 2 Ga subduction zone-eclogites in the Usagaran belt of Tanzania. *Geology*, 23(12):1067–1070.

Möller, A., Mezger, K., and Schenk, V. (1998). Crustal age domains and the evolution of the continental crust in the Mozambique Belt of Tanzania: Combined Sm-Nd, Rb-Sr, and Pb-Pb isotopic evidence. *Journal of Petrology*, 39(4):749–783.

Möller, A., Mezger, K., and Schenk, V. (2000). U-Pb dating of metamorphic minerals: Pan-African metamorphism and prolonged slow cooling of high pressure granulites in Tanzania East Africa. *Precambrian Research*, 104:123–145.

Nyblade, A. (1997). Heat flow across the East African Plateau. *Geophysical Research Letters*, 24(16):2083–2086.

Nyblade, A. and Brazier, R. (2002). Precambrian lithospheric controls on the development of the East African rift system. *Geology*, 30(8):755–758.

Nyblade, A. A. and Pollack, H. N. (1993). A global analysis of heat-flow from Precambrian terrains-Implications for the thermal structure of Archean and Proterozoic lithosphere. *Journal of Geophysical Research-Solid Earth*, 98(B7):12207–12218.

Nyblade, A. A., Pollack, H. N., Jones, D. L., Podmore, F., and Mushayanbedvu, M. (1990). Terrestrial heat-flow in East and Southern Africa. *Journal of Geophysical Research-Solid Earth and Planets*, 95(B11):17371–17384.

O'Neil, J., Carlson, R. W., Francis, D., and Stevenson, R. (2008). Neodymium-142 Evidence for Hadean Mafic Crust. *Science*, 321(5897):1828–1831.

Oversby, V. (1975). Lead isotope systematics of Archean acid intrusives in the Kalgoorlie-Norseman area, Western Australia. *Geochimica et Cosmochimica Acta*, 39:1107–1125.

Oversby, V. (1978). Lead isotope systematics of Archean plutonic rocks. *Earth and Planetary Science Letters*, 38(1):237–248.

Paslick, C., Halliday, A., James, D., and Dawson, J. B. (1995). Enrichment of the continental lithosphere by OIB melts: Isotopic evidence from the volcanic province of northern Tanzania. *Earth and Planetary Science Letters*, 130:109–126.

Patterson, C. (1956). Age of Meteorites and the Earth. *Geochimica et Cosmochimica Acta*, 10(4):230–237.

Paul, B., Woodhead, J. D., and Hergt, J. (2005). Improved in situ isotope analysis of low-Pb materials using LA-MC-ICP-MS with parallel ion counter and faraday detection. *Journal of Analytical Atomic Spectrometry*, 20(12):1350–1357.

Perry, H., Jaupart, C., Mareschal, J., and Bienfait, G. (2006). Crustal heat production in the Superior Province, Canadian Shield, and in North America inferred from heat flow data. *Journal of Geophysical Research-Solid Earth*, 111(B4):B04401.

Pollard, A. (2009). What a long strange trip it's been: lead isotopes and archaeology. *In: Shortland, A.J. Rehren, Th., Freestone, I.C. (Eds.) From Mine to Microscope. Studies in Honour of Mike Tite. Oxbow Books, London.*

Pollard, M., Batt, C., Stern, B., and Young, S. (2007). Analytical Chemistry in Archaeology. *Cambridge Manuals in Archaeology. Cambridge Univeristy Press, Cambridge.*

Rasmussen, K., Malvin, D., Buchwald, V., and Wasson, J. (1984). Compositional trends and coolling rates of group IVB iron meteorites. *Geochimica et Cosmochimica Acta*, 48:805–813.

Reddy, S., Collins, A., and Mruma, A. (2003). Complex high-strain deformation in the Usagaran Orogen, Tanzania: structural setting of Paleoproterozoic eclogites. *Tectonophysics*, 375(1-4):101–123.

Ritsema, J., Ni, S., Helmberger, D., and Crotwell, H. (1998). Evidence for strong shear velocity reductions and velocity gradients in the lower mantle beneath Africa. *Geophysical Research Letters*, 25(23):4245–4248.

Rudnick, R., Gao, S., Ling, W., Liu, Y., and McDonough, W. (2004). Petrology and geochemistry of spinel peridotite xenoliths from Hannuoba and Qixia, North China craton. *Lithos*, 77(1-4):609–637.

Rudnick, R., McDonough, W., and Chappell, B. (1993). Carbonatite metasomatism in the northern Tanzanian mantle: petrographic and geochemical characteristics. *Earth and Planetary Science Letters*, 114:463–476.

Rudnick, R. L. (1992). Xenoliths-samples of the lower continental crust, in Continental Lower Crust. *Eds. Fountain, D.M., Arculus, R., and Kay R.W.*

Rudnick, R. L. and Fountain, D. M. (1995). Nature and composition of the continental-crust - A lower crustal perspective. *Reviews of Geophysics*, 33(3):267–309.

Rudnick, R. L. and Gao, S. (2003). The composition of the continental crust. *In the Crust (ed. R.L. Rudnick) Vol. 3, Treatise on Geochemistry (eds. H.D. Holand and K.K. Turekian)*, Elsevier-Pergamon, Oxford:1–64.

Rudnick, R. L. and Goldstein, S. L. (1990). The Pb isotopic copositions of lower crustal xenoliths and the evolution of the lower crustal Pb. *Earth and Planetary Science Letters*, 98:192–207.

Rudnick, R. L., Ireland, T., Gehrels, G., Irving, A. J., Chesley, J. T., and Hanchar, J. M. (1999). Dating mantle metasomatism: U-Pb geochronology of zircons in cratonic mantle xenoliths from Montana and Tanzania (In Gurney, J.J., Gurney, J.L, Pascoe, M.D., and Richardson, S.H., eds.):. *The Nixon Volume, Proceedings of the Seventh International Kimberlite Conference, p. 728-735.*

Rudnick, R. L., McDonough, W. F., and O'Connell, R. J. (1998). Thermal structure, thickness, and composition of continental lithosphere. *Chemical Geology*, 145:395–411.

Rudnick, R. L., McDonough, W. F., and Orpin, A. (1994). Northern Tanzanian peridotite xenoliths: a comparison with Kaapvaal peridotites and inferences on metasomatic interactions. *In (Meyer, H.O.A. and Leonardos, O., eds.) Kimberlites, Related Rocks, and Mantle Xenoliths*, Vol. 1 (Proceedings Fifth Int. Kimb. Conference), C.P.R.M., Brasilia:336–353.

Rudnick, R. L. and Nyblade, A. A. (1999). The composition and thickness of Archean continental roots: constraints from xenolith thermobarometry in Mantle Petrology: Field Observations and High-Pressure Experimentation: A Tribute to Francis R. (Joe) Boyd in (Fei, Y-W, Bertka, C.M., and Mysen, B.O., eds.). *Geochemical Society Special Publications*, 6:3–12.

Rudnick, R. L. and Taylor, S. (1987). The composition and petrogenesis of the lower crust - a xenolith study. *Journal of Geophysical Research-Solid Earth and Planets*, 92(B13):13981–14005.

Ryan, D., Holzbecher, J., and Brooks, R. (1990). Rhodium and osmium in iron meteorites. *Chemical Geology*, 85(3-4):295–303.

Sandiford, M. and McLaren, S. (2002). Tectonic feedback and the ordering of heat producing elements within the continental lithosphere. *Earth and Planetary Science Letters*, 204(1-2):133–150.

Santos-Zalduegui, J., Garcia de Madinabeita, S., and Gil Ibarguchi, J. (2004). A lead isotope database: the los Pedroches-Alcudia area (Spain): implications for archaeometallurgical connections across Southwestern and Southeastern Iberia. *Archaeometry*, 46:625–634.

Schmitz, M. D. and Bowring, S. A. (2003). Thermal structure, thickness, and composition of continental lithosphere. *Contributions to Mineralogy and Petrology*, 144:592–618.

Schulter, T. (1997). Geology of East Africa. *Geology of East Africa. Borntraeger Verlagsbuchhandlung, Science Publishers, Stuttgart.*

Simon, J. I., Reid, M., and Young, E. (2007). Lead isotopes by LA-MC-ICPMS: Tracking the emergence of mantle signatures in an evolving silicic magma system. *Geochimica et Cosmochimica Acta*, 71(2014-2035).

Smith, J. and Brown, W. (1988). Crystal structures, physical, chemical, and microtextural properties in Feldspar Minerals. 2nd edition. *Springer Verlagsbuchhandlung, Heidelberg, New York, London, Paris, and Tokyo*.

Stacey, J. and Kramers, J. (1975). Approximation of terrestrial lead isotope evolution by a two-stage model. *Earth and Planetary Science Letters*, 26:207–221.

Stos-Gale, Z. and Gale, H. (2009). Metal provenancing using isotopes and the Oxford archaeological lead isotope database (OXALID). *Journal of Archaeological and Anthropological Sciences*, 1:195–213.

Tao, W. and Shen, Z. (2008). Heat flow distribution in Chinese continent and its adjacent areas. *Progress in Natural Science*, 18:843–849.

Taylor, S. and Mclennan, S. (1985). *The Continental Crust: Its Composition and Evolution*. Blackwell, Oxford.

Taylor, S. and Mclennan, S. (1995). The Geochemical Evolution of the Continental Crust. *Reviews of Geophysics*, 33(2):241–265.

Tenczer, V., Hauzenberger, C., Fritz, H., Whitehouse, M., Mogessie, A., Wallbrecher, E., Muhongo, S., and Hoinkes, G. (2006). Anorthosites in the Eastern Granulites of Tanzania-New SIMS zircon U-Pb age data, petrography and geochemistry. *Precambrian Research*, 148(1-2):85–114.

Tian, Y., Zhao, D., Sun, R., and Teng, J. (2009). Seismic imaging of the crust and upper mantle beneath the North China Craton. *Physics of the Earth and Planetary Interiors*, 172:169–182.

Weerarante, D., Forsyth, D., Fischer, K., and Nyblade, A. (2003). Evidence for an upper mantle plume beneath the Tanzanian craton from Rayleigh wave tomography. *Journal of Geophysical Research-Solid Earth*, 108(B9):2427.

Weis, D., Kieffer, B., Maerschalk, C., Barling, J., de Jong, J., Williams, G. A., Hanano, D., Pretorius, W., Mattielli, N., Scoats, J. S., Goolaerts, A., Friedman, R. M., and Mahoney, J. (2006). High-precision isotopic characterization of USGS reference materials by TIMS and MC-ICP-MS. *Geochemistry Geophysics Geosystems*, 7:Q08006.

Wendlandt, E., Depaolo, D. J., and Baldridge, W. S. (1993). Nd and Sr isotope chronostratigraphy of Colorado Plateau lithosphere: Implications for magmatic and tectonic underplating of the continental crust. *Earth and Planetary Science Letters*, 116(1-4):22–43.

White, W. M., Albarede, F., and Telouk, P. (2000). High-precision analysis of Pb isotope ratios by multi-collector ICP-MS. *Chemical Geology*, 167:257–270.

Wilde, S., Valley, J., Peck, W., and Graham, C. (2001). Evidence from detrital zircons for the existence of continental crust on the Earth 4.4 Gyr ago. *Nature*, 409(6817):175–178.

Wu, F., Walker, R., Ren, X., Sun, D., and Zhou, X. (2003). Osmium isotopic constraints on the age of the lithospheric mantle beneath northeastern China. *Chemical Geology*, 196(1-4):107–129.

Wu, F., Walker, R., Yang, Y., Yuan, H., and Yang, J. (2006). The chemical-temporal evolution of lithospheric mantle underlying the North China Craton. *Geochimica et Cosmochimica Acta*, 70:5013–5034.

Xu, Y. (2001). Thermo-tectonic destruction of the Archean lithospheric keel beneath the Sino-Korean Craton in China: Evidence, timing and mechanism. *Physics and Chemistry of the Earth Part a-Solid Earth and Geodesy*, 26:747–757.

Zartman, R. and Haines, S. (1988). The plumbotectonic model for Pb isotopic systematics among major terrestrial reservoirs-a case for bi-directional transport. *Geochimica et Cosmochimica Acta*, 52(6):1327–1339.

Zartman, R. and Richardson, S. (2005). Evidence from kimberlitic zircon for a decreasing mantle Th/U since the Archean. *Chemical Geology*, 220(3-4):263–283.

Zartman, R. and Wasserburg, G. (1969). The isotopic composition of lead in potassium feldspars from some 1.0 By-old North American igneous rocks. *Geochimica et Cosmochimica Acta*, 33:901–942.

Zhang, H., Goldstein, S. L., Zhou, X., Sun, M., Zheng, J., and Cai, Y. (2008). Evolution of subcontinental lithospheric mantle beneath eastern China: Re-Os isotopic evidence from mantle xenoliths in Paleozoic kimberlites and Mesozoic basalts. *Contributions to Mineralogy and Petrology*, 155:271–293.

Zhao, G., Sun, M., Wilde, S., and Li, S. (2005). Late Archean to Paleoproterozoic evolution of the North China Craton: key issues revisted. *Precambrian Research*, 136:177–202.

Zhao, G., Wilde, S., and Cawood, P. (1999). Thermal evolution of two textural types of mafic granulites in the North China Craton: Evidence for both mantle plume and collisional tectonics. *Geological Magazine*, 136:223–240.

Zhao, G., Wilde, S., Cawood, P., and Lu, L. (2000). Petrology and P-T path of the Fuping mafic granulites: Implications for tectonic evolution of the central zone of the North China Craton. *Journal of Metamorphic Geology*, 18:375–391.

Zhao, G., Wilde, S., Cawood, P., and Sun, M. (2001). Archean blocks and their boundaries in the North China Craton: lithological, geochemical, structural, and P-T path constraints and tectonic evolution. *Precambrian Research*, 107:45–73.

Zhao, G., Wilde, S., Guo, J., Cawood, P., Sun, M., and Li, X. (2010). Single zircon grains record two Paleoproterozoic collisional events in the North China Craton. *Precambrian Research*, 177:266–276.

Zheng, J., Griffin, W., O'Reilly, S., Yang, J., Li, T., Zhang, M., Zhang, R., and Liu, J. (2006). Mineral chemistry of peridotites from Paleozoic, Mesozoic, and Cenozoic lithosphere: Constraints on mantle evolution beneath eastern China. *Journal of Petrology*, 47(11):2233–2256.

Zhu, B. (1998). Theory and Applications of Isotope Systematics in Geosciences: Evolution of Continental Crust and Mantle in China. *Science Press*.